DISS. ETH NO. 22357

Constraints on the source of unrest at the Aluto-Langano geothermal field, Ethiopia, inferred from 3-D interpretation of MT measurements

A dissertation submitted to
ETH ZURICH

for the degree of
DOCTOR OF SCIENCES
(Dr. sc. ETH Zurich)

presented by

FRIEDEMANN SAMROCK
Dipl. Geophys., GAU, Göttingen, Germany

born on March 16th 1983
citizen of Germany

accepted on the recommendation of

PD	Dr. Alexey Kuvshinov	Examiner
Prof.	Dr. Andrew Jackson	Co–examiner
Prof.	Dr. Michael Kendall	Co–examiner
	Dr. Heinrich Brasse	Co–examiner

2015

εἰ γὰρ καὶ τὰ μάλιστα τύχοι τετελεσμένον εἰπών,
αὐτὸς ὅμως οὐκ οἶδε · δόκος δ' ἐπὶ πᾶσι τέτυκται.

Xenophanes of Colophon (ca. * 570 BC, † 475 BC), Fragment 34
for interpretation see e.g. *Lesher* (1978)

Abstract

The global energy demand is ever rising and renewable energies are considered to be a major contributor to any future energy mix. A promising candidate is geothermal energy as it is carbon-neutral and readily available in regions that may have no access to conventional energy resources. Geothermal power generation is most attractive in volcanic regions with ready access to shallow high enthalpy systems. As for instance in Iceland and New Zealand, where a well established infrastructure allows profitable exploitation of geothermal resources accounting in a large part for the local energy production. One of the privileged regions possessing a remarkable, but so far largely untapped geothermal potential is the East African Rift system (EARS). The EARS is an active continental break-up zone hosting numerous young volcanic systems with most of them concentrated along its eastern branch between Mozambique and Ethiopia. Considerable progress in geothermal exploration along the EARS is so far limited to Kenya and Ethiopia, where first geothermal power plants have been installed during the 90s. Currently several geothermal projects are in progress in these regions and a considerable development of the renewable energy sector is expected in the near future. One plant is under construction at Corbetti volcano in Ethiopia, once completed it is estimated to generate over 1000 MW electric power and hereby meant to be Africa's largest geothermal power plant (*Reykjavik Geothermal*, 2014).

Recently the International Renewable Energy Agency (IRENA) presented a strategy to build a *Clean Energy Corridor* stretching from Ethiopia to South Africa to exploit the excellent renewable energy potential along the EARS focusing on hydro, geothermal, solar and wind power (*IRENA Headquarters*, 2013). The aim of this project is to meet the increasing energy demand of the rapidly growing economies in East Africa by massive investment in renewable energy. It is worth noting that the advantage of geothermal sources compared to other renewable sources like wind, solar and hydro power is their independence from weather conditions and their constant output with availability around the clock.

The region of interest addressed in this study is the Main Ethiopian Rift System, which encompasses a number of volcanoes that have been identified as potential high enthalpy geothermal systems in the past (*Endeshaw*, 1988). Some of them are known to be actively deforming with reoccurring periods of uplift and setting as indicated by satellite observations (*Biggs et al.*, 2011). One of the regions where temporal changes take place is the Aluto-Langano volcanic complex. It hosts Ethiopia's currently only producing geothermal power plant, which taps a geothermal system with fluid temperatures exceeding 350 °C (*Gianelli and Teklemariam*, 1993). The observed periods of uplift at Aluto took place in 2004 and 2008, they affected a region of around 100 km^2 and were followed by periods of subsidence. The power plant is located in the center of the deforming region where the maximum amplitudes of unrest occur. This state of play clearly raises the question of the unrest's implication on the plant in terms of productivity and geohazard. The working hypothesis is that the causative source for the

deformation is either in the hydrothermal reservoir, in a deeper magmatic system or in coupled magmatic-hydrothermal system.

The aim of this thesis is to discriminate between the different scenarios and to delineate the nature of the deforming source. In order to do this we conducted magnetotelluric (MT) measurements. This geophysical induction method uses natural occurring time-varying electromagnetic fields to decipher subsurface electrical conductivities and is especially sensitive to high conducting zones, as hydrothermal and magmatic reservoirs usually are (*Muñoz*, 2014). Furthermore it easily covers the necessary exploration depth down to approximately 10 km. In the past years MT has been successfully implemented in geothermal research and has proved to be a reliable and cost-efficient method in identifying high enthalpy geothermal systems on the basis of subsurface conductivities. This is supported by recent and ongoing developments of efficient computational numerical methods, which make it capable to interpret and to invert for MT data in a fully 3-D manner.

The study addressed in this thesis involved the whole process of organizing and planning a field campaign, including logistics and customs clearance. The field measurements in Ethiopia were conducted together with a team of scientists from Addis Ababa University, ETH Zurich, the Geological Survey of Ethiopia and local people from the survey region. In total we installed 46 MT sites covering the extent of the Aluto volcanic complex. The acquired data were processed, modeled and interpreted in context of interdisciplinary studies previously conducted at the Aluto volcanic complex and in the Main Ethiopian Rift System. Our recovered 3-D models reveal an electrical resistivity distribution, which is in accord with the conceptual reservoir model of a high enthalpy geothermal system, where a low resistive clay cap overlies the more resistive upflow zone (*Johnston et al.*, 1992). Our models provide no evidence for an active magmatic system, this is why we conclude that the source of unrest is most likely situated within the shallower part of the hydrothermal system. In order to put constraints on possible mechanisms that might trigger the cyclic periods of uplift and setting we studied publications on the analysis of well data and fluids from Aluto that were mainly published in the 90s. These studies consistently report major changes over time in the hydrothermal regime of the geothermal field and reveal complex water-rock interaction processes taking place in at least the upper 2.6 km of the reservoir as known from well logs (e.g. *Gizaw*, 1993; *Teklemariam et al.*, 1996). On the basis of these findings we argue in favor of two different kinematic mechanisms that might trigger the observed unrest: The first mechanism is related to the hydro-mechanical behavior of clay minerals and their tendency to swell and shrink when exposed to changes of water saturation and pore water chemistry (*de Siqueira et al.*, 1999; *Xu et al.*, 2006). The second mechanism we refer to is thermoelastic expansion of fractured rock consequent to forced advection of hot fluids (*Bonafede*, 1991; *Troiano et al.*, 2011). All in all it is very likely that fluids act as causal agent driving kinematic mechanism that finally result in the observed ground level oscillations.

Based on geomagnetic transfer functions, which provide information on lateral resistivity contrasts we conclude that the dominating occurrence of melt is most likely at lower crustal depths along a N-S elongated off-axis zone of volcanism west of the Main Ethiopian Rift System rather than under the Aluto volcanic complex. This interesting finding is well constraint by previous magnetotelluric and seismic studies (*Whaler and Hautot*, 2006; *Bastow et al.*, 2011; *Kim et al.*, 2012) and it clearly shows the importance of making a regional MT survey in order to fully understand the thermal regime in the rifting zone. Understanding the plumbing system associated with the volcanoes in this region could also have a major impact on geothermal exploration and on the future deployment of geothermal power plants in Ethiopia. Widespread development of geothermal energy in the rift could meet a major part of the local energy demand resulting in a vast benefit for the Ethiopian nation.

Zusammenfassung

Der globale Energiebedarf nimmt stetig zu und regenerative Energien gelten als wichtige Komponente einer zukünftigen Energieversorgung. Ein vielversprechender Kandidat ist geothermische Energie, sie ist CO_2-neutral und auch in Regionen verfügbar, die keinen Zugang zu konventionellen Energien haben. Am attraktivsten ist die geothermische Energieerzeugung in vulkanischen Regionen, da hier meist eine einfache Erreichbarkeit zu oberflächennahen Hochenthalpiesystemen gewährleistet ist. So zum Beispiel in Island und Neuseeland, wo eine gut begründete Infrastruktur die profitable Ausbeutung geothermischer Systeme ermöglicht und damit einen grossen Teil zur lokalen Energieerzeugung beiträgt. Eine attraktive Region mit einem bedeutenden geothermischen Potential, das bisher jedoch weitestgehend unangetasted ist, ist der Ostafrikanische Graben. In dieser aktiven kontinentalen Grabenbruchzone befinden sich eine Vielzahl junger vulkanischer Systeme, wobei die meisten entlang des östlichen Arms zwischen Mosambik und Äthiopien liegen. Nennenswerte Fortschritte in geothermischer Exploration entlang des Ostafrikanischen Grabens beschränken sich derzeit auf Kenia und Äthiopien, wo während der 90er Jahre erste Geothermieanlagen installiert wurden. Derzeit sind einige Geothermieprojekte in diesen Regionen in Arbeit und in naher Zukunft ist eine beachtliche Weiterentwicklung im Sektor der regenerativen Energien zu erwarten. Eine Geothermieanlage wird derzeit am Vulkan Corbetti in Äthiopien errichtet, nach Vollendigung wird sie voraussichtlich 1000 MWe elektrische Energie erzeugen und wäre damit das grösste Geothermiekraftwerk Afrikas (*Reykjavik Geothermal*, 2014).

Die *International Renewable Energy Agency* (IRENA) präsentierte jüngst einen Strategienplan zu Errichtung eines *Clean Energy Corridors*, der sich von Äthiopien bis Südafrika erstrecken soll, um das enorme Potential an erneuerbaren Energien entlang des Ostafrikanischen Grabens zu erschliessen mit Schwerpunkt auf Wasserkraft, Geothermie, Solar- und Windkraft (*IRENA Headquarters*, 2013). Ziel dieses Projekts ist es den steigenden Energiebedarf der rapide wachsenden Wirtschaft in Ostafrika durch kräftige Investitionen in erneuerbare Energien zu decken. Hierbei sei der Vorteil geothermischer Energiequellen gegenüber anderen regenerativen Energien wie Wind-, Solar-, und Wasserkraft erwähnt, der in der Unabhängigkeit von Wettereinflüssen liegt, sowie in einer konstanten Leistungsabgabe, die rund um die Uhr verfügbar ist.

Die Region, die im Rahmen dieser Studie untersucht wird, liegt im zentralen äthiopischen Teil des Ostafrikanischen Grabens. Hier befindet sich eine Vielzahl von Vulkanen, die bereits in der Vergangenheit als potentielle geothermische Hochenthalpie-Lagerstätten identifiziert wurden (*Endeshaw*, 1988). Einige von ihnen sind bekannt dafür sich aktiv zu verformen mit wiederkehrenden Perioden des Anhebens und Senkens wie durch Satellitenmessungen gezeigt werden konnte (*Biggs et al.*, 2011). Eine der Regionen, in der zeitliche Änderungen auftreten, ist der vulkanische Komplex Aluto-Langano. Hier befindet sich die derzeit einzige stromerzeugende Geothermieanlage Äthiopiens, die ein geothermisches System mit Fluidtemperaturen von über 350 °C ausbeutet (*Gianelli and*

Teklemariam, 1993). Die bisher beobachteten Perioden des Anhebens am Aluto fanden im Jahr 2004 und 2008 statt, sie betrafen eine Gesamtfläche von ungefähr 100 km^2 und wurden gefolgt von länger andauernden Senkungsphasen. Die Geothermieanlage befindet sich im Zentrum der sich verformenden Region wo die grössten Amplituden der Deformation auftreten. Dieser Stand der Dinge legt unmittelbar die Frage nach den Folgen der Verformungen auf die Geothermieanlage nahe – zum einen hinsichtlich ihrer Produktivität, zum anderen hinsichtlich des Georisikos. Der derzeit geltenden Hypothese nach liegt die Quelle der Deformation entweder im hydrothermalen System, in einem tieferen magmatischen System oder in einem aus den beiden kombinierten System.

Das Ziel dieser Arbeit ist zwischen den genannten Szenarien zu unterscheiden und das Wesen der verformenden Quelle zu ergründen. Um dies zu erreichen, führten wir magnetotellurische (MT) Messungen durch. Diese geophysikalische Induktionsmethode nutzt natürlich auftretende zeitliche Variationen elektromagnetischer Felder, um die elektrische Leitfähigkeitsverteilung des Untergrunds zu ermitteln. Sie ist besonders sensitiv bezüglich elektrisch gut leitfähigen Strukturen, wie sie hydrothermale und magmatische Systeme normalerweise darstellen (*Muñoz*, 2014). Desweiteren deckt MT mit Leichtigkeit die notwendige Explorationstiefe von ungefähr 10 km ab. In der Vergangenheit wurde MT mit grossem Erfolg in der geothermischen Exploration angewandt und erwies sich als verlässliche und kostengünstige Methode um geothermische Hochenthalpie-Lagerstätten auf Grundlage ihrer elektrischen Leitfähigkeitverteilung aufzuspüren. Unterstützt wird dies durch jüngste und andauernde Entwicklungen von effizienten numerischen Methoden, die es ermöglichen MT Daten in 3-D zu invertieren und zu interpretieren.

Die im Rahmen dieser Doktorarbeit behandelte Studie umfasste den gesamten Planungsprozess und die Organisation einer Messkampagne einschliesslich der Logistik und Zollabfertigung. Die Feldmessungen in Äthiopien wurden mit einem Team von Wissenschaftlern der Universität Addis Ababa, der ETH Zürich, des Gelogischen Diensts Äthiopiens und Ortsansässigen der untersuchten Region durchgeführt. Insgesamt installierten wir MT Stationen an 46 Orten im Bereich des Aluto-Langano Komplexes. Die Daten wurden prozessiert, modelliert und im Kontext mit vorherigen interdisziplinären Studien des Aluto-Langano vulkanischen Komplexes und des Äthiopischen Grabensystems interpretiert. Unsere gewonnenen 3-D Modelle decken eine Leitfähigkeitsverteilung auf, die der erwarteten des konzeptuellen geothermischen Hochenthalpie-Reservoir-Modells entspricht, in dem eine hochleitfähige Tonkappe über einer Aufströmzone höheren elektrischen Widerstands liegt (*Johnston et al.*, 1992). Unsere Modelle liefern keinerlei Anzeichen auf das Vorhandensein eines aktiven magmatischen Systems, weshalb wir schlussfolgern, dass die Quelle der Verformung höchstwahrscheinlich im oberflächennahen hydrothermalen System liegt. Um mögliche Mechanismen einzuschränken, die die sich wiederholenden Zyklen des Anhebens und Senkens erklären, studierten wir Veröffentlichungen über die Analyse von Bohrlochdaten und Fluiden von Aluto, die

hauptsächlich in den 90ern veröffentlicht wurden. Diese Studien berichten durchweg von grossen zeitlichen Veränderungen des hydrothermalen Regimes des geothermischen Reservoirs und offenbaren andauernde komplexe Fluid-Gestein Interaktionsprozesse. Diese finden zumindest in den oberen 2.6 km des Reservoirs statt, wie aufgrund von Bohrlochdaten bekannt ist (z.B. *Gizaw*, 1993; *Teklemariam et al.*, 1996). Auf Grundlage dieser Erkenntnisse argumentieren wir zugunsten zweier verschiedener kinematischer Mechanismen, die für die beobachteten Verformungen verantwortlich sein könnten. Der erste Mechanismus ist mit dem hydromechanischen Verhalten von Tonmineralen verknüpft und ihrer Neigung anzuschwellen oder zu schrumpfen sobald sie Veränderungen hinsichtlich der Wassersättigung oder der Chemie des Porenwasses ausgesetzt sind (*de Siqueira et al.*, 1999; *Xu et al.*, 2006). Der zweite Mechanismus auf den wir uns beziehen ist die thermoelastische Expansion frakturierten Gesteins infolge von auftretender Zwangskonvektion heisser Fluide (*Bonafede*, 1991; *Troiano et al.*, 2011). Im grossen Ganzen ist es sehr wahrscheinlich, dass die treibenden Mechanismen hinter der beobachteten zyklischen Oberflächendeformation durch Fluide gesteuert werden.

Basierend auf geomagnetischen Übertragungsfunktionen, die Information über laterale Leitfahigkeitsvariationen beinhalten, konnten wir schlussfolgern, dass sich ein dominierendes Vorkommen an Schmelze eher in der unteren Kruste entlang einer sich in Nord-Süd-Richtung erstreckenden vulkanischen Zone westlich des mittleren äthiopischen Grabens befindet als direkt unter dem Aluto-Komplex. Diese interessante Feststellung wird bestätigt durch und ist in Übereinstimmung mit vorherigen magnetotellurischen und seismischen Studien (*Whaler and Hautot*, 2006; *Bastow et al.*, 2011; *Kim et al.*, 2012). Sie offenbart mit grosser Klarheit die Notwendigkeit der Durchführung einer regionalen Studie im zentralen äthiopischen Graben um das thermische Regime in Gänze zu verstehen. Ein detaillierteres Verständnis des magmatischen Systems, das die Vulkane speist, würde zudem einen grossen Einfluss auf die geothermische Exploration und den zukünftigen Bau weiterer Geothermieanlagen in Äthiopien haben. Eine grossangelegte Entwicklung geothermischer Energie im äthiopischen Graben könnte einen Grossteil des lokalen Energiebedarfs decken und wäre damit von grossem Nutzen für die äthiopische Nation.

Contents

List of Figures

List of Tables

Chapter 1

Principles of electromagnetic induction studies

Induction studies in the context of geophysical depth sounding are based on the analysis of time varying naturally or artificially created electric and magnetic (EM) fields. EM fields by interacting with the electrically conducting Earth provide information about the subsurface conductivity distribution over shallow crustal to lower mantle depths on local to global scales. In principle subsurface conductivities can be linked to physical and chemical properties of the rock and therefore allow to recover the Earth's interior structure. In doing so EM depth sounding methods are non-invasive geophysical techniques as time-varying fields are generally measured at the Earth's surface without affecting the Earth in whole or in part.

1.1 Physical principles of EM induction

Although different EM depth sounding techniques exist, with some of them analyzing electric and magnetic fields alone or simultaneously, their principles are all based on Maxwell's equations. Maxwell's equations are a system of coupled first order linear partial differential equations, which describe the interaction of matter and fields, along with the Lorentz force law they form the foundation of classical electrodynamics. In SI unit system the time domain Maxwell's equations are

$$\nabla \cdot \mathbf{D} = q_e, \tag{1.1}$$

$$\nabla \cdot \mathbf{B} = 0, \tag{1.2}$$

$$\nabla \times \mathbf{E} = -\frac{\partial \mathbf{B}}{\partial t}, \tag{1.3}$$

$$\nabla \times \mathbf{H} = \mathbf{j} + \frac{\partial \mathbf{D}}{\partial t}. \tag{1.4}$$

Here $\mathbf{D}$ is the electric displacement in [Cm^{-2}], q_e is the electric charge density [Cm^{-3}], $\mathbf{B}$ is the magnetic flux density or induction in [T], $\mathbf{E}$ is the electric field in [Vm^{-1}], $\mathbf{H}$ is the magnetic field intensity in [Am^{-1}] and $\mathbf{j}$ is the electric current density in [Am^{-2}].

Maxwell's equations are complemented with the constitutive relations for a material medium, which describe the linear relationship between $\mathbf{H}$ and $\mathbf{B}$, and $\mathbf{D}$ and $\mathbf{E}$:

$$\mathbf{B} = \mu\mathbf{H}, \tag{1.5}$$

$$\mathbf{D} = \epsilon\mathbf{E}. \tag{1.6}$$

The magnetic permeability μ and the electric permittivity ϵ are material-specific properties to describe the interplay between matter and EM fields. Gauss' flux theorem (eq. 1.1) can be rewritten using eq. (1.6) as follows:

$$\nabla \cdot \mathbf{E} = \frac{q_e}{\epsilon}, \tag{1.7}$$

this expression implies that electric field lines $\mathbf{E}$ diverge, i.e. start and end, at electric charges q_e. The solenoidal constraint, also known as Gauss' law for magnetism (eq. 1.2), states that the divergence of a magnetic field $\mathbf{B}$ equals zero. This is equivalent to the non-existence of magnetic monopoles and the fact that magnetic field lines are always closed with neither sources nor sinks. Equation (1.3), Faraday's law, describes the induction phenomenon of a time-varying magnetic field creating an electric field as illustrated in Fig. 1.1. Ampere's law (eq. 1.4) describes the creation of a magnetic field by a current $\mathbf{j}$ and a time-varying electric field $\frac{\partial \mathbf{D}}{\partial t}$, see Fig. 1.2. The current $\mathbf{j}$ on right-hand side of Ampere's law can be split into two parts

$$\mathbf{j} = \sigma\mathbf{E} + \mathbf{j}^{\mathrm{ext}}. \tag{1.8}$$

The first term on the right-hand side (RHS) is known as Ohm's law:

$$\mathbf{j}_c = \sigma\mathbf{E}, \tag{1.9}$$

it states that the electric current $\mathbf{j}_c$ and the electric field are directly proportional in an Ohmic conductor with the conductivity σ in [Sm^{-1}] as an material-specific factor that does not change with the current. In the general case the conductivity σ is anisotropic and has the form of a rank-2 tensor. However, here we confine ourselves to isotropic media where σ is independent from directions and of a scalar form. The second term $\mathbf{j}^{\mathrm{ext}}$ comprises the influence extraneous or primary currents.

In most of geophysical EM induction studies the magnetic permeability μ and the

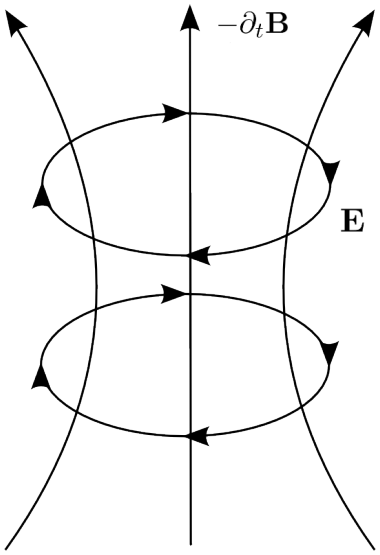

FIGURE 1.1: Schematic illustration of Faraday's law: $\nabla \times \mathbf{E} = -\partial_t \mathbf{B}$.

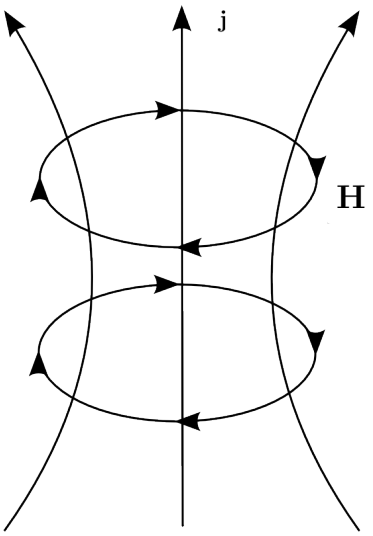

FIGURE 1.2: Schematic illustration of the quasi-static approximation of Ampere's Law: $\nabla \times \mathbf{H} = \mathbf{j}$.

electric permittivity ϵ are assumed to equal their constant values in free space

$$\mu = \mu_0 = 4\pi \cdot 10^{-7}\,\mathrm{Vs/Am}, \tag{1.10}$$

$$\epsilon = \epsilon_0 = \frac{1}{\mu_0 c^2} \approx 8.85 \cdot 10^{-12}\,\mathrm{As/Vm}, \tag{1.11}$$

where c is the defined value for the speed of light in free space.

All induction methods considered here work in frequency domain which is why recorded time series of time varying fields are Fourier transformed to obtain time spectra. Two different conventions for the Fourier transform exist, if not explicitly stated we make use of the following adaption

$$f(t) = \frac{1}{2\pi} \int_{-\infty}^{\infty} \tilde{f}(\omega) \mathrm{e}^{-\mathrm{i}\omega t} \mathrm{d}\omega, \tag{1.12}$$

$$\tilde{f}(\omega) = \int_{-\infty}^{\infty} f(t) \mathrm{e}^{\mathrm{i}\omega t} \mathrm{d}t, \tag{1.13}$$

where $f(t)$ is a function of time, $\tilde{f}(\omega)$ its equivalent in frequency domain and $\omega = \frac{2\pi}{T}$ the angular frequency for a variation of period T. Maxwell's equations in frequency domain with substitution of the constitutive relations eqs. (1.5) and (1.6) read:

$$\nabla \cdot \tilde{\mathbf{E}} = \frac{q_e}{\epsilon_0}, \tag{1.14}$$

$$\nabla \cdot \tilde{\mathbf{H}} = 0, \tag{1.15}$$

$$\nabla \times \tilde{\mathbf{E}} = \mathrm{i}\omega\mu_0\tilde{\mathbf{H}}, \tag{1.16}$$

$$\nabla \times \tilde{\mathbf{H}} = \sigma\tilde{\mathbf{E}} + \mathrm{i}\omega\epsilon_0\tilde{\mathbf{E}} + \tilde{\mathbf{j}}^{\mathrm{ext}}. \tag{1.17}$$

To simplify the nomenclature we will use the same notation for time and frequency-domain electric, magnetic fields namely $\mathbf{E}$, $\mathbf{B}$ and the current $\mathbf{j}^{\mathrm{ext}}$. In the considered period range of EM induction studies of the Earth and for typical observed Earth's conductivities, displacement currents, i.e. the second term in eq. (1.17) can be neglected. Comparing the RHS terms of eq. (1.17) one gets:

$$|\sigma\mathbf{E}| \gg |\omega\epsilon_0\mathbf{E}|. \tag{1.18}$$

From here follows the *quasi-static approximation* of Ampere's law:

$$\nabla \times \mathbf{H} = \sigma\mathbf{E} + \mathbf{j}^{\mathrm{ext}}. \tag{1.19}$$

These set of equations, namely eq. (1.14), eq. (1.15), eq. (1.16) and eq. (1.19), build the basis for EM depth sounding techniques addressed in this study. Note that we use *conductivity* and *resistivity*, which is the reciprocal of conductivity, as interchangeable terms throughout this thesis.

1.2 Origin and variations of the Earth's magnetic field

The total intensity of the geomagnetic field $\mathbf{B}$ at the Earth's surface reaches from 22000 nT to 67000 nT (e.g. *Finlay et al.*, 2010). The weakest magnetic field intensities are observed in the area of the South Atlantic Anomaly. *Gauß* (1839) was the first who suggested a way to separate internal, $\mathbf{B}^{\mathrm{int}}$, and external, $\mathbf{B}^{\mathrm{ext}}$, contributions to $\mathbf{B}$ by introducing the concept of spherical harmonic analysis. Assuming that the electrical conductivity above the point of observation, i.e. the Earth's surface, is zero (insulating atmosphere) and out of the source region the magnetic field can be expressed as the negative gradient of a scalar potential field V:

$$\mathbf{B} = -\nabla V. \tag{1.20}$$

Since $\mathbf{B}$ is solenoidal (eq. 1.2) the potential V satisfies the Laplace's equation, $\nabla^2 V = 0$, which can be solved in terms of a spherical harmonic expansion if a spherical coordinate system is adopted. Hence V at the Earth's surface can be expressed by a set of spherical

harmonics with internal, V^{int}, and external, V^{ext}, parts over the surface of the Earth, where the internal part originates from currents inside the Earth and the external part – from currents in the regions above the insulating atmosphere (cf. *Olsen et al.*, 2010).

The internal and external magnetic fields vary with time. They are undergoing fluctuations that originate from different sources and cover a huge range of timescales as illustrated in Fig. 1.3. On geological time scales of millions of years we find reversals of the magnetic field, which lead the geomagnetic poles to interchange. Secular variations occur on time scales of years to hundreds of years. Both, reversals and secular variations originate from magneto-hydrodynamic processes within the Earth's outer core, where about 90% of the main magnetic field strength is generated. Internal variations have therefore the largest amplitudes in the spectrum, however, they are not part of induction studies considered here, which focus on EM field variations of external origin only.

External variations are related to space weather phenomenons and are mainly caused by interaction of the magnetosphere with the solar wind, which is considered to be the main driver of external geomagnetic activity. The solar wind is a continuous stream of plasma released from the Sun carrying the Sun's magnetic field through the interplanetary space as consequence of frozen-in-flux theorem (*Alfvén*, 1943). The theorem is valid for a plasma in which the mean free path of the charged particles is sufficiently long to allow them for a collision free gyration around the magnetic field. In this case any force that moves the particles also moves the magnetic field and vice versa. The magnetic field transported away from the sun through the interplanetary space is referred to as interplanetary magnetic field (IMF), near the Earth's orbit its strength varies between $4 - 5\,\text{nT}$ (*Bothmer and Daglis*, 2006). The longest periods in external variations are related to the 11 yr solar cycle associated with changes in the Sun's activity and as a result, variations in solar wind velocity, v_s, and plasma density, n_s. Furthermore the Earth's elliptical orbit around the Sun results in annual and semiannual variations and towards shorter periods we find a 27 day oscillation and its harmonics related to the solar rotation (e.g. *Banks*, 1969).

The geomagnetic field generally acts as a natural shield protecting the Earth's biosphere from energetic solar wind particles by avoiding that particles directly enter lower atmospheric regions. The natural barrier that separates the IMF and solar wind from the magnetosphere is a separatrix surface called the magnetopause, see illustration in Fig. 1.4. It is placed, where the dynamic pressure of the solar wind, $p_s \propto n_s v_s^2$, equals the magnetic pressure of the Earth's magnetic field, $p_B \propto B^2$. On the daylight side the magnetopause is in a distance of typically 10 Earth's radii R_E. In cases of high solar wind speeds during solar mass eruptions it can come as close as $5\,\text{R}_\text{E}$ (*Glaßmeier et al.*, 2009). The magnetopause encases the drop-shaped magnetosphere with its tail extending more than $100\,\text{R}_\text{E}$ towards the site facing away from the sun (*Volland*, 1984).

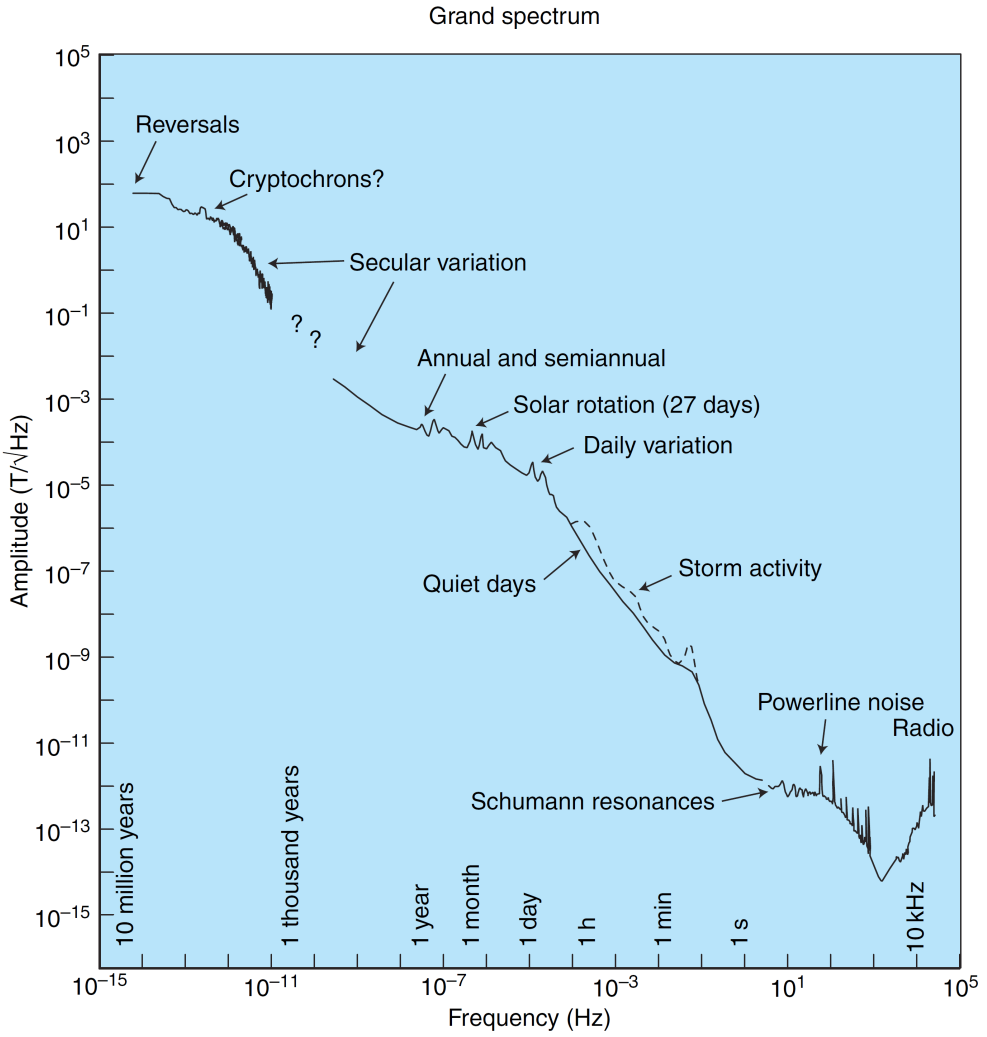

FIGURE 1.3: Illustrative figure of the Earth's magnetic field amplitude spectrum. Frequencies reach from 10^{-15} Hz to several 1000 Hz with the former corresponding to a period of a few million of years. The sources of geomagnetic variations are indicated in the figure. On the longest time scale with periods of a few million years geomagnetic reversals occur, at the high frequency end variations are caused by radio waves. The figure was taken from *Constable* (2007).

According to the laws of ideal magnetohydro-dynamics the magnetopause acts as impermeable layer for solar wind particles as the IMF is tied to the solar wind plasma like the geomagnetic field is tied to the magnetospheric plasma, as the frozen-in flux theorem by *Alfvén* (1943) states. The only exception where solar wind plasma has direct access to the magnetosphere is at the polar cusps, which are two neutral magnetic areas at the dayside magnetosphere where the Earth's magnetic field is normal to the magnetopause. The cusps separate magnetic field lines that pass through the dayside equatorial plane and field lines that are carried away into the magnetotail. In addition several different processes have been proposed that allow plasma to cross the magnetopause and enter the magnetosphere (e.g. *Hultqvist et al.*, 1999; *McPherron*, 2005; *Glaßmeier et al.*,

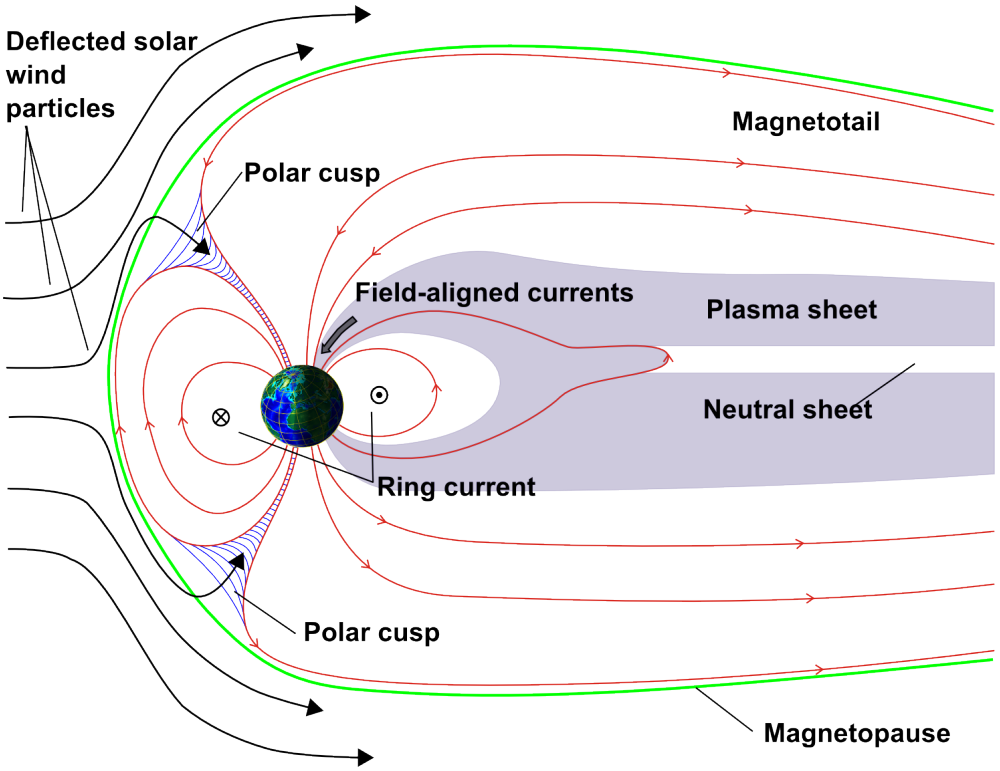

FIGURE 1.4: Illustration of the Earth's magnetosphere, not true to scale. The figure was drawn after *Volland* (1984). Note that the location of the ring current is out the scale. It evolves at a distance of a few (5-10) Earth's radii.

2009). The most efficient one is magnetic reconnection when geomagnetic field lines couple with IMF field lines. Reconnection happens on both day- and night-side of the magnetosphere and allows huge amounts of plasma to enter the magnetosphere. Once the plasma is inside the magnetosphere it drives a variety of complex magnetospheric and ionospheric current systems. These current systems are of a very dynamic nature and result in magnetic field variations that can be seen at the Earth's surface covering a period range in the order of days to seconds. One prominent current system is the ring current (Fig. 1.4), which is a current in the magnetic equatorial plane at a distance of $5 - 10$ R_E causing magnetic field variations of predominantly P_1^0 spherical harmonic geometry, where P_l^m is the associated Legendre function with parameters $l = 1$ and $m = 0$. The P_1^0 geometry implies that the ring current can be expressed by a single zonal harmonic $P_1^0 = \cos\theta$, where θ is the geomagnetic co-latitude. The strength of the ring current is closely related to the solar wind and consequently to the Sun's current activity and the solar cycle. The above mentioned long period variations of 11 yr and 27 days and their harmonics also result in variations in the strength of the ring current and are consequently observed at the Earth's surface. *Banks* (1969) investigated that variations with frequencies between $2\,\mathrm{c\,yr^{-1}}$ and $0.5\,\mathrm{c\,day^{-1}}$ are caused by fluctuations in intensity of the ring current. The strength of the ring current is characterized by the

disturbance storm time (Dst) index, which peaks during magnetic storms (for definition see *Sugiura* (1964)). Magnetic storms are caused by a sudden increase in the dynamic pressure of the solar wind, which leads to an increase in coupling between the Earth's magnetic field and the solar wind and to an earthward movement of the magnetopause to achieve equilibrium between the enhanced solar wind pressure and the magnetic field pressure. During a storm a large amount of energy is extracted from the solar wind and transferred into the magnetosphere increasing the ring current and leading to large geomagnetic variations observed at the Earth's surface with a change in the magnetic field strength of up to 500 nT lasting from hours to a few days (*McPherron*, 2005).

Also during quite solar wind conditions one can observe daily variations and their harmonics on the Earth's surface. These variations originate from a ionospheric dynamo at heights of about 100 km. The ionospheric dynamo is driven by interaction and coupling between ionospheric plasma and ionospheric tidal waves. Ionospheric plasma is produced on the daylit side of the Earth by photoionization when incident solar photons eject electrons from ionospheric molecules. Solar differential heating of the atmosphere generates tidal winds, which move the ionospheric plasma and lead to horizontal ionospheric currents. The most prominent ionospheric current system is the solar quiet (Sq) current system. It consists of a double vortex structure with one anticlockwise rotating vortex in the northern and one clockwise rotating in the southern hemisphere on the sunlit side of the Earth (Fig. 1.5). The Sq vortices are stationary and fixed on the Earth's dayside, while the Earth rotates underneath them. At the Earth's surface one can observe the typical 24 h Sq variations of the magnetic field and their harmonics during solar quiet conditions. At the magnetic dip equator there is a strong eastward-flowing current during daylight hours that separates the two Sq vortices and is referred to as the equatorial electrojet (EEJ). The EEJ is also a cyclic process with a 24 h periodicity as (similar to Sq) it only evolves in the Earth's dayside. Occasionally a reversal of the EEJ is observed especially during afternoon hours. The mechanisms leading to the occurrence of these so-called counter electrojets (CEJs) are not fully understood yet (e.g. *Gurubaran*, 2002; *Vineeth et al.*, 2009). Whether the EEJ and the CEJs are part of the Sq system or have to be considered as independent current systems is under discussion (c.f. *Stening*, 1995).

Magnetic field variations of shorter periods, $T < 3$ h, are stimulated by an auroral electrojet (AEJ) current system, which is driven by field aligned currents (FAC) coupling magnetospheric currents with ionospheric currents at high latitudes (*Glaßmeier et al.*, 2009). The energy input to the AEJ is highly dynamic both in space and time and results in magnetic field variations at the Earth's surface up to 4000 nT during magnetospheric substorms. For an analysis of the spatiotemporal structure of the variations see e.g. *Pulkkinen et al.* (2006). Another source of variations with $T < 3$ h are ultra low frequent (ULF) waves, they can be created both externally and internally to the

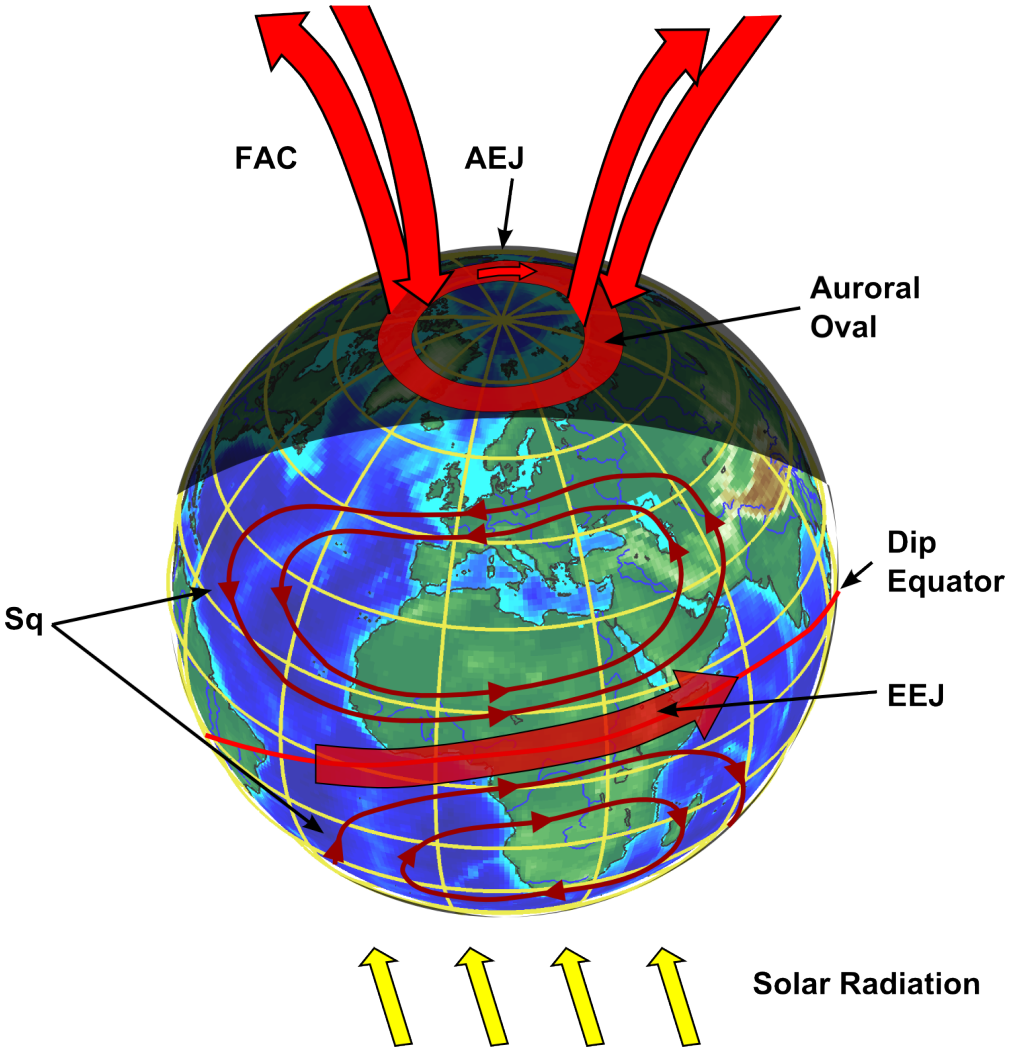

FIGURE 1.5: Schematic overview on main ionospheric current systems. FAC denote field aligned currents, AEJ and EEJ are the auroral respectively the equatorial electrojet. Sq denotes the solar quiet current system. The illustration of counter electrojets (CEJs) was omitted due to reasons of clarity. The figure was drawn after *Glaßmeier et al.* (2009).

magnetosphere (*McPherron*, 2005). External formation of ULF waves happens at the Sun from where they propagate through the solar wind towards the Earth, furthermore they are created by processes in the foreshock and bow shock region, where the solar wind is slowed down by the geomagnetic field, and by processes in the magnetopause. Internal sources of ULF waves are located inside the magnetosphere and are mainly excited during storms and substorms. External ULF waves pass the magnetopause and propagate together with internal ULF waves through the magnetosphere, which acts as resonant cavity and waveguide. Energy of ULF waves is transformed and amplified by different magnetospheric processes like field line and cavity resonances. These resonances can stimulate field lines to resonate like strings that finally drive ionospheric currents. Ionospheric currents re-radiate energy by transmission of electromagnetic waves that

travel down to the Earth, where they are seen as magnetic variations, respectively pulsations of external origin. The pulsations span a period range of 1 s to a few 1000 s. Depending on their source they are classified into Pc and Pi oscillations, where Pc are quasi-sinusoidal continuous variations and Pi are short-term oscillations with an irregular waveform (*Volland*, 1984).

At around 1 s there is a minimum in the spectrum, which marks the transition between magnetic field variations generated by space weather activities and variations stimulated by meteorological activities and atmospheric sources, the latter cover the frequency band $f > 1$ Hz. Short period variations are generated in the Earth-ionosphere waveguide that is formed by the non-conductive cavity between conducting Earth and conducting ionosphere. Standing waves in the Earth-ionosphere cavity are excited by global lightning discharge and show characteristic resonant frequencies, so-called Schumann resonances (*Schumann*, 1952). The fundamental resonance mode has a frequency of around 7.5 Hz, which corresponds to a wavelength equal to the Earth's circumference. *Füllekrug* (2005) estimated 13 modes of Schumann resonances in the frequency range $5 - 90$ Hz from time series recorded at a site in Germany with an electromagnetically quiet environment and little interference from anthropogenic noise. The amplitude of the Schumann resonance spectra is related to global lightning intensity, which peaks during local afternoon on the main tropical land regions. The daily maximum in lightning activity is reached during $14:00 - 16:00$ UT around afternoon on the African continent, then Schumann resonances are mostly distinct in the spectrum.

At the high frequency end of the spectrum of natural variations are so-called extremely low frequency (ELF: $3 - 3000$ Hz) and very low frequency (VLF: $3 - 30$ kHz) variations that propagate within the Earth-ionosphere waveguide. EM energy is radiated by thunderstorms in lightning channels. The emitted pulses, so-called sferics, are highly impulsive and cover a wide frequency-range between a few Hz to the order of 1000 kHz (*Cummer and Inan*, 2000). EM waves are not only transmitted by cloud to ground lightnings but also by intercloud lightnings, red sprites and blue jets that occur at stratospheric altitudes above thunderstorm clouds (*Rodger*, 1999).

EM depth sounding studies, which exploit the previously described time-varying EM fields of natural origin, are so-called passive induction techniques in contrast to active methods which make use of active (or controlled) sources. Natural variations do not only cover a wide period range, but they also differ significantly in their geometry. EM induction methods using these variations have to account for the geometry of time-varying fields depending on the analyzed periods. This is described in the following section.

1.3 Overview on EM depth sounding methods

Amongst the geophysical methods exploiting the previously described natural magnetic field variations of external origin to recover the subsurface conductivity distribution different techniques exist, which use different source field geometries and sound different depth ranges depending on the considered period range. Studies analyzing long period or low frequency variations of magnetospheric origin pioneered with *Banks* (1969), who estimated responses at $1\,\mathrm{c\,yr^{-1}}$ using a P_2^0 zonal source field geometry and responses from $2\,\mathrm{c\,yr^{-1}}$ to $0.25\,\mathrm{c\,day^{-1}}$ using P_1^0 zonal source field geometry. Based on this set of responses he recovered the 1-D conductivity distribution down to lower mantle depths of $> 2000\,\mathrm{km}$. Shortly thereafter *Schmucker* (1970a) and *Weidelt* (1972) introduced the concept of C-responses, which are defined as the ratio (in frequency domain) of the vertical magnetic component to the horizontal magnetic field. Recent developments in deep EM studies using the magnetospheric ring current introduced in Section 1.2 are summarized in a review paper by *Kuvshinov* (2012). Latest work has been done by *Semenov and Kuvshinov* (2012) and *Koyama et al.* (2013), who inverted globally distributed C-responses in a period range between a few days and a few months in terms of 3-D conductivity of the Earth at depths of $410 - 1600\,\mathrm{km}$ at global and semi-global scales, respectively. *Semenov and Kuvshinov* (2012) showed that C-responses estimated in the vicinity of the geomagnetic dip-equator are very unstable, since here the vertical magnetic component is small resulting in a low signal-to-noise ratio. Thus there is a vast zone around the geomagnetic equator where the geomagnetic deep sounding approach based on the analysis of C-responses hardly works. This problem might be overcome if magnetic measurements in equatorial regions are complemented by electric field observations. In this case one can estimate magnetotelluric responses (in detail introduced later in Section 1.4), which relate horizontal magnetic and horizontal electric fields. Owing to the source geometry of the ring current both horizontal electric and magnetic fields are maximum in the vicinity of the dip equator. Thus equipping geomagnetic observatories in this region by electric field measurements would allow to overcome the problem with unstable C-responses. Following this reasoning we equipped the equatorial geomagnetic observatory on Gan Island (Maldives), which is operated by ETH Zurich, with permanent electric measurements. The results of this side project of this PhD study are reported in Appendix C. Note, however, that it is extremely difficult to obtain responses based on electric measurements at periods larger than a few days.

At shorter periods ($3 - 24\,\mathrm{h}$) the dominant source is the ionospheric Sq current system. Early studies using Sq variations have been made by *Schmucker* (1970a,b), who estimated C-responses after spherical harmonic analysis of magnetic field time series collected at a global network of observatories. This technique allows for purely 1-D interpretations and was later further developed by an expansion of the set of spherical

harmonics to higher degrees (*Olsen*, 1992; *Schmucker*, 1999a,b). To avoid problems arising from complexity of the Sq source and 3-D effects, *Koch and Kuvshinov* (2013) introduced a new concept that is not based on the analysis of transfer functions but on the analysis of time spectra of the field and on a simultaneous determination of the Sq source geometry and the subsurface conductivity distribution providing thereby the first numerical solution for 3-D inversion of Sq data. The new concept was successfully applied by *Koch and Kuvshinov* (2015) to the 'Australia Wide Array of Geomagnetic Stations' (AWAGS) data set who recovered the 3-D conductivity distribution under Australia at depths between $100 - 520$ km.

Towards shorter periods of $T < 3$ h the source field is approximated by a vertically propagating uniform plane wave field. The plane wave assumption is justified as the spatial extend of induction studies using variations in this period range is normally orders of magnitude smaller than the distance to the sources of the analyzed variations described in Section 1.2. Note that work with plane-wave signals is performed in Cartesian coordinates where x is pointing northwards, y eastwards and z downwards. The mathematical assumptions on the plane wave field for a 1-D Earth are as follows:

- There are no vertical components of either electric $\mathbf{E}$ or magnetic field $\mathbf{B}$:

$$\mathbf{E} = (E_x, E_y, 0)^T, \tag{1.21}$$

$$\mathbf{B} = (B_x, B_y, 0)^T. \tag{1.22}$$

- The variations of $\mathbf{E}$ and $\mathbf{B}$ along any horizontal plane are constant:

$$\partial_x E_x = \partial_y E_x = \partial_x E_y = \partial_y E_y = 0, \tag{1.23}$$

$$\partial_x B_x = \partial_y B_x = \partial_x B_y = \partial_y B_y = 0. \tag{1.24}$$

These assumptions are valid in regions, which are away from the auroral and equatorial ionospheric electrojets. For studies at high or low latitudes care has to be taken as the assumption might be violated due to the proximity of the EEJ and the AEJ. Towards longer periods $T > 3$ h the plane wave field is *contaminated* by the dominating Sq source field. Recently *Shimizu et al.* (2011) introduced a concept to estimate responses based on the plane wave assumption up to periods of $10^4 - 10^5$ s by removing Sq line spectra.

The plane wave assumption is the underlying principle of the magnetotelluric (MT) method with its standard response, impedance $\mathbf{Z}$, that is derived from horizontal variations in $\mathbf{E}$ and $\mathbf{B}$. Another independent MT response, the so-called tipper $\mathbf{T}$, is purely based on the magnetic field, it can be estimated if besides the horizontal magnetic field also its vertical component B_z is measured. The MT method is the most common and best developed amongst the mentioned induction techniques. The reasons for this

are manifold: Firstly the simplicity of its source geometry makes it relatively easy to obtain stable and high quality responses and the source is always present. Secondly, MT by spanning a period range over several orders of magnitude sounds depths from a few tens of meters down to a few hundred of kilometers, which makes it also attractive for industry in geophysical exploration for exploitable natural resources. Lastly to be mentioned here is another advantage of MT studies: Modern MT data loggers and sensors are convenient to handle and can be easily installed in the field. Measurement times are short with only a few hours to days depending on the depth range of interest. Hence, MT surveys can be accomplished time-efficiently and relatively cheap compared to other geophysical depth sounding methods. The introduction to the MT method and its responses is topic of the following section.

1.4 The MT method

The source of the time varying plane wave field is considered to be far above the Earth ($z \ll 0$) and thus eq. (1.19) within the Earth simplifies to

$$\nabla \times \mathbf{H} = \sigma \mathbf{E}. \tag{1.25}$$

The Earth is conductive for $z > 0$ and isolating with $\sigma \to 0$ for $z < 0$, i.e. the waves are not affected by attenuation on their way from the remote source to the Earth's surface at $z = 0$, later on we assume that σ is constant within the Earth. Electric and magnetic fields vanish when z tends to infinity:

$$\lim_{z \to \infty} (\mathbf{E}, \mathbf{B}) = 0. \tag{1.26}$$

Using the identity $\nabla \cdot (\nabla \times \mathbf{A}) = 0$, which states that the divergence of the curl of any vector field $\mathbf{A}$ equals zero and assuming that the Earth is a uniform conductor we get from eq. (1.25):

$$\nabla \cdot \mathbf{E} = 0. \tag{1.27}$$

Using eq. (1.27) and by applying the curl to eq. (1.16) we arrive to the following equation:

$$\nabla \times \nabla \times \mathbf{E} = \nabla(\nabla \cdot \mathbf{E}) - \nabla^2 \mathbf{E} = -\nabla^2 \mathbf{E} = i\omega\mu_0 \nabla \times \mathbf{H}. \tag{1.28}$$

Here we used the identity for the curl of a curl of a vector field $\mathbf{A}$

$$\nabla \times \nabla \times \mathbf{A} = \nabla(\nabla \cdot \mathbf{A}) - \nabla^2 \mathbf{A}.$$

With eqs. (1.23) and (1.25) we can derive from eq. (1.28) the following diffusion equation for **E**:

$$\frac{\partial^2 \mathbf{E}}{\partial z^2} = -k^2 \mathbf{E}, \tag{1.29}$$

where $k = \sqrt{i\omega\mu_0\sigma}$. In similar fashion a diffusion equation for **H** can be derived:

$$\frac{\partial^2 \mathbf{H}}{\partial z^2} = -k^2 \mathbf{H}. \tag{1.30}$$

The solutions to the diffusion eqs. (1.29) and (1.30) are of the form

$$\mathbf{E}(z) = \mathbf{E}^+ \mathrm{e}^{ikz} + \mathbf{E}^- \mathrm{e}^{-ikz}, \tag{1.31}$$

$$\mathbf{H}(z) = \mathbf{H}^+ \mathrm{e}^{ikz} + \mathbf{H}^- \mathrm{e}^{-ikz}. \tag{1.32}$$

The expression for k can be rewritten using $\sqrt{i} = \frac{1-i}{\sqrt{2}}$ as

$$k = \frac{1-i}{\sqrt{2}}\sqrt{\omega\mu_0\sigma}. \tag{1.33}$$

Substituting the latter equation in eqs. (1.31) and (1.32) we obtain

$$\mathbf{E}(z) = \mathbf{E}^+ \mathrm{e}^{i\sqrt{\frac{\omega\mu_0\sigma}{2}}z - \sqrt{\frac{\omega\mu_0\sigma}{2}}z} + \mathbf{E}^- \mathrm{e}^{-i\sqrt{\frac{\omega\mu_0\sigma}{2}}z + \sqrt{\frac{\omega\mu_0\sigma}{2}}z}, \tag{1.34}$$

$$\mathbf{H}(z) = \mathbf{H}^+ \mathrm{e}^{i\sqrt{\frac{\omega\mu_0\sigma}{2}}z - \sqrt{\frac{\omega\mu_0\sigma}{2}}z} + \mathbf{H}^- \mathrm{e}^{-i\sqrt{\frac{\omega\mu_0\sigma}{2}}z + \sqrt{\frac{\omega\mu_0\sigma}{2}}z}. \tag{1.35}$$

Since the second terms on the RHS of the equations do not fulfill the condition of a vanishing field for $z \to \infty$ (cf. eq. 1.26), we exclude them from further consideration:

$$\mathbf{E}(z) = \mathbf{E}^+ \mathrm{e}^{i\sqrt{\frac{\omega\mu_0\sigma}{2}}z - \sqrt{\frac{\omega\mu_0\sigma}{2}}z} = \mathbf{E}^+ \mathrm{e}^{ikz}, \tag{1.36}$$

$$\mathbf{H}(z) = \mathbf{H}^+ \mathrm{e}^{i\sqrt{\frac{\omega\mu_0\sigma}{2}}z - \sqrt{\frac{\omega\mu_0\sigma}{2}}z} = \mathbf{H}^+ \mathrm{e}^{ikz}. \tag{1.37}$$

From eqs. (1.36) and (1.37) we can see that the EM fields decay with depth depending on their frequency ω and the subsurface conductivity σ. The depth where **E** and **H** are attenuated by a factor of $1/e$ relative to their surface amplitudes $\mathbf{E}(z=0) = \mathbf{E}^+$ and $\mathbf{H}(z=0) = \mathbf{H}^+$ is called *skin depth*:

$$d(\omega, \sigma) = \frac{1}{\mathrm{Re}(k)} = -\frac{1}{\mathrm{Im}(k)} = \sqrt{\frac{2}{\omega\mu_0\sigma}}. \tag{1.38}$$

Fig. 1.6 shows the skin depth for three different homogeneous halfspaces with resistivities of 10, 100 and 1000 Ωm in a period range of 10^{-3} to 10^3 s. It can be seen that the skin depth is significantly smaller for a less resistive, respectively more conductive, halfspace. The skin depth is also called penetration depth, which reflects the fact that EM fields

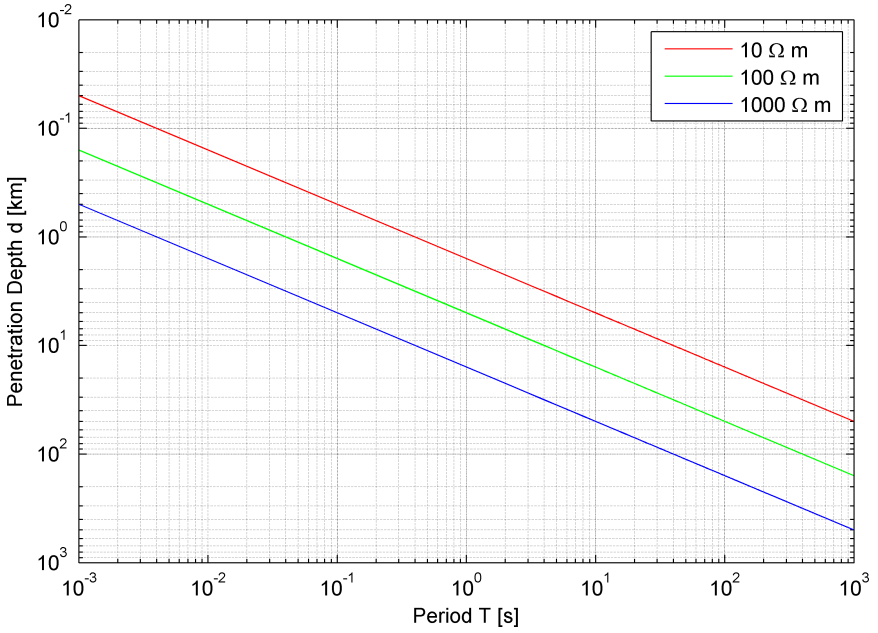

FIGURE 1.6: Skin depth d versus period for different homogeneous halfspaces. Typical material that can be assigned to the given resistivity values are sediments (10 Ωm), Earth's upper mantle (100 Ωm) and igneous rock (1000 Ωm).

are considered to be much less sensitive to structures below the skin depth although the fields are attenuated only by $1/e$ of their surface amplitude. The penetration depth d [m] can be translated into a period and resistivity dependent expression and approximated by

$$d(T, \rho) \approx 500\sqrt{\rho T}, \tag{1.39}$$

where ρ is measured in [Ωm] and T in [s]. By introducing a harmonic time dependence of the form $\mathrm{e}^{-i\omega t}$ for the surface fields $\mathbf{E}^+ = \mathbf{E}_0^+ \mathrm{e}^{-i\omega t}$ and $\mathbf{H}^+ = \mathbf{H}_0^+ \mathrm{e}^{-i\omega t}$, where $\mathbf{E}_0^+$ and $\mathbf{H}_0^+$ are constant, we get the full spatio-temporal expression for a time-varying plane wave field over a conductive halfspace:

$$\mathbf{E}(t, k, z) = = \mathbf{E}_0^+ \mathrm{e}^{-i\omega t + ikz}, \tag{1.40}$$

$$\mathbf{H}(t, k, z) = = \mathbf{H}_0^+ \mathrm{e}^{-i\omega t + ikz}. \tag{1.41}$$

1.4.1 The MT impedance and the concept of apparent resistivity and phase

There is an ongoing discussion about the beginnings of the theory about magnetotellurics, however, a detailed overview about the history of EM depth sounding is beyond the topic of this thesis. The interested reader is referred to the introduction in *Chave*

and Jones (2012). It is clear that important contributions and pioneering work regarding the MT method has been done by *Tikhonov* (1950) and *Cagniard* (1953), who developed the *Tikhonov-Cagniard model*, that consists of a vertically incident plane wave above a horizontally layered isotropic Earth. The complex-valued Tikhonov-Cagniard impedance, Z, is defined as the ratio between the complex amplitudes of the electric and the magnetic field. In the following we derive Z for the simple case of a homogeneous halfspace to introduce the main properties of Z. Starting from eq. (1.16) and with eq. (1.23) we get the following expressions in written-out component-wise form:

$$-\frac{\partial E_y}{\partial z} = \mathrm{i}\omega\mu_0 H_x, \tag{1.42}$$

$$\frac{\partial E_x}{\partial z} = \mathrm{i}\omega\mu_0 H_y. \tag{1.43}$$

From these equations and using eq. (1.40) we can derive two expressions for Z:

$$Z_{xy} = \frac{E_x}{H_y} = \sqrt{\frac{\mu_0\omega}{\sigma}}\frac{1-\mathrm{i}}{\sqrt{2}}, \tag{1.44}$$

$$Z_{yx} = \frac{E_y}{H_x} = -\sqrt{\frac{\mu_0\omega}{\sigma}}\frac{1-\mathrm{i}}{\sqrt{2}}. \tag{1.45}$$

The equations show that $Z_{xy} = -Z_{yx}$ for a homogeneous halfspace, furthermore Z_{xy} and Z_{yx} have the same amplitude $\sqrt{\frac{\mu_0\omega}{\sigma}}$ and there is a phase shift $|\Delta\Phi|$ between the magnetic and electric field of 45° for Z_{xy} and 135° for Z_{yx}. From the amplitude of Z we can derive the apparent resistivity of the subsurface, which is defined as

$$\rho_{a,ij}(\omega) = \frac{1}{\mu_0\omega}|Z_{ij}(\omega)|^2, \qquad i \neq j \in [x, y]. \tag{1.46}$$

In case of the homogeneous halfspace of conductivity σ, $\rho_{a,ij}$ reflects the true subsurface resistivity and $\rho_{a,xy} = \rho_{a,yx} = \frac{1}{\sigma}$. The phase Φ is defined as

$$\Phi_{ij}(\omega) = \mathrm{atan}\left(\frac{\mathrm{Im}(Z_{ij}(\omega))}{\mathrm{Re}(Z_{ij}(\omega))}\right), \qquad i \neq j \in [x, y]. \tag{1.47}$$

Φ is most commonly displayed in the quadrant $[0°, 90°]$.

The impedance $Z_{ij}(\omega)$ in the general case of a 3-D Earth is expressed as 2×2 tensor transfer function relating the horizontal electric and magnetic field:

$$\begin{pmatrix} E_x(\omega) \\ E_y(\omega) \end{pmatrix} = \begin{pmatrix} Z_{xx}(\omega) & Z_{xy}(\omega) \\ Z_{yx}(\omega) & Z_{yy}(\omega) \end{pmatrix} \cdot \begin{pmatrix} H_x(\omega) \\ H_y(\omega) \end{pmatrix} \tag{1.48}$$

or, in a more condensed form

$$\mathbf{E}(\omega) = \mathbf{Z}(\omega)\mathbf{H}(\omega). \tag{1.49}$$

The structure of **Z** depends on the dimensionality of the subsurface conductivity distribution at the place where **E** and **H** are measured. This is discussed in the next sections. To simplify the notation in the following we will omit but imply the explicit frequency dependency.

1.4.2 The impedance for a 1-D layered halfspace

As we have already shown the off-diagonal elements are equal except for their sign $Z_{xy} = -Z_{yx}$ and the diagonal elements are zero due to the orthogonality of EM fields, $Z_{xx} = Z_{yy} = 0$, in case of a homogeneous halfspace. This is also true for a 1-D layered

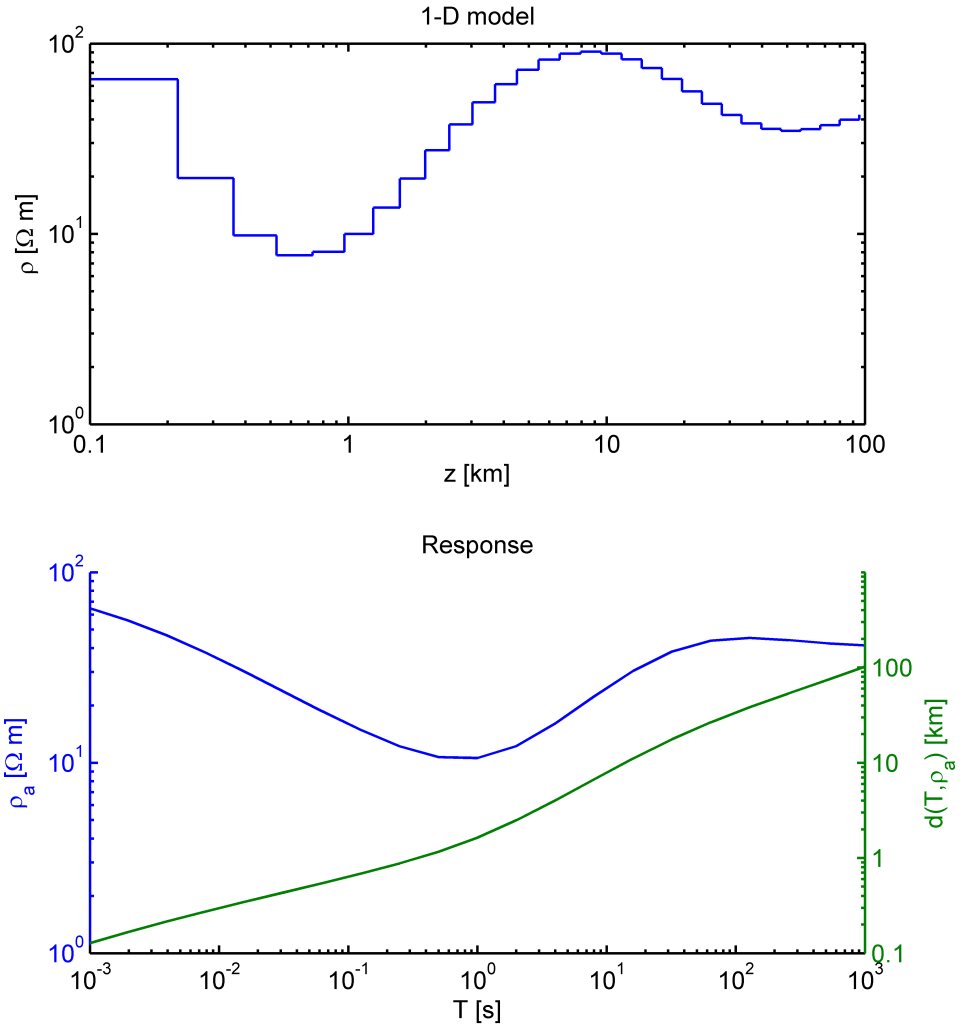

FIGURE 1.7: Example of the recursion formula eq. (1.51) applied to a 1-D halfspace as shown in the the upper part of the figure. The lower part of the figure shows the apparent resistivity $\rho_a(T)$ (blue line) and the penetration depth $d(T, \rho_a)$ (green line) derived using eq. (1.39) for T and corresponding $\rho_a(T)$.

Earth, where $\sigma(z)$ varies only with depth z. In this case the impedance can be derived analytically using a recursion formula (cf. *Wait* (1954), *Simpson and Bahr* (2005)). The impedance tensor $\mathbf{Z}$ in a 1-D case has the following form:

$$\mathbf{Z}_{1D} = \begin{pmatrix} 0 & Z_{1D} \\ -Z_{1D} & 0 \end{pmatrix}. \tag{1.50}$$

Assuming 1-D layered Earth with N layers and continuity of horizontal field components at the layer boundaries, the recursion formula gives $Z_{1D,n}$ at the roof of the n-th layer:

$$Z_{1D,n}(z_{n-1}) = \mathrm{i}\omega\frac{1}{k_n}\frac{k_n Z_{1D,n+1}(z_n) + \tanh(k_n l_n)}{1 + k_n Z_{1D,n+1}(z_n)\tanh(k_n l_n)}, \tag{1.51}$$

where $n = 1 : N$, $k_n = \sqrt{\mathrm{i}\omega\mu_0\sigma_n}$, $l_n = z_n - z_{n-1}$ is the thickness of the n-th layer and σ_n is the conductivity in the n-th layer. The lowermost layer N is defined as homogeneous halfspace with

$$Z_{1D,N} = \mathrm{i}\omega\frac{1}{k_N}. \tag{1.52}$$

Starting with eq. (1.52) and iteratively applying eq. (1.51) $N-1$ times we can derive Z_{1D} at the Earth's surface. As the governing equations of the MT method, that describe the propagation of EM fields in the subsurface, are diffusion equations, the responses obtained at the Earth's surface always have to be seen as volume averages and only in the case of a homogenous halfspace the resistivity ρ derived from Z reflects the true subsurface resistivity. For non-homogeneous conductivity distributions the apparent resistivity ρ_a defined by eq. (1.46) reflects a resistivity average over the whole halfspace that is penetrated. An example with a 1-D halfspace and its apparent resistivity derived by using the recursion formula is shown in Fig. 1.7. It is clearly seen that ρ_a is an average over the true 1-D halfspace.

1.4.3 The impedance tensor in higher dimensional cases (2-D, 3-D)

For non 1-D conductivity distributions the impedance tensor $\mathbf{Z}$ has no longer the simple form as in eq. (1.50). In case of a 2-D subsurface structure when $\sigma \equiv \sigma(x, z)$ or $\sigma \equiv \sigma(y, z)$ the impedance tensor is of the form

$$\mathbf{Z}_{2D} = \begin{pmatrix} 0 & Z_{xy} \\ Z_{yx} & 0 \end{pmatrix}, \tag{1.53}$$

if $\mathbf{E}$ and $\mathbf{B}$ are measured along the geoelectric strike direction with $Z_{xy} \neq Z_{yx}$. In the general case the fields are not measured in geoelectric strike coordinate frame, then the

strike direction has to be found by rotation of $\mathbf{Z}$

$$\mathbf{Z}(\alpha) = \mathbf{R}(\alpha)\mathbf{Z}\mathbf{R}^T(\alpha), \tag{1.54}$$

where α is the anticlockwise rotation angle and $\mathbf{R}$ is the rotational operator

$$\mathbf{R} = \begin{pmatrix} \cos\alpha & \sin\alpha \\ -\sin\alpha & \cos\alpha \end{pmatrix}. \tag{1.55}$$

Different methods to determine the geoelectric strike direction α from the impedance tensor $\mathbf{Z}$ exist. Some are based on the amplitudes of the tensor elements, others – on their phases. In the strike coordinate frame the diagonal elements of $\mathbf{Z}$ are zero, thus by maximizing one of the off-diagonal elements, their sum or squared sum or *vice versa*, by minimizing the diagonal elements one should obtain the same strike direction in a true 2-D case. For example, *Swift* (1967) minimized the squared sum of $|Z_{xx}|$ and $|Z_{yy}|$:

$$\frac{\partial}{\partial\alpha}(|Z_{xx}(\alpha)|^2 + |Z_{yy}(\alpha)|^2) = 0. \tag{1.56}$$

From here it follows

$$\tan 4\alpha = \frac{2\mathrm{Re}(S_2' D_1')}{|D_1'|^2 - |S_1'|^2}, \tag{1.57}$$

where S_1, S_2, D_1 and D_2 are modified impedances (*Vozoff*, 1972):

$$\begin{aligned} S_1 &= Z_{xx} + Z_{yy}, \qquad & S_2 &= Z_{xy} + Z_{yx}, \\ D_1 &= Z_{xx} - Z_{yy}, \qquad & D_2 &= Z_{xy} - Z_{yx}. \end{aligned}$$

For a 3-D subsurface conductivity distribution the EM fields are no longer orthogonal and no coordinate system with strike direction α can be found in which the diagonal elements are significantly smaller than the off-diagonal elements, i.e. $(|Z_{xx}|^2 + |Z_{yy}|^2) \approx (|Z_{xy}|^2 + |Z_{yx}|^2)$:

$$\mathbf{Z}_{3D} = \begin{pmatrix} Z_{xx} & Z_{xy} \\ Z_{yx} & Z_{yy} \end{pmatrix}. \tag{1.58}$$

However care has to be taken during dimensionality analysis of the impedance tensor, as small diagonal elements do also occur over 3-D structures (*Bahr*, 1991).

1.4.4 Dispersion relations in the impedance tensor

In this section dispersion relations are introduced, which connect the real and the imaginary parts of $\mathbf{Z}$. The proof of the existence of dispersion relations is based on an analysis of the analytical properties of the impedance tensor in the complex frequency plane, which is a non-trivial and rather difficult problem of EM induction. *Weidelt* (1972) and

Parker (1980) gave an analytical proof about the existence of Kramers-Kronig dispersion relations for **Z** in case of a 1-D conductivity distribution. The main conditions that need to be fulfilled can be summarized with words as follows:

(i) The impedance tensor describes a linear input-output relationship, respectively response function, where **H** is the input and **E** is the output of the system Earth.

(ii) The Earth is passive, i.e. it does not produce electromagnetic energy by itself and the conductivity does not change during the measurement.

(iii) The Earth behaves as causal linear system, where an output is always consequential to an input.

For the 1-D case *Weidelt* (1972) derived the Kramers-Kronig dispersion relations for **Z** and translated them in terms of apparent resistivity ρ_a and phase Φ:

$$\Phi(\omega_0) = \frac{\pi}{4} - \frac{\omega_0}{\pi} \fint_0^\infty \log\left(\frac{\rho_a(\omega)}{\rho_0}\right) \frac{\mathrm{d}\omega}{\omega^2 - \omega_0^2}, \tag{1.59}$$

where $\rho_0 = \rho(\omega = 0)$ and $\fint$ denotes the Cauchy principal value. Equation (1.59) can be approximated by

$$\Phi(T) \approx \frac{\pi}{4}\left(1 - \frac{\mathrm{d}\log\rho_a(T)}{\mathrm{d}\log T}\right), \tag{1.60}$$

where $T = \frac{2\pi}{\omega_0}$. The major conclusions we can draw from eq. (1.60) are:

(i) $\Phi = 45°$ for a homogeneous halfspace where $\frac{\mathrm{d}\log\rho_a(T)}{\mathrm{d}\log T} = 0$. This already follows from eqs. (1.44) and (1.45) if phases are shifted into the upper right quadrant of the complex plane.

(ii) $\Phi > 45°$ if the apparent resistivity *decreases* with period T: $\frac{\mathrm{d}\log\rho_a(T)}{\mathrm{d}\log T} < 0$.

(iii) $\Phi < 45°$ if the apparent resistivity *increases* with period T: $\frac{\mathrm{d}\log\rho_a(T)}{\mathrm{d}\log T} > 0$.

(iv) The absolute values of $\rho_a(\omega)$ have no influence on the shape of $\Phi(\omega)$. Sets of ρ_a-curves with equal $\frac{\mathrm{d}\log\rho_a(T)}{\mathrm{d}\log T}$ have an identical Φ-curve and are unaffected by the choice of ρ_0 in eq. (1.59).

There has been a controversial discussion under which conditions **Z** meets the requirements for the existence of the dispersion relationships. Violations of the dispersion relations have been observed in magnetotelluric observations and numerical models (cf. *Berdichevsky and Dmitriev*, 2008). For the discussion whether the dispersion relations are valid for a higher dimensional Earth see *Yee and Paulson* (1988), *Egbert* (1990), *Yee and Paulson* (1990) and *Egbert* (1992).

1.4.5 Distortion of responses and topographic effects

Shallow and unresolvable small-scale conductivity heterogeneities lead to a distortion of MT data in such a way that ρ_a curves are shifted to higher or lower values whereas Φ curves are mostly unaffected. Interpretation of biased data can lead to erroneous models, which do not reflect true subsurface conductivities. The origin of distortion are charge accumulations at the boundaries of small-scale anomalous bodies, which are produced by the primary electric field $\mathbf{E}^p$. This boundary charges lead to so-called galvanic or static effects independent from period that in its turn lead to a secondary electric field $\mathbf{E}^s$, which is in phase with the primary electric field $\mathbf{E}^p$ that is considered to be the *true* undistorted output response of the system Earth (*Jiracek*, 1990; *Bahr*, 1988). Galvanic scatterers may either have a reduced conductivity σ_s relative to the host subsurface conductivity σ_0 or an enhanced conductivity $\sigma_s > \sigma_0$. In the first case, $\sigma_s < \sigma_0$, the amplitude of the observed distorted electric field at the Earth's surface, $\mathbf{E}^d = \mathbf{E}^p + \mathbf{E}^s$ is increased, whereas in the second case $\mathbf{E}^d$ is decreased as illustrated in Fig. 1.8.

The secondary electric field $\mathbf{E}^s$, which sums up with the primary electric field $\mathbf{E}^p$ to

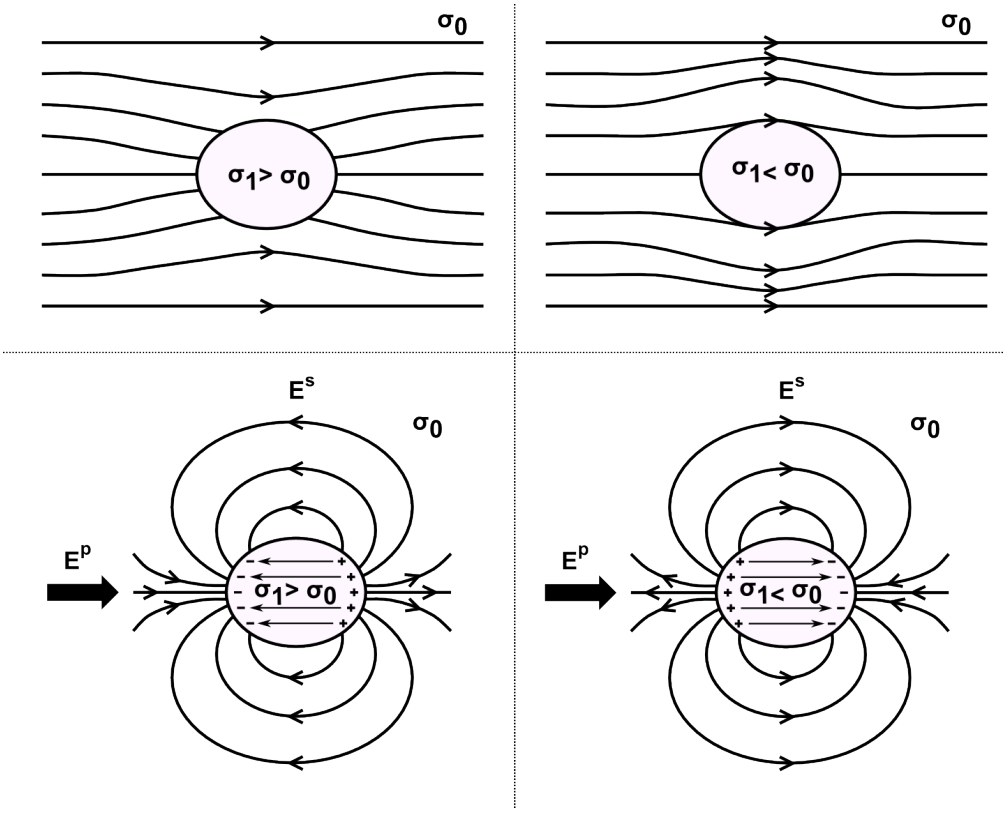

FIGURE 1.8: Schematic illustration of the effect of galvanic scatterers on the primary electric field $\mathbf{E}^p$. Total field lines are shown on top for a conductive (left) and a resistive body (right). Boundary charges accumulate at the surface of the bodies generating a secondary electric field $\mathbf{E}^s$ which adds vectorially to $\mathbf{E}^p$ as shown in the lower part of the figure. The figure was redrawn after *Jiracek* (1990).

the observed distorted electric field $\mathbf{E}^d$ can be mathematically expressed as real-valued, frequency-independent distortion tensor $\mathbf{C}$ that acts on the primary electric field $\mathbf{E}_p$:

$$\mathbf{E}^d = \mathbf{E}^s + \mathbf{E}^p = \mathbf{C} \cdot \mathbf{E}^p = \begin{pmatrix} C_{xx} & C_{xy} \\ C_{yx} & C_{yy} \end{pmatrix} \cdot \begin{pmatrix} E_x^p \\ E_y^p \end{pmatrix}. \tag{1.61}$$

The distorted observed electric field results in a distorted impedance $\mathbf{Z}^d$. By substituting eq. (1.61) in (1.49) we get:

$$\mathbf{E}^d = \mathbf{C} \cdot \mathbf{E}^p = \mathbf{C}(\mathbf{ZH}) = (\mathbf{CZ})\mathbf{H} = \mathbf{Z}^d\mathbf{H}. \tag{1.62}$$

Note, that the magnetic field is assumed not to be disturbed. In the general 3-D case the distorted impedance tensor $\mathbf{Z}^d$ has the following form:

$$\mathbf{Z}^d = \begin{pmatrix} C_{xx}Z_{xx} + C_{xy}Z_{yx} & C_{xx}Z_{xy} + C_{xy}Z_{yy} \\ C_{yx}Z_{xx} + C_{yy}Z_{yx} & C_{yx}Z_{xy} + C_{yy}Z_{yy} \end{pmatrix}, \tag{1.63}$$

where Z_{ij} are the elements of the undistorted impedance tensor. In a 1-D and 2-D case eq. (1.63) can be simplified to:

$$\mathbf{Z}^d_{1D,2D} = \begin{pmatrix} C_{xy}Z_{yx} & C_{xx}Z_{xy} \\ C_{yy}Z_{yx} & C_{yx}Z_{xy} \end{pmatrix}. \tag{1.64}$$

As the elements C_{ij} are real-valued they do not affect the phases Φ and from eq. (1.64) it follows that in 2-D geometry a coordinate system can be found by rotation where the phases in the columns of the distorted tensor $\mathbf{Z}^d_{2D}$ are equal. *Bahr* (1988) introduced a phase-sensitive strike angle to find the geoelectric strike direction in case of a distorted tensor when the strike angle defined by *Swift* (1967) fails, as it is based on the amplitudes of $\mathbf{Z}$. In 1-D or 2-D cases galvanic distortion by small-scale scatterers affects the apparent resistivity in such a way that ρ_a-curves are shifted to higher or lower values, e.g. with the off-diagonal elements of $\mathbf{Z}^d_{2D}$ follows:

$$\rho^d_{a,xy} = \frac{1}{\mu_0\omega}|C_{xx}Z_{xy}|^2 = C^2_{xx}\rho_{a,xy}, \tag{1.65}$$

$$\rho^d_{a,yx} = \frac{1}{\mu_0\omega}|C_{yy}Z_{yx}|^2 = C^2_{yy}\rho_{a,yx}. \tag{1.66}$$

$$\tag{1.67}$$

This effect is called *static shift* and probably the most serious problem emerging in MT studies, since there is no way to directly determine $\mathbf{C}$. Quite recently *Caldwell et al.* (2004) introduced the concept of the magnetotelluric phase tensor to overcome the problem of static shift.

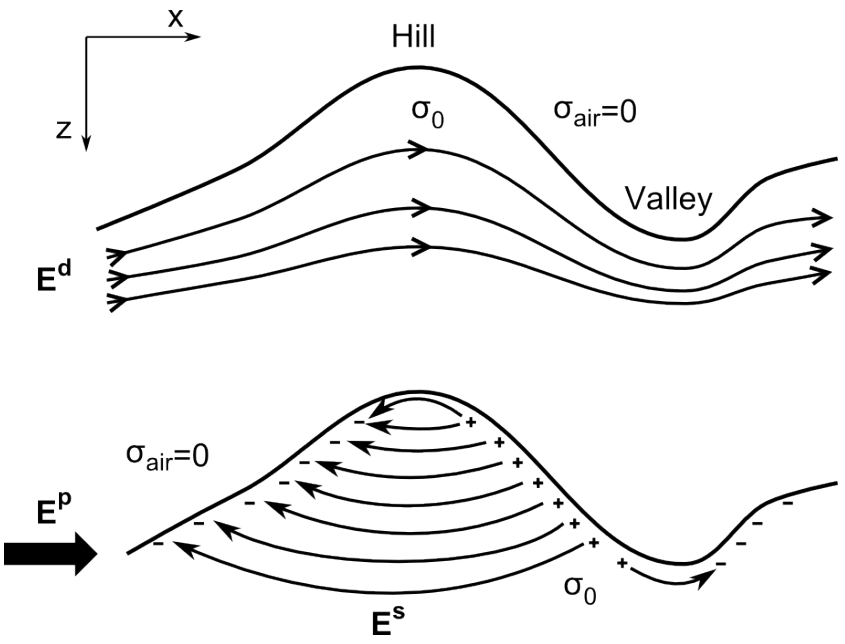

FIGURE 1.9: Schematic illustration of the galvanic effect of topography on the electric field $\mathbf{E}^p$. Total field lines $\mathbf{E}^d$ are shown on top for a simple hill-valley-scenario. Due to the topography related lateral conductivity contrast between resistive air and conductive Earth charges accumulate beneath the surface generating a secondary electric field $\mathbf{E}^s$, which adds vectorially to $\mathbf{E}^p$ as shown in the lower part of the figure. The figure was redrawn after *Jiracek* (1990).

Pronounced topography in the surrounding of a MT measurement site can also lead to galvanic distortion and a static shift effect in the ρ_a-curves. This is caused by charge accumulation at lateral conductivity contrasts between conductive Earth ($\sigma_0 > 0$) and non-conductive air ($\sigma_a ir = 0$). The charge accumulations lead to a secondary electric field $\mathbf{E}^s$ orthogonal to the local topography gradient that adds vectorially to the undistorted primary electric field $\mathbf{E}^p$. The resulting electric field $\mathbf{E}^d$ is reduced on hill tops and increased in valleys. In the idealized 2-D example in Fig. 1.9 only the E_x^d-component is distorted. Apparent resistivities $\rho_{a,xy}$, which relate the distorted electric field component E_x^d with the horizontal magnetic field component H_y, are also decreased on hill tops and increased in valleys (*Jiracek*, 1990).

1.5 Magnetic transfer functions

Additional and independent information about the subsurface conductivity structure can be derived from vertical magnetic transfer functions, if besides the horizontal **H**-field variations H_x and H_y also vertical magnetic variations H_z are measured. The vertical magnetic transfer function **T** is referred to as tipper or induction arrow, the choice of this nomenclature will be clear after the following explanations. **T** is a quantity which

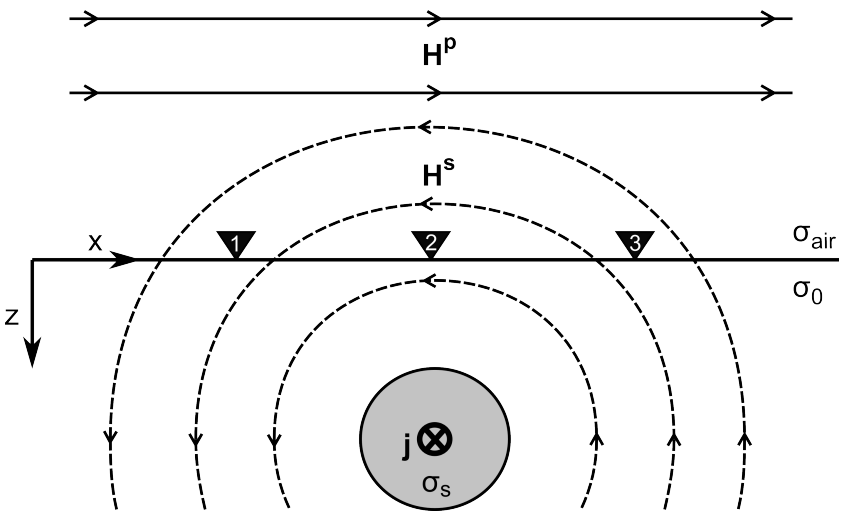

FIGURE 1.10: Tippers, see details in the text. Proposed observation sites are denoted as black triangles numbered from 1 to 3.

connects the vertical magnetic field with the horizontal magnetic field:

$$H_z = T_x H_x + T_y H_y. \tag{1.68}$$

As a consequence of the plane wave excitation, variations in H_z (and thus $\mathbf{T}$) are non zero only above *non* 1-D conductivity structures. $\mathbf{T}$ is complex-valued and frequency dependent like the impedance $\mathbf{Z}$. Tippers are often displayed as arrows with their real parts pointing away from the conductive zone in the Wiese-convention (*Wiese*, 1965). The length of real tipper arrows is given by

$$\mathrm{Re_T} = \sqrt{\mathrm{Re}(T_x^2) + \mathrm{Re}(T_y^2)}, \tag{1.69}$$

their direction is determined by

$$\alpha = \arctan \frac{\mathrm{Re}(T_y)}{\mathrm{Re}(T_x)}, \tag{1.70}$$

where α is a clockwise positive angle starting from North. Imaginary tipper arrows are derived analogously. In a purely 2-D case real and imaginary tipper arrows are collinear directed orthogonal to the geoelectric strike direction. Deviation from collinearity between real and imaginary parts can be seen as measure for deviation from a 2-D structure. A sketch to illustrate a situation that results in non-zero tippers is shown in Fig. 1.10. The horizontal primary magnetic source field $\mathbf{H}^p$ induces a current $\mathbf{j}$ in a tube-shaped buried conductor, which in turn creates a secondary magnetic field $\mathbf{H}^s$ in compliance with Ampere's law (eq. 1.19, Fig. 1.2). Unlike the primary magnetic field $\mathbf{H}^p$ the secondary magnetic field $\mathbf{H}^s$ clearly has a vertical component H_z^s. Under the assumption

that the model in Fig. 1.10 extends to infinity in y-direction, the tipper at a proposed measurement site 1 is of the form $\mathbf{T}^1 = (T_x^1, 0)^T$. At a measurement site 2 located in the center above the tube-shaped conductor the tipper is zero as there is no vertical magnetic component $\mathbf{T}^2 = (0, 0)^T$. At a site 3 $\mathbf{T}^3$ equals $\mathbf{T}^1$ except for the sign $\mathbf{T}^3 = (T_x^3, 0)^T = (-T_x^1, 0)^T$. Thus $\mathbf{T}$ can be interpreted as a measure for the tipping of the magnetic field out of the horizontal plane. When real parts of $\mathbf{T}^{1,3}$ are displayed as arrows in the Wiese-convention $\mathbf{T}^{1,3}$ both point away from the conductor, whereas $\mathbf{T}^2$ above the conductor is zero. The vertical component H_z is of a purely inductive origin as a non-zero H_z-component indicates the presence of induced currents $\mathbf{j}$ in the subsurface oriented along lateral conductivity contrasts, therefore tippers are also referred to as *induction arrows*. Since tippers are purely based on the magnetic field, they are generally not affected by galvanic distortion like the impedance.

Marcuello et al. (2005) derived dispersion relations for the tipper transfer function, claiming the conditions for their existence, i.e. causality, passivity and linearity, are fulfilled if the horizontal magnetic field is non-zero $\mathbf{H}_h \neq 0$. For this case they showed that the imaginary part of the tippers $X(y) = \mathrm{Im}(\mathbf{T}(y))$ can be represented as the derivative of the real part $R(y) = \mathrm{Re}(\mathbf{T}(y))$, where $y = \ln \omega$.

$$X(y) \approx \frac{\mathrm{d}(R(y))}{\mathrm{d}y}. \tag{1.71}$$

In observed and synthetic data one often obtains that tippers fulfill this relationship and it is often seen that imaginary parts vanish when the real parts reach an extremum. However, in their study *Marcuello et al.* (2005) also give examples where the relationship eq. (1.71) is clearly violated.

As previously mentioned tippers are only non-zero above non-1-D conductivity structures. However, tippers at island and coastal geomagnetic observatories are large owing to the so-called ocean effect even if the crustal structure is essentially 1-D (e.g. *Parkinson*, 1962). The ocean effect is caused by the horizontal conductivity contrast between resistive continental bedrock and conductive sea water. In a side project of this PhD study we demonstrated that the overall behavior of tippers at island observatories is well explained by the ocean effect, if topography and bathymetry are adequately modeled. Furthermore we could show that tippers are also sensitive to the 1-D conductivity section underneath such observatories and could be used to recover the 1-D conductivity section in oceanic regions by inverting them in terms of 1-D conductivity distribution in the presence of a realistic 3-D bathymetry. The details of this study can be found the the Appendix D and have been published in *Samrock and Kuvshinov* (2013).

1.6 Estimation of transfer functions

In the most general case transfer functions relate the output of a system to the input of the system. They allow to characterize a system by its response to an input signal. The concept of transfer functions as applied, for example, to the MT impedance gives a linear relation that maps the horizontal magnetic field $\mathbf{H}_h$ onto the horizontal electric field $\mathbf{E}_h$. In this context $\mathbf{H}_h$ is considered as input and $\mathbf{E}_h$ – as output of the Earth, acting as linear time-invariant system, which we seek to characterize by its response. In case of tipper transfer functions, $\mathbf{H}_h$ is considered as input and the vertical magnetic field H_z is defined as output.

In order to estimate the transfer functions (impedance and tippers) relevant for this study we used the EMTF code by *Egbert and Eisel* (1998), which allows to estimate a linear frequency dependent relationship between a defined set of input and output time series. The main steps involved in the code are described in the following. The exact solution of the MT relationship eq. (1.49) in frequency-domain is

$$\mathbf{Z} = (\mathbf{E} \otimes \mathbf{H}^*) \cdot (\mathbf{H} \otimes \mathbf{H}^*)^{-1}, \tag{1.72}$$

where $\otimes$ defines the outer product, $\mathbf{H}^*$ is the complex-conjugate of the spectrum $\mathbf{H}$, and the terms in brackets are consequently the cross- and auto-spectra (*Chave and Jones*, 2012). However, in real data the recorded time-series are discrete, have a finite length and are affected by noise. Therefore $\mathbf{Z}$ and its uncertainty $\Delta\mathbf{Z}$ have to be estimated in a statistical manner, which can be summarized as follows: The first step of the time series processing comprises windowing and pre-whitening of the time-series. The data segments (windows) are then Fourier-transformed from time into frequency domain. In a second step the response functions are estimated in frequency domain using robust single site and remote reference processing techniques (*Egbert and Booker*, 1986; *Egbert*, 1997). The robust algorithm reduces the impact of outliers on the responses by iterative down-weighting of data segments with poor data, this illustrates the advantage of a proper windowing of the data. However, robust processing techniques only improve the responses if the signal to noise ratio is not too low. The remote reference method makes use of additional magnetic time-series recorded at a so-called remote reference site, which is from several to tens of kilometers away of the survey sites. Due to the distance between reference and survey site the condition is assumed to be fulfilled that only the signal of the natural field variations between the sites is coherent, whereas noise is usually random and incoherent. Thus by correlating the variations between the sites, the effects arising from noise can be removed. The quality of responses usually improves significantly by remote reference processing, especially in the so called dead band ($1 - 0.01$ Hz) where the signal to noise ratio is typically very low (see Section 1.2).

The exact solution for the remote reference estimate is of the form

$$\mathbf{Z} = (\mathbf{E}_S \otimes \mathbf{H}_R^*) \cdot (\mathbf{H}_S \otimes \mathbf{H}_R^*)^{-1}, \tag{1.73}$$

where subscript R denotes spectra at the reference site and subscript S – spectra at the survey site (*Gamble et al.*, 1979).

Chapter 2

The survey area

This chapter gives an overview about the Aluto-Langano geothermal field and its tectonic environment within the Main Ethiopian Rift (MER) valley as part of the great East African Rift System (EARS), that separates the Nubian and the Somalian plates. Rift systems are tectonically active zones that describe the continental spreading phase of the Wilson cycle (*Wilson*, 1968): the Earth's surface is continuously reshaped in a quasi-periodic plate tectonic cycle, which main initial stages are continental rifting, continental break-up and subsequent formation of an oceanic spreading center with passive continental margins. Continental rifts are seismically and volcanically active zones, which often form trough-like basins hosting sedimentary basins and lakes. This architecture makes rift valleys promising targets for renewable energy exploration and exploitation with an especially high potential for hydro and geothermal power.

The EARS is also known for having developed a diverse and rich flora and fauna throughout Earth's history and it is believed to be the *cradle of humankind*: the oldest hominid skeletons are found along the EARS, one of the oldest is the skeleton of a female australopithecus afarensis, which is believed to have lived 3.2 Ma ago. The skeleton is commonly known as *Lucy* and was found in the Afar region in Ethiopia (e.g. *Kimbel and Delezene*, 2009). Recently the oldest-known stone tools of human mankind were found at the Gademotta formation at Aluto (*Sahle et al.*, 2014).

2.1 The East African Rift System

The EARS is an intercontinental active rifting zone that extends for more than 3500 km from the southern coast in Mozambique to the North of Ethiopia. At its northern end, in the so-called Afar depression, it meets the Red Sea Rift and the Gulf of Aden Rift. This complex triple junction zone marks the boundary between three divergent plates, which are the Nubian plate in the West, the Somalian plate in the East and the Arabian plate in the North (Fig. 2.1). Rifting started in the Afar region from where it propagated southwards. Along its way from North to South the EARS shows all

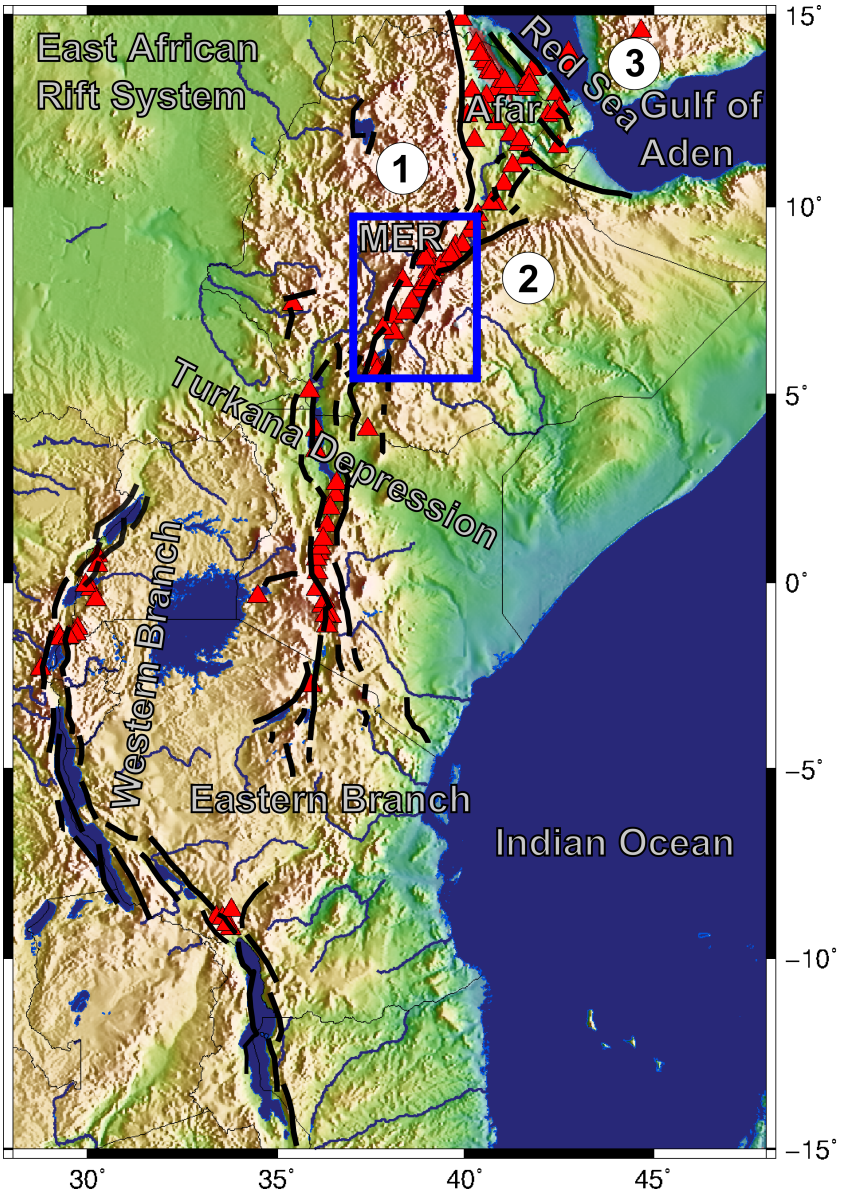

FIGURE 2.1: Overview map on the East African Rift system. Black lines denote border faults redrawn from *Ebinger* (2005). Numbers 1, 2 and 3 denote location of the Nubian, Somalian and Arabian plate. Red triangles mark volcanoes listed in the Smithonian volcano database (`http://www.volcano.si.edu/`). The blue rectangle marks the area shown in Fig. 2.3.

stages of continental rift evolution: from early stages of rift initiation at the southern branches to incipient continental break-up and final stages associated with the formation of oceanic crust in the Afar depression (*Ebinger*, 2005). The Afar region has experienced extensive volcanism since 45 Ma with the onset of rifting around 30 Ma ago, here the highest spreading rates in the EARS are observed with up to $6 \pm 1.5\,\mathrm{mm\,a^{-1}}$ separation (*Chu and Gordon*, 1999). A remnant of the pre-rift volcanism is the Ethiopian flood basalt province, which covers around $600,000\,\mathrm{km}^2$. The volume of basalts is estimated to $300,000 - 350,000\,\mathrm{km}^3$ with local thicknesses of up to 2000 m (*Mohr*, 1983). The basalts

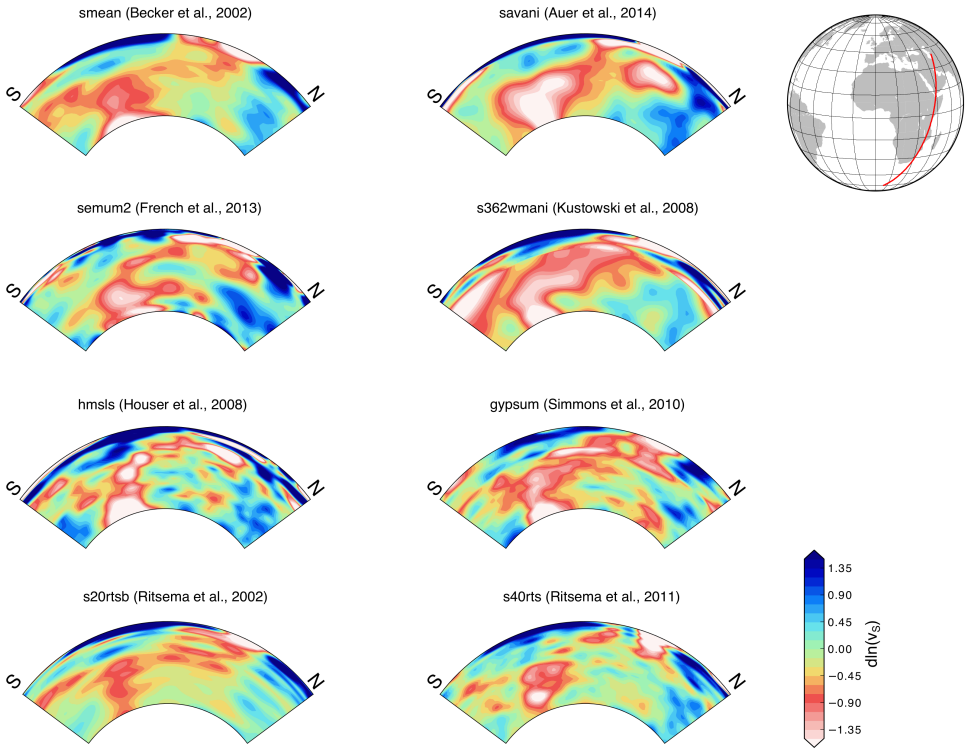

FIGURE 2.2: Comparison of seismic global tomography models along a vertical cross-section from the South Atlantic along the EARS to the Afar region denoted as red line on the the upper right globe. Lower and upper boundaries are the core mantle boundary and the Earths surface. Shear-wave velocity variations ($\mathrm{d}\ln(v_s)$) are given with respect to a reference model. The figure was provided by Ludwig Auer (personal communication).

show a distinct geochemical signature consistent with mantle plume material. However, open questions remain concerning the location and extent of the proposed mantle plume as well as the number of plume events (*Yirgu et al.*, 2006, and references therein). The number of proposed plumes underneath Africa reaches from only one to as many as 40 (*Davies*, 1998).

Seismic studies reveal a low-velocity zone (LVZ) in the upper mantle underneath the Ethiopian plateau and the eastern branch of the EARS, which can be explained by increased temperatures of several hundred °C relative to the ambient mantle (*Nyblade*, 2011, and references therein). Underneath the Ethiopian plateau, where the lithosphere is thin with only $80 - 90\,\mathrm{km}$, the LVZ extends from $150 - 200\,\mathrm{km}$ depth to at least as deep as the mantle transition zone. Beneath the south eastern branch the low-velocity zone does not extend to the base of the lithosphere but it reaches down to greater depths and the 410 km discontinuity is depressed by $20 - 40\,\mathrm{km}$.

The LVZ underneath the African rift is part of a larger LVZ, which is often referred to as African superplume, however, its nature and extend are still under debate. Some global tomography studies find that the anomaly continuously extends from the upper

mantle underneath the Afar region towards South Africa and the South Atlantic where it stretches down to the core-mantle boundary (*Ritsema et al.*, 1999; *Becker and Boschi*, 2002; *Kustowski et al.*, 2008; *Houser et al.*, 2008; *Simmons et al.*, 2010; *Auer et al.*, 2014; *French et al.*, 2013). Such a superplume structure would reveal a direct linkage between a hot core-mantle boundary region with the flood basalt province and ongoing volcanism and rifting in the Afar region, see Fig. 2.2. However, in a newer study by *Ritsema et al.* (2011) the continuation of the African superplume from the core-mantle boundary into the upper mantle in East Africa is less clear.

The Ethiopian Rift Valley and the eastern branch of the rift show a distinct volcanic activity, occurrence of earthquake swarm events and microseismic activity, most volcanoes of the EARS are located here, see Fig. 2.1. Volcanism plays a minor role at the western branch, here the rift is dominated by high sedimentation rates and lake filled basins (*Saemundsson*, 2008). The lakes of the western branch belong to the world's largest freshwater reservoirs, with Lake Tanganyika reaching depths of more than 1400 m. Although the western branch is volcanically less active compared to the eastern branch it hosts Africa's most active volcano: the Nyiragongo, which is part of the Virunga volcanic chain along the border of Rwanda and the Democratic Republic of the Congo.

2.2 The Main Ethiopian Rift System

Our study area, the Aluto volcanic complex, is located in the central Main Ethiopian Rift System (MER), which denotes the northern part of the EARS between the Turkana and the Afar depression. The MER separates the Nubian and the Somalian plate, its trough is between $35 - 80$ km wide and bounded by large normal boundary faults which developed during the Miocene. The major escarpment between the rift floor and the flanking plateaus is built up by steep N-E striking normal boundary faults with some of them exceeding a vertical throw of 100 m, the relative displacement reaches overall differences in height of up to 2000 m (*Gebregzabher*, 1986; *Corti*, 2008). Today the boundary faults are considered to be inactive, a study of their morphology east of Aluto volcano by *Pizzi et al.* (2006) suggests a tectonically induced rather than a magma-induced faulting. Strain accommodation by mechanical stretching and formation of large border faults is typical for the young stadium of rifting and is currently observed in the southern part of the EARS (*Kendall et al.*, 2006). The rift floor in the central MER is dominated by a narrow network of active NNE-SSW oriented faults (Fig. 2.3). This extensional fault system developed in the past 2 Ma and is the youngest part of the MER, it is referred to as Wonji Fault Belt (WFB). Main Quaternary volcanism occurs in en echelon disposed segments along the WFB within the Rift Valley. Seismic measurements have revealed that most of the present-day seismicity coincides with these magmatic segments and by

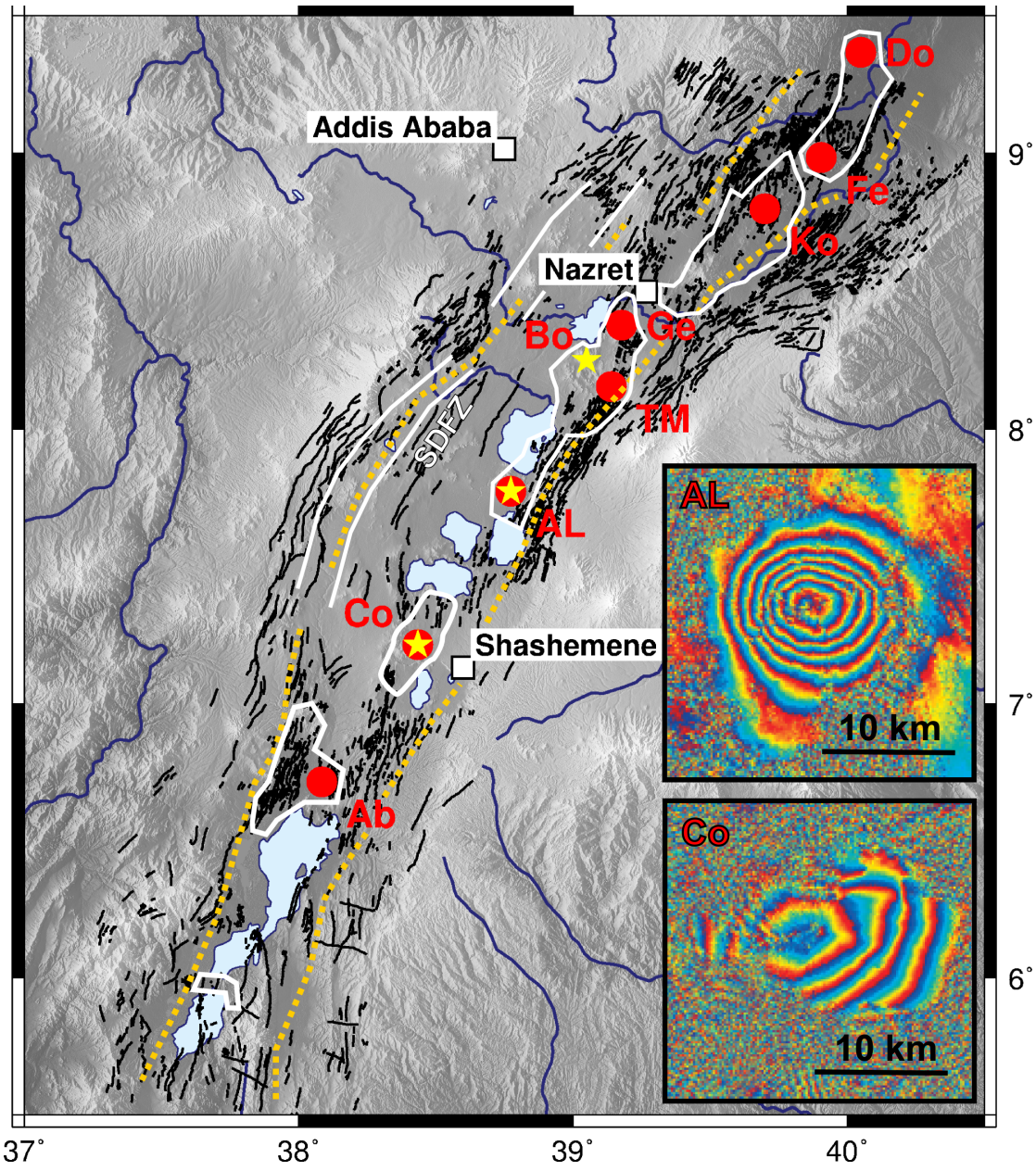

FIGURE 2.3: Overview map on the Main Ethiopian Rift system. Black lines denote border and Wonji faults based on the fault database from *Agostini et al.* (2011), faults between the dotted yellow lines are considered to be part of the active Wonji fault belt, for a detailed classification of Wonji and border faults see *Corti* (2009). White lines mark centers of Quaternary magmatic segments, the Silti Debre Zeit fault zone (SDFZ) is located west of Aluto. Geothermal fields are marked as red dots: Abaya (Ab), Corbetti (Co), Aluto-Langano (AL), Tulu Moye (TM), Gedemsa (Ge), Kone (Ko), Fentale (Fe) and Dofan (Do). Yellow stars show places with observed surface deformation. The subfigures on the lower right show InSAR interferograms taken from *Biggs et al.* (2011) for the uplift at Aluto (AL, 17. Dec. 2003-18. Aug. 2004) and for subsidence at Corbetti (Co, 23. Sep. 1997 to 13. Sep. 2000). Each fringe represents 2.8 cm of motion in the satellite line of view.

GPS measurements it was shown that up to 80% of the present day strain is accommodated across the WFB. The faults in the rift floor show recent activity with slip rates up to 2 mm/yr (*Bilham et al.*, 1999; *Pizzi et al.*, 2006). As driving force a mixture of tectonic faulting and dyke injection is considered (*Corti*, 2008).

Kendall et al. (2005) use observations of seismic shear-wave splitting to reveal a seismically anisotropic upper mantle with a fast shear wave direction parallel to the Ethiopian Rift. The magnitude of splitting varies significantly within short distances (50 km) which is why its reason is most likely situated within the upper 100 km of the subsurface. An increased splitting is observed within the Quaternary magmatic segments, where fast shear-wave polarization is oriented parallel to the faults and dykes within the WFB. Amongst several mechanisms that could cause the observed anisotropy *Kendall et al.* (2006) argue in favor of oriented melt pockets like vertically aligned crack-like melt inclusions that arise from magma injection into the lithosphere and dyke injection within the magmatic segments. This is in agreement with the above mentioned dyke injection as driving mechanism for active faulting within the WFB.

A few off-axis belts of Quaternary volcanism occur at the Western margin of the central MER, e.g. at the Butajira volcanic chain west of Aluto, which is also referred to as Silti Debre Zeit fault zone (SDFZ), Bishoftu volcanic chain or Guraghe escarpment (*Woldegabriel et al.*, 1990).

The Aluto volcanic complex is located in the Lakes District of the MER hosting the four major lakes Ziway, Langano, Shala and Abiyata. These lakes have been exposed to significant lake level fluctuations in the past and are believed to be remnants of an ancient Megalake during the Pleistocene, which has separated into the present day isolated lake system during the late Holocene (*Benvenuti et al.*, 2002). Aluto is enclosed by Lake Ziway in the North and Lake Langano in the South, it is set close to the eastern escarpment of the rift along the WFB. Rather than a volcano with a main eruptive center Aluto is considered to be built up by a cluster of overlapping rhyolithic domes, glassy lava flows, pumiceous cones and craters, which are localized along NNE tending normal faults (*Benoit et al.*, 2007). Within the Aluto-Langano geothermal field the normal faults are considered to act as upflow zone for hot geothermal fluids. The radiometric ages of Aluto volcanic products have been determined to range from 155,000 a to 2000 a (*Battaglia*, 2004, and references therein). At present Aluto is in a stage of fumarolic activity. Natural hot springs are found at the end of the southern flanks at the shore of Lake Langano.

2.3 Surface deformation at Aluto-Langano geothermal field and motivation for MT studies

Biggs et al. (2011) identified four areas of significant deformation in the MER, namely at Haledebi, Bora, Aluto and Corbetti by using Interferometric Synthetic Aperture Radar (InSAR) observations. InSAR is a powerful satellite technique for remote sensing of surface deformation. By comparing the phase of radar images taken at different times surface displacements of > 1 cm at a lateral resolution of around 90 m can be detected. InSAR interferograms at Aluto and Corbetti show a symmetric circular deformation pattern, which is centered on the volcano (Fig. 2.3). The largest deformation occurs at Aluto, here two cycles of rapid uplift followed by slow subsidence have been observed since 2004. The two pulses of uplift ($10 - 15$ cm) in 2004 and 2008 were followed by subsidence at an averaging rate of 3-5 cm/a (Fig. 2.4). Modeling studies revealed two possible scenarios to explain the observed deformation (*Biggs et al.*, 2011): (i) a shallow penny shaped crack in around 2.5 km depth with $3-10$ km in diameter, or (ii) a deeper ($\sim$ 5 km) point source. The working hypothesis is that the causative source of unrest is either the shallow hydrothermal reservoir, or the deeper situated magmatic system at depths of greater than 3 km, or a hybrid of the two. However, by using solely information about surface deformation it is not possible to discriminate between a deep or a shallow source of driving force. Further information can be gained using geophysical deep sounding techniques such as seismic, seismological and electromagnetic (EM) methods like MT. The reason for using MT to identify the source of unrest is two-fold, firstly MT easily

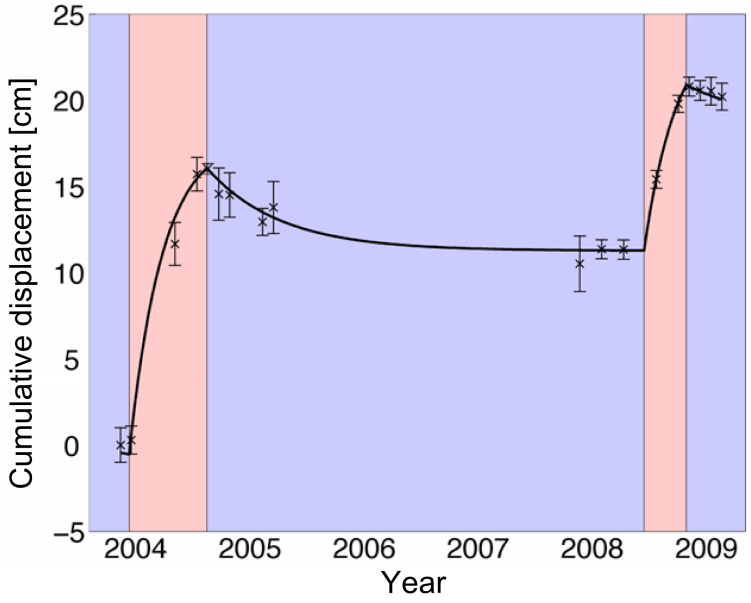

FIGURE 2.4: Time series of deformation at Aluto (taken from *Biggs et al.*, 2011). Aluto shows two pulses of uplift in 2004 and 2008 with intervening phases of subsidence.

covers exploration depths down to a few kilometers and secondly it is especially sensitive to zones of high electrical conductivity, which, in geothermal environments, are typically related to high temperature hydrothermal or magmatic reservoirs (e.g. *Muñoz*, 2014). The application of MT to geothermal research and exploration is introduced in the next chapter.

Chapter 3

Application of the MT method to geothermal exploration

The main goal of geothermal resource exploration is to infer an isotherm pattern of the subsurface based on surface data ultimately for targeting geothermal wells and to assess resource capacities. Typical geothermal data sets consist of surface geochemistry, hydrology and hydrothermal alteration, geology and structure, and geophysics. In this study we focus on *high enthalpy* geothermal systems, which are typically related to volcanically active, magmatic and extensional zones like continental rifts. They are often manifested by surface expressions like hot springs, fumaroles and geysers. Their potential for energy production is commonly classified in terms of the specific enthalpy h of fluids extracted from the system, which can be seen as a measure for the heat content of the fluids. The enthalpy H is generally defined as sum of the internal energy U and the product pV of pressure and volume of the system:

$$H = U + pV. \tag{3.1}$$

Specific enthalpy h is the enthalpy H divided by the mass, it is measured in $\left[\frac{\text{kJ}}{\text{kg}}\right]$. It can be shown that the specific enthalpy of a geothermal fluid is more or less proportional to the temperature (*Dickson and Fanelli*, 2013). Note that the classification of geothermal resources solely by their enthalpy and/or temperature can be inadequate since it does not reflect the *maximum work available of the fluid* as discussed in *Lee* (2001). High enthalpy systems have been widely characterized by conventional permeable geothermal formations with temperatures reaching from 150 to over 350 °C in some cases. The main characteristics of such a reservoir can be derived from the acquired surface data jointly with the *conceptual high enthalpy reservoir model* (e.g. *Cumming*, 2009). The conceptual reservoir model puts constraints on the parameters expected in a geothermal data set based on the assumption that a hydrothermal system is mainly described by hot circulating fluids that affect the host rock and leave a specific imprint depending on their

temperature that can be detected by the above mentioned methods. This approach has proven to be the most plausible method in geothermal exploration so far as confirmed by its great success in volcanic regions. Its application to the MT method is to ascertain reservoir characteristics based on recovered subsurface electrical conductivities, which follow a very typical distribution controlled by the hydrothermal alteration mineralogy as we will see later in this chapter.

3.1 Resistivity distribution in high enthalpy geothermal systems

In search for geothermal reservoirs, in particular high enthalpy hydrothermal systems, electrical resistivity has proven to be the most useful *geophysical* parameter in order to classify a potential reservoir and for siting initial exploration wells. By using MT one can map the subsurface conductivity distribution easily down to depths of several kilometers. Volcanic high enthalpy hydrothermal systems are typically built up by a deep active or relict magmatic heat source, which is overlain by a convective hydrothermal system (e.g. *Muñoz*, 2014). The electrical resistivities found in a geothermal reservoir are mainly governed by the mineral composition of the rocks and the reservoir fluids filling the pore space (*Ussher et al.*, 2000). The influence of fluids depends strongly on their resistivity, which in turn is determined by their salinity and to a lesser extend by their temperature. In addition the fluid saturation, porosity and permeability of the system is of great importance as only a well interconnected network of fluids may influence the bulk electrical resistivity. A permeable system saturated with hot geothermal fluids is affected by hydrothermal alteration processes, which are epigenetic modifications of the pre-existing host rock. Common hydrothermal alteration products in igneous rock are clays that have a great effect on the bulk electrical resistivity depending on their type.

In terms of resistivity the conceptual model of a high enthalpy system is mainly characterized by the following features: The shallow part of the reservoir is built by a resistive surface layer depicted as zone 1 in Figure 3.1. Underneath is a highly conductive cap (Figure 3.1, zone 2), which is located above the more resistive reservoir (Figure 3.1, zone 3). The reservoir is underlain by the heat source where resistivities are decreasing again (Figure 3.1, zone 4). The shallow surface layer consists mainly of fresh volcanic material like tephra, pyroclastic rock or tuff, here the temperature is $T < 70\,^{\circ}\mathrm{C}$, the water saturation is generally low and thus rocks are unaffected by alteration, which, altogether, results in high resistivities in the order of $100\,\Omega\mathrm{m}$. The low resistivity in the deeper seated cap layer is caused by presence of either saline fluids and/or the presence of conductive hydrothermal alteration products. Hydrothermal alteration is a metamorphic process as a result of the interaction of high temperature fluids with the host rock. At temperatures below $200\,^{\circ}\mathrm{C}$ argillic hydrothermal alteration takes place which most common products

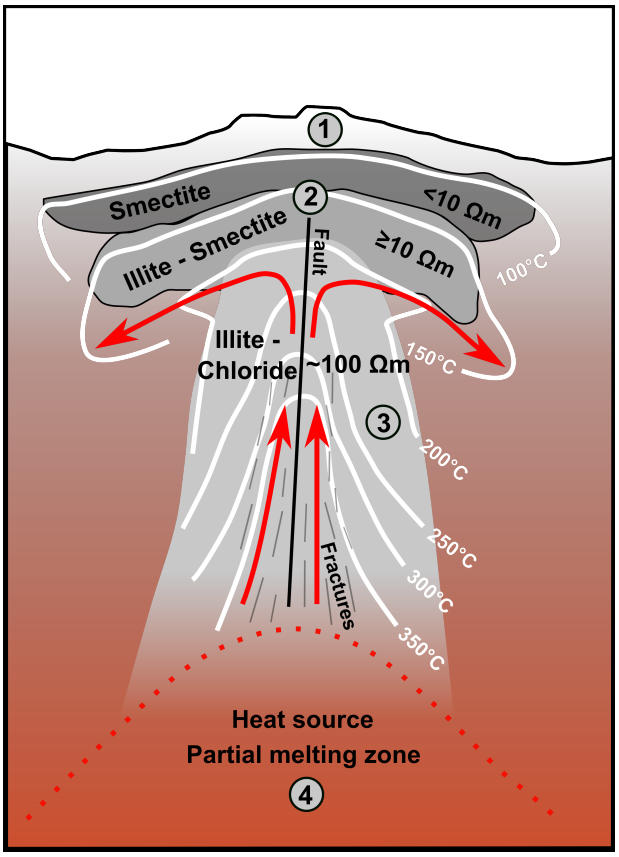

FIGURE 3.1: Sketch of the conceptual model of a high enthalpy geothermal reservoir redrawn from *Johnston et al.* (1992) and *Cumming* (2009). 1 - resistive shallow layer, 2 - conductive clay cap, 3 - reservoir, 4 - heat source. Red arrows describe the fluid flow and white lines the isotherms.

are smectite and illite towards higher temperatures. Above 200 °C propyllitic alteration forms mainly chlorite (e.g. *Teklemariam et al.*, 1996). Smectite clays have resistivities below 10 Ωm whereas illite and chlorite clays have resistivities typically above 10 Ωm. This leads to higher resistivities in the hotter part of the geothermal system (zone 3), which is covered by the conductive clay cap (zone 2) in which temperatures are between 70 and 200 °C (*Ussher et al.*, 2000). The propyllitic reservoir in zone 3 is built up by a permeable upflow zone where hot geothermal fluids migrate upwards along fractured formations and/or narrow faults driven by thermal buoyancy. In this upflow zone the temperature generally increases with depth. On top of the upflow zone is the outflow zone with a predominant lateral flow below the less permeable clay cap. A characteristics for the outflow zone is the negative temperature gradient with depth. The isotherm pattern inside such a a geothermal reservoir is mainly governed by the flow pattern of the geothermal fluids (*Cumming*, 2009).

An active volcanic heat source (zone 4) underneath the reservoir is associated with the presence of partial melt or a magmatic chamber. Melt is known for having a considerably low resistivity, an active magmatic heat source underneath a geothermal system

is therefore identified by a another good conductor at greater depths.

In the past the resistive propyllitic reservoir (zone 3) beneath the conductive clay cap (zone 2) has turned out to be the most suitable target for drilling in geothermal exploration, as here temperatures are expected to be maximum and fluid saturation, porosity and/or permeability of the system are high enough to allow for productive exploitation (e.g. *Muñoz*, 2014).

Note that temperatures inferred from conductivities are always maximum values that have been reached in the reservoir during its evolution, current temperatures can be generally lower. The electrically high conducting properties of clay caps makes them ideal targets for MT soundings. But care has to be taken as high conducting anomalies in geothermal environments are not always correlated with clay caps sitting on top of high enthalpy reservoirs (*Cumming*, 2009). So-called *anomaly hunting* may be misleading and to avoid misinterpretations additional information from the above mentioned different exploration methods should be taken into account to construct a consistent model.

Recently *Younger* (2014) criticized shortcomings of the introduced conceptual reservoir model as many geothermal systems might exist that are worth to be exploited but that have an electrical conductivity distribution, that differs from the introduced one. Furthermore, conceptual reservoir models do not exist for many tectonic settings. It is important to note that the formation of attractive geothermal targets can principally appear in any kind of rock – volcanic, sedimentary and metamorphic. It might be misleading to focus on the identification of hydrothermal alteration zones only, as not all kind of rock formations tend to form clay minerals when exposed to hydrothermal fluids. However, the geothermal field studied within this thesis is a volcanic high enthalpy system, which we expect to be in agreement with the main features of the introduced conceptual reservoir model. The following section will treat the main conduction mechanisms that are responsible for the obtained electrical conductivity distribution in the previously described high enthalpy conceptual reservoir model.

3.2 Electrical conduction mechanisms in high enthalpy geothermal systems

Clays in this context are considered as hydrothermal alteration products that are built up by a porous mineral phase with an interstitial pore fluid phase. They are known to exhibit non-zero surface charge densities in contact with liquids, which arise from mainly three processes (*Çelik*, 2004):

1. Dissociation: Most clays have components which tend to dissociate and exhibit surface charges depending on the pH of the fluid. In such a case the potential across the surface is determined by H^+ and OH^- ions.

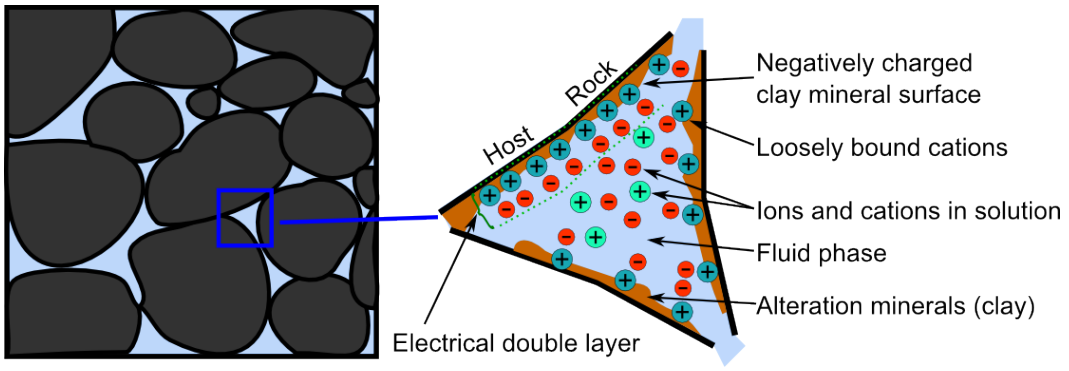

FIGURE 3.2: Sketch of a porous rock matrix with a hydrothermally altered mineral phase and an interstitial fluid (left). Details of a pore (right) illustrating the origin of free charges that are dissolved in the fluid and accumulate in form of electrical double layers at the clay-fluid-interface.

2. Adsorption: Clay surfaces can undergo either chemical or physical adsorption of ions dissolved in the fluid phase.

3. Isomorphic substitution: Clays can be generally characterized as aluminosilicates that tend to substitute Al^{3+} for Si^{4+} and Mg^{2+} for Al^{3+} into their crystal lattice in contact with water. Isomorphic substitution leads consequently to an overall negative surface charge of the clays.

In contact of clays with liquids a thin electrically charged double boundary layer develops at the clay-water-interface, which is referred to as *Gouy-Chapman layer*. The bulk electrical properties of porous clays are mainly governed by this boundary layer and the pore water itself, see Fig. 3.2.

In a highly permeable fluid dominated system with formation of a well interconnected fluid network the electrical the resistivity ρ can be mathematically approximated by the following modified Archie's equation introduced by *Caldwell et al.* (1986):

$$\rho = a\rho_W \Phi^{-n} S_W^{-m} (1 + KC\rho_W)^{-1}. \tag{3.2}$$

Here ρ describes the bulk resistivity, ρ_W is the resistivity of the fluid phase, Φ is the porosity, S_W the fluid saturation and a, n, and m are empirical constants that describe the character of the porosity (see also *Ussher et al.* (2000)). C is the proportion of clay minerals and K is a constant depending on the clay species present. Equation (3.2) states that conduction in porous water saturated clay system is mainly governed by ionic conduction in the fluid and clay surface conduction whereas rock matrix conduction is negligible. In fluid dominated systems conductivity depends mainly on the salinity and the mobility of the ions in the water. The charge mobility in a fluid is related to the fluids viscosity, which generally decreases with temperature. This leads consequently to an inverse exponential dependence of resistivity with temperature (see *Ussher et al.*

(2000) for detailed examples):

$$\rho = \rho_0 e^{\epsilon/kT}, \tag{3.3}$$

where ϵ is the activation energy, k the Boltzmann's constant and T the temperature in [°K]. ρ_0 is the resistivity at a theoretically infinite temperature.

In an impermeable clay dominated system with a poorly interconnected fluid network surface conduction of the clay minerals becomes the dominating mechanism on bulk resistivity. The surface charge density of clays and thereby their capability for electric conduction depends on their cation exchange capacity (CEC), which again differs strongly for different clay types. In a clay dominated system the conductivity is proportional to the CEC of the clays (*Ussher et al.*, 2000).

Common clay minerals formed by hydrothermal alteration are smectite clays at temperatures below 200 °C and chlorite clays at temperatures above 200 °C and illite clays in the transition zone as described in Section 3.1. Smectite has an averaged CEC that exceeds the one of illite and chlorite by a factor of 6 (*Çelik*, 2004), which gives rise to the observed low resistivities below 10 Ωm in the argillic hydrothermal alteration zone of geothermal systems that cover temperatures below 200 °C. At temperatures above 200 °C the formation of chlorite correlates with a sudden increase in resistivity in the propyllitic hydrothermal alteration zone, where resistivities rise to values in the order of 100 Ωm.

The previously described resistivity distribution in a geothermal system appears to be mainly controlled by the temperature dependent hydrothermal alteration clay products. Although fluids may contribute to the low resistivities in the smectite clay cap in high salinity reservoirs. Towards greater depths the conductivity of fluids generally increases as both salinity and temperature increase with depth. However, their capability to reduce resistivities in the resistive propyllitic zone is suppressed by lower porosities at greater depths. Here the upflow of fluids is mainly controlled by narrow vertical fractures and faults, rather than by a broad and well interconnected network, thus there is no significant affect on the resistivity obtained by MT soundings, which average over a large volume. The hottest part of a reservoir is furthermore often steam dominated as fluids undergo a phase change with increasing temperatures resulting in a the presence of a significant vapor fraction that dominates within the large fractures and voids of the reservoir. Hereby the capability of the fluid to lower bulk resistivity is reduced as the electrical resistivity of a fluid increases dramatically with increasing vapor fraction (*Milsch et al.*, 2010).

In the following section a few case studies are presented, which show the successful application of the MT method to geothermal exploration.

3.3 Case studies of MT in geothermal exploration

The high enthalpy geothermal systems located within the Taupo Volcanic Zone in New Zealand belong to the most-investigated worldwide. Here 23 geothermal fields have been identified in a large part based on their reduced shallow resistivities within the clay cap relative to the surrounding (*Bibby et al.*, 1995). 6 of the 23 geothermal fields have been exploited for energy production so far. The total electricity generating installed capacity of the Taupo Volcanic Zone sums up to 750 MWe[1]. Some of the geothermal fields there have been also investigated by 3-D interpretation of MT data. *Heise et al.* (2008) determined the resistivity structure down to depths of $\sim$ 5 km under the Rotokawa geothermal field based on data at 64 sites using the inversion scheme by *Siripunvaraporn et al.* (2005). Within the Rotokawa geothermal field the recovered structure is mainly described by resistivities below 10 Ωm at depths greater than 500 m and towards the deeper part $>$ 1200 m resistivities increase to values $>$ 100 Ωm. From drillings it is known that the conductive part is associated with the smectite clay cap, whereas the highest temperatures $>$ 250 °C are observed within the high-resistivity zone in the center of the geothermal field. This zone is considered to act as main upflow zone that feeds

[1]Information taken from www.nzgeothermal.org.nz

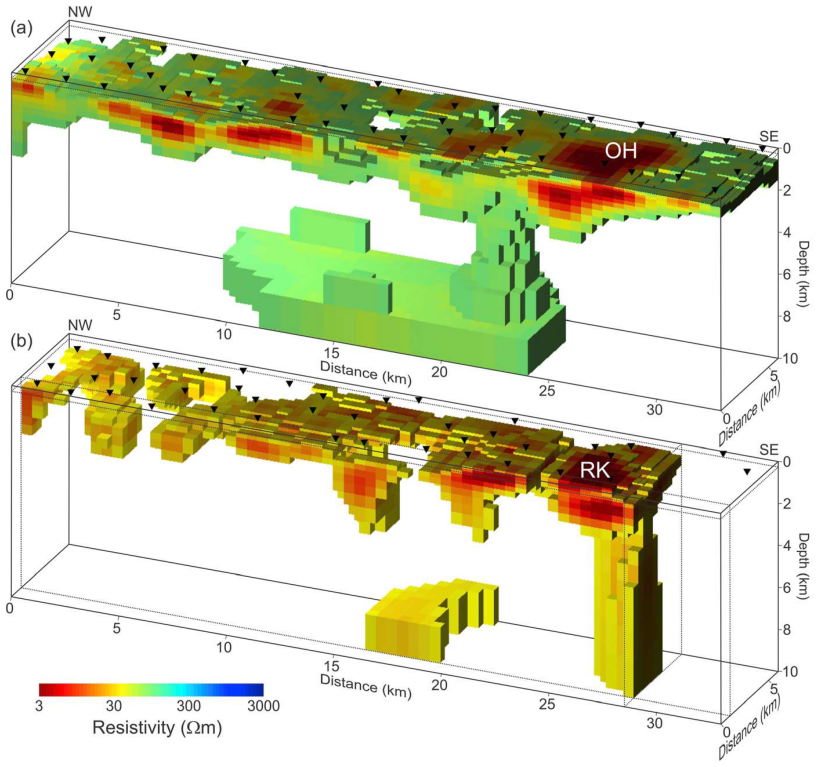

FIGURE 3.3: 3-D models of the full MT impedance tensor data for (a) Ohaaki (OH) and (b) Rotokawa (RK). The Figure was taken from *Bertrand et al.* (2012). It can be seen that a low-resistivity plume is situated directly under RK, whereas it is offset to the north-west under OH.

high-temperature fluids from below into the geothermal system. In a regional MT survey of the Taupo Volcanic Zone *Bertrand et al.* (2012) succeeded to image a low-resistivity structure that connects the shallow part (< 3 km) of the Rotokawa geothermal field with a widespread low-resistivity zone ($10 - 30\,\Omega$m) at depths greater than $7 - 8$ km as shown in Fig. 3.3 (b). This deep conductor is interpreted as magmatic heat source with $\sim 4\,\%$ of partial melt (*Heise et al.*, 2007). The low-resistivity structure that rises up from the magmatic heat source and connects with the shallow part of the Rotokawa geothermal field is considered as plume consisting of uprising hydrothermal fluids, that feed and provide energy for the system.

The Ohaaki geothermal field is also located within the Taupo Volcanic Zone about $\sim$ 20 km NW of Rotokawa, it was studied by *Bertrand et al.* (2013) with both 2-D and 3-D interpretation of MT data along a single $\sim$ 30 km long profile. Their 2-D and 3-D models are consistent within the upper $\sim$ 3 km and correspond to the conceptual reservoir model. The conductive clay cap is clearly seen in the upper part, and the productive wells are drilled down to depths of $2 - 2.5$ km through the clay cap into the underlying resistive zone. However, the resistivity models from Ohaaki show no distinct conductor at greater depths > 5 km that may be interpreted as active magmatic heat source (see Fig. 4 (a) and (b) in *Bertrand et al.* (2013)). By including MT data along four additional profiles a conductor at $3 - 7$ km depth appeared offside to the geothermal field, see Fig. 3.3 (a). It remains under discussion whether this offside conductor acts as upflow zone and whether a pathway exists that allows hot geothermal fluids to laterally migrate towards the Ohaaki geothermal field.

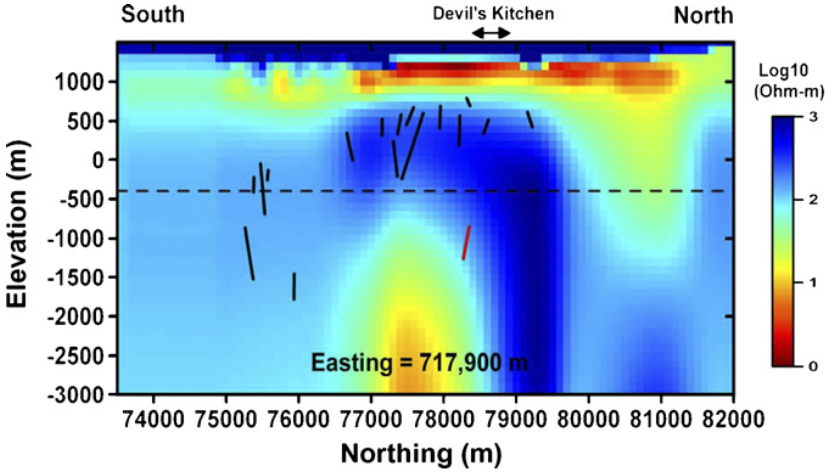

FIGURE 3.4: Vertical (N-S) resistivity section through the Devil's Kitchen area of the Coso geothermal field. Black and red lines indicate producing and injection well intervals, respectively. The Figure was taken from *Newman et al.* (2008).

Newman et al. (2008) interpreted MT data from the electricity generating Coso geothermal field in California, which currently has an overall installed capacity of 270 MWe

(*Bertani*, 2012). They inverted MT responses covering a period range from $0.004 - 1$ s using the 3-D inversion algorithm by *Newman and Alumbaugh* (2000). In the so-called Devil's Kitchen area wells revealed subsurface temperatures exceeding 230 °C. Under the Devil's Kitchen the shallow low-resistive smectite clay cap can be clearly identified in the model, see Fig. 3.4. All productive wells are drilled into the resistive zone under the clay cap starting at depths below 500 m.a.s.l, which could be identified as propyllitic alteration zone with abundance of illite and chlorite. At greater depths below 1500 m.b.s.l. a narrow vertical conductor appears, which was interpreted as brittle-ductile transition zone. However, *Newman et al.* (2008) did not map any deeper conductors that could be interpreted as active magmatic reservoirs as they analyzed variations with periods shorter than 1 s and thereby sounding the uppermost 4-5 km below surface only. Later *Wamalwa et al.* (2013) reinterpreted the data of *Newman et al.* (2008) inverting periods up to 100 s in a 2-D manner using the inversion scheme by *Rodi and Mackie* (2001). They could resolve the subsurface resistivity structure under the Devil's Kitchen area to greater depths. In their recovered model a conductive zone ($4 - 12\,\Omega$m) is imaged below 6 km, which they interpret as zone of cooling magma dikes and partial melt that provides heat for the Coso geothermal field, see Fig. 5 in *Wamalwa et al.* (2013).

Another extensively studied geothermal field is the Hengill area, which is located within an active spreading zone in the southwest of Iceland on the Reykjanes Peninsula. The Hengill volcanic complex hosts three main volcanoes and geothermal power plants with an overall installed capacity of 333 MWe. *Árnason et al.* (2010) recovered the resistivity distribution under Hengill by 1-D joint inversion of transient electromagnetic (TEM) and MT data and by 3-D inversion of MT data as well. It is interesting that the model recovered from stitched 1-D inversions (shown here in Fig. 3.5) coincides with the model recovered by 3-D inversion in a large part and resolves the major structures of the 3-D model. A shallow conductive structure between around $0 - 700$ m.b.s.l appears in the model, which is underlain by a resistive zone ($\sim 1000 - 3000$ m.b.s.l) that in turn is followed by a conductor at depths below around 5000 m.b.s.l.. Conductivities in the Hengill geothermal field are mainly controlled by the alteration mineralogy: Low resistivities ($< 10\,\Omega$m) in the upper part correspond to the smectite zone, whereas below in the resistive part chlorite is the dominating alteration mineral, here temperatures exceed 250 °C. The nature of the deep conductor ($< 10\,\Omega$m) at depths between around $7 - 13$ km is not completely clear: The presence of shallow magma chambers and partial melt would result in an attenuation of seismic S-waves, which is not observed under the Hengill area. This is why *Árnason et al.* (2010) interpret the deep conductor as brittle-ductile transition zone built up by solidified basaltic dikes and intrusions. Its high conductivity is most likely caused by magmatic brines, which are trapped in the intrusive rocks rather than by the presence of partial melt.

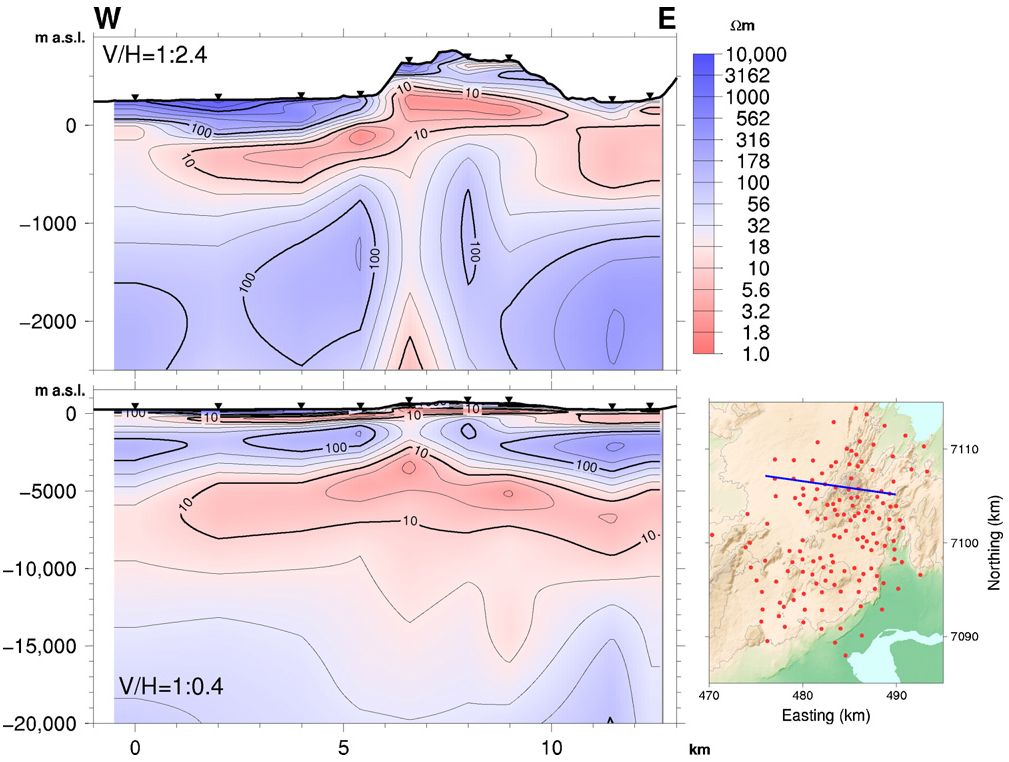

FIGURE 3.5: West-east resistivity sections across the Hengill area for two different depth ranges obtained from stitched joint 1D inversions of TEM and determinant MT data. Inverted triangles: MT stations; V/H: ratio between vertical and horizontal axes. Section location is shown as a blue line in the map to the right. Red dots in that map: MT stations. The Figure and its caption was taken from *Árnason et al.* (2010), see reference for more details.

Exceptional reserves of geothermal energy are also found in the Kamchatka Peninsula in Eastern Russia with an estimated potential of 2000 MWe for the production of electrical energy. Here *Nurmukhamedov et al.* (2010) analyzed MT data collected in the vicinity of the Mutnov steam deposit. They constructed a 3-D model by interpolating the results of 2-D inversions on a 3-D spatial grid. The 2-D inversions were performed using the code by *Mackie and Madden* (1993). Based on interpretations of the constructed 3-D model a productive well could be drilled into a permeable and high-resistive zone ($200 - 800\,\Omega$m) with overheated water underlying a conductive hydrothermally altered rock zone. As a result the installed capacity of the Mutnov geothermal power plant was increased by 10 MWe to 50 MWe in total (*Svalova and Povarov*, 2015).

The presented studies demonstrate that the conceptual reservoir model for high enthalpy geothermal systems (introduced in Section 3.1) was successfully applied in many cases in order to interpret and to identify geothermal systems and to site well locations. This shows that electrical conductivity models of the subsurface recovered from MT data are of an outstanding importance in geothermal exploration as they contribute in a large part to the achievement of assessing the resource capacity of a geothermal site.

Chapter 4

The MT survey and data analysis

This chapter addresses and describes the major steps from fieldwork, data collection and processing to data analysis. After a reconnaissance trip to Ethiopia in November 2011 we entered into all agreements with local project partners and the MT project at the Aluto-Langano geothermal field was ready to be put into realization. Note that the study presented in this thesis started with the organization of the MT survey from scratch, including the sourcing of MT instrumentation and peripherals, shipment of the equipment to Ethiopia, customs clearing as well as organization of local transport and logistics.

The MT survey is part of a collaboration between ETH Zurich, Addis Ababa University, the University of Bristol, and the Geological Survey of Ethiopia. This joint project encompasses different geophysical techniques and it is named **ARGOS**, which is an acronym for *Aluto Research and Geophysical Observations*. Besides MT this project involves seismic techniques, GPS measurements, InSAR, LiDAR, geochemistry and geological mapping and it aims to better understand the magmatic and hydrothermal interactions at the Aluto volcanic complex.

4.1 The MT survey

We carried out the MT survey in January and February 2012. The MT sites were installed by a team of six people in average. Personnel in the field included two PhD students from ETH Zurich, Jenneke Baker and the author, two Master students from Addis Ababa University, Fantahun Gebrie and Bereket Gebresilassie, two members of the GSE, Yohannes Lemma and Behailu Woldesmayet and three local workers from the EEPCO Aluto-Langano geothermal power plant, namely Bonso, Bashir and Hussen. Two drivers, Mifta and Dagem, were hired during the survey with one 2-wheel drive van and one 4-wheel drive off-road car. The involved students from Addis Ababa joined the fieldwork temporarily and were trained to meet the challenges of practical magnetotellurics with successful installation and operation of survey stations.

During the survey the team, except local workers from Aluto, resided in the Bethlehem Hotel in Ziway around 18 km NW of Aluto. The power plant was used as base camp during the fieldwork: Here we parked and maintained vehicles and equipment, and recharged batteries. It also was the meeting point for the team to start with fieldwork every morning. For MT measurements we used broadband Metronix instruments of type ADU06, ADU07 and ADU07e. The details about instrumentation are listed in Table 4.1).

Logger	S/N	Coil type	Electrode type	Recorded frequency bands	Lender
ADU06	003	MFS05	Ag-AgCl	128 Hz	FU Berlin
ADU06	030	MFS05	Ag-AgCl	128 Hz	FU Berlin
ADU07	058	MFS06	Cu-$CuSO_4$	128 Hz, 4096 Hz	University of Neuchatel
ADU07	059	MFS06	Cu-$CuSO_4$	128 Hz, 4096 Hz	University of Neuchatel
ADU07e	125	MFS06e	Ag-AgCl	128 Hz, 4096 Hz	University of Münster

TABLE 4.1: Detailed information about instrumentation, recorded frequency bands and origin of instruments.

The survey began with a parallel test of the data loggers, which lasted one day. Recordings hereby only were successful for part of the loggers due to initial problems in the network communication. In the end all loggers were put into operation. Polaris six-wheel bikes for fieldwork were kindly provided by Reykjavik Geothermal[1]. They were stored in a garage in Shashemene 90 km south of Ziway. Organizing the transport from the garage in Shashemene to Aluto lasted almost 3 days due to time consuming negotiations with truck drivers and the owner of the garage. The main point of discussion was to find a driver, who was willing to drive the rough road from the village Adami Tulu up to the power plant on Aluto. After arrival at Aluto problems with bikes occurred, because impure benzine contaminated with diesel has been used for refilling. Maintenance of the bikes and cleaning the tanks required another day. Maintenance of the vehicles accompanied us throughout the whole survey.

The morning of a typical survey day started at 6:30, work began between 8:00 and 9:00, depending on how much organizational work had to be done before. From the hotel in Ziway it was a half an hour drive to the power plant on Aluto volcano. After arrival we discussed where to install the new MT stations, packed the equipment onto the six-wheel bikes and drove to the currently operating MT sites. Depending on where on Aluto the stations were located, driving to there from the power plant needed up to one hour and even longer in exceptional situations, despite the fact that the covered area

[1] www.rg.is

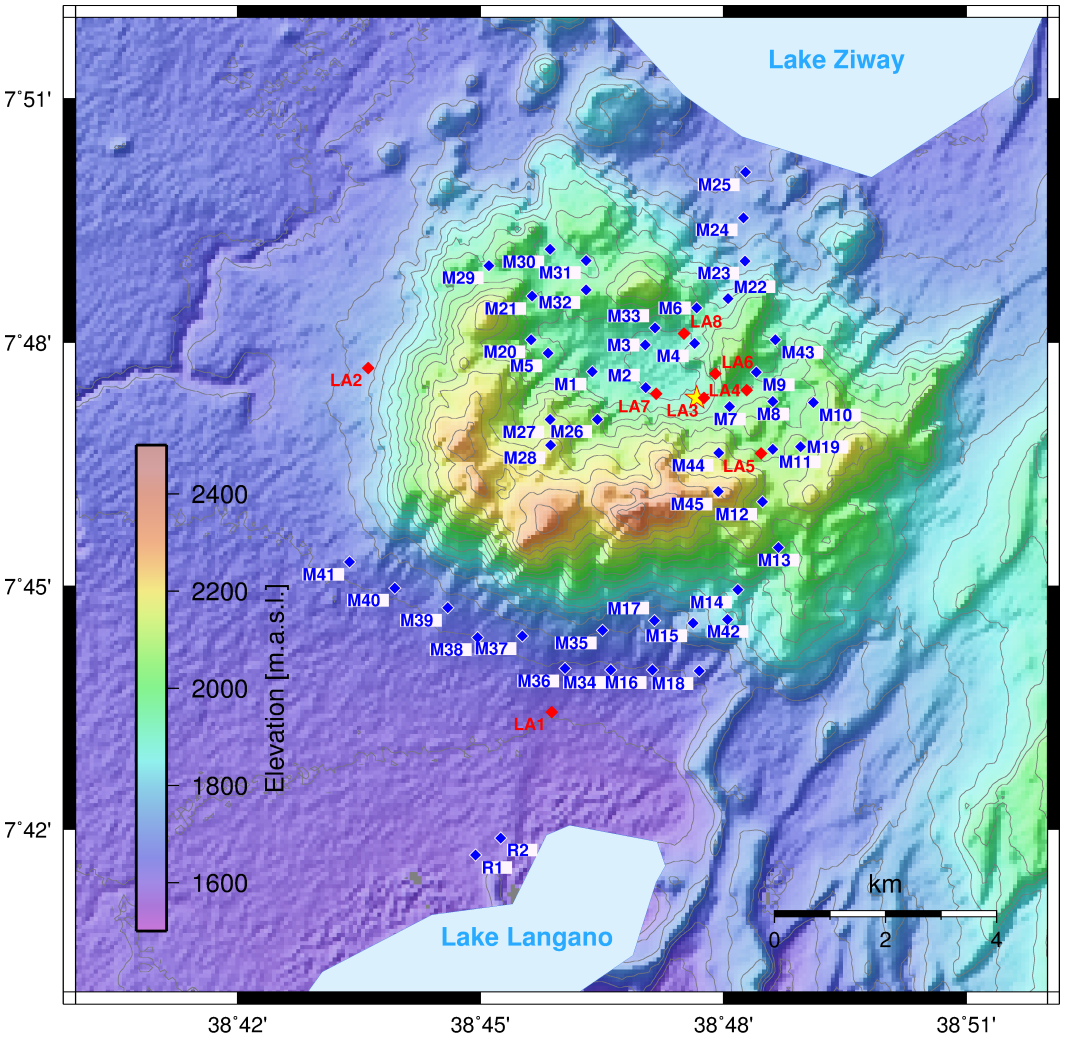

FIGURE 4.1: Map showing the elevation along with the survey site locations M1 to M45 and the remote reference sites R1 and R2. The location of the power plant is indicated as yellow star. Red dots denote location of wells LA-1 to LA-7.

measures only 10 km to 15 km. After arrival at the sites we stopped the measurements and transferred the acquired data to two field notebooks. A quick quality check and data analysis was performed using the `Mapros` time series processing tool by Metronix to ensure that the measurements were successful. Afterwards the station was dismantled and the station guards were rewarded. Station guards were needed for every site during day and night to prevent damage of loggers, disordering and chewing on cables by wild animals like hyenas, baboons, rodents and domestic animals, especially goats. Employing guards was essential but often accompanied with time consuming negotiations. During the whole survey the salary for guarding stations was fixed to 50 ETB (2.65 CHF in 2012) and 100 ETB (5.3 CHF in 2012) for day and night shifts, respectively. Most of the days we managed to dismantle and rebuild two stations per day. A detailed timetable is shown in Fig. A.1 in the Appendix A. The end of a working day was at least half an hour before sundown, which is around 18:30, as driving after dark was not

recommended due to safety reasons.

At each MT site we buried three coils to measure the two horizontal (x,y) and the vertical (z) magnetic field. To ensure a good electric coupling with the ground we embedded the buried telluric electrodes into a muddy mixture of salt, water and bentonite. Bentonite is known for its feature to store water very well, which is necessary to keep moisture around the electrodes and to ensure electric coupling between electrodes and dry soil. 50 kg of bentonite were sufficient for 3 weeks, after that we were forced to find another solution. We found out that animal losses can be used equivalently to bentonite. This is an important finding for future surveys as carrying around several kilograms of bentonite in the field is often exhausting. A challenging task during the survey was transport and mobility. Consequent to the dusty environment and rough terrain all bikes had to be maintained daily. Most common problems on a daily rate were flat tires, due to the widespread abundance of olivine splinters and thorny bushes. The extremely dusty environment resulted in blocked air filters, which had to be cleaned up to several times a day and needed replacement after a few weeks. At one point comprehensive maintenance of all bikes was required and we were forced to hire donkeys in order to transport the equipment. Using donkeys was finally an advantage as we managed to reach higher regions of Aluto and to install sites in regions, which are impossible to access with a vehicle.

In total data have been acquired at 45 survey sites using the ADU07 and ADU07e loggers with a spatial resolution of around 1 km $\times$ 1 km. In addition one reference site R1 (ADU06) was set up in the south of Aluto close to the Lake Langano. It was relocated after a few days to the new position R2 due to R1's proximity to a dwelling camp, where we expected the noise level to be higher than as at the new location R2. The site locations are shown in Figure 4.1. A good site coverage was achieved in the surrounding of the power plant in the central region of the volcanic complex, whereas it was not possible to install any sites at the inaccessible steep western and southern slopes of Aluto. The survey area has a pronounced topography with altitudes reaching from $\sim$ 1600 m at the Lake Langano to more than 2300 m at the peak of Aluto. The maximum altitude difference between the sites is 659 m. Another reference site R3 was temporarily installed around 28 km NW of Aluto on the western margin of the rift. This site completely failed due to internal storage problems, which is very unfortunate as it was located at the SDFZ, an off-axis volcanic chain west of the rift (see Section 2.1). For coordinates of all measured site see Table A.1 in Appendix A.

Table 4.2 provides an overview on the survey costs. It is seen that the largest amount with more than 60% is for logistics and transport, whereas housing and food for the crew only account for around 20% of the expenses.

Expense type	Amount in CHF	Portion of costs in %
Shipment Zurich to Addis	5610	24.3
Shipment Addis to Zurich	2220	9.6
Transport in Ethiopia	6370	27.6
Material costs in Ethiopia	1790	7.7
Housing	3010	13.0
Food	1770	7.7
Salaries for local workers	2330	10.1
Total costs	23100	

TABLE 4.2: Distribution of project costs in rounded amounts and percentages. The listed costs comprise the shipment and survey expenses between January and March 2012. Not included are expenses for MT equipment, MT supplies, travel expenses, salaries of ETH staff and the reconnaissance trip.

4.2 Data analysis

In general any digital data-logger does not measure a physical quantity. Instead, when measuring time series of physical observables the data-logger provides the data in form of simple integers or counts of the A/D-converter. To get the current voltage value on the input of the A/D-converter these integers have to be multiplied with the least significant bit (LSB) value of the A/D-converter. From the voltage values one can derive the physical quantities by multiplication with the calibration value specified by the sensor. In the EMTF time series processing code by *Egbert and Eisel* (1998) the count conversion factor is defined independently for each input (predicting) and output (predicted) channel. The standard unit convention in MT is to use $\frac{\mathrm{nT}}{\mathrm{count}}$ for the **B**-field and $\frac{\frac{\mathrm{mV}}{\mathrm{km}}}{\mathrm{count}}$ for the **E**-field. This convention is in the following referred to as field unit system. In addition the frequency characteristics for each channel, i.e. sensor, has to be specified. This is essential for the induction coil magnetometers, where each sensor is characterized by an individual transfer function that has to be known in order to convert the raw data into calibrated spectra of the magnetic field. Electric sensors are assumed to have a unit response frequency characteristics. The MT transfer function $\mathbf{Z_F}$ estimated from time series in the field unit system has consequently the unit

$$[\mathbf{Z_F}] = \frac{\frac{\mathrm{mV}}{\mathrm{km}}}{\mathrm{nT}} = \frac{1}{10^{-3}} \frac{\frac{\mathrm{V}}{\mathrm{m}}}{\frac{\mathrm{Vs}}{\mathrm{m}^2}} = \frac{\mathrm{km}}{\mathrm{s}}, \tag{4.1}$$

which is strictly spoken not an impedance. In order to convert the transfer function from field unit system to the impedance tensor in the S.I. system $\mathbf{Z}_{\mathrm{SI}}$, $\mathbf{Z}_{\mathrm{F}}$ has to be multiplied with the magnetic permeability constant $[\mu_0] = \frac{\mathrm{Vs}}{\mathrm{Am}}$:

$$[\mathbf{Z}_{\mathrm{F}} \cdot 1000 \cdot \mu_0] = 1000 \frac{\frac{\mathrm{mV}}{\mathrm{km}}}{\mathrm{nT}} \frac{\mathrm{Vs}}{\mathrm{Am}} = \frac{\mathrm{m}}{\mathrm{s}} \frac{\mathrm{Vs}}{\mathrm{Am}} = \frac{\mathrm{V}}{\mathrm{A}} = [\mathbf{Z}_{\mathrm{SI}}]. \tag{4.2}$$

The apparent resistivity ρ_a in the S.I. unit system is derived as defined in eq. (1.46). In the field unit system ρ_a is computed as follows (from now on indices (i,j) are omitted in this paragraph for of reasons of clarity):

$$\rho_a = \frac{|Z_{SI}|^2}{\mu_0 \omega} = \frac{|Z_F \cdot 1000 \cdot \mu_0|^2}{\mu_0 \omega} = \frac{T|Z_F|^2}{5}. \tag{4.3}$$

The corresponding phases are derived using eq. (1.47). Besides transfer function estimates the EMTF code provides also full information about the uncertainties δ of the elements of $\mathbf{Z}_F$ as described in detail in *Eisel and Egbert* (2001). The uncertainties δ of the impedances are translated into uncertainties of apparent resistivity δ_ρ and phase δ_Φ as follows:

$$\delta_\rho = \left[\frac{2T\sigma^2}{5}\rho_a\right]^{\frac{1}{2}}, \tag{4.4}$$

and

$$\delta_\Phi = \frac{180}{\pi|Z|}\left[\frac{\sigma^2}{2}\right]^{\frac{1}{2}}. \tag{4.5}$$

The dimensionless tipper transfer functions and their uncertainties were also estimated using the EMTF code.

Care had to be taken regarding the remote reference processing as the different data-logger generations used for this study have an offset in the time stamp given by the GPS clock unit. Time series were synchronized between reference and survey sites individually for each site by a visual comparison. This revealed a constant offset between the ADU06 and ADU07, respectively ADU07e, data-loggers throughout the whole survey. All transfer function estimates presented and utilized in this thesis were computed by the author.

4.2.1 Spectra

To give an impression about the measured EM signals Fig. 4.2 shows the uncalibrated raw power spectra at site M12. They have been estimated using the Welch's method with 0% overlap of the data segments. Spectral data between $0.001\,\mathrm{s} < T < 0.02\,\mathrm{s}$ are derived from the time series with 4096 Hz sampling frequency, between $0.02\,\mathrm{s} < T < 1000\,\mathrm{s}$ from the time series with 128 Hz sampling frequency. Starting at 0.001 Hz the first significant feature is the 0.02 s (50 Hz) peak, this is the frequency of the local power grid and is filtered out during processing. In the period range between 0.02 s and 0.2 s one can clearly identify the first 7 Schumann-resonances, which are resonance frequencies in the waveguide between conducting ionosphere and conducting Earth (e.g. *Füllekrug*, 2005). Schumann resonances are considered to be the main source of the MT signal in the mentioned period range. Towards longer periods the power of the spectra increases except at periods of around 10 s, this is the so-called dead band where the MT signal is

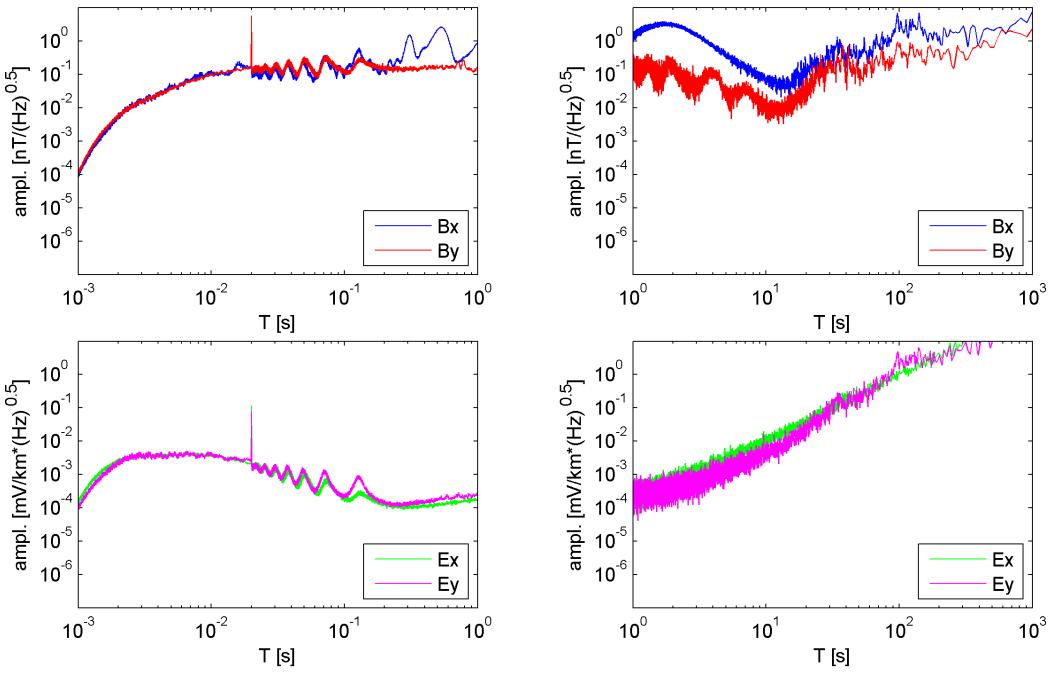

FIGURE 4.2: Power spectra at site M12.

very low by nature. The dead band marks the transition between EM field generated by meteorological activities and EM fields generated by space weather activities. The low power of the source signal in the dead band makes it often a challenging task to estimate stable MT responses.

4.2.2 Response functions

In this study the responses in the 4096-Hz-band have been estimated using robust single site processing for the period range $0.00098 - 0.00272\,\mathrm{s}$. Since data in the 128-Hz-band have been recorded simultaneously at the reference and the field sites we used both single site and remote reference processing. For periods $0.00391 - 0.08695\,\mathrm{s}$ the quality of the responses is best with single-site processing, whereas for periods $0.12500 - 1024\,\mathrm{s}$ remote reference processing gained the best quality. A significant improvement could be achieved in the dead band between $0.1 - 10\,\mathrm{s}$. Fig. 4.3 shows a representative plot with a comparison of different processing methods for site M12. Whereas the phases are comparable for all processing methods the apparent resistivities differ in the interval $0.2 - 20\,\mathrm{s}$ at $\rho_{a,yx}$. Here quality of single-site processed responses is poor, which can be concluded from a clear violation of the Kramers-Kronig relationship (cf. eq. 1.60). With remote reference processing the drop-down of $\rho_{a,yx}$ in the dead band disappears.

Two further examples of ρ_a and Φ curves are presented in Fig. 4.4. At site M26 the curves are smooth over the whole period range and apparent resistivities of the main diagonal elements Z_{xx} and Z_{yy} are significantly smaller than ρ_a of the off-diagonal

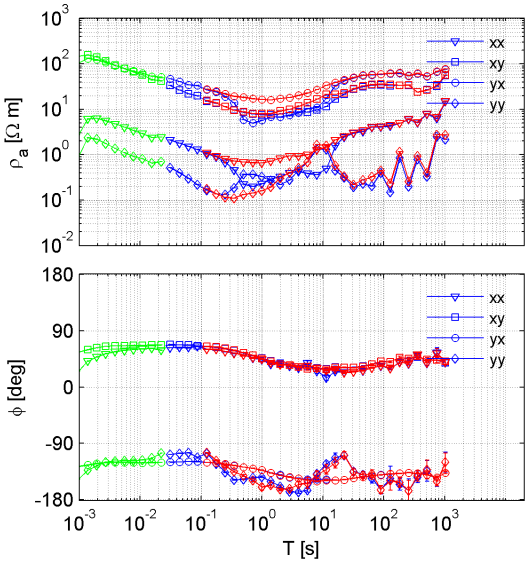

FIGURE 4.3: Apparent resistivity and phase at site M12 estimated by different processing methods. Data in the 4096 Hz band (green symbols) have been processed using a single-site algorithm. Data in the 128-Hz band are shown for single-site (blue) and remote reference processing (red).

elements, which is typical for non-3-D conductivity distributions (e.g. *Simpson and Bahr*, 2005). At most sites we obtained good responses, an example with bad data is site M16 where quality of the responses decreases significantly for periods $T > 1\,\mathrm{s}$. This could be caused by e.g. insufficient electric coupling between electrodes and soil or wind induced noise due to movement of roots by a nearby tree.

An overview on all observed off-diagonal apparent resistivities and phases at the survey sites is shown in Fig. 4.5. It it obvious that both ρ_a and Φ curves are significantly scattered, which could be caused by (i) static shift, (ii) target anomalies or (iii) topography effects.

Static shift (discussed in more detail in Section 1.4.5 of Chapter 1) is common problem in MT studies, it is caused by shallow small scale electrical heterogeneities, so-called galvanic scatterers. The effect of this scatterers on the observed electric field $\mathbf{E}^{obs}$ is described by a real-valued frequency-independent tensor $\mathbf{C}$ which acts on the undistorted horizontal electric field $\mathbf{E}^{r}$:

$$\mathbf{E}^{obs} = \mathbf{C} \cdot \mathbf{E}^{r}.$$

Note that the magnetic field is assumed not to be influenced by these scatterers. As $\mathbf{C}$ is real-valued, the distortion of galvanic scatterers is considered to have weak effect on MT phases, but apparent resistivities are shifted to higher or lower values, which might be a possible explanation for the scattering of ρ_a in Fig. 4.5. However, scattering is also observed in Φ, thus it might be related to large scale geological structures with strong conductivity contrasts or topography effects (*Jiracek*, 1990), the latter are studied in

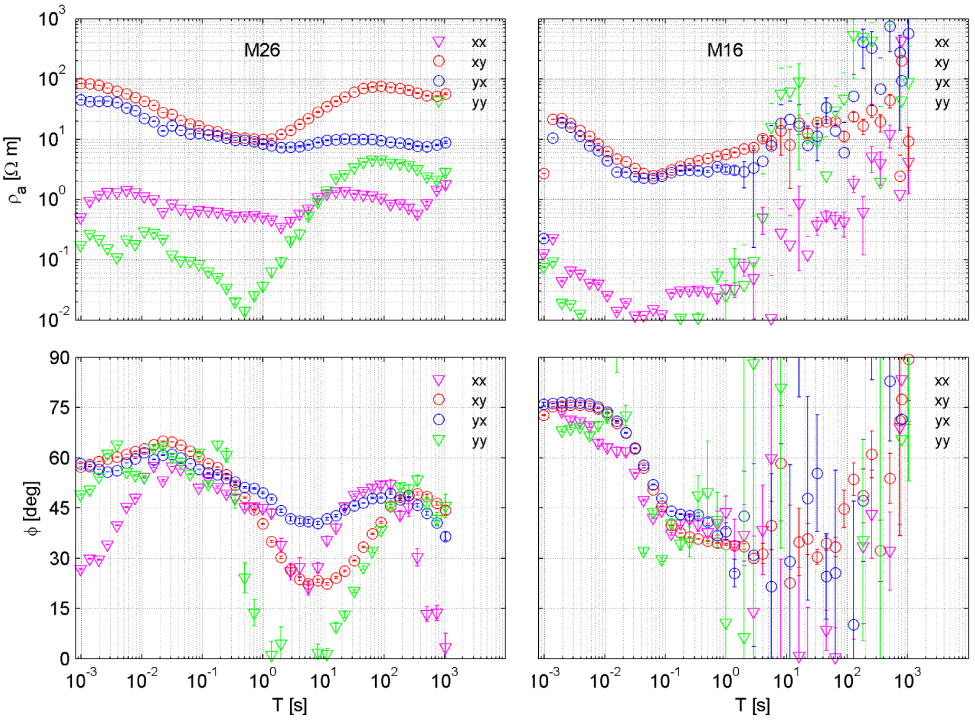

FIGURE 4.4: Apparent resistivity and phase at site M26 (left) and M16 (right). Phases have been shifted into the [0°, 90°] quadrant.

more detail in a following chapter.

The tipper responses are shown in arrow representation for four different periods in Fig. 4.6. At shorter periods ($T \leq 32\,\mathrm{s}$) they show no regular behavior. Towards longer periods ($T \geq 128\,\mathrm{s}$) they begin to stabilize with their real parts pointing continuously to an eastward direction. At $T = 1024\,\mathrm{s}$ real tippers show almost the same behavior over the whole study area with their imaginary part approximately aligned to the real part. This is a clear hint on a North-South elongated conductor west of Aluto, which is sensed by the tippers as the most dominating feature at longer periods. Another contributor to the regular behavior of tippers at longer periods might be a resistive N-S oriented block at crustal to lower crustal depths east of Aluto.

4.3 Source effect of the EEJ on responses

The underlying principle of MT is a laterally uniform primary source field, which satisfies the plane wave criterion. This is generally true in regions that are sufficiently far away from polar and equatorial zones. At high and low latitudes ionospheric electrojets may produce variations that invalidate the plane wave assumption. EM variations at the Earth's surface in equatorial regions might be affected by the EEJ, a strong electric current flowing eastwards in ionospheric altitudes along the magnetic dip equator. A

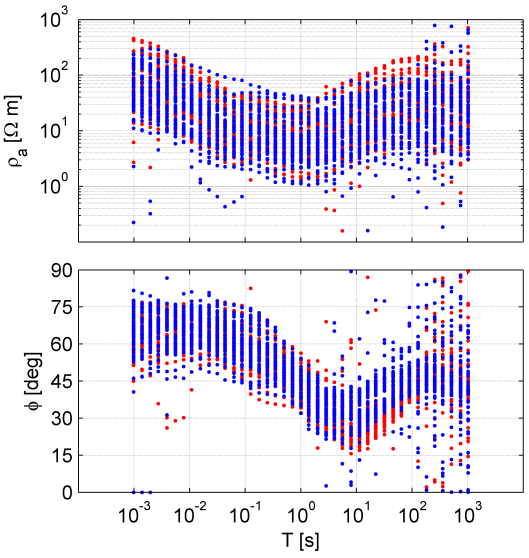

FIGURE 4.5: Cloud plot of off-diagonal ρ_a and Φ at all survey sites. Red dots denote data based on xy-component, blue dots denote data based on the yx-component. Data are plotted without uncertainties. Phases have been shifted into the [0°, 90°] quadrant.

well constrained and well known source signal is crucial for estimating response functions. Otherwise it may result in a so-called source effect, when transfer functions do not only contain the information about the conductivity inside the Earth but are also significantly affected by the source field geometry different from plane wave. The interpretation of source field affected transfer functions may consequently lead to serious misinterpretation (*Mareschal*, 1986; *Viljanen et al.*, 1999).

This clearly raises the question about source field effects in MT data collected at the Aluto-Langano geothermal field, which is situated in the immediate vicinity (0.5 ° south) of the geomagnetic dip equator in East Africa (*Finlay et al.*, 2010).

Padilha (1999) have shown that MT data collected along the geomagnetic dip equator are not affected by the source field effect in a region ±3° of dip latitude and for periods up to ∼ 2000 s. This is valid for MT transfer functions but not necessarily for tipper transfer functions, which are known to be more sensitive to source effects (*Sokolova and Varentsov*, 2007).

To test the influence of the EEJ on tippers we estimated transfer functions for local day and night time separately in the considered period range of 0.001-1000 s. As the EEJ is a phenomenon that only occurs on the day side of the Earth, there should be significant differences in transfer functions estimated for daytime data and nighttime data separately if the EEJ indeed influences the responses. We estimated transfer functions using single-site processing at site R2 for daytime data between 9:00 and 12:00 local time and for nighttime data between 21:00 and 3:00 local time between 2012/02/06 and 2012/02/13, and for nighttime and daytime data simultaneously, the results are shown

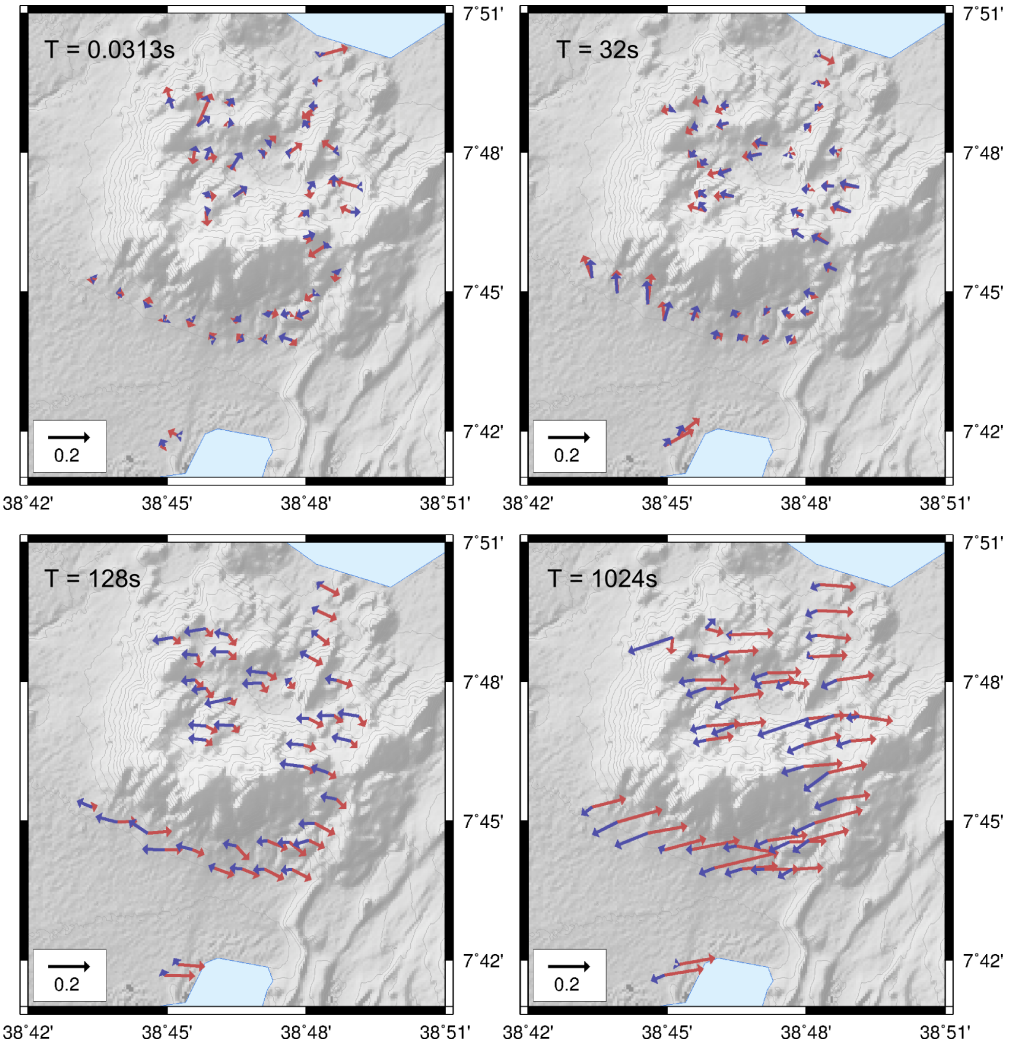

FIGURE 4.6: Tipper responses in arrow representation at four different periods. Red arrows denote real, blue arrows imaginary tippers. Towards longer periods the real tippers point continuously Eastwards away from a good conductor in the West.

in Fig. 4.7(a). Slight differences in ρ_a and Φ between different time selections occur in the dead band around 10 s and at long periods, where the uncertainties increase due to the reduced number of available time windows. Tippers for different time selections are almost identical up to a few seconds with slight differences in the amplitude of the maximum in T_{yr}. Towards longer periods all time windows show a dominated T_{yr}-component and also a clearly increased scattering most likely due to the previously mentioned reduced number of available windows.

As the observed differences in tippers cannot be definitely ascribed to variations in the power and quality of the source signal, we also estimated transfer functions at site M44 for different time windows. This site was measuring from 2012/2/27 16:00 local time for 17.5 hrs. Since this site was not operating over noon we analyzed nighttime data between 21:00 and 3:00 local time and daytime data from 16:00 to 19:00 local time

and 6:00 to 9:00 local time. The results are shown in Fig. 4.7(b). The responses were again estimated using single site processing, the overall data quality at M44 is very good considering its relatively short recording time. Again slight differences occur in the dead band in ρ_a and Φ and towards longer periods due to the reduced amount of data, but the general agreement is good. The tippers agree very well up to 100 s, but are more scattered towards the longest analyzed periods. However, their general behavior is clearly identical over the whole period range and the dominating T_{yr}-component is clearly seen for all time selections. From this analysis we conclude that impedances and tippers measured at Aluto are not influenced by any source effects.

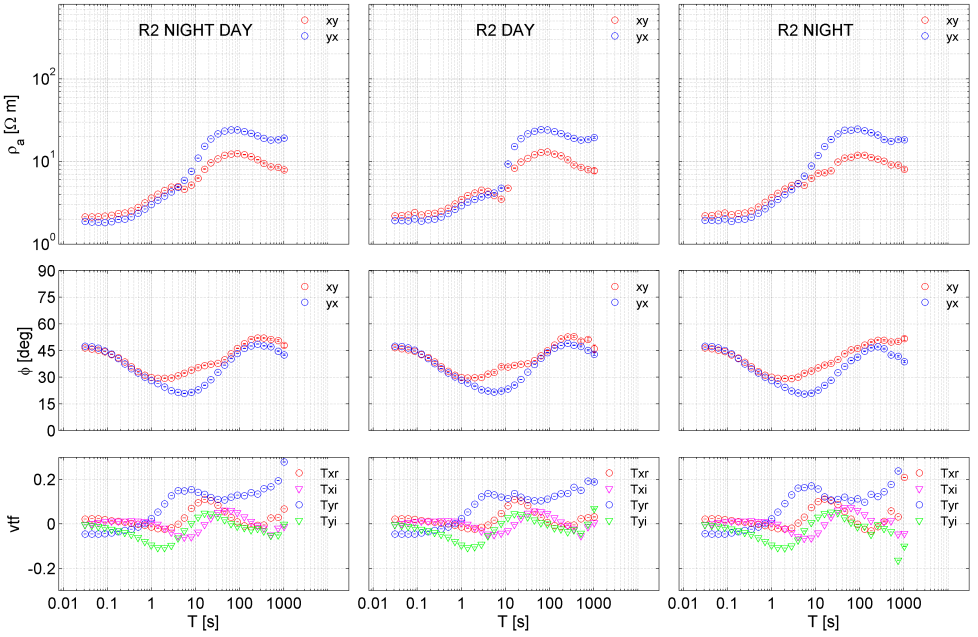

(a) Site R2.

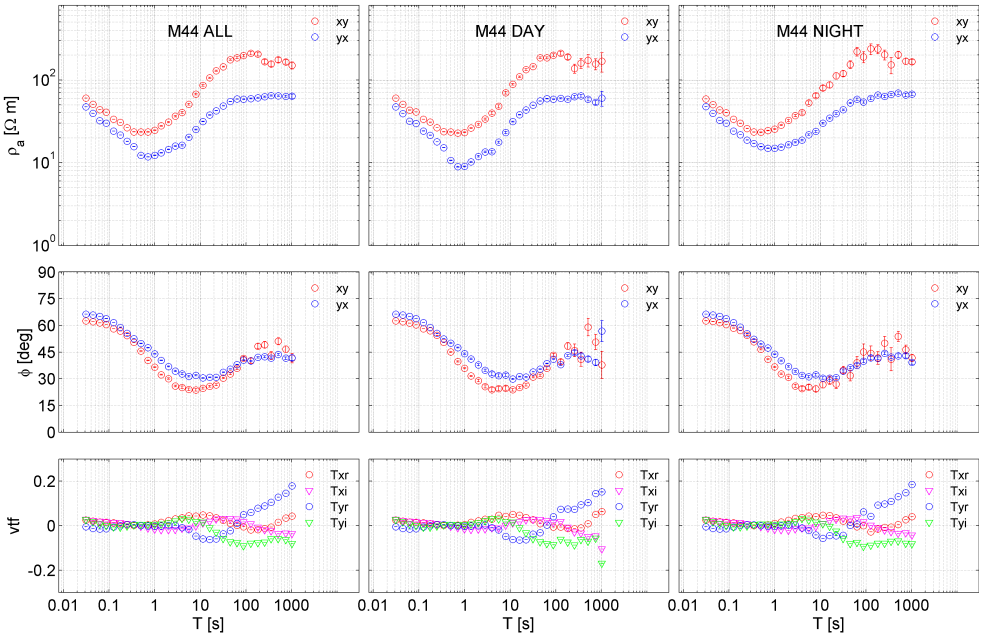

(b) Site M44.

FIGURE 4.7: Transfer function ρ_a, Φ and tippers (vtf) from top to bottom at (a) site R2 and (b) site M44 estimated for night- and daytime data (left), for daytime data (middle) and for nighttime data only (right). 'r' and 'i' in vtf stand for real and imaginary parts, respectively.

Chapter 5

Modeling and inversion

In the past decade a variety of 3-D magnetotelluric forward and inversion codes have been developed, hence it became possible to interpret the subsurface structure based on MT data in a fully 3-D manner. The progress of 3-D codes was driven on the one hand by growing computational power and advances in numerical methods and on the other hand by an increasing demand from academics and industry, that was actuated also by great advances in instrumentation. The need for 3-D codes became obvious as 2-D interpretations of MT profile data are ambiguous under the influence of 3-D effects. Furthermore, MT data acquisition is often performed in a way, which implicitly suggests a 3-D interpretation as for the common case when data are acquired along parallel profiles. Instead of a neglecting 3-D effects for a 2-D interpretation of the data along parallel profiles the most appropriate way to address the problem is a 3-D interpretation on a 2-D surface grid, as illustrated in Fig. 5.1.

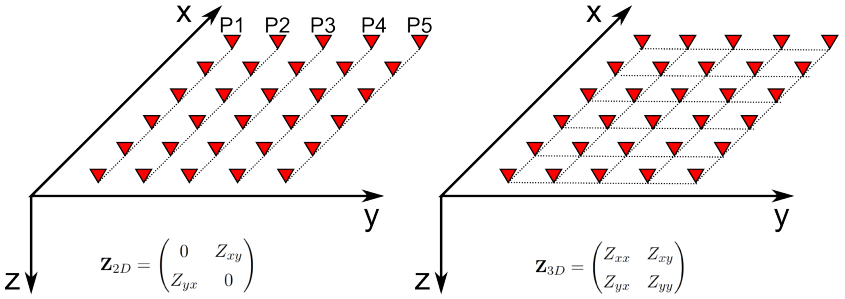

FIGURE 5.1: 2-D interpretation of data along independent profiles P1 to P5 versus 3-D interpretation of the same data set.

This chapter begins with some general remarks about forward modeling and inversion of MT data, the codes used for this study are introduced and the remaining part will address forward and inversion studies of the acquired data at Aluto.

5.1 General remarks about MT forward and inverse problems

The MT forward problem stands for the prediction of the electric field $\mathbf{E}(x, y, z, \omega)$ and magnetic field $\mathbf{H}(x, y, z, \omega)$ at arbitrary locations and frequencies for a given parametrized conductivity structure $\mathbf{m}$ with the source field considered to be described by a plane wave. The predicted electric and magnetic fields permit to compute MT responses $\mathbf{d}^{\text{pred}}$. In numerical modeling (prediction) both $\mathbf{m}$ and $\mathbf{d}$ are discrete: vector $\mathbf{d}$ consists of d_i^{pred}, $i = 1, ..., N$, data and vector $\mathbf{m}$ consists of m_j, $j = 1, ..., M$, model parameters, which define the electrical conductivity distribution. The predictions d_i^{pred} are obtained by a set of functions $F_i(\mathbf{m})$ that are summarized in the forward operator or functional $F = (F_1(\mathbf{m}), F_2(\mathbf{m}), ..., F_N(\mathbf{m}))$. In MT forward problems F comprises a numerical solution of Maxwell's equations and the translation of the solution into responses $\mathbf{d}^{\text{pred}}$. In other words, F maps the model space vectors $\mathbf{m}$ to the space of the predicted data $\mathbf{d}^{\text{pred}}$:

$$F(\mathbf{m}) = \mathbf{d}^{\text{pred}}. \tag{5.1}$$

The MT inverse problem stands for recovery of the unknown model $\mathbf{m}$ from observed responses $\mathbf{d}^{\text{obs}}$. It is important to note that MT inverse problems are ill-posed due to errors in the data, the finite interval of periods, and the generally irregular and limited net of observations. The ill-posedness means that different solutions to the inverse problem exist that equally fit the observed data within their uncertainties but strongly differ in the conductivity distribution of the recovered models.

5.1.1 General remarks on 3-D MT forward modeling

There are three basic simulation techniques for computing 3-D EM fields, respectively responses, in frequency domain (or in other words numerical solutions of Maxwell's equations in frequency domain), namely finite-difference (FD) methods, finite-element (FE) methods and volume integral equation (IE) methods. For decades FD schemes (*Mackie et al.* (1994), *Haber and Ascher* (2001), *Newman and Alumbaugh* (2002), *Egbert and Kelbert* (2012), among others) dominated in geoelectromagnetism. However, in the last years FE schemes (*Schwarzbach et al.* (2011), *Farquharson and Miensopust* (2011), *Puzyrev et al.* (2013); *Zhengyong et al.* (2013), *Um et al.* (2013), *Grayver and Burg* (2014), among others) and IE schemes (*Avdeev et al.* (2002), *Hursan and Zhdanov* (2002), *Singer* (2008), *Koyama et al.* (2008), *Nie et al.* (2013), *Kamm and Pedersen* (2014), among others) gained growing popularity.

Each type of solution has its own advantages and drawbacks. The main attraction of the FD approach is its relatively simple numerical implementation, especially when compared to other approaches as well as its effectiveness. One then works with a sparse

system matrix after discretization of the second-order differential equation (either with respect to electric or magnetic fields) deduced from Maxwell's equations. The drawback is that the convergence of an iterative solution of the system matrix is not guaranteed even after preconditioning. In addition the large computational volume (both in lateral and vertical directions, compare Figs. 5.6, 5.7 and 5.8) needed to allow for decay (or stabilization) of EM fields at the boundaries of the domain is another disadvantage.

In the FE method, the modeling volume is decomposed into elementary volumes (such as prisms, tetrahedrons or volumes of more complex shapes) that specify the geometry of the conductivity model. Accordingly, the electric field (or its potentials) is decomposed via some basis functions and the coefficients of decomposition are usually sought using the Galerkin method. Like with the FD approach, one again arrives at a sparse system of linear equations. The drawbacks of the FD approach generally also apply to the FE approach. The main attraction of FE methods is that they are very convenient to treat conductivity models that involve complicated structures and curved interfaces like free surface topography or bathymetry.

Finally, with the (standard) IE method, Maxwell's equations are first reduced to the integral equation with respect to electric field. To derive the IE a Green's function technique is applied. The discretization of the IE yields a linear system resulting in a dense matrix (with all entries filled), but it is much more compact than matrices used in FD and FE methods. The reason for the compactness is that the boundary conditions can be exactly accounted for via the Green's functions, and thus the modeling region is confined only to 3-D anomalies embedded into the conductivity background. Moreover, the system matrix resulting from modern versions of the IE method (contracting IE method; cf. *Pankratov et al.* (1995)) does not require any preconditioning, whereas FD and FE do, especially for models with large conductivity contrasts. Nonetheless, many EM software developers refrain from implementations of the IE method, because the accurate computation of the resulting system matrix is a tedious and nontrivial problem.

5.1.2 General remarks on 3-D MT inverse modeling

Nowadays 3-D MT inversion becomes common practice due to the availability of better instrumentation to record large MT data-sets, continuously increasing computational power and advances in the development of fast, robust and scalable 3-D MT inverse solutions. In the past two decades a number of 3-D MT inverse solvers have been developed (*Mackie and Madden* (1993), *Newman and Alumbaugh* (2000), *Farquharson et al.* (2002), *Siripunvaraporn et al.* (2005), *Sasaki and Meju* (2006), *Hautot et al.* (2007), *Han et al.* (2008), *Avdeev and Avdeeva* (2009), *Zhdanov et al.* (2010), *Egbert and Kelbert* (2012) and *Zhang et al.* (2012), among others). With the ultimate goal of 3-D EM inverse modeling being the same – namely, imaging the 3-D electrical conductivity distribution

in the Earth's interiors – there are a number of differences between the specific inverse solvers. These differences lie, for example, in the way which method for solving the 3-D forward problem is invoked, which optimization scheme is used to minimize penalty function (penalty function will be discussed later in this Chapter), which response functions are inverted etc. Most of existing MT inverse solvers rely on the FD solution of the forward problem (e.g. *Newman and Alumbaugh* (2000), *Farquharson et al.* (2002), *Siripunvaraporn et al.* (2005), *Sasaki and Meju* (2006), *Hautot et al.* (2007), *Han et al.* (2008), *Egbert and Kelbert* (2012)). A number of solvers are based on the IE forward solution (*Avdeev and Avdeeva* (2009), *Zhdanov et al.* (2010), *Zhang et al.* (2012)), and hitherto very few – on a FE formulation (e.g. *Schwarzbach and Haber* (2013)). Regarding the optimization methods the inverse problem is either solved with conjugate gradients (*Mackie and Madden* (1993), *Newman and Alumbaugh* (2000), *Hautot et al.* (2007), *Zhdanov et al.* (2010), *Egbert and Kelbert* (2012)), with a Gauss-Newton method (*Farquharson et al.* (2002), *Siripunvaraporn et al.* (2005), *Sasaki and Meju* (2006), *Han et al.* (2008), *Schwarzbach and Haber* (2013)) or with a quasi-Newton method (*Avdeev and Avdeeva* (2009), *Zhang et al.* (2012)). Note that only one 3-D inverse solver, ModEM (*Egbert and Kelbert*, 2012), is currently freely available for the scientific community. A summary of ModEM is presented later in this Chapter. The different codes also differ in the kind of response functions that can be inverted, most common practice is to work with the impedance tensor. However, also tippers have been employed during inversion (*Siripunvaraporn et al.* (2005), *Egbert and Kelbert* (2012)). Recently, the phase tensor was introduced in WSINV3DMT by *Patro et al.* (2013) and in ModEM by *Tietze and Ritter* (2013). ModEM also allows for working with inter-site horizontal magnetic tensors, but so far case studies with inversions of this response functions were not reported, at least in a 3-D frame.

5.2 The X3D code

To study topography effects on responses we used the X3D forward modeling code described in *Avdeev et al.* (1997) and *Avdeev et al.* (2002). X3D is based on a particular class of IE (cf. *Pankratov et al.* (1995) and *Singer* (1995)) with a contracting kernel (hereinafter denoted as *contracting integral equation* (CIE)). The CIE possesses an important property: its system matrix is well-conditioned irrespective of discretization, frequency and conductivity contrasts. It is known that any IE approach is based on the solution of scattering equation, which is, in case of standard IE, of the following form

$$\mathbf{E}(\mathbf{r}) = \mathbf{E}_0(\mathbf{r}) + \int_{V_s} G_b(\mathbf{r}, \mathbf{r}')(\sigma(\mathbf{r}) - \sigma_b(\mathbf{z}'))\mathbf{E}(\mathbf{r}')\mathrm{d}\mathbf{v}'. \tag{5.2}$$

Here $\mathbf{E}(\mathbf{r})$ is the scattered electric field (with $\mathbf{r} \in V$, where V is the volume where $\sigma - \sigma_b$ deviates from background conductivity σ_b), $\mathbf{E}_0$ is the known free term and $G_b(\mathbf{r}, \mathbf{r}')$ is the electric Green's tensor of the background section. Note that in the CIE approach the underlying IE differs from that presented by eq. (5.2) but has a similar structure. A non-trivial task of any IE approach is the construction and calculation of the Green's functions. This topic is addressed in detail in *Avdeev et al.* (1997). Note also that the shift invariance of the Green's functions defined on lateral regular grids under horizontally layered structure allows an efficient storage and fast application (convolution with some vector) of Green's operators, leading to fast implementation of Krylov subspace iterates (*Greenbaum*, 1997) to the solution of IE. The compact storage and fast convolution are also discussed in *Avdeev et al.* (1997).

5.3 The ModEM code

The ModEM code with implemented solutions to the forward and inverse problems based on FD is described in *Egbert and Kelbert* (2012) and *Kelbert et al.* (2014). In the FD approach magnetic fields can be eliminated and Maxwell's equations are reduced to a curl-curl-vector equation of the electric field, which is the core of the forward problem:

$$\nabla \times \nabla \times \mathbf{E}(\mathbf{r}) - \mathrm{i}\omega\mu_0\sigma(\mathbf{r})\mathbf{E}(\mathbf{r}) = 0. \tag{5.3}$$

This differential equation is numerically solved by discrete finite difference approximations on a staggered Yee-grid (*Yee*, 1966). The primitive cell of a Yee-grid is illustrated in Fig. (5.2). The total 3-D grid of the model space is constructed by a number of $M = N_x \cdot N_y \cdot N_z$ cells, where N_x, N_y and N_z denote the discretization along x, y and z, respectively. This leads to a system of $3M$ complex-valued linear equations with respect to the electric field values along the mesh edges. Details about how this system is solved can be found e.g. in *Egbert and Kelbert* (2012) and *Kelbert et al.* (2014). Note that the FD technique requires a volume significantly larger than the region of interest.

The inversion implemented in ModEM is based on minimization of the objective or penalty function

$$\Psi(\mathbf{m}, \mathbf{d}^{obs}) = (\mathbf{d}^{obs} - F(\mathbf{m}))^T \mathbf{C}_d^{-1} (\mathbf{d}^{obs} - F(\mathbf{m})) + \lambda(\mathbf{m} - \mathbf{m}_0)^T \mathbf{C}_m^{-1} (\mathbf{m} - \mathbf{m}_0). \tag{5.4}$$

The first term on the right-hand side of the penalty function is a measure of the fit between observed $\mathbf{d}^{obs}$ and predicted (modeled) data $\mathbf{d}^{pred} = F(\mathbf{m})$, the data covariance matrix $\mathbf{C}_d$ contains information about the data errors. The second term can be interpreted as a measure of the model complexity. Here $\mathbf{m}_0$ is the prior model, $\mathbf{C}_m$ is the model covariance, which describes the model smoothness, and λ is the regularization parameter. The penalty function can be minimized using an approach based on the

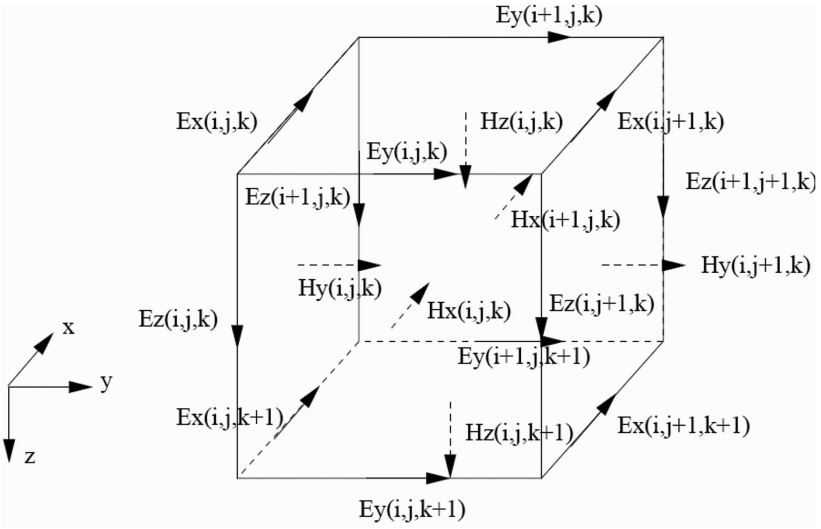

FIGURE 5.2: Primitive cell of the staggered Yee grid for the finite difference approach of the 3-D MT forward problem. The discrete electric field vector components are defined along the edges, whereas the magnetic components are defined on the cell faces. Figure taken from *Egbert and Kelbert* (2012).

linearization of $F(\mathbf{m})$ by a first order Taylor-expansion around the prior or initial-guess model $\mathbf{m}_0$:

$$F(\mathbf{m}) = F(\mathbf{m}_0) + \frac{\partial F(\mathbf{m})}{\partial \mathbf{m}}\Big|_{\mathbf{m}=\mathbf{m}_0} (\mathbf{m} - \mathbf{m}_0) = F(\mathbf{m}_0) + J\Delta\mathbf{m}, \tag{5.5}$$

where $\Delta\mathbf{m}$ is a small perturbation about $\mathbf{m}_0$. The derivatives $\frac{\partial F(\mathbf{m})}{\partial \mathbf{m}}$ of F with respect to the model parameters $\mathbf{m}$ are collected in the $(N \times M)$ matrix J, that describes the sensitivity of the predicted data $\mathbf{d}^{pred} = F(\mathbf{m})$ to small perturbations $\Delta\mathbf{m}$, it is called the Jacobian or sensitivity matrix. By substituting eq. (5.5) into eq. (5.4) one gets the linearized penalty function. Linearized inversion problems require an iterative procedure to be employed, where the initial starting model is updated after each iteration k by the model updates $\Delta\mathbf{m}_k$, which are added to $\mathbf{m}_0$. The model updates are determined for each iteration k, the search direction to minimize eq. (5.4) is determined by the gradient $\frac{\partial \Psi}{\partial \mathbf{m}}|_{\mathbf{m}=\mathbf{m}_k}$. This requires to compute the Jacobian J at each step of iteration, its computational cost is high and requires a large storage space. In ModEM the penalty function eq. (5.4) is minimized using a non-linear conjugate gradient (NLCG) approach, which is known for its small amount of memory usage as it avoids to explicitly compute and store the Jacobian J. Within the NLCG approach the starting model $\mathbf{m}_{initial}$ is iteratively updated by a line search strategy

$$\mathbf{m}_{k+1} = \mathbf{m}_k + \alpha_k \mathbf{u}_k, \tag{5.6}$$

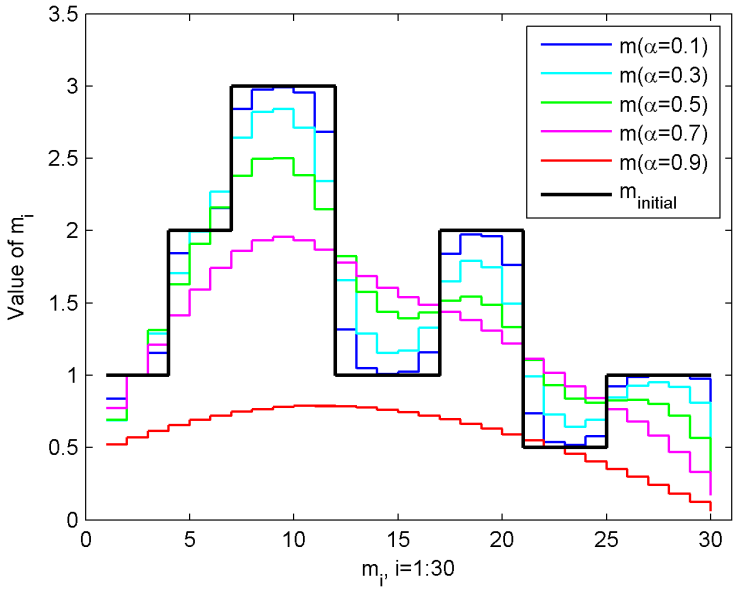

FIGURE 5.3: Plot showing smoothed model vectors $\mathbf{m}(\alpha)$ of a starting model $\mathbf{m}_{\text{initial}}$ using the smoothing operator implemented in ModEM for different smoothing parameters α.

which yields to find α_k $(0 < \alpha_k < 1)$ such that $\Psi(\mathbf{m}_k + \alpha_k \mathbf{u}_k)$ is minimized along the search direction given by the conjugate gradient $\mathbf{u}_k$. The details of this procedure are described in *Fletcher and Reeves* (1964), *Egbert and Kelbert* (2012), *Kelbert et al.* (2014) and reference therein.

In ModEM model regularization is implemented in a flexible manner. The model regularization parameter λ in eq. (5.4) has to be preselected and decreases after predetermined criteria during the inversion. Hereby the model regularization term, which determines i.a. the model smoothness, dominates during the first iterations whereas with progressing inversion the data misfit takes on the dominating role. The smoothing parameter α can be defined independently along all three dimensions allowing to define e.g. different smoothing in horizontal and vertical directions. The implemented spatial smoother is an recursive auto-regressive covariance operator with a quasi Gaussian smoothing kernel (*Kelbert et al.*, 2014). The smoothing parameter has to be chosen from the interval $[0, 1[$, where higher values result in smoother models. To illustrate the impact of the smoothing operator on model smoothness we show its implications on a starting model vector $\mathbf{m}_{\text{initial}}$ for different smoothing parameters α in Fig. 5.3 for a simple 1-D case.

ModEM is parallelized with respect to frequencies and source field polarization so that the minimum computing time is achieved by distributing the problem on $N_c = 2 \cdot N_f + 1$ processors, where N_f is the number of frequencies and the factor 2 takes into account the two source field polarizations. The addend 1 is needed for the master processor, which distributes the problem and summarizes the results.

ModEM can invert for a variety of MT, magnetic and magnetic inter-site transfer functions, and responses can be chosen arbitrarily with respect to sites and periods. The advantage of an individual selection of responses for each site is that obviously bad data can be omitted without excluding a complete set of responses for a whole period range. The model domain significantly exceeds the area of interest, which is necessary to obtain accurate forward solutions. In addition the forward and inverse model domains in ModEM coincide and the prior model corresponds to the starting model. This has been changed in a recent update of the code when a nested modeling approach was implemented to reduce the size of the model domain (*Meqbel et al.*, 2014). Note also that including topography is allowed in ModEM.

5.4 Topography effect model studies

In presence of locally pronounced topography or surface roughness in the vicinity of a MT site apparent resistivity curves can be shifted towards lower or higher values, like in the case of galvanic distortion above a plain surface without topography (e.g. *Jiracek*, 1990). We performed forward modeling studies aiming to analyze whether topography can explain the scattering of the responses and to correct for topography effects. In order to obtain corrected MT responses we applied the method described by *Baba and Chave* (2005, and references therein). In this approach topography is interpreted as distortion $\mathbf{D}$ acting on an undistorted tensor $\mathbf{Z}_S$ which purely contains information about the underlying structure without topography. This results in a tensor $\mathbf{Z}_{S,topo}$ comprising the information of the structure and topography:

$$\mathbf{Z}_{S,topo} = \mathbf{D} \cdot \mathbf{Z}_S. \tag{5.7}$$

$\mathbf{Z}_{S,topo}$ can be calculated by forward modeling provided that we have (i) a priori information about the underlying structure $\mathbf{Z}_S$ and (ii) topography data for the entire survey area. An expression for $\mathbf{D}$ follows from equation 5.7 :

$$\mathbf{D} = \mathbf{Z}_{S,topo} \cdot \mathbf{Z}_S^{-1}. \tag{5.8}$$

The following assumptions are made to derive topography corrected MT responses $\mathbf{Z}_{corr}$ from observed MT responses $\mathbf{Z}_{obs}$:

$$\mathbf{Z}_{obs} = \mathbf{Z}_{S,topo} \quad \text{and} \quad \mathbf{Z}_{corr} = \mathbf{Z}_S. \tag{5.9}$$

Combining eqs. (5.7), (5.8) and (5.9) we get

$$\mathbf{Z}_{obs} = \mathbf{Z}_{S,topo} \cdot \mathbf{Z}_S^{-1} \cdot \mathbf{Z}_{corr}. \tag{5.10}$$

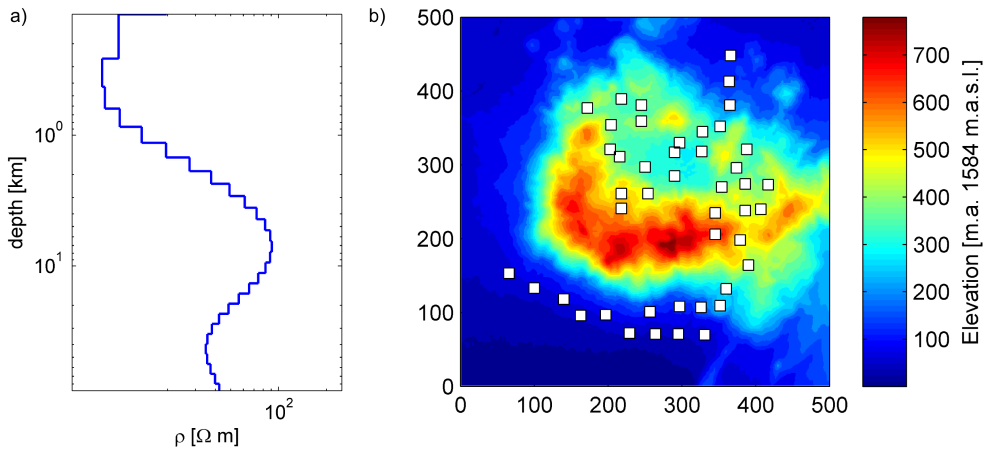

FIGURE 5.4: a) 1-D section derived from the median of all survey sites. b) 500 cells × 500 cells array of extrapolated topography data with survey site locations.

The expression for the corrected responses follows from rearranging eq. (5.10):

$$\mathbf{Z}_{corr} = \mathbf{Z}_S \cdot \mathbf{Z}_{S,topo}^{-1} \cdot \mathbf{Z}_{obs}. \tag{5.11}$$

In this model study $\mathbf{Z}_S$ was assumed to be 1-D. We derived it by 1-D inversion of the median of ρ_a and Φ of the sites shown in Fig. 4.5 using the Occam's inversion algorithm by *Constable et al.* (1987). The resulting 1-D section is shown in Fig. 5.4. Based on the 1-D section we derived the corresponding response $\mathbf{Z}_S$ with Wait's recursion formula (e.g. *Simpson and Bahr*, 2005).

The 3-D forward model studies to obtain $\mathbf{Z}_{S,topo}$ were performed using the X3D code (*Avdeev et al.*, 2002), which is discussed in Section 5.2. This frequency-domain code allows for calculating plane-wave electric and magnetic fields and thus MT response functions in Earth's models with a 3-D conductivity distribution. In X3D the topography is mimicked by means of a discretized 3-D conductivity distribution with high-resistive cells (air, 10^{-6} S/m) and conductive cells (Earth) conformed to the true topography. Topography data have been taken from the SRTM digital elevation database[1]. These data are provided with a horizontal resolution of 3 arcsec, which corresponds to approximately 90 m. For our studies we chose an area spanning 15 km × 15 km with Aluto at its center (Figure 5.4 b), the topography data within this area were extrapolated to a 500 cells × 500 cells array with a horizontal cell size of 30 m × 30 m. Minimum and maximum values of the chosen area are 1584 m to 2378 m, in vertical direction the topography was discretized to 30 vertical layers of ∼ 26.50 m thickness each, see Figure 5.4 b). The conductivity σ_T of the topography cells in the 3-D forward model above 1584 m was chosen to be homogeneously 0.01 S/m. Below 1584 m the model is assumed to be 1-D with

[1] http://srtm.csi.cgiar.org/

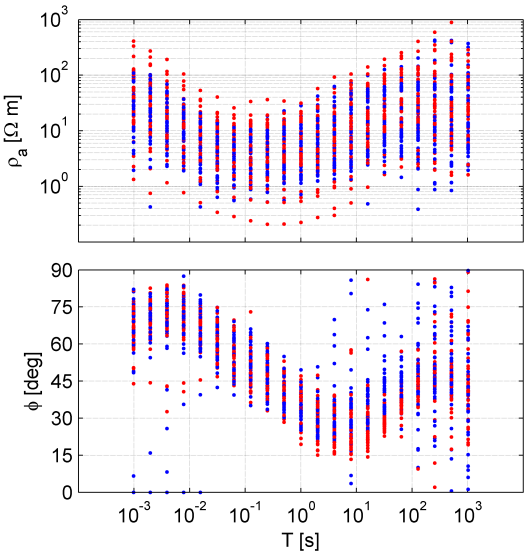

FIGURE 5.5: Cloud plot of topography corrected off-diagonal ρ_a and Φ at all survey sites, xy-elements, red, yx-elements, blue. Data are plotted without uncertainties.

the conductivity distribution shown in Figure 5.4 a. With this 3-D forward model we derived the responses at the corresponding survey site locations and subsequently calculated the corrected responses $\mathbf{Z}_{corr}$. Figure 5.5 shows the corrected responses in terms of apparent resistivity and phase. Comparing this plot with the uncorrected responses (Fig. 4.5) one can see that by correcting for topography effects the observed scattering of the responses cannot be eliminated. One effect of the correction is that the minimum in ρ_a moves slightly towards shorter periods. As the scattering still remains we conclude that (i) it cannot be ascribed to topography effect, or (ii) the described approach is not applicable to correct responses for topographic effect due to insufficient accuracy used for the discretization of the 3-D model or due to oversimplified assumptions about the underlying conductivity structure.

5.5 3-D inversion of the MT data

In order to get 3-D conductivity models of the subsurface we inverted the MT data in the period range of $10^{-3} - 10^3$ s at 41 logarithmically uniform distributed discrete periods using the ModEM code.

The overall modeling area for our studies is chosen to be 406 km (N-S or x) by 402 km (E-W or y) by 271 km (depth or z). Embedded into the large model domain is the area of interest, or core, with 50 cells in x and 38 cells in y direction, each cell has a horizontal size of 400 m to 400 m, thus resulting in a core with 20 km in the x and 15.2 km in the y directions. We implemented topography by vertically discretizing the topography data for the area of interest into 14 layers with 50 m thickness each. To greater depths cells

are continued with a subsequently increasing thickness by a factor of 1.2 until a total cell number in vertical direction of 54 (271 km). In the horizontal direction towards the margins cell sizes increase by a factor of 1.3. The total number of model parameters sum up to $86 \times 74 \times 54 = 343656$. The total model grid is shown in Fig. 5.6 along N-S and in Fig. 5.7 along E-W direction. Note that the modeled volume significantly exceeds the area of interest, respectively the model core, shown in Fig. 5.8.

All inversions were run on $2 \cdot N_{per} + 1$ processors, where N_{per} denotes the number of periods, in our case this results in a total of 83 processors.

In order to evaluate the quality of the final recovered model, we analyze the root mean square misfit (RMS) and the distribution of the residuals r_i. The overall RMS is given by ModEM for each iteration and is calculated as follows

$$RMS = \sqrt{\frac{1}{N} \sum_{i=1}^{N} \frac{(d_i^{obs} - d_i^{pred})^2}{e_i^2}}, \tag{5.12}$$

where d_i^{obs} and d_i^{pred} are observed and predicted responses and e_i are the errors of the observed responses, N counts the responses at all considered sites and at all considered periods. The residuals are estimates of the errors derived from the differences between observed and predicted responses and are calculated as follows

$$r_i = \frac{d_i^{obs} - d_i^{pred}}{d_i^{obs}}. \tag{5.13}$$

The distribution of residuals provides important insight about the observed data, which are not explained by the fitted model. Recovered models are considered to be appropriate if the residuals are at least distributed with a mean of 0 and if their variance is small.

The data used for inversion were first selected visually and obviously bad responses were omitted. The chosen apparent resistivities ρ_a and phases Φ at all sites are shown in Fig. B.1 to B.12 in Appendix B. We did not apply any corrections for static shift effects as ModEM accounts for these effects by introducing a scattered conductivity distribution

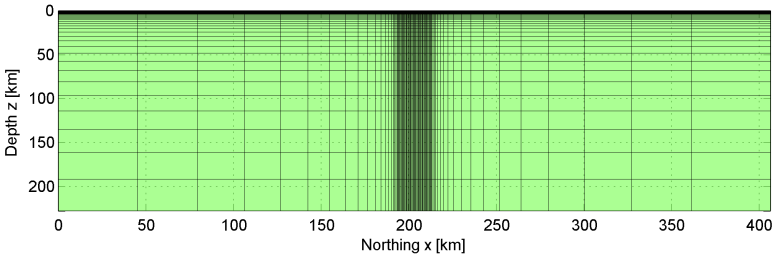

FIGURE 5.6: Illustration of grid along N-S direction spanning the whole extent of model.

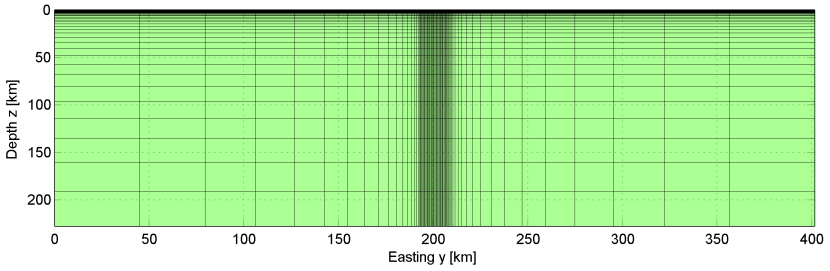

FIGURE 5.7: Illustration of grid along E-W direction spanning the whole extent of model.

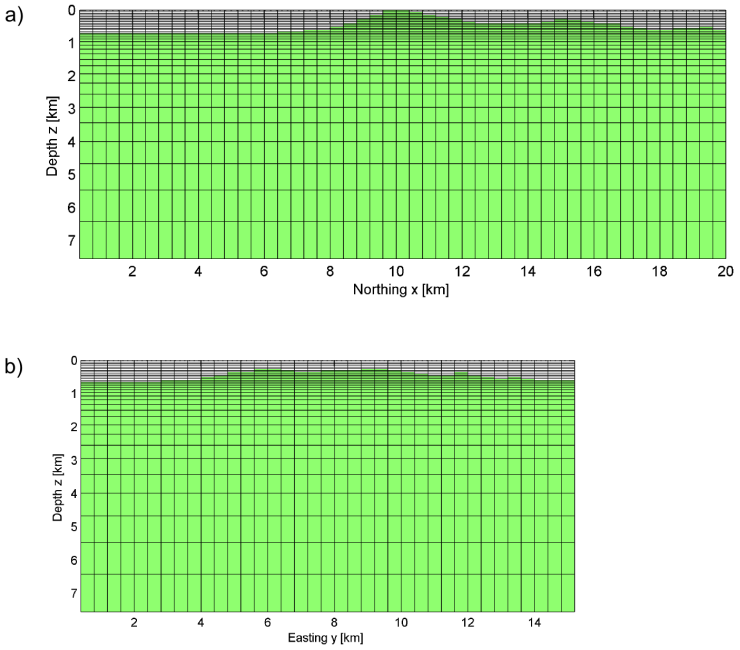

FIGURE 5.8: Illustration of model core grid along a) N-S direction and b) E-W direction of the upper $\sim 7\,\mathrm{km}$. Air cells to mimic topography were assigned a conductivity of $10^{-6}\,\mathrm{S/m}$, they are kept blank in the plot.

in the near surface layers to model distortion effects (*Tietze and Ritter*, 2013; *Meqbel et al.*, 2014).

5.5.1 Inversion of off-diagonal tensor elements

To derive the first model we inverted only off-diagonal impedance tensor elements Z_{xy} and Z_{yx}, the data were not rotated as the coordinate system of the measurement already corresponds to the geoelectric strike direction inferred from tippers at long periods (see Fig. 4.6). We assigned errors of 5% of $|Z_{ij}|$ for real and imaginary parts of Z_{ij} and the true errors if they exceeded 5%. As prior or starting model we used a homogeneous

half space. The resistivity of the half-space (20 Ωm) was chosen to have minimum starting RMS, compared to alternative starting models with 50 Ωm and 100 Ωm. We chose a smoothing parameter of 0.3 in the horizontal and vertical directions, however, smoothing between land and air layers is turned off in the model covariance file. The inversions using these parameters are referred to as `ALS3ZOFF`. The starting RMS of `ALS3ZOFF` was 11.17, within 39 iterations it is decreased to 1.20. The distribution of the normalized residuals for the starting and final inversion run is shown in Fig. 5.9. It can be seen that the variance for the initial iteration is large and residuals are non-uniformly distributed and centered around zero. The latter justifies the choice of the starting model while the non-uniformity and the large variance denote the oversimplified assumptions made by the choice of the homogeneous halfspace. The variance of the residuals for the final iteration is significantly smaller and the residuals are symmetrically distributed around zero. Thus we conclude that the final model gives a reliable representation of the subsurface's conductivity distribution.

The horizontal slice of the final model (Fig. 5.10) clearly shows the influence of the non-uniform site distribution especially at shallow depths, where sensitivity is only given close to the site locations. To avoid misinterpretations we show vertical slices of the 3-D model only along sections with a good site coverage denoted as AA', BB' and CC' in Fig. 5.10. Slices are shown to a maximum depth of 8 km, since there are no significant structures towards greater depths.

The vertical slice along AA' shows a low resistive zone ($\rho < 5\,\Omega$m) at depths down to $\sim$ 1.5 km in the central region of Aluto (7 km $< y <$ 14 km), the shallow layers in the upper few hundred meters are resistive ($\rho \geq 100\,\Omega$m). At greater depths below 2 km resistivity increases again reaching maximum values of $\rho > 100\,\Omega$m at depths of around 5 km at 11 km east (Fig. 5.12, a). The E-W slice along BB' south of Aluto shows a pronounced shallow conductor in the central part between 7-12 km East, which

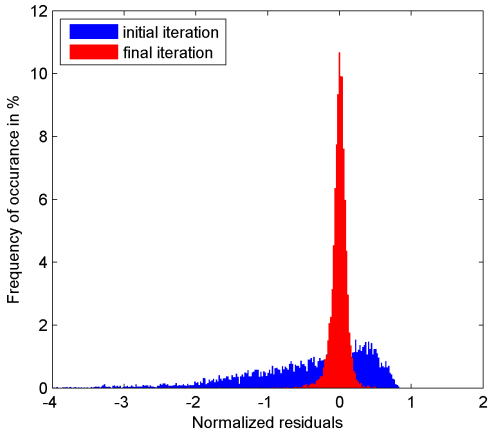

FIGURE 5.9: Distribution of initial and final residuals for `ALTS3ZOFF`.

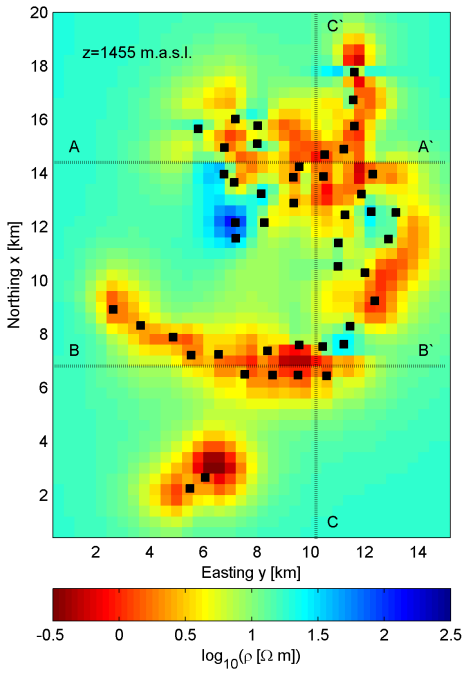

FIGURE 5.10: Horizontal slice at z=1455 m.a.s.l. for `ALTS3ZOFF`. Projected surface site locations are indicated as black squares. The depth of the horizontal slice corresponds to the first subsurface layer without topography.

is only around 100 m thick and situated at depths between $100 - 200$ m below surface. Between $2 - 6$ km East the shallow conductor appears more blurred, which could be an artifact of the inversion as the MT sites are $1 - 2$ km north of the section BB' in this part. Below the shallow conductor resistivities are between $10 - 50\,\Omega$m (Fig. 5.12, b). The low resistive zone identified in AA' is also found in the N-S slice along CC' (Fig. 5.12, c), here it starts at the central part of Aluto at 13 km North and ends at around 17 km North, as in the case of section AA' it reaches depths down to ~ 1.5 km. At greater depths this zone is followed by a resistive body that clearly exceeds resistivities of $100\,\Omega$m. The recovered model shows no significant structure at depths below 8 km.

5.5.2 Inversion of full impedance tensor

In a next step we inverted the full impedance tensor with the same starting model and smoothing parameter as for the previous inversion run with off-diagonal elements only, the corresponding inversion run is referred to as `ALS3ZFULL`. We used the same data selection regarding the period range for Z_{xx} as for Z_{xy} and the same for Z_{yy} as for Z_{yx}, the assigned an errors are 5% of $|Z_{ij}|$ and higher if the true errors exceed 5%. The starting RMS for the full tensor inversion is 8.28. For `ALS3ZFULL` the RMS decreased to 1.43 within 52 iterations. The distribution of the normalized residuals for

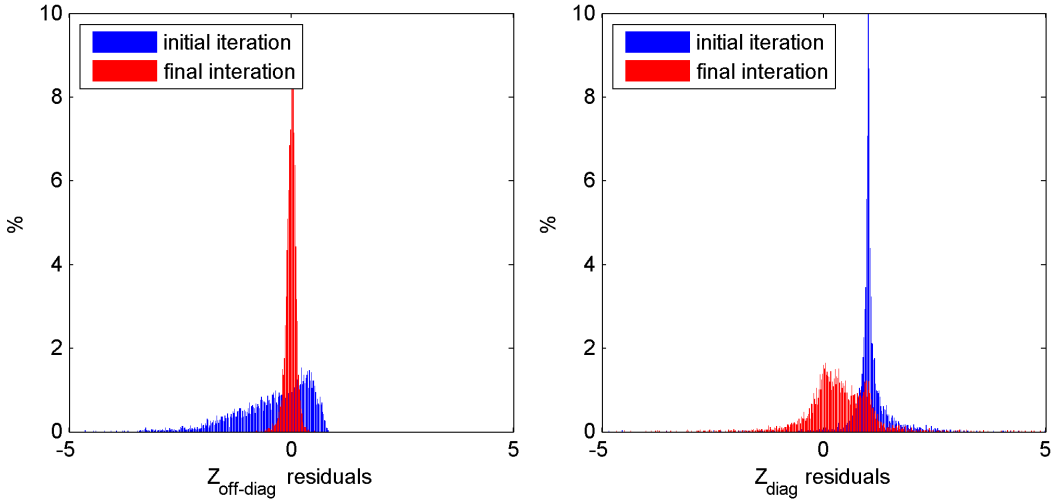

FIGURE 5.11: Distribution of initial and final residuals for `ALTS3ZFULL` for off-diagonal elements of **Z** (left) and diagonal elements (right).

the starting and final inversion run is shown in Fig. 5.11 separately for diagonal and off-diagonal elements of **Z**. It can be seen that the off-diagonal residuals show a comparable behavior like in the inversion runs of `ALS3ZOFF`. The distribution of the diagonal residuals shows one specialty: for the initial iteration the residuals are centered around 1. This is due to the fact that our starting model is basically 1-D except for 3-D effects arising from topography. The way to calculate the residuals (eq. (5.13)) consequently implies a starting residual of 1 as the d_i^{pred} of the starting model are zero for the diagonal elements except where we have 3-D topographic effects. The diagonal residuals distribution of the final iteration is less distinct centered around zero compared to the off-diagonal residuals. This reflects the fact that the diagonal elements are orders off magnitude smaller than the diagonal elements, respectively close to zero. Thus even a small deviation between observed and predicted data result in a larger absolute misfit. The vertical slices along AA', BB' and CC' for the full tensor inversion `ALS3ZFULL` are shown in Fig. 5.12 (d-f). In comparison with `ALS3ZOFF` it can be seen that the main features that were recovered by inverting off-diagonal elements also appear after inverting the full tensor except for minimal changes.

Figure 5.13 shows a 3-D volume plot of the central part of the volcanic complex as recovered by inversion `ALS3ZFULL` where we have a good site density. The conductive cap with $\rho \leq 5\,\Omega$m extends over the whole part of the central area and overlies the resistive deeper structure with $\rho \geq 80\,\Omega$m. The approximate location of the productive wells LA-3 and LA-6 are marked in the figure and it can be seen that they are located above the conductive cap and the deep roughly N-S oriented resistive body. Well LA-3 is drilled down to a depth of 2144 m below the surface and LA-6 to a depth of 2201 m. Both wells are thereby tapping the upper part of the resistive body.

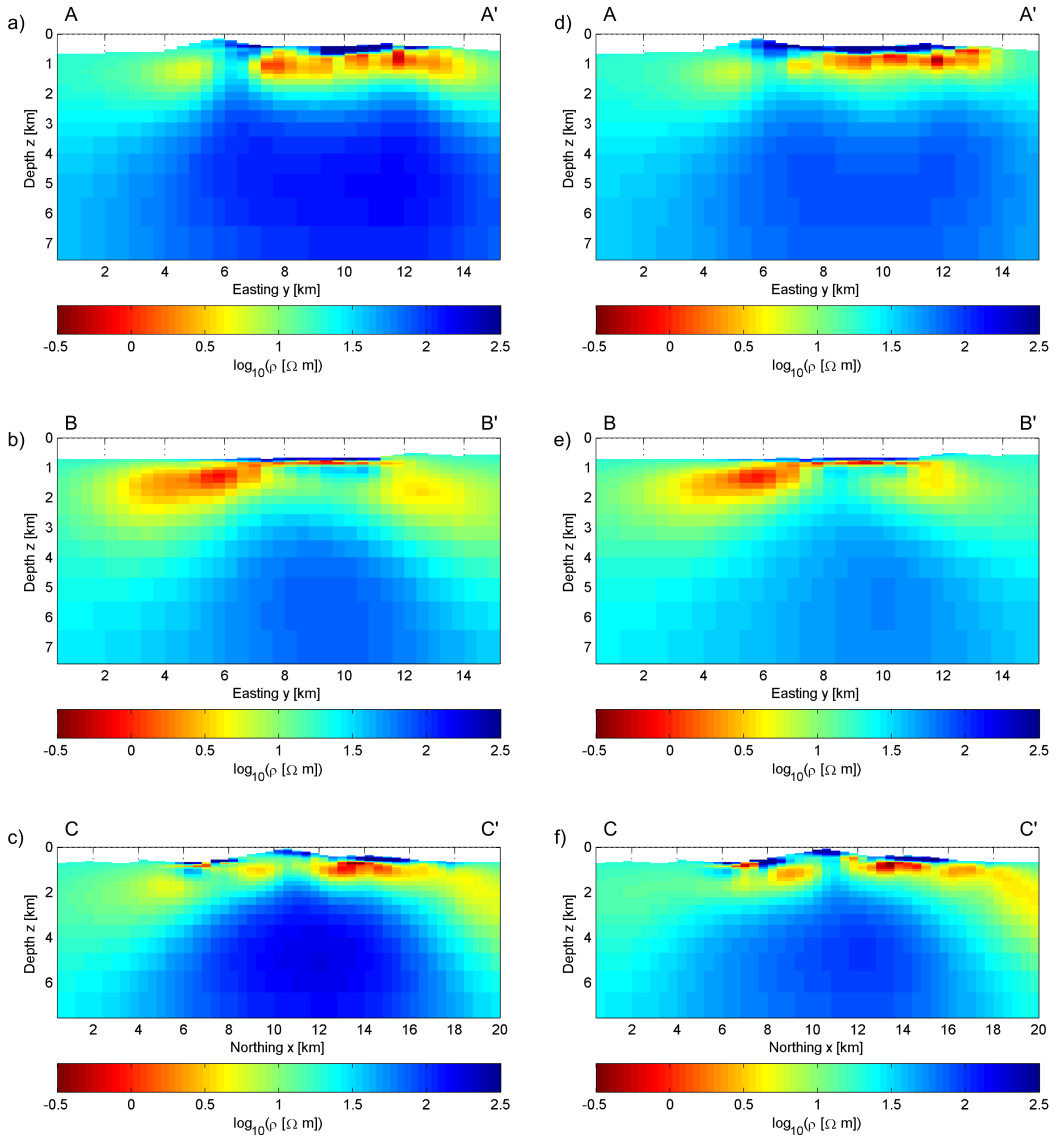

FIGURE 5.12: Vertical slices along AA', BB' and CC' for `ALS3ZOFF` (a-c in left column) and `ALS3ZFULL` (d-f in right column).

Note that the recovered resistivity structures appeared to be stable irrespective of different starting models, grid discretizations and model constraints. None of the models we obtained in various inversion runs could recover any distinct structures below the resistive body in the center of the volcanic complex at depths greater than 8 km, where resistivities stay at moderate values close to the chosen starting model. This basically answers the expectation one already gets from a visual interpretation of the ρ_a-curves as it can be seen in Fig. 4.3: There is only one minimum in ρ_a at around 1 s related to the shallow conductor, towards longer periods ρ_a increases again and stays at an almost constant level for periods $T > 100$ s not indicating any deeper conductive structures.

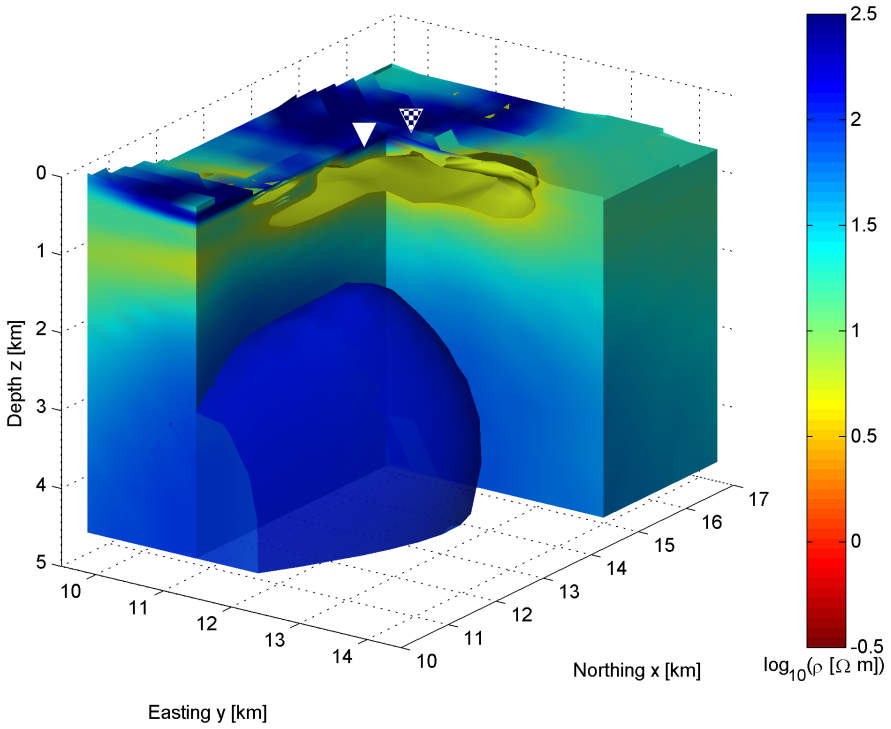

FIGURE 5.13: 3-D volume plot showing the central part of the volcanic complex. As values for the shown isosurfaces we chose 80 Ωm for the resistive deep structure and 5 Ωm for the conductive shallow structure. The locations of well LA-3 and LA-6 are marked as triangle, white for LA-3 and LA-6 with a checkerboard pattern.

5.6 Interpretation of the conductivity structure

The recovered 3-D resistivity models show a highly conductive zone with a diameter of around 6 km in the center of the Aluto volcanic complex at depths between $\sim 500 - 1500$ m and a resistive body at depths below 2000 m underneath the conductive cap. The identified resistivity distribution corresponds very well to the conceptual reservoir model of a high enthalpy geothermal system with its mushroom shaped zoning comprising a resistive upflow zone overlain by a conductive clay cap as discussed in Section 3.1 and illustrated in Fig. 3.1. From well data analysis it is known that the conductive cap at Aluto is related to an argillic hydrothermal alteration zone with temperatures below 200 °C and marked by the abundance of calcite and clay minerals with an estimated overall amount of 20% of smectite in the illite/smectite mixed layer (*Teklemariam et al.*, 1996). The clay cap follows mainly the fluid flow pattern of the outflow zone. The deep resistive body could be identified as zone of upflow and hottest part of the geothermal field characterized by maximum temperatures up to 363 °C and the presence of propyllitic alteration. Here most common alteration products are chlorite, epidote, calcit and quartz as major phases. The two wells LA-3 and LA-6 are drilled into this zone and show a very small temperature gradient for depths below 1000 m,

which is a typical feature of upflow zones. In LA-3 the temperature profile exceeds the boiling point pressure curve showing that the upflow zone is clearly steam dominated with a dominating gas phase at the well head as reported by (*Gizaw*, 1993). All other wells exhibit temperature inversions with depth indicating that they were drilled into the outflow zone.

In the full tensor inversion runs (and less clearly in off-diagonal inversion runs) there is a maximum in the conductivity section along AA' at 11.5 km east in the upper 1.5 km (Fig. 5.12), which corresponds to the position of the NNE tending fault structure of the WFB along which the productive wells are located. By gravity data analysis *Saibi et al.* (2012) could clearly identify the WFB as highly fractured area intersecting the volcanic complex at the location of the productive wells LA-3 and LA-6. However, the model setup with a the horizontal cell size of 400 m and the averaged site spacing of $\sim$ 1 km are not sufficient to clearly resolve narrow vertical features like the fault. We did not find any deep low resistivity structure as one would expect in case of an active magmatic system with the presence of partial melt. The heat source seems therefore to be a post-magmatic relic of a former active magmatic system.

The clay cap seems not to extend to the south of Aluto, where only a thin shallow conductive layer is found, which is most likely related with a groundwater aquifer fed by highly saline waters of Lake Langano. Well LA-1, which was drilled in this area, revealed only one permeable zone at depths corresponding to the shallow conductor. The maximum temperatures in this well are slightly exceeding 100 °C and the pressure profile is close to cold-hydrostatic (*Gizaw*, 1993).

As we found no evidence for an active deep magmatic system we conclude that the source of unrest obtained by InSAR studies is most likely related to changes in the hydrothermal regime of the geothermal system in the shallow argillic alteration zone and in the deeper propyllitic alteration zone in the central part of Aluto. Possible explanations and mechanisms will be addressed in Chapter 6. In the next Section we will provide a forward model in order to explain the observed tippers and to put constraints on the possible occurrence of melt within in MER. It is remarkable that the tippers reveal a N-S elongated highly conductive structure west of the geothermal field. The distance to this conductor can be restricted to several tens of kilometers, based on the penetration depth for periods between 100 s and 1000 s.

5.7 Modeling the tippers

Inverting impedances and tippers simultaneously revealed that the regular eastward pointing behavior of the real tippers at long periods (Fig. 4.6 c, d) can not be explained by any structure inside the modeling region with its horizontal extent of 20 km in N-S to 15 km in E-W. However, it is clear that the regular behavior of the tippers towards long

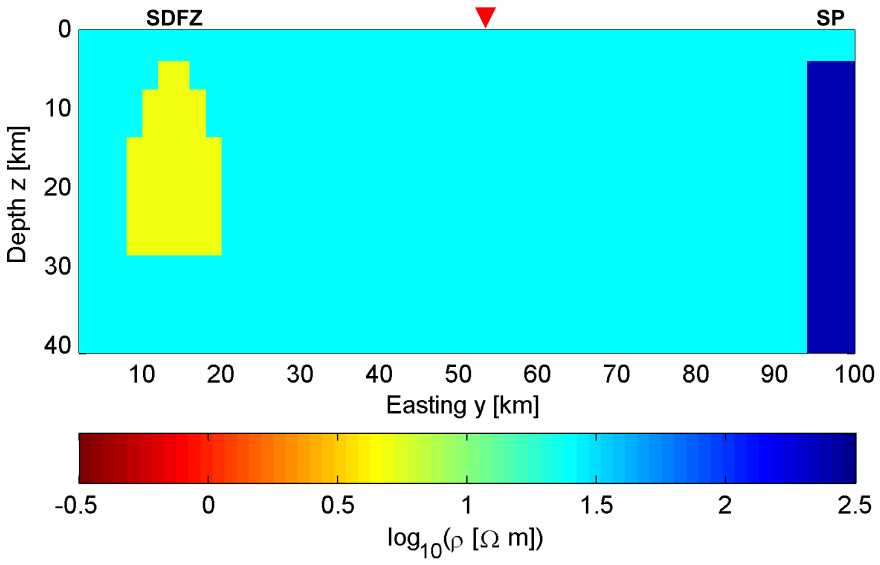

FIGURE 5.14: Vertical slice showing the core of the `ALTIP` forward model to recover the influence on tippers of a N-S elongated conductor at the SDFZ 40 km west of Aluto and a resistive lithosphere east under the southern plateau (SP) of Aluto. The resistive part extends to the model boundary. The location of Aluto is marked as red triangle.

periods is caused by a N-S elongated conductive structure at lower crustal depths west of Aluto, respectively a resistive structure east of Aluto or a combination of both. The only known structure coming into question as potential conductor is the SDFZ 40 km west of Aluto at the western rift margin (see Fig. 2.3). Here seismic studies analyzing the crustal S-wave velocity structure have revealed the presence of a significant amount of melt. In contrast to the WFB magma bodies at the SDFZ extend throughout the crust down to depths of > 20 km (*Bastow et al.*, 2011; *Kim et al.*, 2012). MT studies by *Whaler and Hautot* (2006) along a NW-SE profile crossing the MER ~ 120 km N-W of Aluto revealed a conductor ($\rho = 1.5 - 2.5\,\Omega$m) at depths between 20 and 25 km apart from the western rift margin. They related it with the Bishoftu volcanic chain, the northern part of the SDFZ, which is not directly intersected by their profile that crossed a few tens of kilometers north of it. In the same study *Whaler and Hautot* (2006) found out that resistivities in upper and lower crust beneath the southern plateau east of the rift are with about one order of magnitude higher than beneath the northern plateau west of the rift, this might also contribute to the observed behavior of the tippers.

In order to analyze the influence of a possible N-S elongated conductor underneath the SDFZ and a resistive lithosphere underneath the southern Ethiopian plateau on the tippers at Aluto, we constructed a minimum structure forward model referred to as `ALTIP` with a modeling core that spans 100 km in E-W and 80 km in N-S direction. `ALTIP` consists of a conductive structure representing the SDFZ embedded into a 25 Ωm homogeneous halfspace. The vertical extent of the conductor reaches from 5 to 28 km

depth, in E-W direction it is 4 km wide at its top and with 12 km wider at its lower end, in N-S it is elongated over the whole core. For its resistivity we assigned 5 Ωm, a typical value which was found for magmatic bodies in the Afar region (*Desissa et al.*, 2013). Additionally we added a resistive lithosphere with $\rho = 250\,\Omega$m in the eastern part of the model to mimic high resistivities beneath the southern plateau as obtained by *Whaler and Hautot* (2006). A vertical E-W slice of the `ALTIP` model core is shown in Fig. 5.14.

Observed and predicted tippers of the model are shown in Fig. 5.15 for the period of 1024 s. It can be seen that the predicted tippers have a T_x component of zero as a result of the purely 2-D conductivity distribution of `ALTIP`. Structures are only varying along the y direction resulting in strictly E-W oriented tipper arrows. Regarding their amplitude at least the predicted real tippers agree well with the observed tippers, whereas imaginary parts are slightly underestimated. Figure 5.16 shows a comparison of observed and predicted tippers for periods $T > 1$ s. Again it is clear that the T_x component of predicted tippers is zero over the whole period range due to the above mentioned reasons. Thus the predicted T_x component does generally not fit the slight variations in the corresponding observed component. The T_y component of the predicted tippers matches the overall behavior of observed tippers quite well for periods $T > 30$ s. Especially the agreement in the real parts is encouraging, whereas `ALTIP` does not reproduce the slightly undulating observed imaginary parts at longer periods. At shorter periods the forward model does not explain the observed tippers as we omitted to include any small scale structures in the vicinity of Aluto in order to focus on the analysis of effects arising from the proposed large scale structures under the SDFZ and under the Somalian plateau. These structures affect the predicted responses only at periods $T > 30$ s as can be seen from Fig. 5.16, at shorter periods both imaginary and real parts of T_x and T_y are zero.

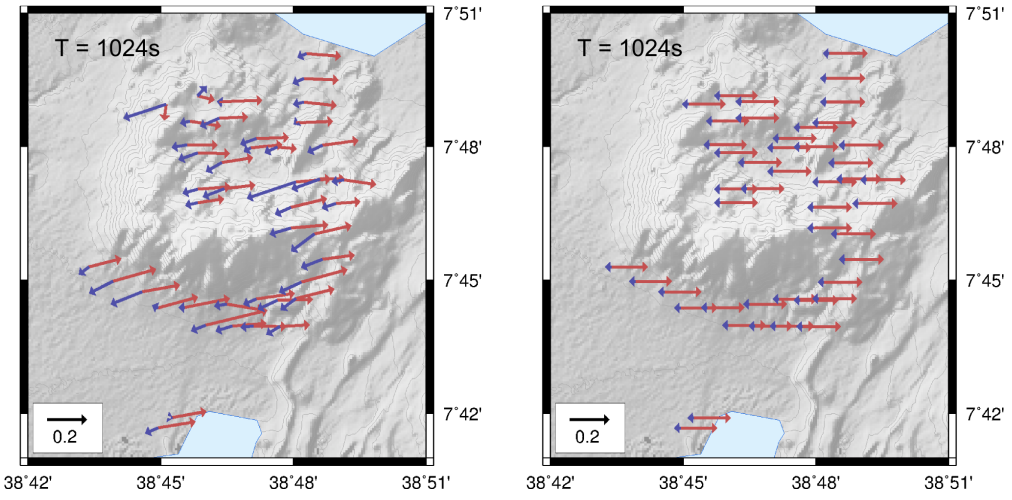

FIGURE 5.15: Observed (left) and predicted tippers of model `ALTIP` shown in Figure 5.14 at a period of 1024 s.

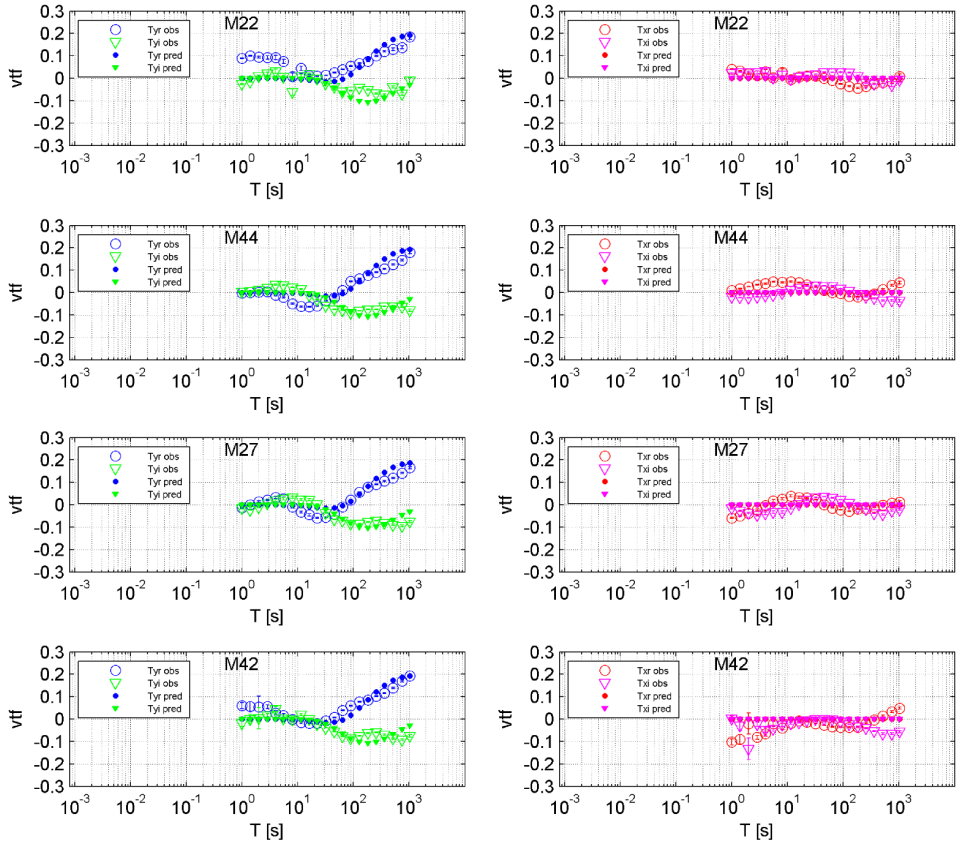

FIGURE 5.16: Comparison of observed and predicted tippers of model `ALTIP` with respect to period at four representative sites reaching from north to south: M22, M44, M27 and M42. The plots on the left show the T_y, the plots on the right – the T_x component. See Fig. 4.1 for site locations.

The tipper forward modeling studies show that the minimum structure model `ALTIP` featuring the N-S elongated conductor west of Aluto and the resistive lithosphere under the southern plateau is able to explain the main behavior of the tippers at long periods in a large part. Thus we think that model `ALTIP` is, despite its simplicity, a step in the right direction as it is well constrained by data of previous magnetotelluric and seismic studies (*Whaler and Hautot*, 2006; *Kim et al.*, 2012). However, more regional data would be necessary in order to recover the local 3-D conductivity distribution in the MER by investigating the extent, geometry and true conductivities of the conductor under the SDFZ and the lithosphere under the southern plateau.

5.8 Inverting the tippers

In order to test the stability of the minimum structure forward model `ALTIP` and to find a model that better fits the observed tippers we run an inversion using the forward model `ALTIP` as starting model with a low smoothing of 0.1 only. We inverted for tippers only at periods $T > 1$ s. Note that we omitted responses at a few sites with poor data quality

and assigned an error floor of 5% of $|T_{x,y}|$ and higher if the true errors exceed 5%. The starting RMS of the inversion was 8.73, it reached a final RMS of 3.68 after 46 iterations. The recovered model is shown in Fig. 5.17. In order to account for effects that are not explained by the starting model `ALTIP` 3-D structures are introduced by the inversion in the region surrounding Aluto. The conductive structure representing the SDFZ and the resistive structure representing the lithosphere under the southern plateau remain as stable features in the model. It is clear that the introduced 3-D structures in the model are not well constraint by the data as they appear mainly in regions that lack site coverage. However, the tipper responses recovered by the inversion give a better fit the observed ones than the responses of the minimum structure model `ALTIP`, especially at shorter periods as can be seen in the plot in Fig. 5.18, which shows the fit at the same four selected sites as in Fig 5.16. In the T_y component also tippers at periods shorter than 50 s are fitted well and the T_x component is non-zero being mainly reproduced by the recovered model.

The inversion of the tippers confirms that their overall behavior at periods $T > 50$ s

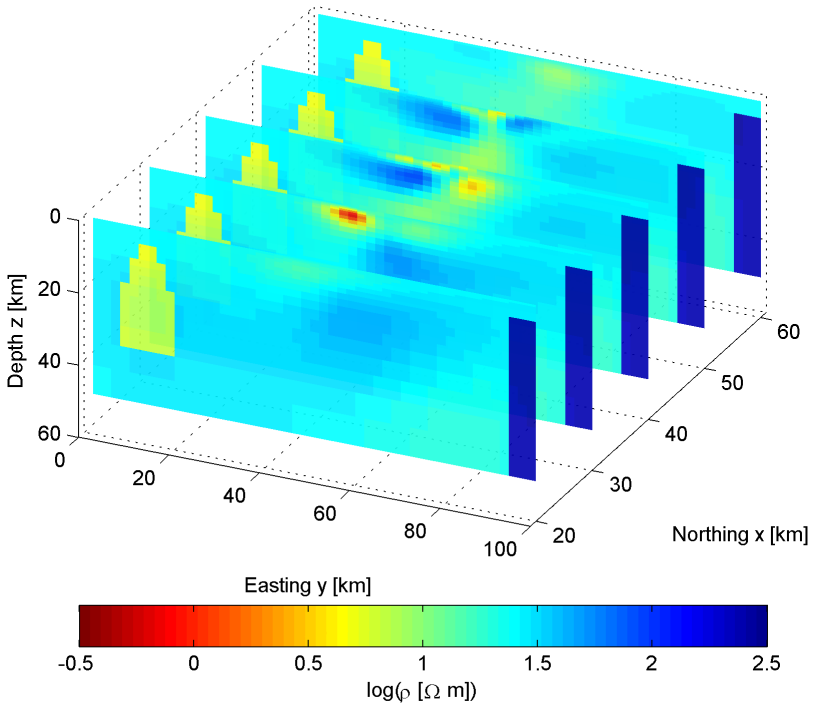

FIGURE 5.17: Model recovered by inverting for tippers using the forward model `ALTIP` shown in Fig. 5.14 as starting model. It can be seen that the structures representing the SDFZ and the resistive lithosphere under the southern plateau remain stable whereas 3-D structures are introduced in the region surrounding Aluto located at about 50 km east and 40 km north.

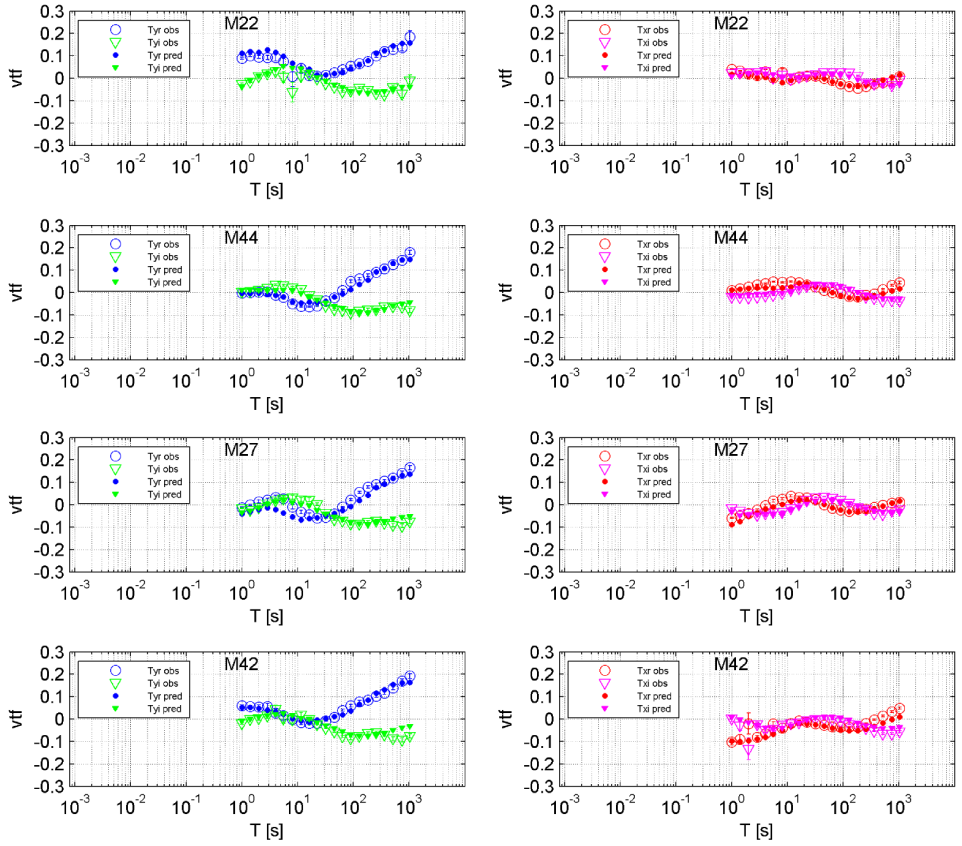

FIGURE 5.18: Comparison of observed and predicted tippers by the inversion using `ALTIP` at starting model. Tippers are shown with respect to period at four representative sites reaching from north to south: M22, M44, M27 and M42. The plots on the left show the T_y, the plots on the right – the T_x component. See Fig. 4.1 for site locations.

is indeed explained by the structure incorporated into the model `ALTIP`. The tippers behavior deviating from the responses recovered by the forward model `ALTIP` arises from 3-D structures, which mainly occur in the surrounding of Aluto.

Chapter 6

Constraints on the source of unrest

Our MT studies have identified a resistive $\sim 100\,\Omega$m body at depths between $2-10\,$km under Aluto. This body is intersected by a highly fractured zone, which could be identified as major upflow zone of the geothermal field with observed temperatures of up to $350\,^{\circ}$C. Overlain of the upflow zone is a clay cap with low resistivities $< 10\,\Omega$m and temperatures below $200\,^{\circ}$C, which is located at depths between $500-2000\,$m in the center of the volcanic complex. Our data reveal no indications for the presence of significant amounts of melt under Aluto. Thus we conclude that the source of unrest is most likely located within the upper part of the reservoir and not in a deeper active magmatic system. Our favored scenario is compliant to the shallow penny shaped source suggested by *Biggs et al.* (2011) as best fitting source model for the deformation patterns. Based on our observations we rule out the alternative explanation, which relates the surface deformation to a 10 km deep point source. This so-called Mogi model is commonly adduced to describe ground deformation in volcanic areas in terms of volume and pressure changes within a magma chamber (*Mogi*, 1958). The question remains about possible mechanisms at shallow depths and within the clay cap that may cause the observed deformation.

In the following we will outline a hypothesis and present two possible explanations for the source of the observed unrest, which are both based on major changes over time in the hydrothermal regime of the geothermal field and complex water-rock interaction processes. It is very likely that fluids act as causal agent driving kinematic mechanism that finally result in the observed ground level oscillations. The first mechanism is related to the hydro-mechanical behavior of clay minerals and their tendency to swell and shrink when exposed to changes of water saturation and pore water chemistry. The second mechanism we refer to is thermoelastic expansion of fractured rock consequent to

forced advection of hot fluids. Hereafter we first introduce the two mechanisms and subsequently discuss possibilities how they might initiate the kinematic mechanisms which lead to the observed unrest at Aluto.

6.1 Clay swelling

Illite and smectite clays, which account for the low resistivities observed within the clay cap, are layered aluminosilicates that are built up by negative charge layers and hold together by positively charged interlayer counterions. These counterions have a great tendency to hydrate and to include water molecules between layers inducing the swelling of clay aggregates, which consequently exhibit a macroscopic swelling response. Studies of clay swelling in clay-water-cation systems under crustal pressure and temperature conditions showed that the layer spacing of dry smectite-rich clay samples increases by a factor of two due to hydration under pressure conditions corresponding to depths down to 6 km (*de Siqueira et al.*, 1999). Clay swelling is a reversible process and several cycles of swelling and shrinking can occur whereas the swelling ability may decrease or increase depending on whether a clay sample is fully hydrated and dehydrated or not (*Basma et al.*, 1996; *Tambach et al.*, 2006). Clay swelling is not only controlled by the water content itself but also by the pore water chemistry such as the pH and ionic strength of the water (*Laird*, 2006). *Xu et al.* (2006) developed a simulation program to study the impact of reinjected waters on clays in fractured geothermal reservoirs. They report that clays may swell to a multiple of their original volume when reinjected geothermal water is diluted with freshwater. However, it is possible that clays shrink back when the ionic strength of the diluted water increases again due to evaporation, decreasing freshwater supply or manipulation of the reinjected water. Clay swelling under freshwater exposure leads to a modest decrease in porosity as minerals precipitate and form a porosity reducing gel, this results in obstruction of flow paths and a large reduction of the overall permeability.

6.2 Thermoelastic expansion

Bonafede (1991) suggests a mechanism driven by hot geothermal fluids to explain periods of uplift and setting at the Campi-Flegrei volcano in Italy. A sudden formation of flow paths by opening faults allows hot pressurized geothermal fluids from greater depths to migrate upwards. Fluids raise relatively fast into the shallower and cooler low-pressure part of the reservoir below the clay cap. This efficient heat transfer increases the host rock temperature, which leads to thermoelastic expansion. *Bonafede*

(1991) showed that forced advection of hot fluids is an efficient source of ground deformation as the associated thermal and pressure uplift easily explains a ground deformation in the order of a few tens of centimeters. In a more recent study *Troiano et al.* (2011) succeeded to fit ground deformation data with consecutive cycles of uplift and subsidence at Campi-Flegrei by numerical modeling of deep geothermal fluid injection into a shallow geothermal system. Their numerical approach allows for modeling multidimensional flow of multiphase geothermal fluids in a porous media initiating thermoelastic deformation. The numerically recovered inflation/deflation curves for Campi-Flegrei adequately match the observed deformation pattern using realistic permeability values and injection rates consistent with observed microgravitiy changes. *Troiano et al.* (2011) related small uplift events in the range of 10 cm, comparable to the ones observed at Aluto, to occasional permeability enhancements by fracture opening in the rock matrix forcing deep hot fluids to migrate upwards. This advective heating events are relatively brief and followed by longer cooling events characterized by setting. Cooling starts either due to exhaustion of the deep source or consequent to obstruction of conduits that allow hot fluids to migrate upwards. However, in their study the question in how far magmatic processes are involved in the genesis of unrest remains unanswered.

6.3 Mechanisms of unrest at Aluto

The introduced mechanisms could give rise to the unrest at Aluto being triggered by stress accommodation along the active faults of the WFB that intersect the volcanic complex, this is discussed in the following. From seismic studies it is known that the region around Aluto shows a diffuse seismicity pattern. Epicenters are widely distributed within a ~ 30 km wide zone and down to depths of 20 km along the Aluto-Gedemsa magmatic segment (*Keir et al.*, 2006). Increasing tensile stress leads to seismic activity and the opening of fractures and flow paths. Firstly, this allows groundwater and lake water to infiltrate laterally into shallower part of the geothermal system. Inflowing freshwater and enhanced circulation of fluids in the shallow part at depths of the smectite/illite cap will provoke clay swelling with major affects on the ground level depending on the affected volume. With time consequent swelling reduces the permeability and flow paths are finally closed again. This would correlate with the end of an uplift event. Subsequently evaporation and fumarolic activity leads to dehydration and an increase in ionic strength of the pore water ultimately resulting in clay shrinking. This period would correspond to the observed periods of setting in the InSAR time series of deformation until the next rifting event allows new flow paths to open within the clay cap. Secondly, the opening of deep faults would simultaneously enforce hot geothermal fluids from a proposed deeper reservoir to move upwards within the fractured upflow zone leading

to thermally induced elastic expansion in the upper part of the reservoir. The end of an uplift in this scenario would correspond to the exhaustion of the deep source or the obstruction of flow paths.

Evidence for both scenarios is given in previous studies about the Aluto-Langano geothermal field. The first one of clay cap swelling by freshwater infiltration is supported by studies of *Ayenew* (2003), who found evidence for a strong hydraulic link between the lakes Ziway and Langano based on isotope studies. The groundwater flow follows active NE-SW tending faults and fractures that partially intersect the Aluto volcanic complex and is driven by the potential gradient between Lake Ziway (1636 m.a.s.l.) and Lake Langano (1582 m.a.s.l.). Isotope studies of rift waters by *Rango et al.* (2010) confirm that the faults of the WFB facilitate a fast water circulation that feeds hot springs, groundwater and geothermal wells around the Aluto volcanic complex. They found direct evidence for lake water mixing in shallow wells that were drilled for geothermal gradient studies around Aluto, which supports the subsurface hydraulic connection between the lakes. A study of hot spring waters further reveals mixing of deep geothermal fluids with lake water and meteoric water. The reported mixing of fluids in the shallower part of the geothermal system reveals a dynamic hydrologic regime where changes in water chemistry are likely to occur and will lead to clay swelling and shrinking.

The second scenario of thermoelastic expansion is evidenced by analyses of well fluids and fluid inclusions, which report a continuous and ongoing dynamic evolution of the hydrothermal system with important mixing processes of fluids from shallow and deep sources that even affect the deepest part of the system. *Teklemariam et al.* (1996) found out that argillic alteration in the lateral outflow zone actually overprints and replaces a previous zone of propyllitic alteration. Trapping temperatures recovered from fluid inclusions exceed recent temperatures in the outflow zone by up to 170 °C indicating that a major change with significant cooling happened during the evolution of the geothermal system. This is confirmed by the occurrence of epidote in the outflow zone at temperatures below 250 °C in the wells LA-2, LA-4, LA-5 and LA-7, which is only formed at higher temperatures that must have existed previously (*Gianelli and Teklemariam*, 1993). On the opposite direct evidence for recent heating by fast upflow of hot fluids is found in the upflow zone tapped by wells LA-3 and LA-6. Here the in-hole temperatures are almost 100 °C hotter than *Valori et al.* (1992) concluded from studies of fluid inclusion trapped in hydrothermal alteration products in the same wells. Such an increase in temperature is very likely to implicate thermoelastic expansion within the volume penetrated by the hot fluids. *Valori et al.* (1992) explain the observed heating by recent intake of a high enthalpy fluid rising from greater depths with a temperature of at least 350 °C. Well LA-7, which is nowadays used as an injection well, is around 1.1 km west of the identified upflow zone. This well is affected by the inflow of cooler waters from a shallow aquifer that result in a temperature reversal and a depression from

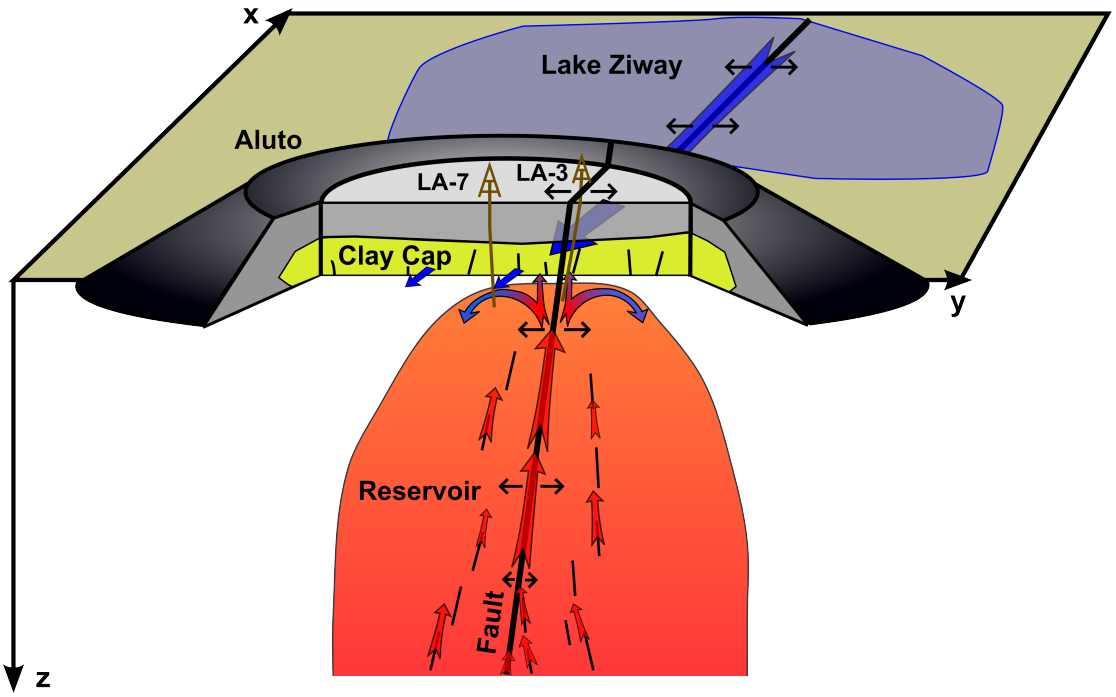

FIGURE 6.1: Sketch illustrating the origin of fluids, fluid circulation and mixing that may lead to the observed unrest. Red arrows indicate upwards flow of deep hot fluids, blue arrows show the lateral infiltration of water from Lake Ziway into the clay cap along opening faults. Hot fluids lead to thermoelastic expansion in the upper part of the reservoir, cooler fluids lead to clay cap swelling in the outflow zone. Well LA-7 is drilled into the outflow zone where hot fluids mix with cooler fluids of the upper aquifer, LA-3 is drilled into the hot upflow zone.

225 °C at 800 m depth to 125 °C at around 2000 m depth (*Gianelli and Teklemariam*, 1993). The huge differences in the hydrothermal regime between neighboring wells LA-3, LA-6 and LA-7 illustrate the complexity of the flow pattern and the dynamics of the hydrological system at Aluto. Complex fluid mixing processes have been reported in numerous hydrogeochemical studies (*Gianelli and Teklemariam*, 1993; *Teklemariam et al.*, 1996; *Pürschel et al.*, 2013): the common conclusion is that all of the present day well fluids are immature waters with none of them being in full equilibrium with the host rock. Significant mixing takes place over a wide area in the geothermal field with dilution factors defining the ratio between shallow and geothermal waters of up to 10 in the outflow zone. Mixing even affects the deep hottest part of the reservoir where a deep running fault system allows migration and interaction of fluids from a deep thermal reservoir with meteoric water from shallower sources. The described circulation of fluids geothermal fluids is illustrated in Fig. 6.1.

We believe that the reported fluid driven dynamics in the hydrologic regime of the geothermal field might trigger the kinematic mechanisms of clay swelling and thermoelastic expansion respectively shrinking and will consequently result in the observed cyclic surface deformations.

Chapter 7

Summary and outlook

During the MT fieldwork from January to March 2012 we succeeded to measure MT data at 45 sites covering the extend of the Aluto-Langano geothermal field with a good site coverage in the center of the main deforming region. By remote reference processing of the recorded electric and magnetic time series I obtained an overall high quality of the responses. At most sites transfer functions are smooth over the whole period range from $10^{-3} - 10^{3}$ s and show only small uncertainties. A cloud plot of the apparent resistivities at all sites suggests that the responses are affected by static shift. Static shift effects can either arise from galvanic distortion due to small scale scatterers or from topography effects (*Jiracek*, 1990). In order to investigate the latter I conducted forward modeling studies with the result that topography effects can be excluded as cause for the observed scattering. To invert the MT responses in a fully 3-D manner I used the ModEM code (e.g. *Kelbert et al.*, 2014). This code can model galvanic distortion effects by introducing layers with a scattered conductivity distribution in the shallow part of the model (*Tietze and Ritter*, 2013; *Meqbel et al.*, 2014) and it can account for topography. I performed numerous inversion runs inverting for off-diagonal impedance tensor elements only and for the full impedance tensor. These tests revealed that the main recovered resistivity structures in the model appear as stable features independent from data selection and different model discretizations I used. The obtained 3-D electrical resistivity distribution under Aluto corresponds well with the expected resistivities of the conceptual high enthalpy model (*Johnston et al.*, 1992). The conductive clay cap is located down to depths of ~ 1.5 km and overlies the resistive propyllitic upflow zone as confirmed by the well data (e.g. *Gizaw*, 1993; *Teklemariam et al.*, 1996). In such a high enthalpy geothermal system the electrical conductivity is mainly controlled by surface conductance of hydrothermal alteration minerals that are present in the system. The clay cap could not be identified south of Aluto, where only a thin shallow conductive layer is found, which is most likely related to a groundwater aquifer fed by saline water of Lake Langano. The 3-D resistivity models show no distinct electrically conductive structures below the resistive upflow zone at depths > 7 km, as one would expect if a

magmatic chamber with presence of melt would exist under Aluto.

Based on these results I conclude that there is no active magmatic system under the Aluto volcanic complex and the source of unrest is most likely related with hydrothermal system rather than with a magmatic system (*Biggs et al.*, 2011). As possible mechanisms resulting in cyclic surface deformations I suggest processes of thermoelastic expansion (*Bonafede*, 1991; *Troiano et al.*, 2011) and clay swelling (*de Siqueira et al.*, 1999; *Xu et al.*, 2006) triggered by the complex and dynamic fluid flow within the reservoir with mixing of shallow and deep fluids. The dynamics of the fluid flow are driven by seismic activities with permanent formation and obstruction of flow paths related to the active fault system of the WFB intersecting the volcanic complex (*Saibi et al.*, 2012). Major changes over time in the hydrothermal regime of the geothermal system, that support the suggested mechanisms, have been reported before, mainly in studies during the nineties (e.g. *Valori et al.*, 1992; *Teklemariam et al.*, 1996). However, we have no recent data that could be compared with the observed uplift events in 2004 and 2008.

A forward model to predict the tippers at Aluto suggests that their observed behavior is mainly explained by a conductor at lower crustal depths along the SDFZ 40 km west of Aluto and by a resistive lithosphere under the Somalian plate. This conductor corresponds to a seismic low velocity zone (*Bastow et al.*, 2011; *Kim et al.*, 2012) and evidence regarding its existence was already found in a previous MT study (*Whaler and Hautot*, 2006). However, so far no MT data have been measured at the SDFZ itself, which is why there is no information about the local resistivity distribution and the exact location, shape and extend of the proposed conductor. Nevertheless I conclude from the MT data that the main occurrence of magma and melt in the Lake District of the MER is prevalently at lower crustal depths along the SDFZ west of the main rift axis and not at the seismically active faults along the central rift axis.

In a next step we would like to compare the results of the MT study with the outcomes of the other multidisciplinary studies that were conducted at Aluto within the project ARGOS. The main aims are to construct a consistent image of the processes within the hydrothermal system and to further investigate the apparent absence of an active magmatic system as revealed by this study.

Our study shows the importance of making a regional resistivity study in the rift valley. Understanding the plumbing system of the volcanoes in the MER and the nature of the proposed deep conductor underneath the SDFZ could play a major role in getting a clear picture of the magmatic evolution and the thermal regime in the MER. Important new scientific findings about the MER are expected within the next years as outcome of *RiftVolc* – a NERC-funded project, which started in September 2014 and that aims to investigate the past and current rift volcanism in the MER.

Appendix A

Survey information

A.1 Site locations

Table A.1: Locations of measured MT sites at the Aluto-Langano geothermal field.

Site	Date	ADU	Latitude	Longitude	Altitude
M 1	26.01.12	059	07:47:38.34	38:46:23.90	1908
M 2	27.01.12	058	07:47:26.62	38:47:02.55	1897
M 2B	11.03.12	058	07:47:26.62	38:47:02.55	1897
M 3	27.01.12	059	07:47:58.35	38:47:02.50	1890
M 4	28.01.12	059	07:47:59.31	38:47:38.53	1887
M 5	28.01.12	125	07:47:51.43	38:45:49.12	1959
M 6	30.01.12	058	07:48:24.85	38:47:40.60	1942
M 7	31.01.12	059	07:47:12.34	38:48:04.63	1966
M 8	01.02.12	059	07:47:16.7	38:48:36.93	2010
M 9	01.02.12	058	07:47:37.83	38:48:24.54	1945
M 10	02.02.12	059	07:47:15.57	38:49:06.71	2022
M 11	02.02.12	058	07:46:40.83	38:48:36.54	2031
M 12	03.02.12	059	07:46:02.70	38:48:29.40	2071
M 13	03.02.12	125	07:45:28.25	38:48:40.56	1999
M 14	04.02.12	059	07:44:57.19	38:48:10.59	1874
M 15	04.02.12	125	07:44:32.70	38:47:37.55	1767
M 16	06.02.12	125	07:43:58.14	38:47:07.61	1642
M 17	06.02.12	059	07:44:32.73	38:47:37.62	1760
M 18	07.02.12	125	07:43:57.23	38:47:42.28	1671
M 19	07.02.12	059	07:46:42.99	38:48:57.26	2054
M 20	08.02.12	059	07:48:02.05	38:45:37.58	1962
M 21	08.02.12	125	07:48:34.14	38:45:38.16	1950

Continued on next page

Table A.1 – continued from previous page

Site	Date	ADU	Latitude	Longitude	Altitude
M 22	09.02.12	125	07:48:32.27	38:48:03.36	1894
M 23	09.02.12	059	07:49:00.16	38:48:15.78	1774
M 24	10.02.12	059	07:49:00.25	38:48:15.76	1770
M 25	10.02.12	125	07:50:05.77	38:48:16.29	1681
M 26	14.02.12	059	07:47:03.24	38:46:26.70	2059
M 27	15.02.12	125	07:47:02.90	38:45:51.63	2105
M 28	15.02.12	059	07:46:44.17	38:45:52.11	2158
M 29	16.02.12	059	07:48:56.94	38:45:06.30	1959
M 30	16.02.12	125	07:49:08.64	38:45:51.64	1926
M 31	17.02.12	125	07:49:00.66	38:46:18.47	1929
M 32	17.02.12	059	07:48:38.59	38:46:18.27	1993
M 33	18.02.12	125	07:48:10.81	38:47:09.23	1890
M 34	20.02.12	059	07:43:57.96	38:46:36.64	1643
M 35	20.02.12	125	07:44:27.30	38:46:30.55	1701
M 36	21.02.12	125	07:43:58.88	38:46:02.73	1636
M 37	22.02.12	059	07:44:22.60	38:45:31.19	1670
M 38	22.02.12	125	07:44:22.25	38:44:57.96	1655
M 39	23.02.12	125	07:44:44.00	38:44:35.76	1671
M 40	23.02.12	059	07:44:58.37	38:43:56.40	1649
M 41	24.02.12	125	07:45:17.76	38:43:23.11	1653
M 42	24.02.12	059	07:44:35.15	38:48:03.30	1841
M 43	27.02.12	125	07:48:01.90	38:48:38.47	1952
M 44	28.02.12	125	07:46:38.31	38:47:56.81	2139
M 45	28.02.12	059	07:46:09.77	38:47:56.08	2250
M 46	29.02.12	125	07:47:38.34	38:46:23.90	1908
R 1		003	07:41:40.68	38:44:56.40	1596
R 2		003	07:41:53.73	38:45:14.93	1586
R 3		030	07:58:39.08	38:37:18.24	1838

A.2 Survey schedule

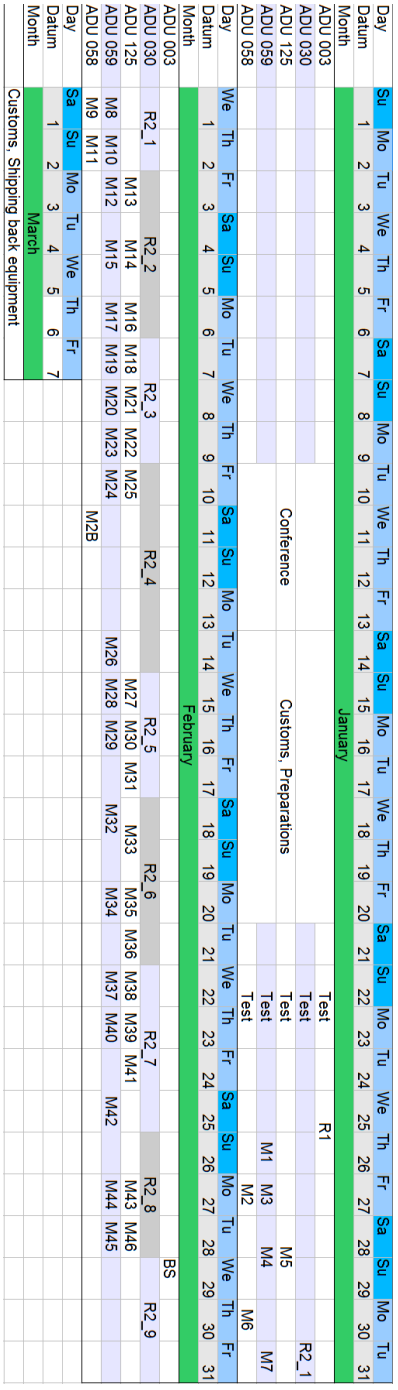

FIGURE A.1: Time table of MT survey.

A.3 Plots of observed responses

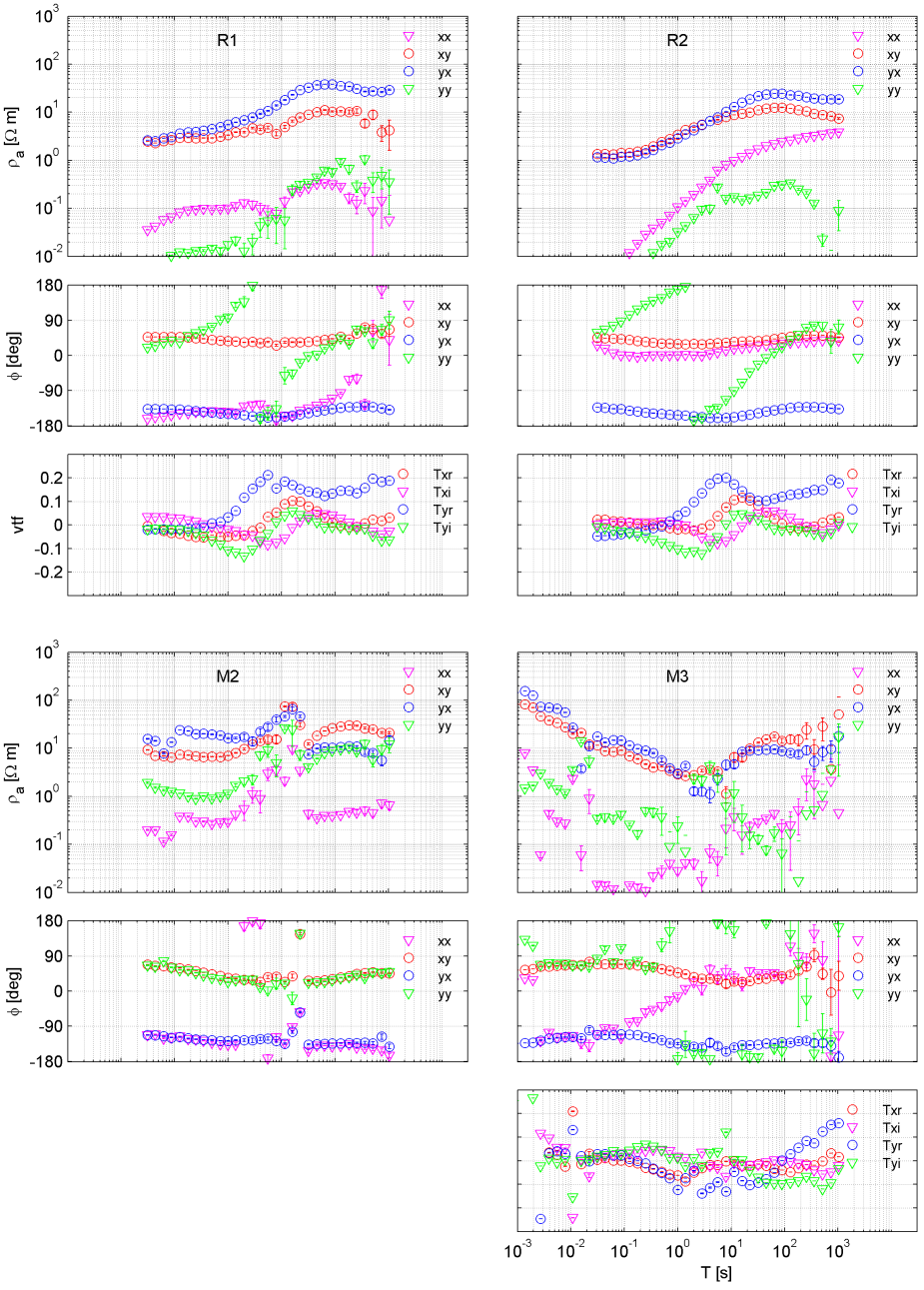

FIGURE A.2: Observed responses at sites R1, R2, M2 and M3.

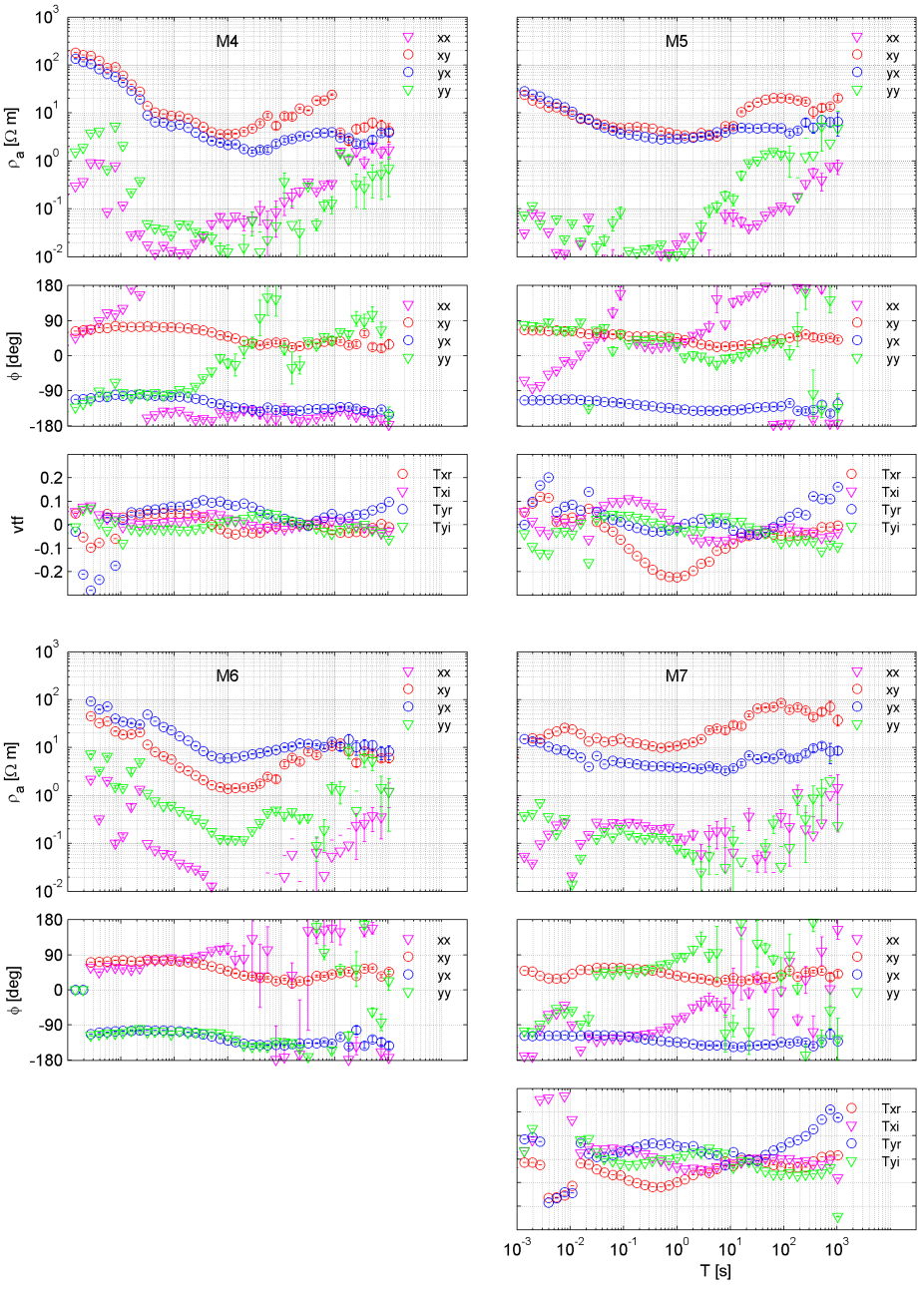

FIGURE A.3: Observed responses at sites M4 to M7.

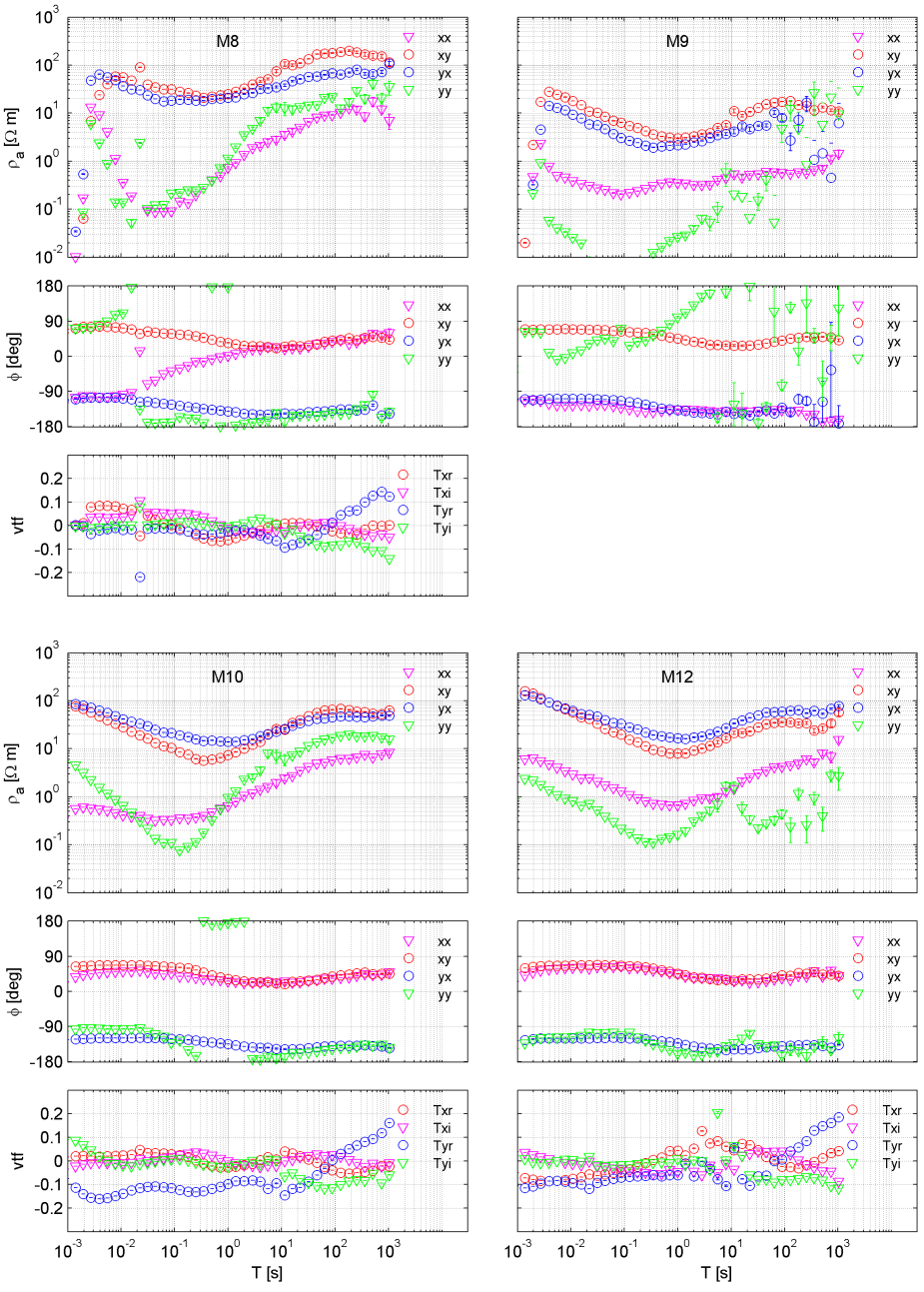

FIGURE A.4: Observed responses at sites M8 to M10 and M12.

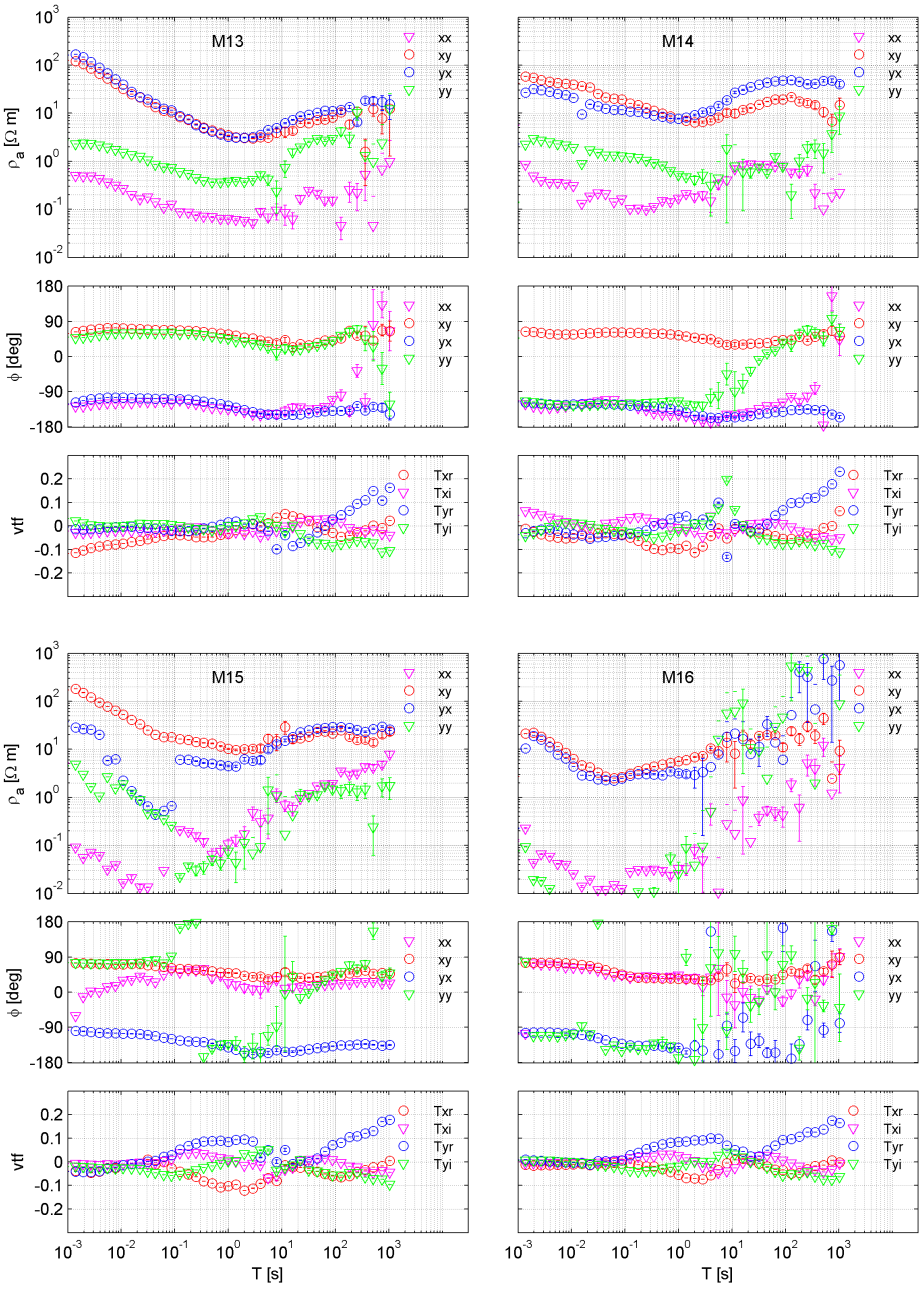

FIGURE A.5: Observed responses at sites M13 to M16.

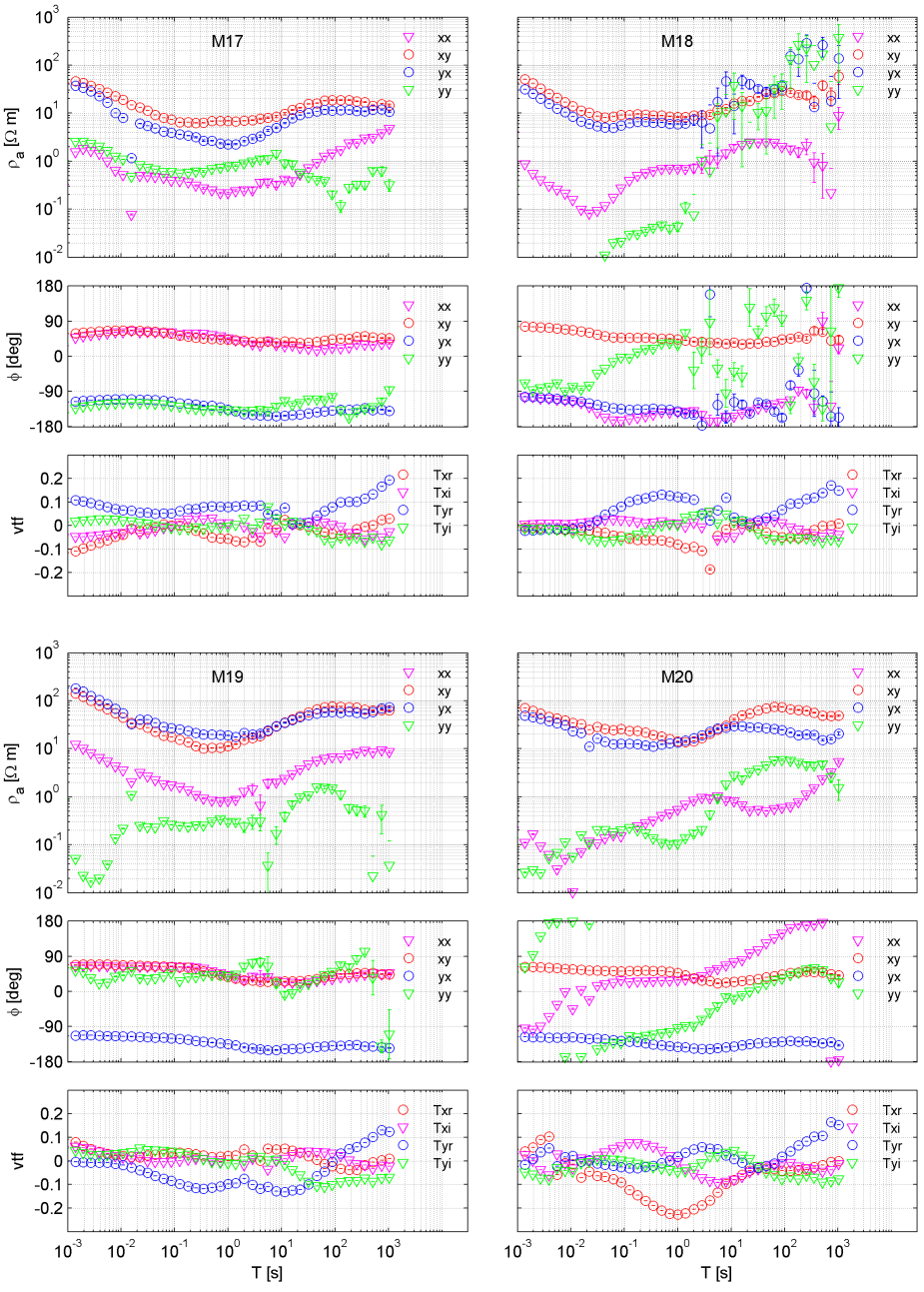

FIGURE A.6: Observed responses at sites M17 to M20.

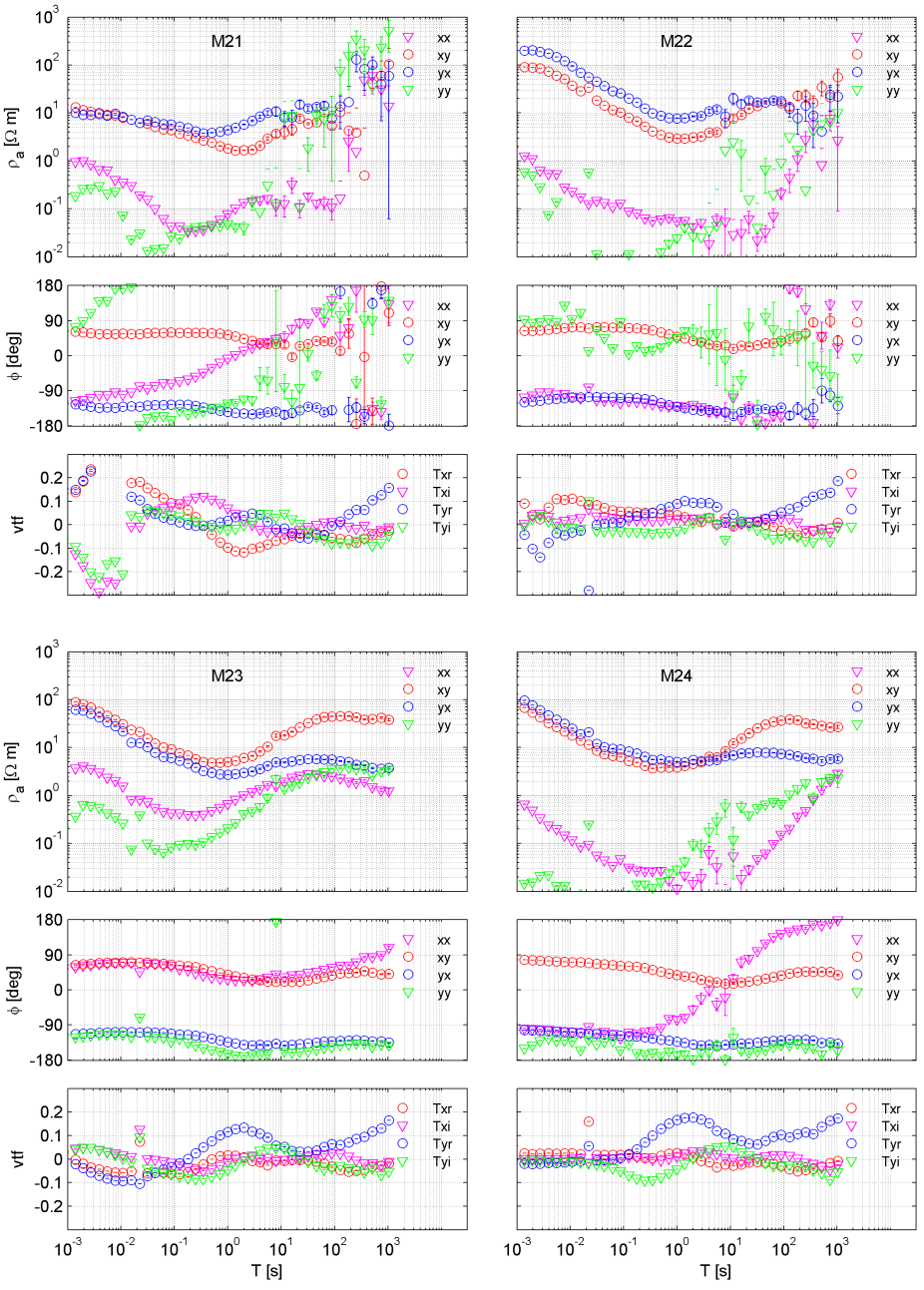

FIGURE A.7: Observed responses at sites M21 to M24.

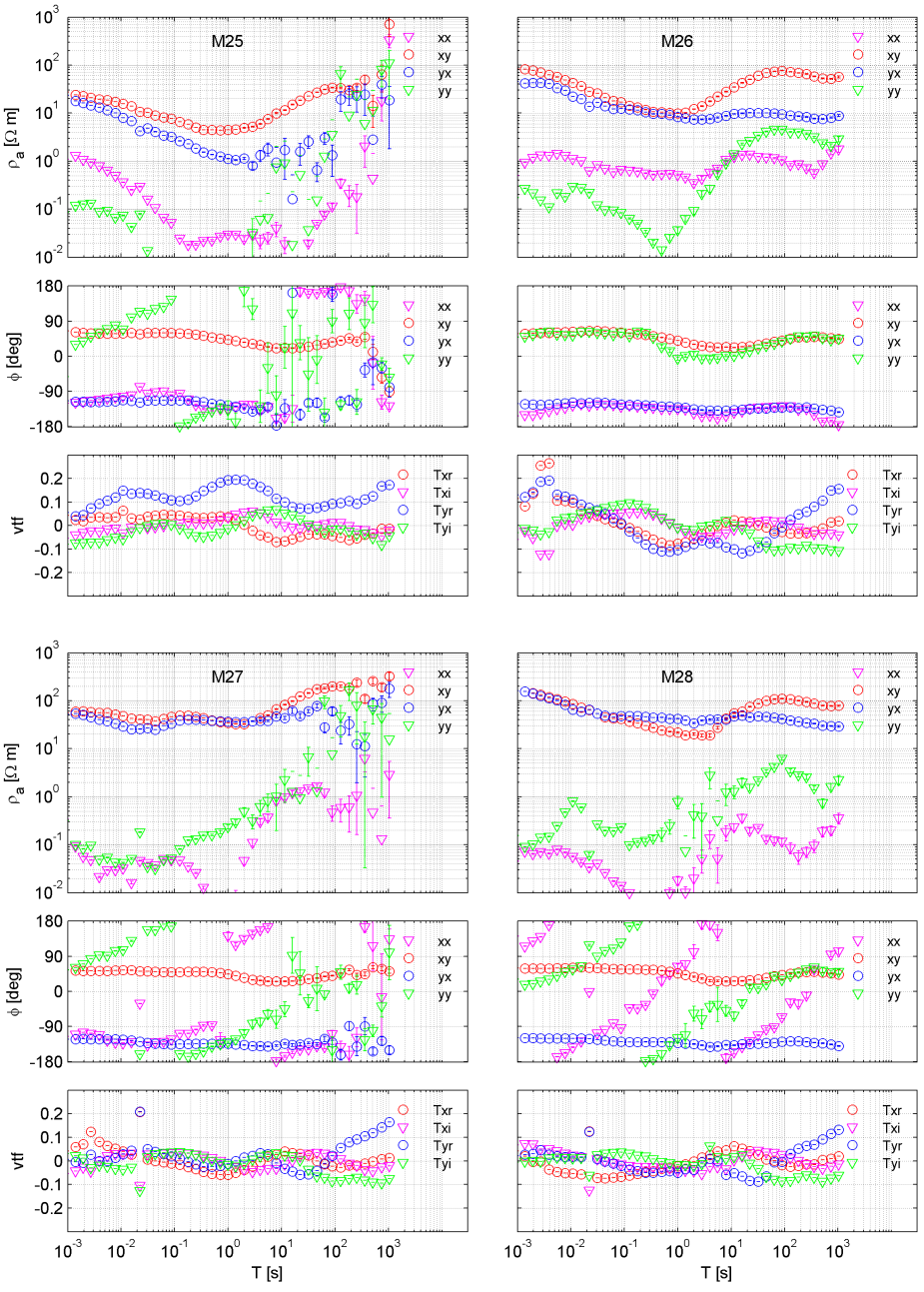

FIGURE A.8: Observed responses at sites M25 to M28.

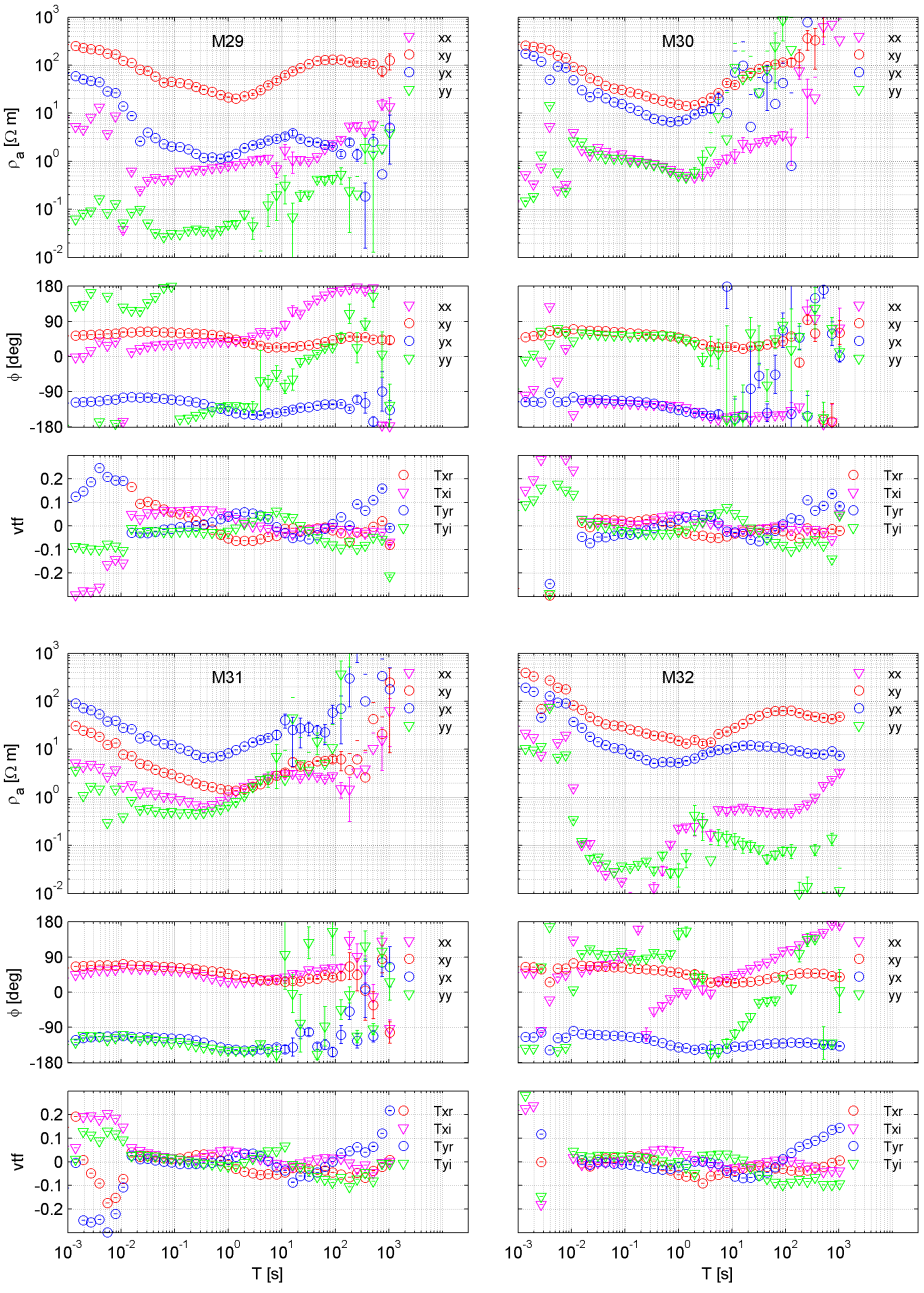

FIGURE A.9: Observed responses at sites M29 to M32.

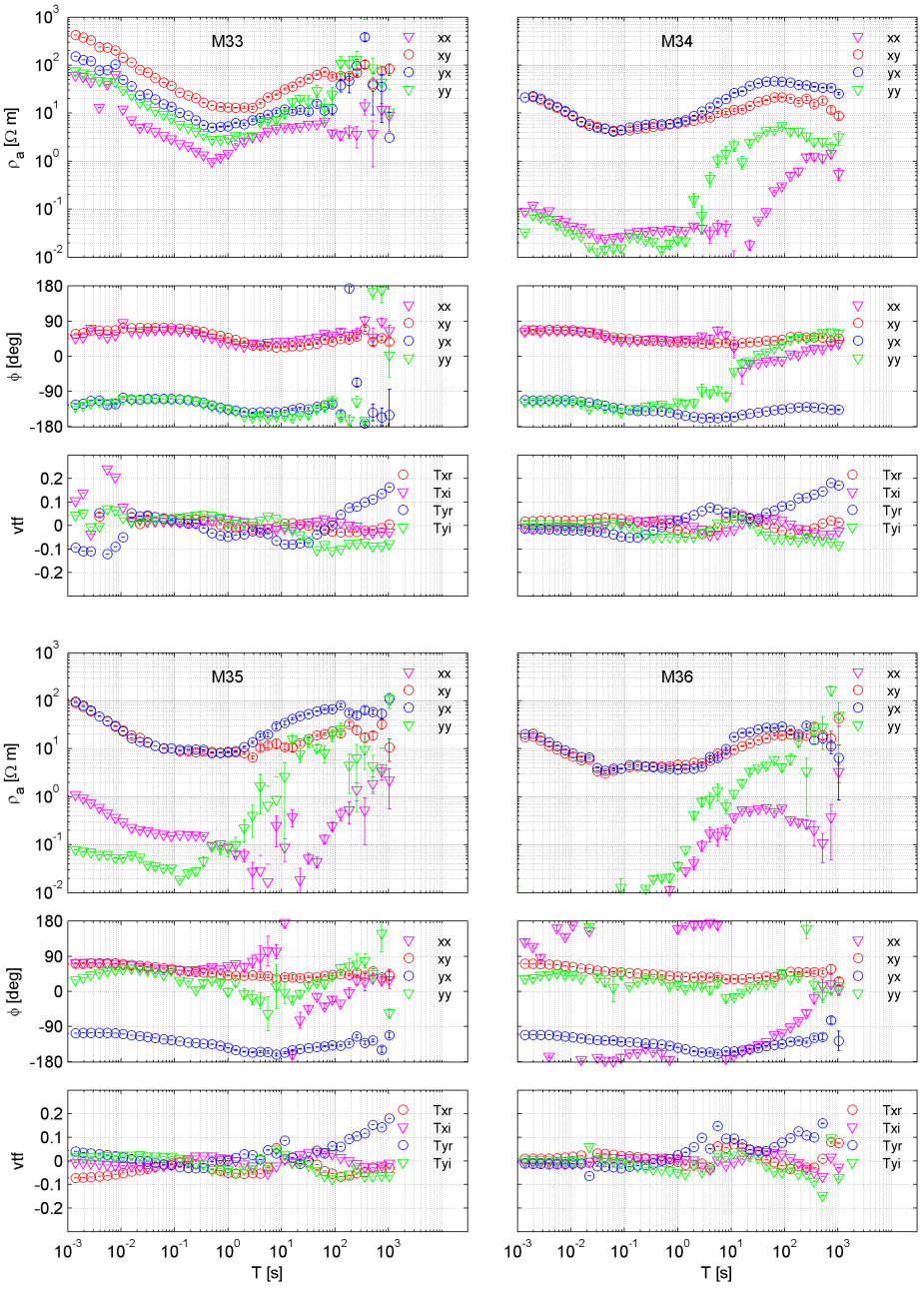

FIGURE A.10: Observed responses at sites M33 to M36.

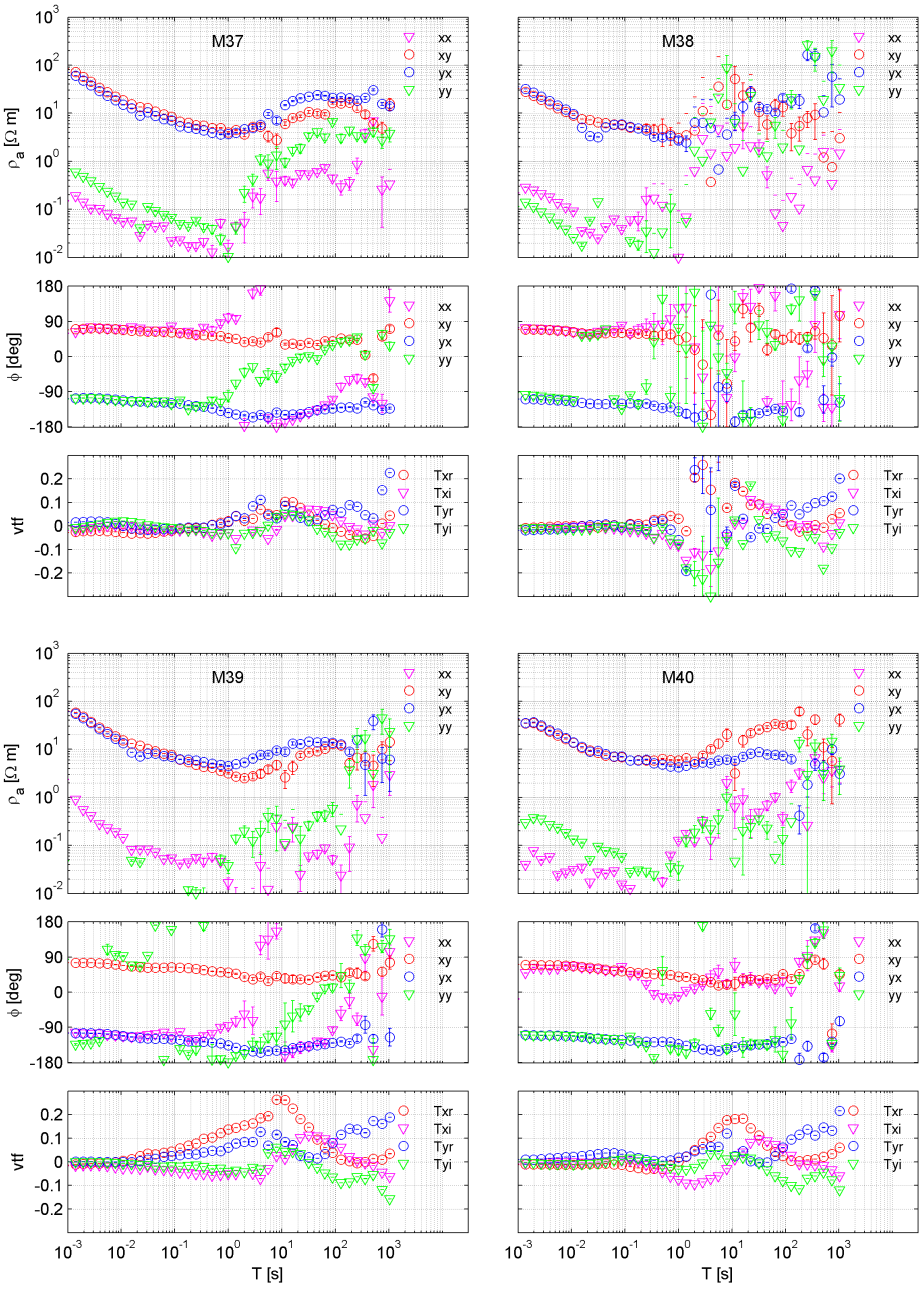

FIGURE A.11: Observed responses at sites M37 to M40.

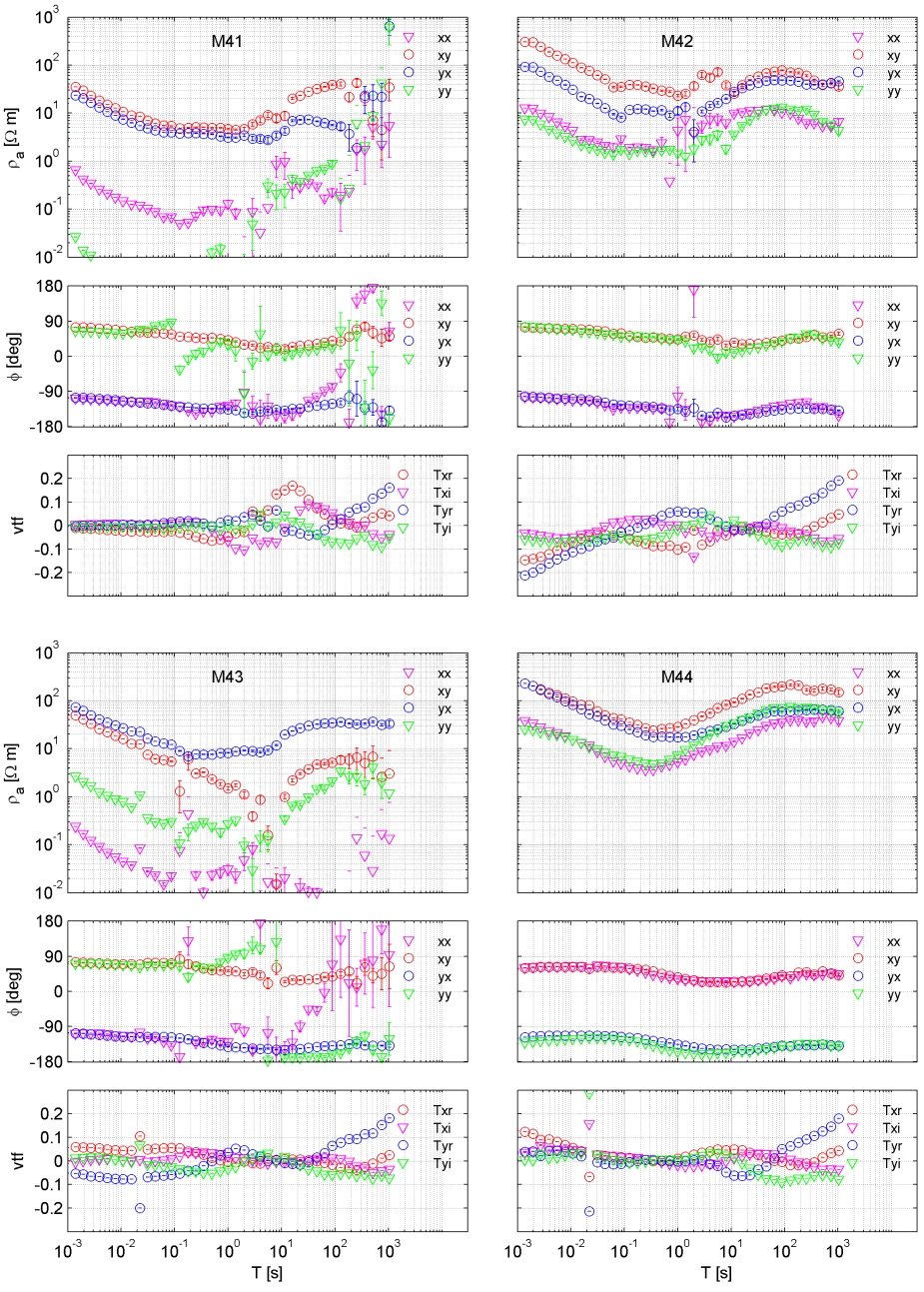

FIGURE A.12: Observed responses at sites M41 to M44.

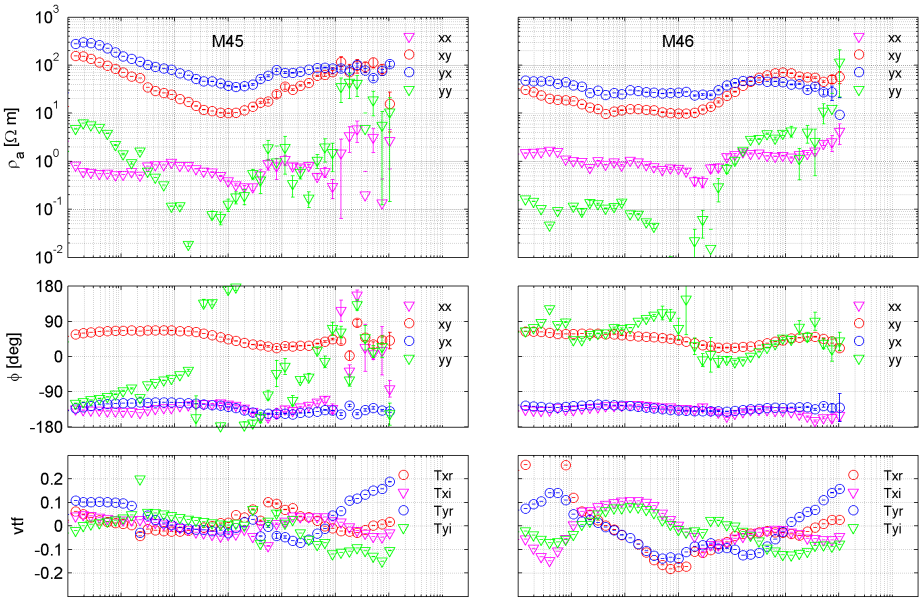

FIGURE A.13: Observed responses at sites M45 and M46.

Appendix B

Observed and predicted responses for ALS3ZFULL

This Appendix shows the comparison between observed and predicted responses of the inversion run ALS3ZFULL for the processed site and period selection.

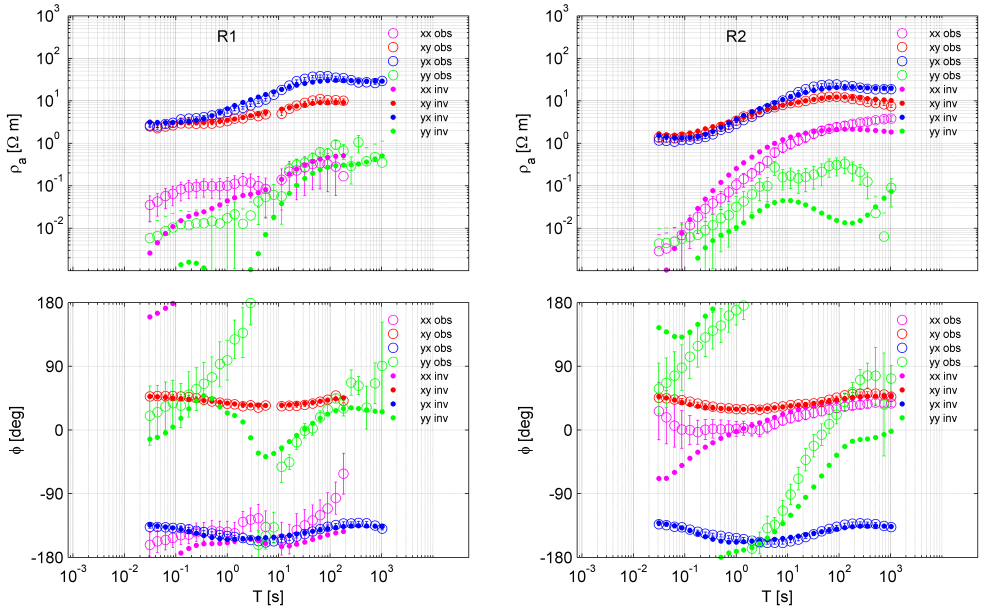

FIGURE B.1: Observed (empty plot symbols) and predicted (filled plot symbols) responses at site R1 and R2.

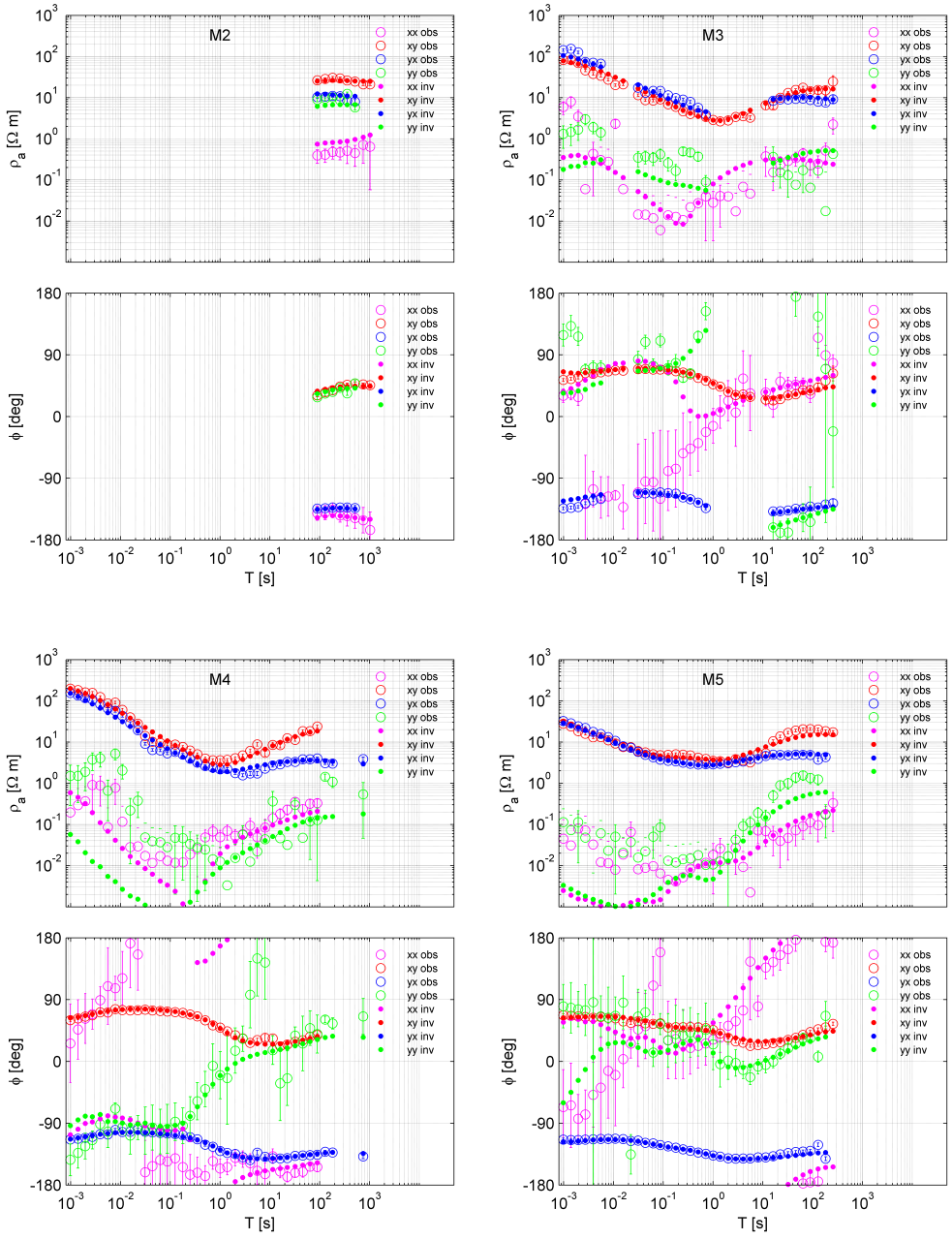

FIGURE B.2: Observed and predicted responses at site M2 to M5.

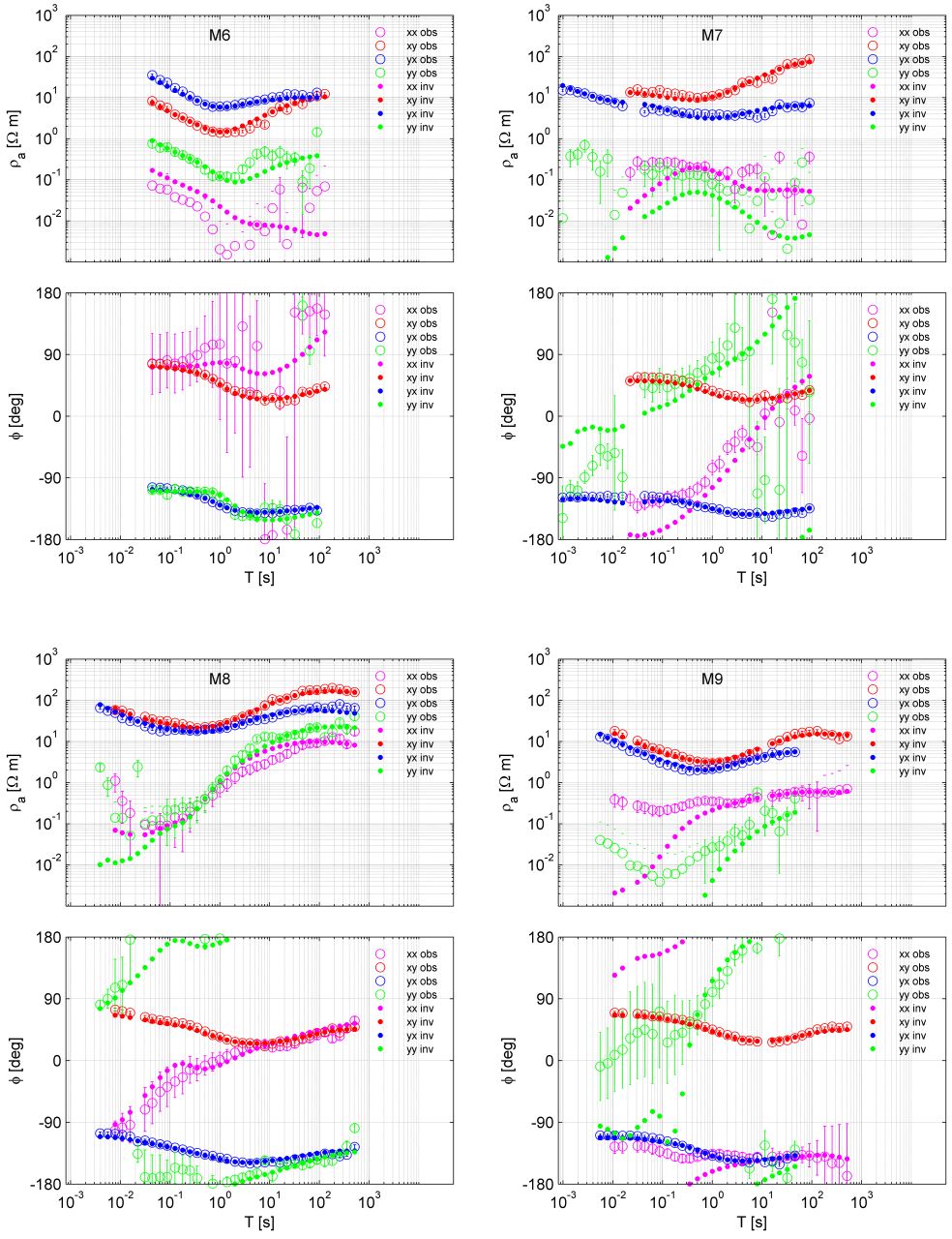

FIGURE B.3: Observed and predicted responses at site M6 to M9.

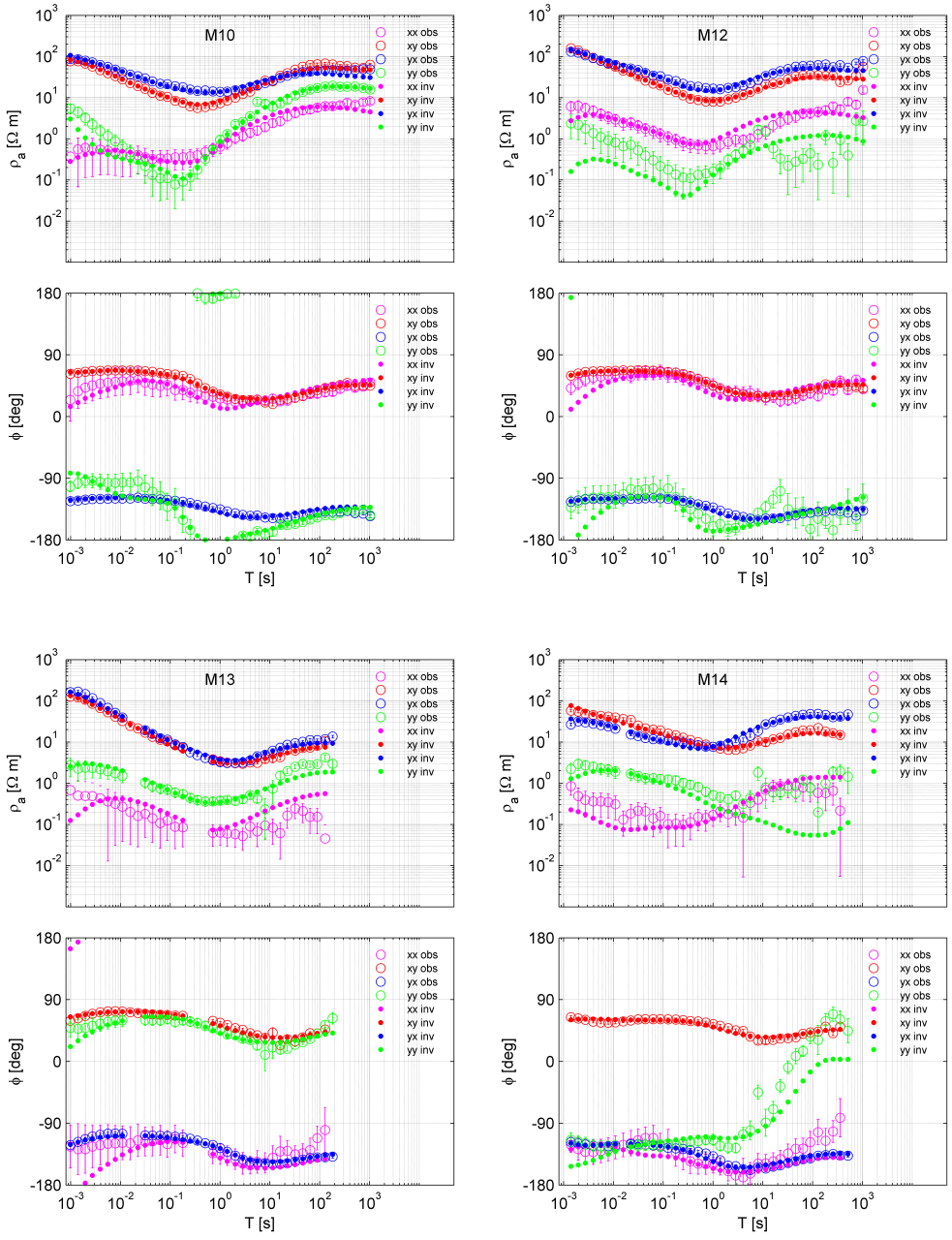

FIGURE B.4: Observed and predicted responses at site M10 and M12 to M14.

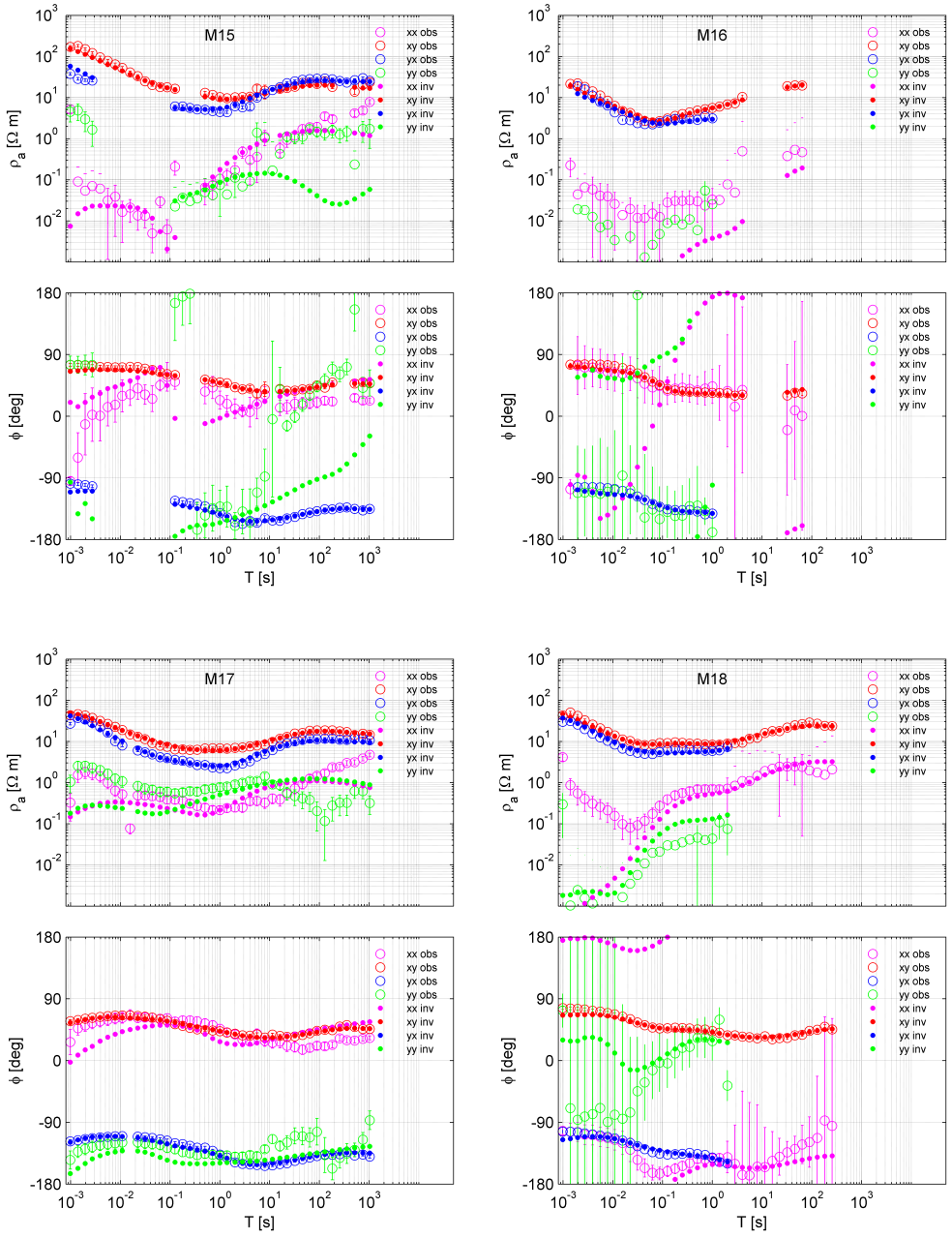

FIGURE B.5: Observed and predicted responses at site M15 to M18.

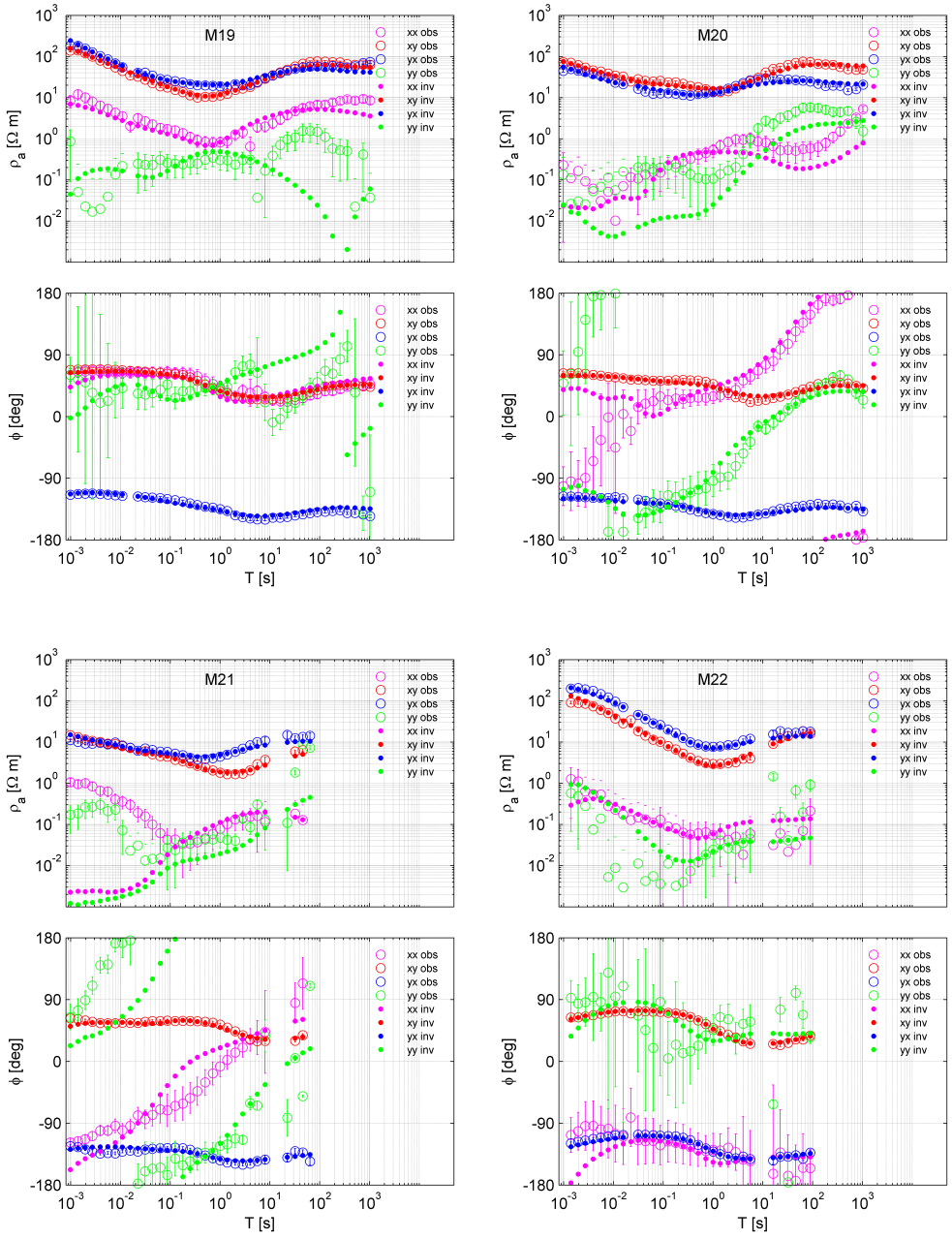

FIGURE B.6: Observed and predicted responses at site M19 to M22.

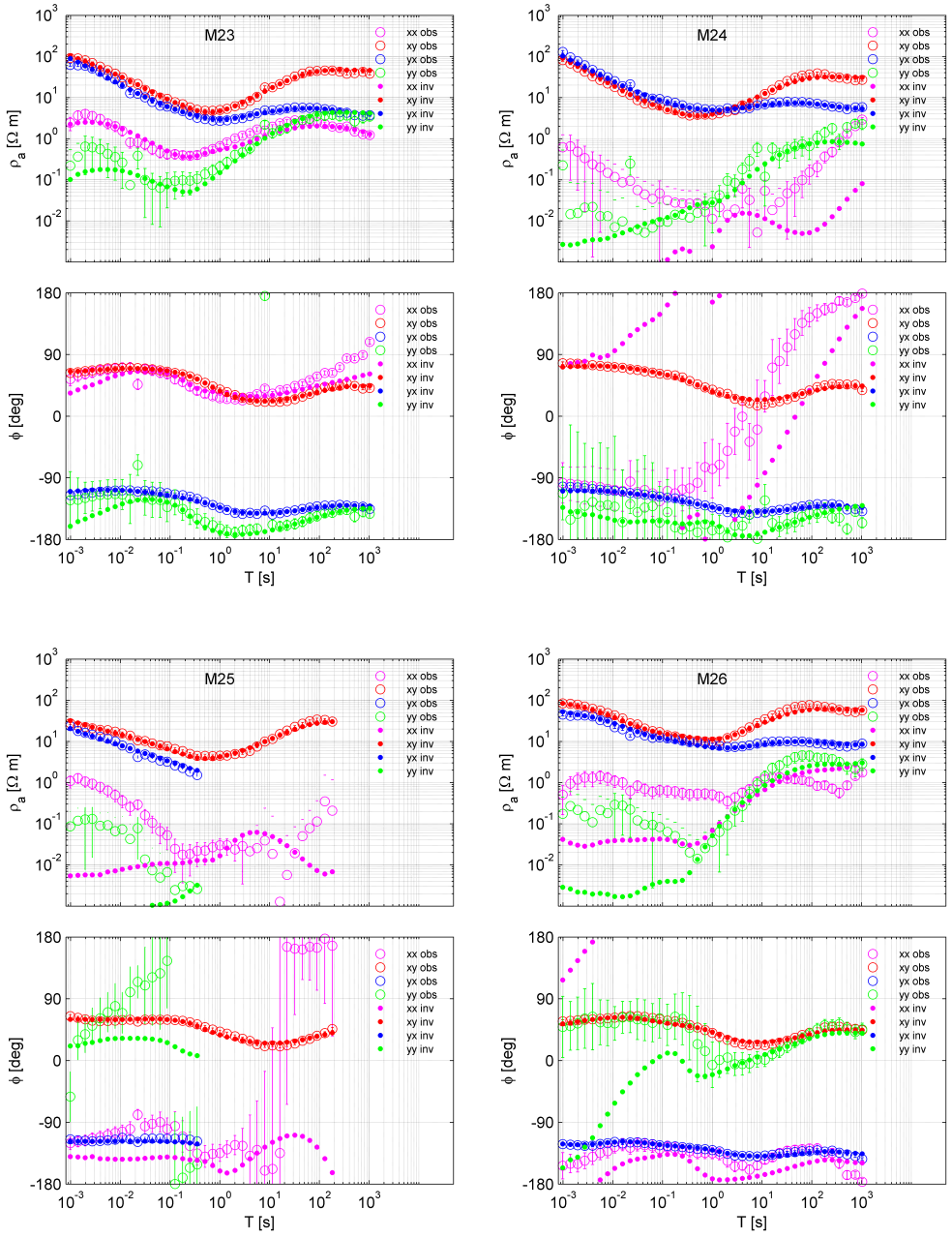

FIGURE B.7: Observed and predicted responses at site M23 to M26.

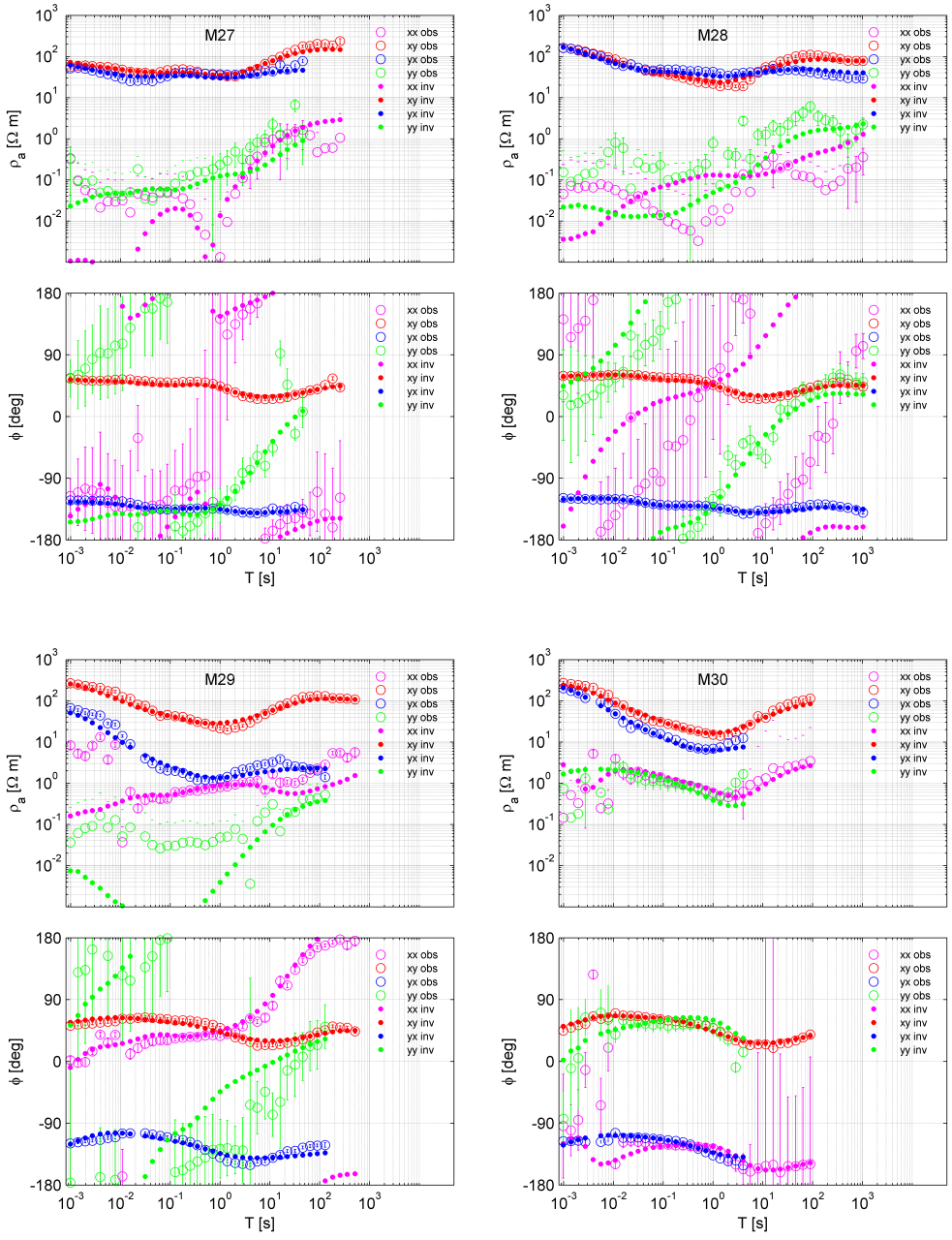

FIGURE B.8: Observed and predicted responses at site M27 to M30.

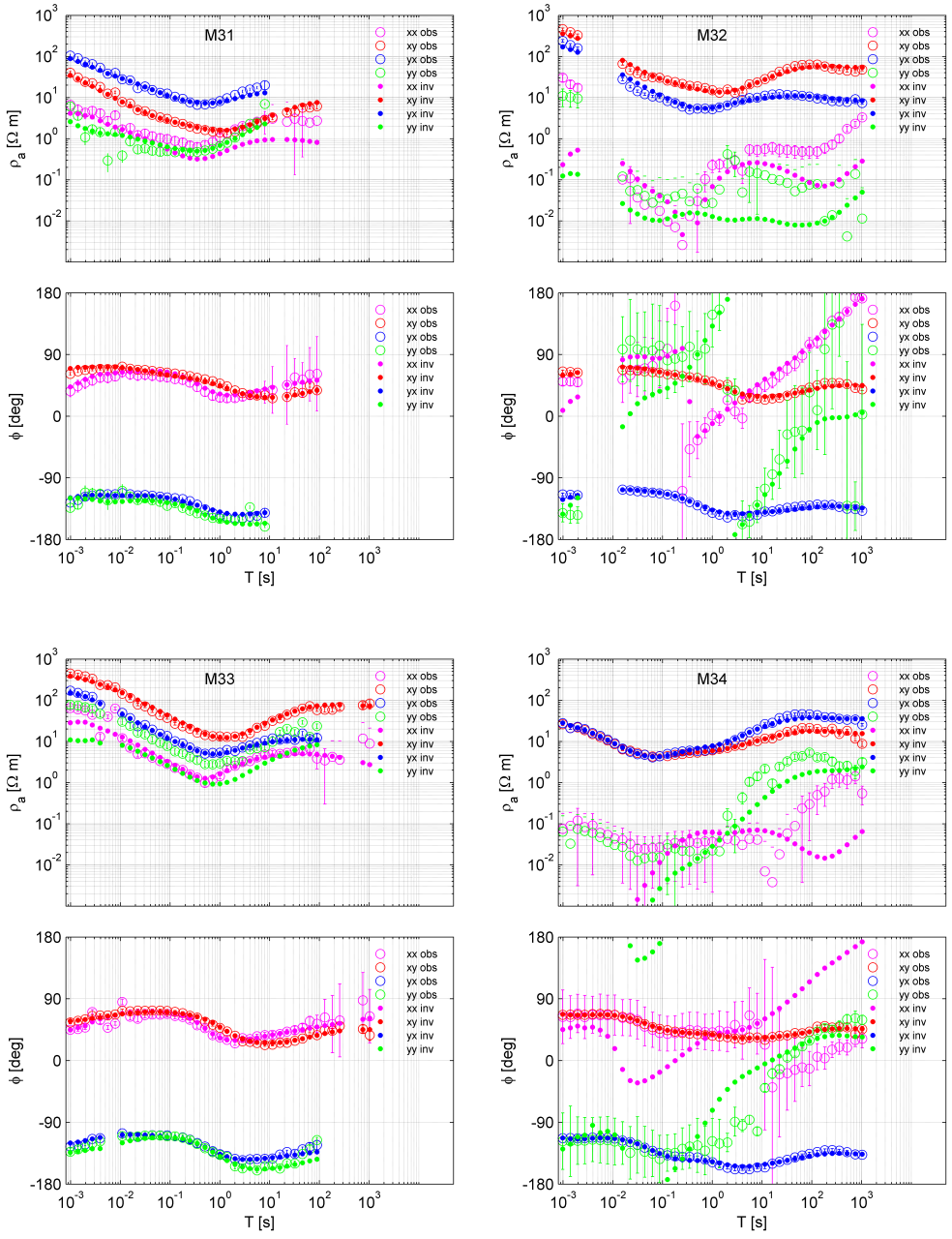

FIGURE B.9: Observed and predicted responses at site M31 to M34.

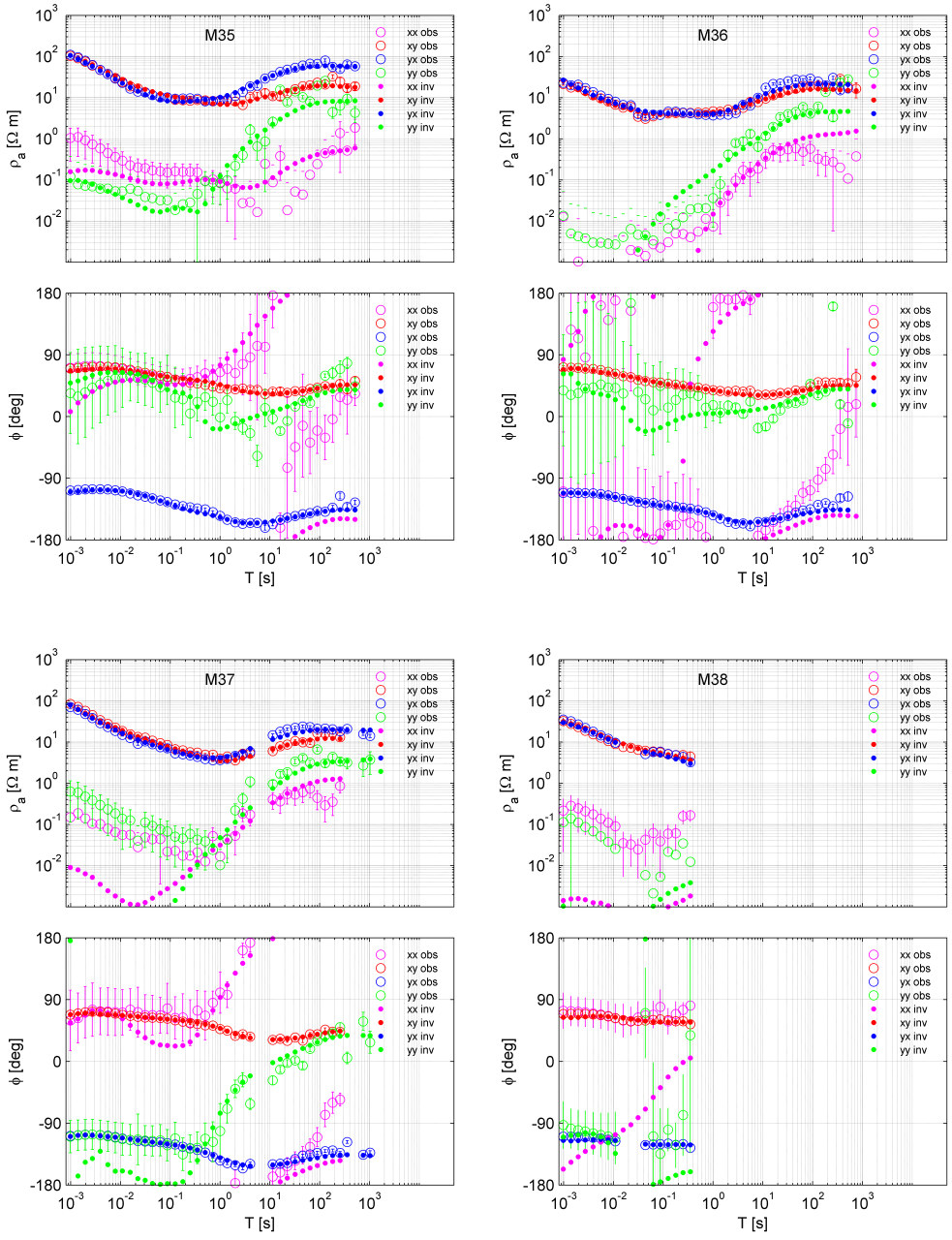

FIGURE B.10: Observed and predicted responses at site M35 to M38.

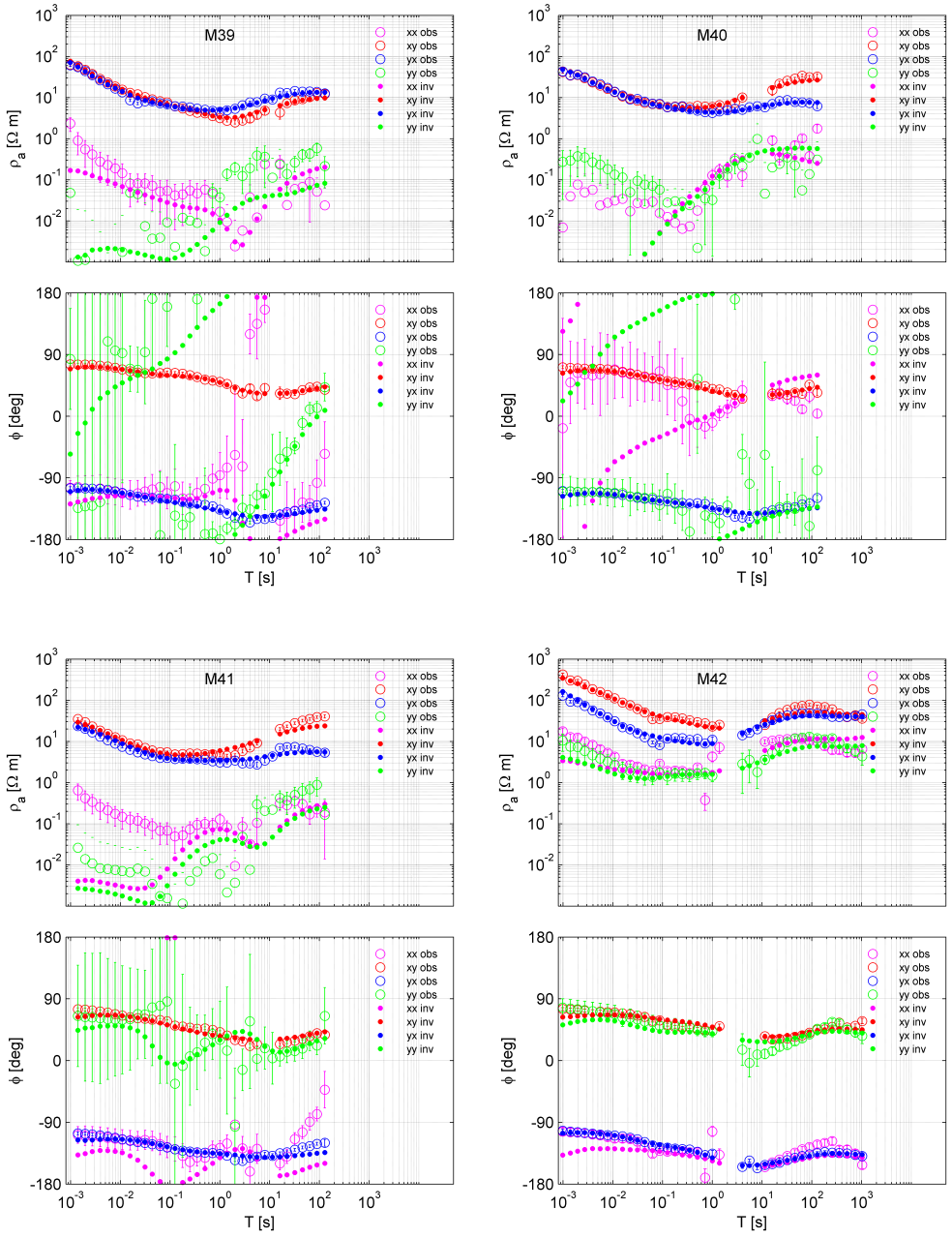

FIGURE B.11: Observed and predicted responses at site M39 to M42.

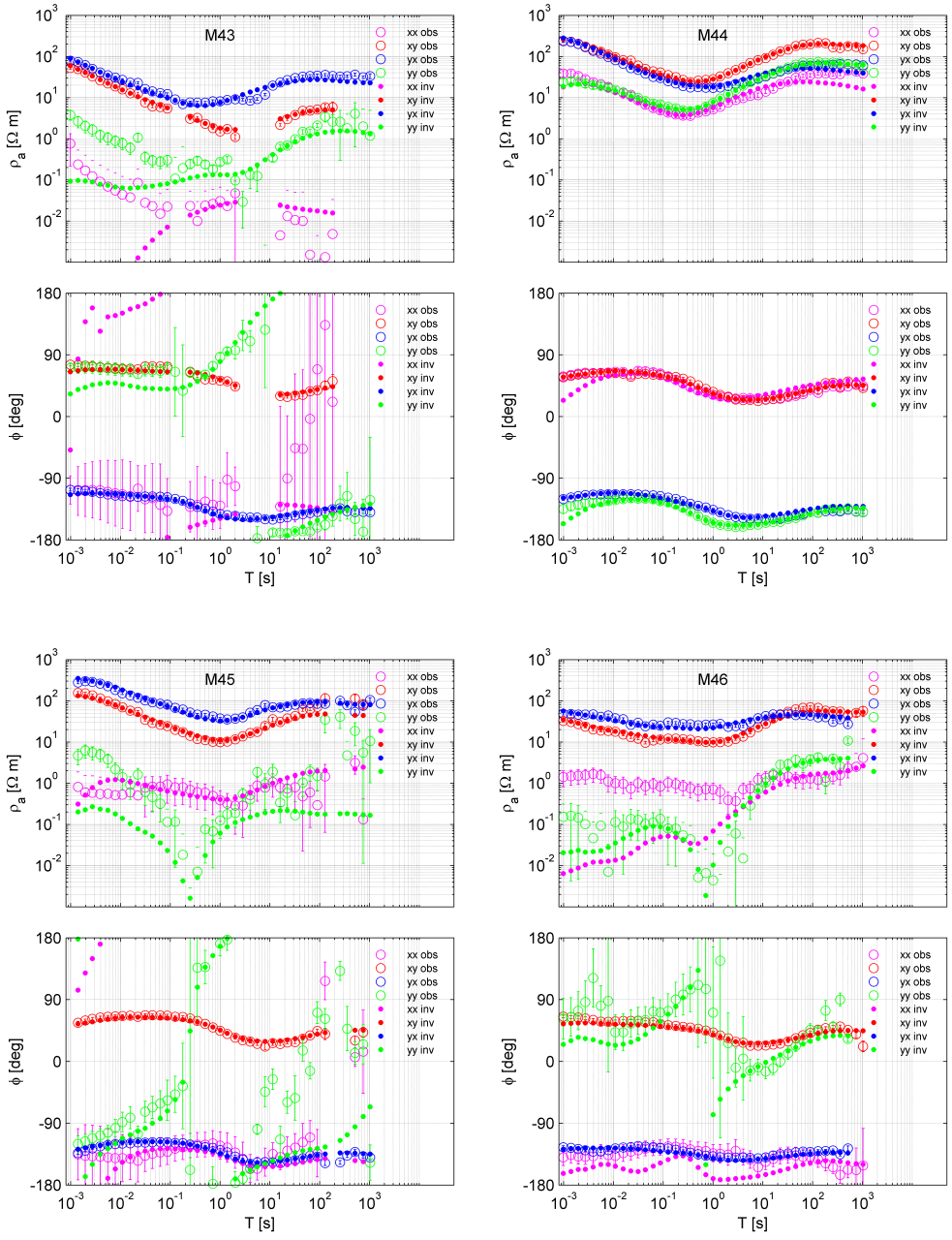

FIGURE B.12: Observed and predicted responses at site M43 to M46.

Appendix C

Permanent telluric observations at Gan observatory

C.1 Introduction

Long-period magnetic data from the global network of geomagnetic observatories have been used for global and semi-global 3-D EM inversions to recover the electrical conductivity distribution in the Earth's mantle (*Fukao et al.*, 2004; *Koyama et al.*, 2006; *Utada et al.*, 2009; *Kelbert et al.*, 2009; *Shimizu et al.*, 2010; *Tarits and Mandea*, 2010; *Semenov and Kuvshinov*, 2012; *Koyama et al.*, 2013). However, these studies are based on so-called C-responses relating the vertical to the horizontal magnetic field component in frequency domain (*Banks*, 1969). The underlying assumption about the source-field geometry of the C-response concept is that magnetic variations arise from a large-scale magnetospheric ring current. At the Earth's surface this magnetic field is described by the first zonal spherical harmonic in geomagnetic coordinates, which corresponds to a dipole structure. In equatorial regions the estimation of stable C-responses is challenging, here the vertical magnetic field is vanishing and signal to noise ratio is very small, which results is unstable responses (*Semenov and Kuvshinov*, 2012). Thus for equatorial observatories the C-response concept is hardly possible. The solution to this problem is to complement the magnetic with electric field measurements. This allows to obtain magnetotelluric (MT) responses which relate the horizontal magnetic and electric fields. Due to the source geometry both horizontal magnetic and electric fields are maximum in equatorial regions and thereby estimated MT responses are expected to be very stable. Thus by complementing geomagnetic observatories in equatorial regions by electric field measurements one can improve the knowledge about the mantle conductivity distribution in this problematic zone. If magnetic and electric observatory data are precisely

Table C.1: LEMI-417E technical parameters.

Frequency band (fourth-order LF filter)	DC-0.15 Hz
Measured range	±600 mV
Resolution	0.075 mV
Noise in the frequency band 0.03 - 0.3 Hz	$< 1\,\mu$V rms
Sample rate	1 Hz
Digital output	USB type B
Operating temperature range	-20 to 60 °C
Power supply	$+12^{+6}_{-3}$ V
Power consumption	< 0.8 W

sampled in 1 s intervals, short period MT responses can also allow to recover the electrical conductivity distribution in the crust and upper mantle. However, so far most observatories provide data only in form of minute means.

C.2 Instrumentation and setup

In September 2012 we complemented GAN geomagnetic observatory with a telluric measurement unit. This telluric unit provides accurate 1 s data of the horizontal electric field (**E**-field) at the observatory site. The **E**-field measurements are undertaken with a separate logger and streamed to the UNIX based PC, which controls the magnetic data collection. Like the magnetic data the electric data are collected at the Meteorological Office in Gan Airport and transmitted to Zurich. Note that GAN observatory is operated by ETH Zurich and now it is a part of the Intermagnet global network of observatories.

For the telluric data acquisition a 4-channel LEMI-417E[1] unit with GPS timing is used, the main technical parameters are listed in Table C.1. In the standard telluric setup the electric field is measured in two orthogonal directions, typically N-S and E-W. Four channels allow to measure the electric field in four horizontal directions or to do parallel measurements in the standard setup. Parallel measurements are useful in a sense to have one backup line in case one fails or to make comparison measurements with e.g. different kind of electrodes. Comparison measurements can be used to analyze and compare the long term behavior of different electrode types and to figure out which type is best suited for permanent observatory measurements. For the first installation in September 2012 we used only two channels with electric field measurements along N-S and E-W direction using two-chamber gel-type Pb-Pb-Cl-electrodes. The electrodes were fabricated at Oregon State University (contact person Prof. Adam Schultz). For a detailed description of the electrodes see Fig. C.1. The electrodes are buried in the ground at around 70 cm depth, as illustrated in Fig. C.3. This depth is already within the

[1] `http://www.isr.lviv.ua/products.htm`

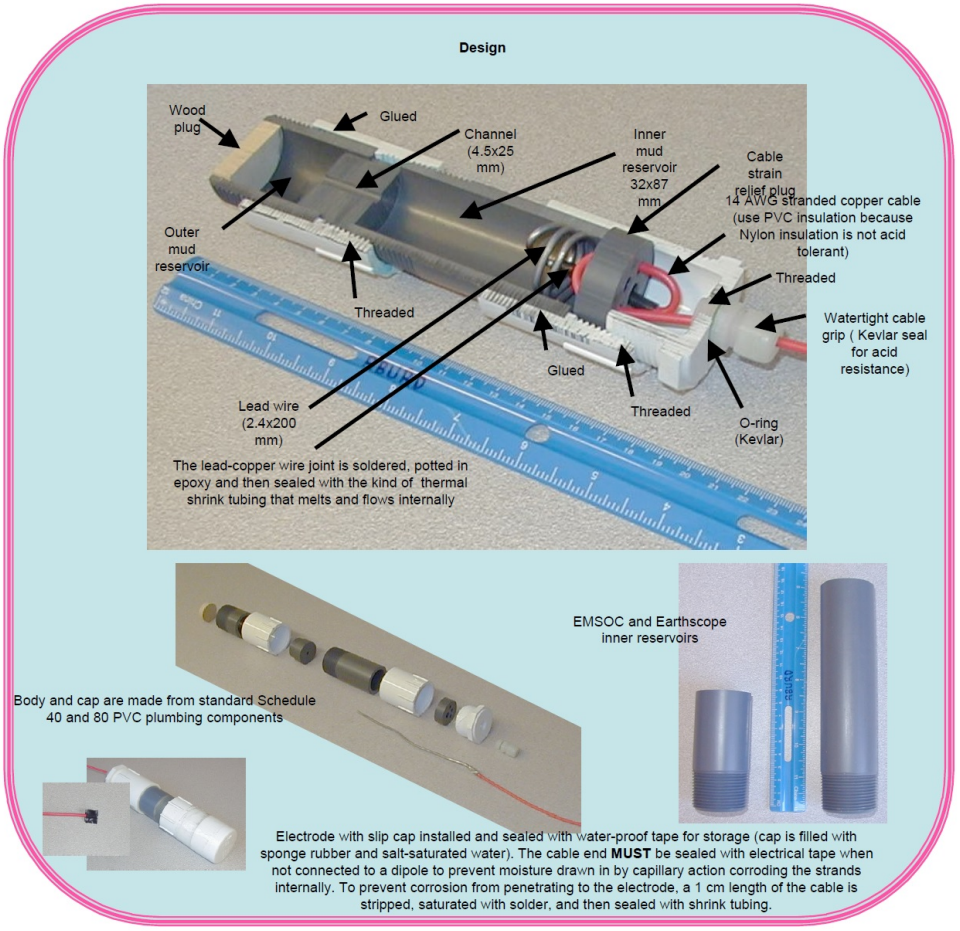

FIGURE C.1: Description of the Oregon Pb-Pb-Cl-electrodes.

freshwater lens of the island where temperature and moisture conditions are expected to be stable throughout the year. Such stable conditions are indispensable in order to ensure a stable telluric signal. For the connection between electrodes and logger a shielded coaxial cable of type RG-58 is used, the shield is connected to the same grounding like the logger at the electronic hut. With the use of a coaxial cable the influence of noise on the telluric signal is meant to be minimized. All cables between electrode location and electronic hut are buried 7-10 cm under ground. The electrode spacing in N-S (E_x) is 150 m and 200 m in E-W (E_y). Detailed electrode locations are given in Table C.2, for a map showing the approximate locations see Fig. C.2.

First problems in the signal of the N-S component occurred in early 2013 when the cable leading to the North electrode was cut by a mowing machine. However, it was repaired during a visit in February 2013. Problems occurred again in October 2013. During May 2014 we relocated the N-S telluric line and added an additional electrode setup parallel to the existing using a prototype of Ag-Ag-Cl electrodes fabricated at University of Münster (contact person Prof. Michael Becken). For 2014 electrode locations see Fig C.2.

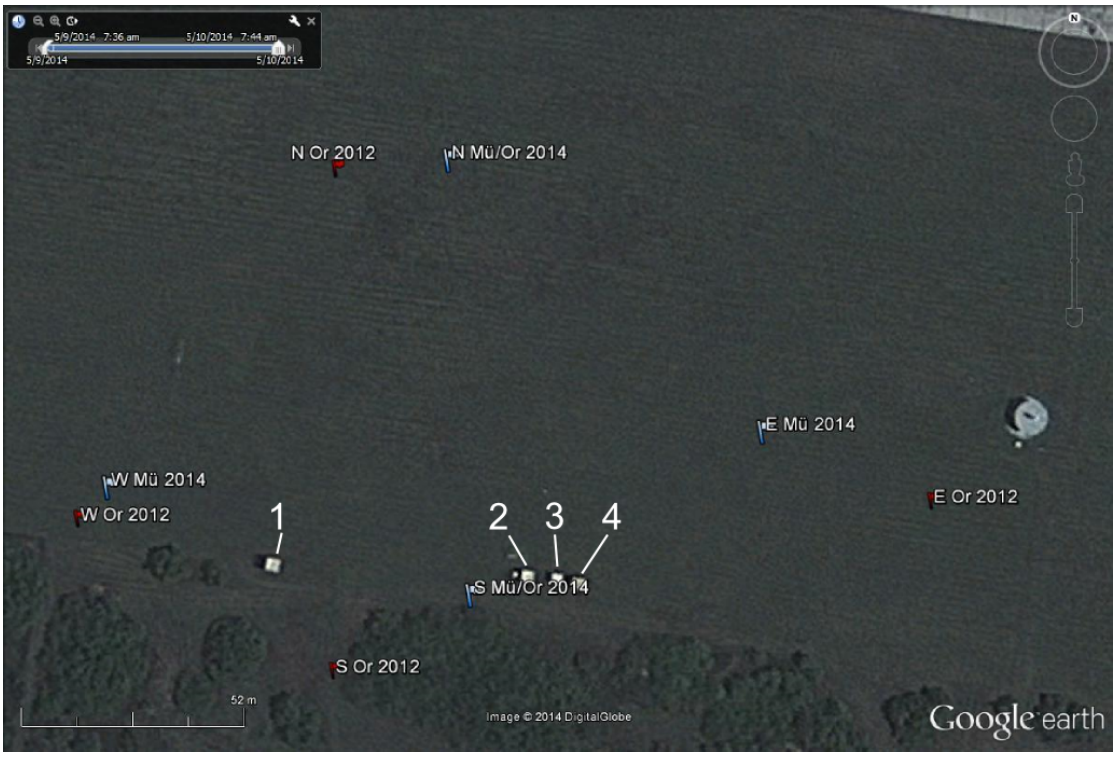

FIGURE C.2: Map with location of electrodes and year of installation. Or stands for Oregon electrodes, Mü for Münster electrodes. For details see Table C.2. Nr. 1 shows the location of the absolute hut, Nr. 2 – of the electronic hut, Nr. 3 – of the absolute hut and Nr. 4 – of the variometer hut.

TABLE C.2: Electrode locations for the 2013 setup using Oregon electrodes only (Or) and for the 2014 setup with additional installation of Münster electrodes (Mü) and relocated N-S line of the Oregon electrodes.

Electrode	Manufacturer	Year	Coordinates	Spacing
N	Or	2012 - 2014	−0.693761 °S, 73.154031 °E	150 m
S	Or	2012 - 2014	−0.694828 °S, 73.154031 °E	
E	Or	since 2012	−0.694469 °S, 73.155300 °E	200 m
W	Or	since 2012	−0.694507 °S, 73.153489 °E	
N	Or	since 2014	−0.693752 °S, 73.154300 °E	97 m
S	Or	since 2014	−0.694678 °S, 73.154300 °E	
N	Mü	since 2014	−0.693752 °S, 73.154300 °E	97 m
S	Mü	since 2014	−0.694678 °S, 73.154300 °E	
E	Mü	since 2014	−0.694450 °S, 73.154943 °E	159 m
W	Mü	since 2014	−0.694450 °S, 73.153553 °E	

C.3 Data

Figures C.4 and C.5 show representative telluric data in September 2013 and October 2013. The daily variations can be clearly seen in the plots. The fact that daily **E**-field variations along E_x are smaller regarding their amplitude than those along E_y reflects the dominating E-W oriented nature of the EEJ. The E_y component shows a significant drift of around $-70\,\frac{\mathrm{mV}}{\mathrm{km\cdot month}}$. It remains unclear whether the drift is caused by

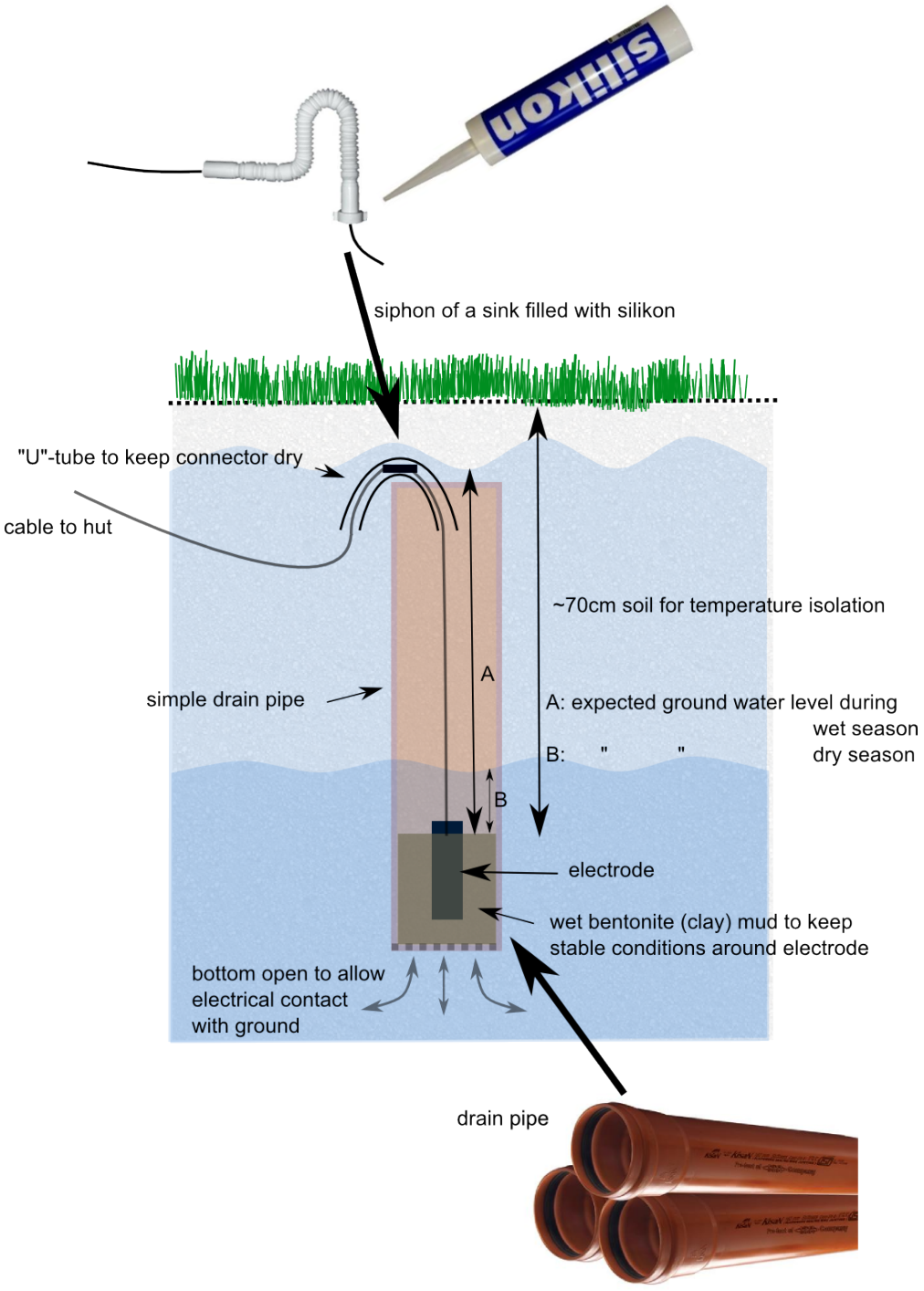

FIGURE C.3: Electrode setup.

a) changes in the subsurface self-potential, or

b) technical issues with the electrodes.

On the 14th of October 2013 a sudden drop in the Ex component occurred. Since then the Ex component was extremely unstable and data quality was no more acceptable, see Fig. C.5. This issue was solved during a visit in May 2014. We found out that the cable

leading from the electric hut to the southern electrode was cut during mowing activities in the wet and bushy area around the southern electrode. Here the cable was pushed to the surface in deep wheel ruts caused by the heavy mowing machines and ultimately cut. Hereafter we replaced the southern electrode out of the bushy area closer to the electronic hut, see Fig C.2, which results in a shorter N-S electrode spacing.

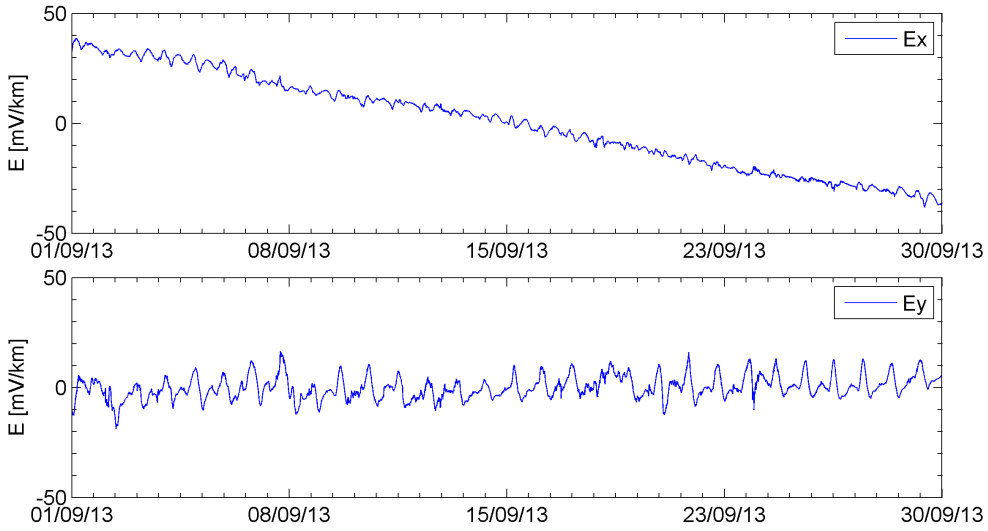

FIGURE C.4: Telluric data observed by Or electrodes for September 2013.

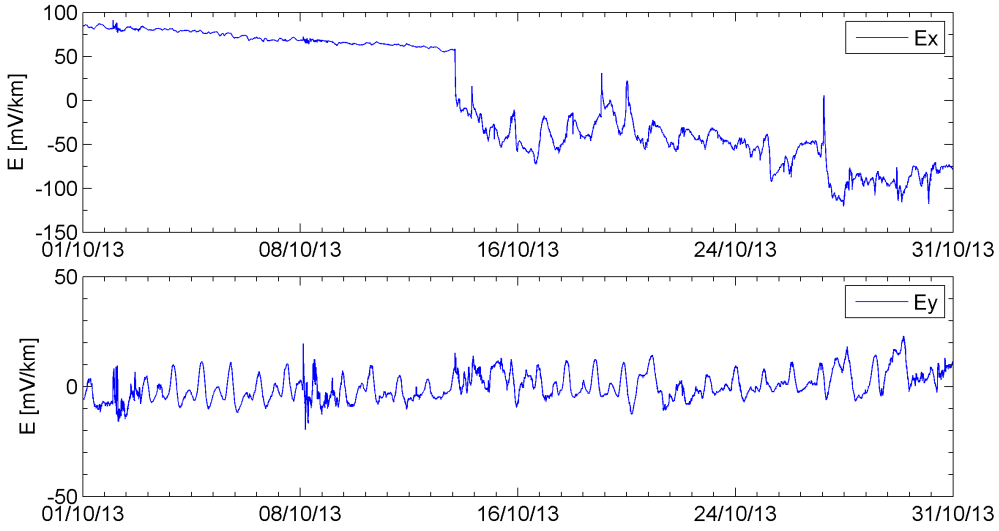

FIGURE C.5: Telluric data observed by Or electrodes for October 2013.

Data of the new setup installed in May 2014 are shown in Fig. C.6. It can be seen that the E_x component of the prototype Ag-Ag-Cl Mü electrode is extremely unstable and provides no acceptable data quality. Whereas the E_x component of the Or type electrodes is very stable over the whole period from June to September 2014. The E_y component of the Or type electrode remains relatively stable on the same level, the

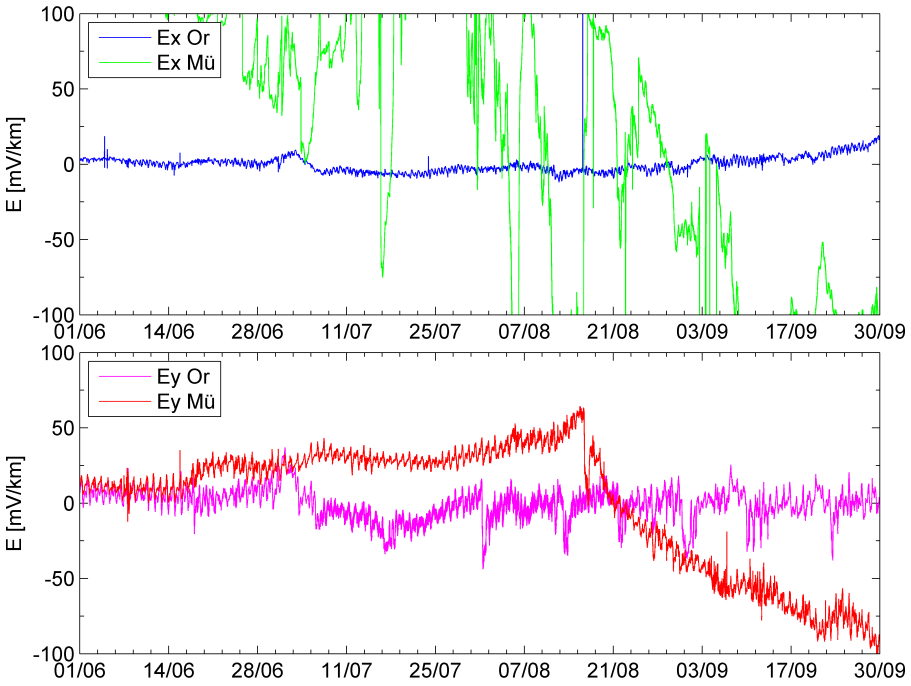

FIGURE C.6: Telluric data observed by parallel measurements of Mü and Or electrodes for June to September 2014.

corresponding component of the Mü type electrode is clearly affected by a large drift of around $-100\,\frac{\text{mV}}{\text{km}\cdot\text{month}}$, which does not appear in the E_y component of the Or type electrodes installed in parallel. This illustrates the difficulties in **E**-field measurements, further developments are needed in order to improve the Mü type Ag-Ag-Cl electrodes and to increase their long term stability.

The telluric data provided by the Or type Pb-Pb-Cl electrodes show that stable measurements are possible if the electrodes are installed carefully. However, further parallel tests using several sets of electrodes would be necessary in order to allow for a comprehensive comparison of high quality data.

C.4 Responses

In this section we show impedances and tippers estimated from magnetic and telluric data observed at Gan in order to provide an insight into the responses' quality and the effect of the unstable telluric line on the impedances. The responses were estimated using a Matlab processing tool by *Püthe and Kuvshinov* (2014) developed at ETH Zurich. All responses were estimated using the data collected in June 2014. Figure C.7 shows the estimated tippers. The tippers have a dominating real T_x component, which remains almost on the same level up to periods of $10^4\,\text{s}$. Compared to real T_x, the real T_y component is relatively small and rises slightly for periods larger than $10^3\,\text{s}$. At longer

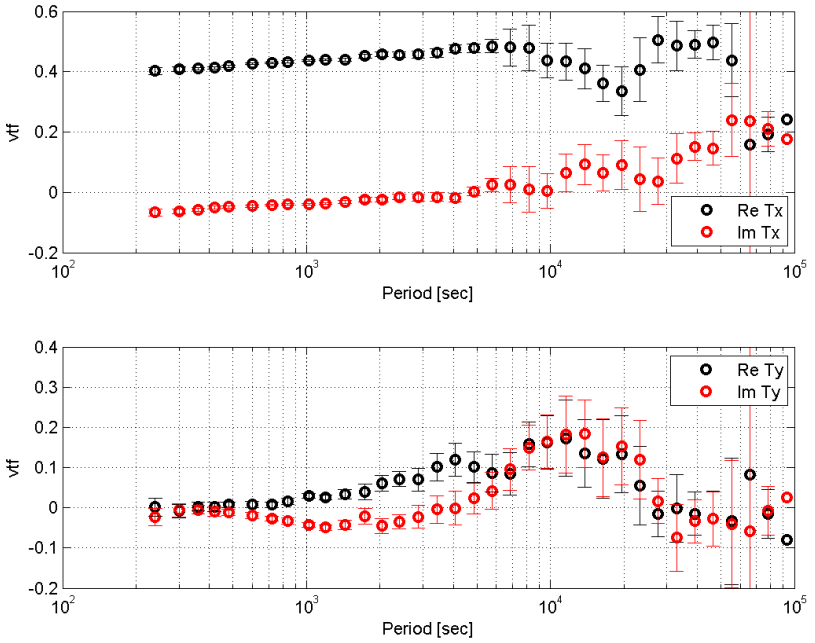

FIGURE C.7: Tippers at Gan estimated from quasi definitive magnetic data of June 2014.

periods $> 6 \cdot 10^3$ s the uncertainties increase but the overall behavior of the responses remains smooth. The dominating T_x component can be explained by the location of the observatory at the southern end of the Addu atoll ring structure, which again is the southernmost atoll of the Maldivian row of atolls situated on top of a $\sim$ 900 km long submarine ridge (e.g. *Lüdmann et al.*, 2013). This results in a large conductivity contrast in N-S direction at the observatory location and a dominating T_x component of the tippers.

The upper two plots in Fig. C.8 show the raw impedance tensor elements Z_{yx} and Z_{xy} estimated from the June 2014 data and using the Or type electrode signal. The responses in Z_{yx} are smooth up to around $2 \cdot 10^4$ s, then the uncertainties are increasing. For Z_{xy} the responses appear to be smooth over the whole period range showing that based on the measured data it is in principle possible to estimate high quality responses at least up to periods of around one day. The impedances estimated using the Mü type electrode data are shown in the lower plot in Fig C.8. The Z_{yx} component, which relates E_y to B_x is of comparable high quality as the corresponding impedances estimated from the Or type electrode data. This shows that the drift, which occurs in the E_y component of the Mü type electrodes does not seriously affect variations with periods below one day.

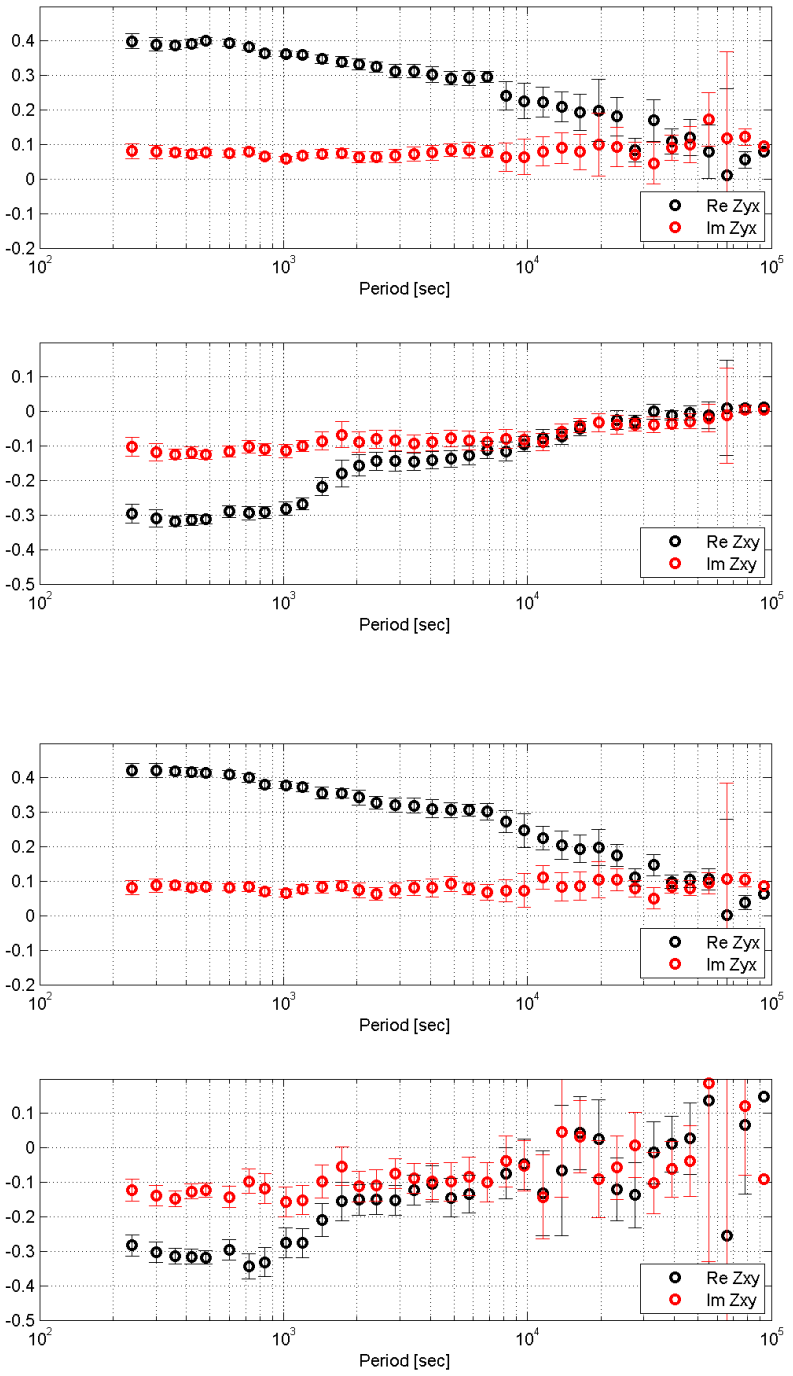

FIGURE C.8: Impedances at Gan estimated from quasi definitive magnetic data and telluric data of Or type Pb-Pb-Cl electrodes (upper two plots) and Mü type Ag-Ag-Cl electrodes (lower two plots) of June 2014. Impedances are given in field units $\left[\frac{\text{km}}{\text{s}}\right]$, see Section 4.2

The impedances of the Z_{xy} component clearly have larger uncertainties due to the very unstable measurements in the E_x component of the Mü type electrodes. However, the behavior of the responses is comparable to the one estimated from the Or type

electrode data up to periods of 10^4 s with significantly larger uncertainties. Towards longer periods the quality of the impedances decreases to an unacceptable level.

C.5 Conclusion

Our attempt in equipping geomagnetic observatories with permanent telluric measurements shows promising results and indicates the prior topics to be addressed in future work. The estimated impedances appear to be stable and have small uncertainties up to periods of around $2 \cdot 10^4$ s despite the fact that at least one of the telluric channels (E_y Mü) appears to be unstable and is affected by drifting. Responses estimated from data of the unstable channel (E_x Mü) are of a poor quality as expected. Here we only used four weeks of data in total and better results at long periods can be achieved if longer continuous time series are used. However, the influence of the source field effect in the period range of $10^4 - 10^5$ s should be studied in detail as deviations of the plane wave source field excitation are expected to bias the responses. In Gan the main source field effects are expected to arise from the EEJ rather than from the Sq current system, due to it's geographical location. An important focus of any future work will be the selection of proper electrodes adapted for permanent telluric measurements. So far the two-chamber mud-filled Or type Pb-Pb-Cl electrodes do the better job. The fluid-filled Mu type Ag-Ag-Cl electrodes are so far only at an developmental stage and require some improvements regarding their long term stability.

Appendix D

Tippers at island observatories: Can we use them to probe electrical conductivity of the Earth's crust and upper mantle?

This Appendix presents the study published in *Samrock and Kuvshinov* (2013).

D.1 Abstract

For decades time series of *hourly-mean* values of the geomagnetic field measured on a global network of observatories have been routinely used to recover the electrical conductivity distribution in mid-mantle depths. Nowadays most observatories provide data in the form of *minute-means*. This allows for analysis of short-period geomagnetic variations, which, in principle, contain information about geoelectric structures in the crust and upper mantle. However, so far these data have been ignored for induction studies of the Earth due to a theoretical preconception. In this paper we demonstrate that short-period responses (tippers) at island observatories, being large owing to the ocean effect, are also sensitive to 1-D structures, and thus can be used for probing the Earth. This means that a huge amount of data that was not exploited hitherto for induction studies should be reconsidered as a useful source of information about geoelectric structures in oceanic regions where our knowledge is still very limited.

D.2 Introduction

Hourly-mean time series of the geomagnetic field measured on a global net of geomagnetic observatories have been routinely used for decades in induction studies that aim

to recover mantle electrical conductivity (e.g. *Schmucker*, 1999b; *Kelbert et al.*, 2009). Bearing in mind the one hour sampling interval, and depending on the period, two global sources are used for these studies: (1) solar quiet (Sq) variations with periods between 4 and 24 hours, caused by electric currents flowing in the ionosphere; (2) irregular (Dst) variations with periods longer than one day, caused by modulation of the ring current flowing in the magnetosphere. An interpretation of these data yields the recovery of electrical conductivities in the depth range from about 400 km down to about 1600 km. Recent progress in deep electromagnetic (EM) sounding of the Earth is summarized in a review paper by *Kuvshinov* (2012). Nowadays most geomagnetic observatories provide minute-mean data, which gives an opportunity to analyze the variations at shorter periods, namely, in the period range between a few minutes and a few hours. There is common consensus that these variations are generated by an auroral ionospheric current system which is seen at mid-latitude observatories as a vertically propagated plane wave of time-varying polarization (cf. discussion in *Chave and Jones*, 2012, page 10). These variations can, in principle, provide information about geoelectric structures at crustal and upper mantle depths (< 400 km). However, to the best of our knowledge there have been no attempts yet to use these data (short-period geomagnetic field variations at observatory locations) to infer the conductivity of the Earth. The reason for this seems to be rather intuitive and appears to be as follows. For a given and isolated observatory (and for the considered period range) one can at best determine the one-dimensional (1-D) local conductivity structure beneath the observatory site. Moreover, assuming plane wave excitation, the only response functions which might be then constructed from geomagnetic data is the first-order tensor of complex-valued and dimensionless tippers, $\mathbf{T}=(T_x, T_y)$, which connects the vertical magnetic component B_z with two horizontal components B_x and B_y:

$$B_z(\omega) = T_x(\omega)B_x(\omega) + T_y(\omega)B_y(\omega).$$

Here $\omega = 2\pi/p$ is the circular frequency, where p is a period, z points positive downwards, x points to geographic North and y points to geographic East. However, as a consequence of the plane wave excitation, variations in B_z (and thus $\mathbf{T}$) are non zero only above *non* 1-D conductivity structures. In fact one can interpret $\mathbf{T}$ as a measure of the tipping of the magnetic field out of the horizontal plane above non 1-D conductivity structures, which cause anomalous variations in B_z (*Parkinson*, 1959; *Jones and Price*, 1970).

This line of reasoning advocates ignoring minute-mean data to probe the Earth's crust in the frame of 1-D models. This is probably true for inland observatories, but it is not for island and coastal sites where the ocean plays a role. Here the horizontal conductivity contrast between resistive continental bedrock and conductive sea water results in large tipper amplitudes even if the crustal structure is essentially 1-D. This

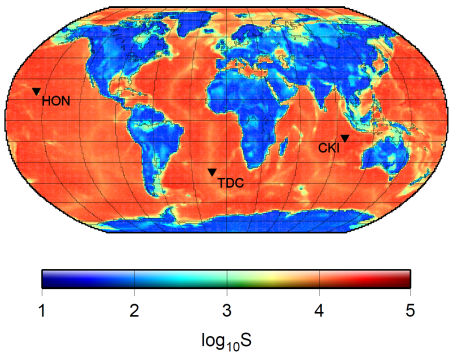

FIGURE D.1: World surface conductance map (*Manoj et al.*, 2006), using a logarithmic scale, and location of the observatories TDC, HON and CKI. The surface conductance is based on contributions from seawater and sediments. Note the large horizontal conductivity contrast along the coasts.

is referred to as the ocean (or coast) effect (e.g. *Parkinson*, 1962). Note that real and imaginary parts of tippers are often displayed separately as arrows with respective coordinates $-(Re\,T_x, Re\,T_y)$ and $-(Im\,T_x, Im\,T_y)$. Minus sign means that the Parkinson convention is used.

Under the assumption that both the conductivity of the land, σ_{land}, and the conductivity of seawater, σ_{sea}, are constant with $\sigma_{land} << \sigma_{sea}$, and considering induction methods as volume sounding techniques, the real part of tippers always points towards the nearest deepest ocean. Furthermore, tippers reach their maximum amplitudes at those periods where conductivity contrast is maximum within the penetrated volume. At roughly the same periods the reversal of the imaginary parts occurs (e.g. *Dosso and Chen*, 2000). In this paper we perform model studies in order to answer the following two questions: (1) Is it possible to reproduce the complex frequency-dependent behavior of the observed tippers at island observatories with rigorous 3-D modeling of the ocean effect? (2) Are these tippers sensitive to 1-D conductivity structures beneath ocean?

D.3 Observations

For analysis we have chosen data consisting of minute-mean time series of the geomagnetic field from three island observatories which are located in the Atlantic, Pacific and Indian oceans. Their location is shown in Fig. D.1. The first observatory (TDC) is situated in the northwestern part of Tristan da Cunha island, which is part of the Tristan da Cunha archipelago in the South Atlantic Ocean and consists of a large oceanic shield volcano that rises more than 5000 m from the seafloor to an altitude of 2000 m (*Matzka et al.*, 2009). The second observatory HON (Honolulu) is located in the south of the volcanic Hawaiian island Oahu, which reaches an altitude of 1200 m and is surrounded by 5000 m deep ocean. Unlike TDC and HON the third observatory, provisionally acronymed by

CKI, is not part of the INTERMAGNET network, it was established very recently on southern Cocos (Keeling) Island and is currently in experimental operation status. Southern Cocos Island is a coral ring atoll in the Indian ocean, and CKI observatory is located on a southwestern island of the atoll. The Cocos Islands are situated on top of seamounts of volcanic origin on Cocos Rise and are also surrounded by 5000 m deep ocean. The maximum altitude of the islands is a few meters only. The tippers were estimated from the data using the BIRRP-code (*Chave and Thomson*, 2003, 2004) in a period range between 2 min and 1 day. BIRRP stands for *Bounded Influence, Remote Reference Processing*, the code is based on section-averaging of the time series with a jackknife estimator of the uncertainties. The section length is variable and depends on the period (shorter sections for shorter periods). Before processing the geomagnetic data were visually preselected, and days with obvious spikes and boxcar offsets were removed. Repetitive processing of data with varying time spans has shown that an approximately 30 day period of geomagnetic data are sufficient to gain stable responses in the considered period range. Fig. D.2 shows real and imaginary parts of the observed tippers. It is seen that at all observatories at least the real parts of tippers are substantially larger than 0. Their behavior is smooth and their uncertainties are small up to periods of 10000 s $\approx$ 3 h with overall tendency for uncertainties to be larger at longer periods. This can be explained as follows: The number of sections used to estimate tippers (and

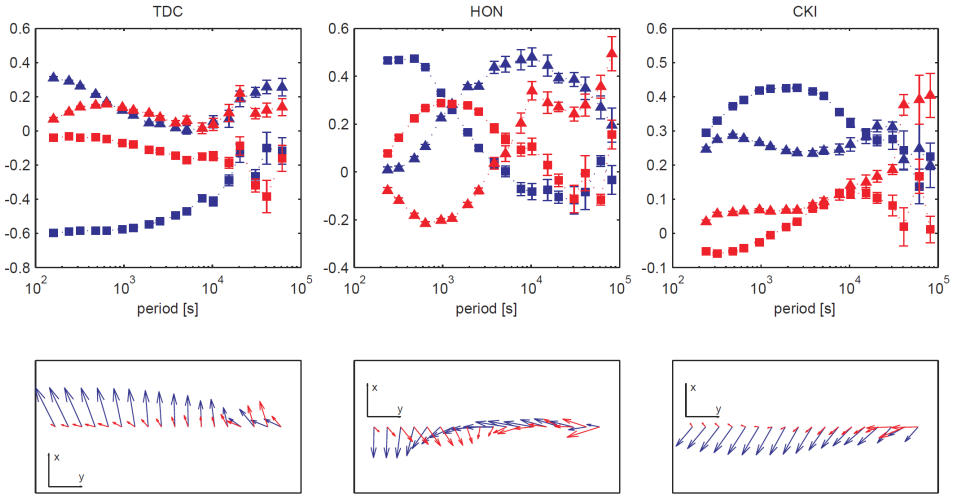

FIGURE D.2: Plots from left to right, observed tippers at TDC, HON and CKI. In the upper plots T_x are shown as squares and T_y as triangles. Real and imaginary parts are depicted in blue and red, respectively. In the lower plots tippers are displayed as arrows in the Parkinson convention, i.e. real parts point towards the most conductive region within the penetrated volume. The length of each arrow signifies the norm of the tippers real part and imaginary part, respectively. Coordinate systems are shown in the plots with the axes having a reference length of 0.5. The orders of periods in the arrow plots are the same as in the upper plots.

thus the number of degrees of freedom) is smaller for longer periods compared to shorter periods. Since the statistical error is inversely proportional to the number of degrees of freedom, this results in larger uncertainties at longer periods. Another observation is that at periods larger than 3 h, the responses become more scattered and their uncertainties increase. This is most probably due to Sq source contamination and thereby violation of the plane wave assumption (e.g. *Shimizu et al.*, 2011). In the following we concentrate therefore on analysis of the responses at periods less than 3 h.

At all observatories and at periods up to 3000 s the real tipper component perpendicular to the local coast line dominates, cf. Fig. D.3. This confirms that the responses are strongly influenced by the ocean effect. Otherwise, the behavior of the tippers at different sites is substantially different. At TDC, real parts of the tipper are maximum (with largest magnitude of 0.6) at short periods and decrease with increasing periods. This is consistent with the fact that here the conductivity contrast within the penetrated volume decreases with period. As for HON, a clearly dominating real T_x component for periods below 1000 s is in agreement with the east-west elongated coast line in the vicinity of the observatory. With increasing period, tipper arrows smoothly change to point westwards, then for periods greater than 3000 s real parts of T_y are dominating. This is explained by concentration of the main landmass east of the observatory for larger penetrated volume, cf. Fig. D.3b. The maximum magnitude of the observed tippers at HON is 0.5. At CKI, the real parts of the tippers point constantly towards southwest over the whole period range. With their southwestern direction they point away from the center of the ring atoll towards deep ocean as one would expect in this scenario. Real tipper amplitudes are increasing till a period of 2000 s with dominating T_x. The maximum magnitude of the observed tippers at CKI is 0.45.

D.4 Model studies

The model studies were performed using the X3D code (*Avdeev et al.*, 2002), which is based on the contracting integral equation technique. This frequency-domain code allows for calculating plane-wave electric and magnetic fields (and thus various response functions, including tippers) in Earth's models with a three-dimensional conductivity distribution. Bathymetry and topography data have been taken from the ETOPO1 Global Relief Model database (*Amante and Eakins*, 2009). Models for TDC and HON consist of eight anomalous top layers (three layers account for topography and five for bathymetry), the models for CKI consist of only five anomalous top layers due to absence of topography. Anomalous layers are built based on ETOPO1 data and are followed with depth by a one-dimensional (1-D) conductivity section. The shallow three-dimensional (3-D) conductivity distribution is derived from ETOPO1 data under the assumption of a sea water conductivity of $\sigma_{sea} = 3.2\,\mathrm{S/m}$ and a land conductivity

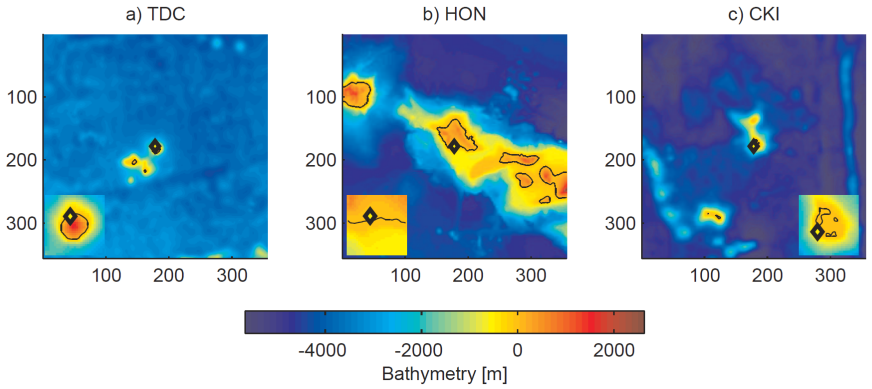

FIGURE D.3: a) - c) show interpolated ETOPO1 bathymetry data (*Amante and Eakins*, 2009) around observatories TDC, HON and CKI, respectively; the coastline is indicated as a black line. The location of each observatory is marked with a diamond symbol. Zoomed subfigures show coastlines around observatory location in detail. Numbers on the axes stand for the model cell numbers; the total horizontal size of all models is 356 km × 356 km.

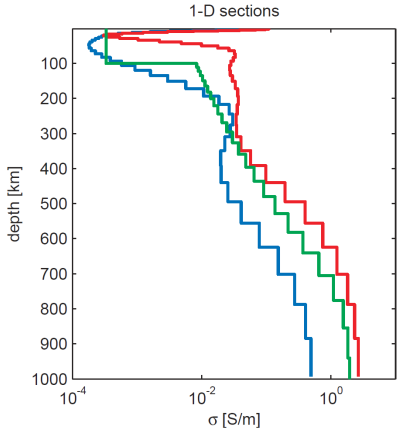

FIGURE D.4: 1-D conductivity sections GLO (green) (*Kuvshinov and Olsen*, 2006), PAC (blue) and PHS (red) (*Baba et al.*, 2010), which are used in 3-D modeling; see details in the text.

of $\sigma_{land} = 10^{-2}$ S/m. The original one arc-minute data of bathymetry and topography used for estimating conductivity distributions in the anomalous layers were interpolated to a regular Cartesian grid with a horizontal cell size of 1 km × 1 km. Based on these assumptions, vertically averaged conductivities for all cells of the anomalous layers were calculated. Interpolated ETOPO1 bathymetry and topography data around TDC, HON and CKI are shown in Fig. D.3a-c. The total horizontal size for all (TDC, HON and CKI) models is 356 km × 356 km. Note that we performed extensive and systematic model studies to justify the parameters describing the models (cell and mesh sizes, number of

anomalous layers, values for sea water and land conductivities). In particular from these studies we learned that the effect from varying sea water and land conductivities is less than the effect from varying the 1-D section.

The sensitivity of tippers to conductivity variations in the crust and upper mantle was investigated with respect to three different 1-D conductivity sections. These sections are shown in Fig. D.4. The section labeled as GLO is (a modified) global conductivity section that has been inferred from satellite magnetic data by *Kuvshinov and Olsen* (2006). The modification is assigning a realistic low conductivity value to the upper 100 km as these depths are not resolvable by satellite magnetic data. Sections here denoted as PHS and PAC are sections for Philippine Sea and for North Pacific region, respectively, which have been recovered from the seafloor magnetotelluric data (*Baba et al.*, 2010). The most significant differences between sections appear at shallow depths, where, integrated over the upper 200 km, PHS is the most conductive and GLO is the most resistive section.

The predicted tippers are shown in Fig. D.5 in comparison with observed ones. At observatory TDC the general shape of the observed tipper curves is well reproduced by prediction irrespective which 1-D section is used. However, all predicted real parts of tippers are shifted to lower values except in the period range above 3000 s. The largest deviations occur in the T_x component whereby predicted real parts of T_x from the model with GLO 1-D section are closest to the observed ones. The variability at a certain period in the predicted tippers, determined as

$$var = |\max(T^{\text{pred}}) - \min(T^{\text{pred}})|,$$

appeared to be maximum (0.12) in the real part of T_x at period of 5000 s, which is $\sim 20\%$ of the magnitude of the observed response at this period.

Predicted tippers for HON show much more variability compared with the results for TDC. The maximum variability in the predicted tippers with respect to three different 1-D sections is in T_y. At a period of 5000 s the variability in real T_y is ~ 0.37, which is $\sim 80\%$ of the magnitude of the observed response at this period. The agreement between predictions and observations is worse than at TDC; however the observed transition from dominating real part of T_x to dominating real part of T_y with increasing period is well reproduced with all 1-D sections. In contrast to TDC, the results for the GLO 1-D section generally show the highest misfit for both real and imaginary parts.

At CKI, the overall behavior is well reproduced by all models and the maximum variability in the predicted tippers with respect to three different 1-D sections is 0.05 in the real part of T_x, which is $\sim 12\%$ of the magnitude of the observed response. This is the minimum amongst the three sites, but nevertheless it far exceeds the uncertainty of the observed responses.

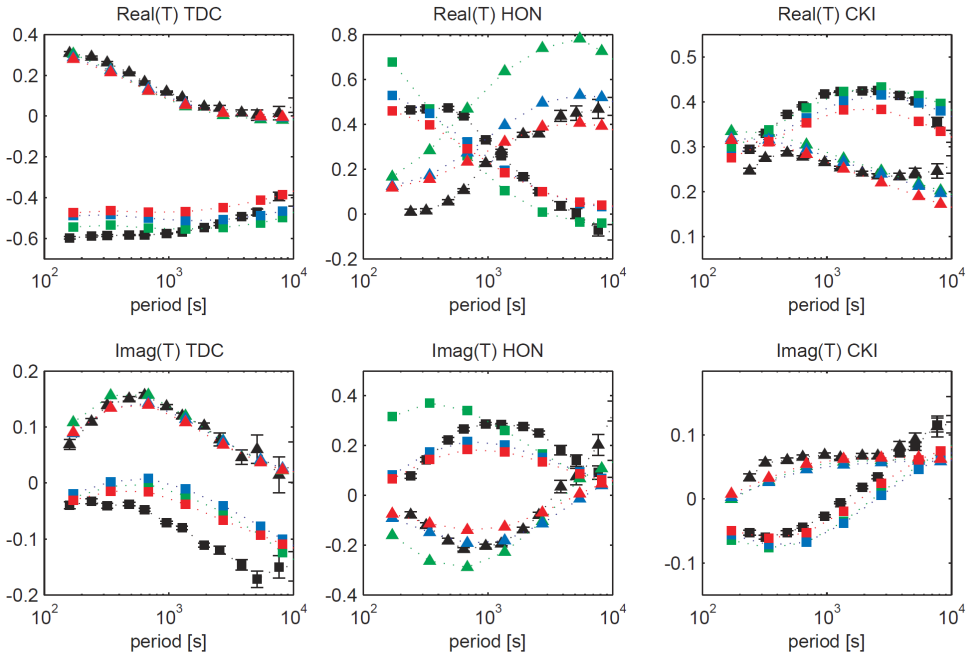

FIGURE D.5: Plots from left to right: observed and predicted responses at observatories TDC, HON and CKI. Upper and lower plots show real and imaginary parts, respectively. T_x are denoted as squares, T_y as triangles. Predicted tippers for GLO, PAC and PHS 1-D section are plotted in green, blue and red, respectively. Observed responses and their uncertainties are shown in black. As a whole the predicted tippers for different 1-D conductivity sections show significant differences.

D.5 Conclusions and outlook

We demonstrate that the overall behavior of tippers at island observatories is well explained by the ocean effect, if topography and bathymetry are adequately modeled. We also clearly show that tippers at island observatories are sensitive to the 1-D conductivity section underneath. The largest sensitivity is observed at observatory site locations with a high land-to-sea ratio in upper layers. From the aforementioned conclusions we can state that a huge amount of data that was not exploited so far for induction studies can be reconsidered as a useful source of information at many (island) observatories. Of particular importance is that these data allow us to, at least partially, surmount an evident lack of knowledge about crustal and upper mantle structures in the oceanic regions. We observe different levels of agreement between predicted and observed tippers at different island observatories, which suggests a regional difference in conducting structures at crustal and upper mantle depths. In order to quantitatively specify the variability of the underlying conductivities with respect to observatories and regions, we plan to develop a numerical scheme, which will allow for inverting for tippers in terms of 1-D conductivity distribution in the presence of a realistic 3-D bathymetry. Finally, we would like to extend our studies to coastal observatories, although our first studies

have revealed substantial disagreement between observations and predictions. This is most probably due to inherent 3-D complications in the transition zone between ocean and land that are not easy to account for.

D.6 Acknowledgments

The authors would like to thank Susan Macmillan and an anonymous reviewer for their valuable comments and suggestions to improve the quality of the paper. Furthermore we thank William Lowrie for help with improving the English presentation of this paper, and Thomas Kalscheuer for valuable comments on an initial version of the paper. The results presented in this paper rely on data collected at magnetic observatories. We thank the national institutes that support them and INTERMAGNET for promoting high standards of magnetic observatory practice (www.intermagnet.org). We especially thank Juergen Matzka (DTU Space, Copenhagen) for motivating us to work on TDC observatory data and Geoscience Australia for enabling us to work on CKI data. This work has been supported by ETH grant No. ETH-3010-3.

Bibliography

Agostini, A., M. Bonini, G. Corti, F. Sani, and P. Manetti (2011), Distribution of quaternary deformation in the central Main Ethiopian Rift, East Africa, *Tectonics*, *30*(4).

Alfvén, H. (1943), On the existence of electromagnetic-hydrodynamic waves, *Ark. Astron.*, *29*, 1–7.

Amante, C., and B. Eakins (2009), *ETOPO1 1 arc-minute global relief model: procedures, data sources and analysis*, US Department of Commerce, National Oceanic and Atmospheric Administration, National Environmental Satellite, Data, and Information Service, National Geophysical Data Center, Marine Geology and Geophysics Division.

Árnason, K., H. Eysteinsson, and G. P. Hersir (2010), Joint 1D inversion of TEM and MT data and 3D inversion of MT data in the Hengill area, SW Iceland, *Geothermics*, *39*(1), 13–34.

Auer, L., L. Boschi, T. Becker, T. Nissen-Meyer, and D. Giardini (2014), Savani: A variable resolution whole-mantle model of anisotropic shear velocity variations based on multiple data sets, *J. Geophys. Res.*, *119*(4), 3006–3034.

Avdeev, D., and A. Avdeeva (2009), 3-d magnetotelluric inversion using a limited-memory quasi-Newton optimization, *Geophysics*, *74*(3), F45–F57.

Avdeev, D., A. Kuvshinov, O. Pankratov, and G. Newman (1997), High-performance three-dimensional electromagnetic modelling using modified Neumann series. Wide-band numerical solution and examples, *J. Geomagn. Geoelectr.*, *49*(11), 1519–1540.

Avdeev, D., A. Kuvshinov, O. Pankratov, and G. Newman (2002), Three-dimensional induction logging problems, Part I: An integral equation solution and model comparisons, *Geophysics*, *67*(2), 413–426.

Ayenew, T. (2003), Environmental isotope-based integrated hydrogeological study of some Ethiopian rift lakes, *J. Radioanal. Nucl. Chem.*, *257*(1), 11–16.

Baba, K., and A. Chave (2005), Correction of seafloor magnetotelluric data for topographic effects during inversion, *J. Geophys. Res.*, *110*(B12).

Baba, K., H. Utada, T. Goto, T. Kasaya, H. Shimizu, and N. Tada (2010), Electrical conductivity imaging of the Philippine Sea upper mantle using seafloor magnetotelluric data, *Phys.Earth Planet. In.*, *183*(1), 44–62.

Bahr, K. (1988), Interpretation of the magnetotelluric impedance tensor: regional induction and local telluric distortion, *J. Geophys. Res.*, *62*(1), 119–127.

Bahr, K. (1991), Geological noise in magnetotelluric data: a classification of distortion types, *Phys. Earth Planet. Inter.*, *66*(1-2), 24–38.

Banks, R. (1969), Geomagnetic variations and the electrical conductivity of the upper mantle, *Geophys. J. R. Astron. Soc.*, *17*(5), 457–487.

Basma, A., A. Al-Homoud, A. Husein Malkawi, and M. Al-Bashabsheh (1996), Swelling-shrinkage behavior of natural expansive clays, *Appl. Clay Sci.*, *11*(2), 211–227.

Bastow, I., D. Keir, and E. Daly (2011), The Ethiopia Afar Geoscientific Lithospheric Experiment (EAGLE): Probing the transition from continental rifting to incipient seafloor spreading, *Spec. Pap. - Geol. Soc. Am.*, *478*, 51–76.

Battaglia, S. (2004), Variations in the chemical composition of illite from five geothermal fields: a possible geothermometer, *Clay Miner.*, *39*(4), 501–510.

Becker, T., and L. Boschi (2002), A comparison of tomographic and geodynamic mantle models, *Geochem., Geophys., Geosyst.*, *3*(1).

Benoit, D., M. Asaye, and M. Tessaw (2007), A Review of the Aluto Langano Geothermal Project and Recent Temperature and Pressure Logging, *GRC Trans.*, *31*, 47–51.

Benvenuti, M., S. Carnicelli, G. Belluomini, N. Dainelli, S. Di Grazia, G. Ferrari, C. Iasio, M. Sagri, D. Ventra, B. Atnafu, et al. (2002), The Ziway–Shala lake basin (Main Ethiopian rift, Ethiopia): a revision of basin evolution with special reference to the Late Quaternary, *J. Afr. Earth Sci.*, *35*(2), 247–269.

Berdichevsky, M., and V. Dmitriev (Eds.) (2008), *Models and Methods of Magnetotellurics*, Springer, Berlin, Heidelberg.

Bertani, R. (2012), Geothermal power generation in the world 2005–2010 update report, *Geothermics*, *41*, 1–29.

Bertrand, E., T. Caldwell, G. Hill, E. Wallin, S. Bennie, N. Cozens, S. Onacha, G. Ryan, C. Walter, A. Zaino, et al. (2012), Magnetotelluric imaging of upper-crustal convection plumes beneath the Taupo Volcanic Zone, New Zealand, *Geophys. Res. Lett.*, *39*(2).

Bertrand, E., T. Caldwell, G. Hill, S. Bennie, and S. Soengkono (2013), Magnetotelluric imaging of the Ohaaki geothermal system, New Zealand: Implications for locating basement permeability, *J. Volcanol. Geotherm. Res.*, *268*, 36–45.

Bibby, H., T. Caldwell, F. Davey, and T. Webb (1995), Geophysical evidence on the structure of the Taupo Volcanic Zone and its hydrothermal circulation, *J. Volcanol. Geotherm. Res.*, *68*(1), 29–58.

Biggs, J., I. Bastow, D. Keir, and E. Lewi (2011), Pulses of deformation reveal frequently recurring shallow magmatic activity beneath the Main Ethiopian Rift, *Geochem., Geophys., Geosyst.*, *12*(9).

Bilham, R., R. Bendick, K. Larson, P. Mohr, J. Braun, S. Tesfaye, and L. Asfaw (1999), Secular and tidal strain across the Main Ethiopian Rift, *Geophys. Res. Lett.*, *26*(18), 2789–2792.

Bonafede, M. (1991), Hot fluid migration: an efficient source of ground deformation: application to the 1982–1985 crisis at Campi Flegrei – Italy, *J. Volcanol. Geotherm. Res.*, *48*(1), 187–198.

Bothmer, V., and I. Daglis (2006), *Space Weather: Physics and Effects (Springer Praxis Books / Environmental Sciences)*, 1 ed., Springer, Berlin.

Cagniard, L. (1953), Basic theory of the magnetotelluric method of geophysical prospecting, *Geophysics*, *18*, 603–635.

Caldwell, G., C. Pearson, and H. Zayadi (1986), Resistivity of rocks in geothermal systems: a laboratory study, in *Proceedings 8th NZ geothermal workshop*, pp. 227–231.

Caldwell, T., H. Bibby, and C. Brown (2004), The magnetotelluric phase tensor, *Geophys. J. Int.*, *158*(2), 457–469.

Çelik, M. (2004), Electrokinetic behavior of clay surfaces, *Interface Sci. Technol.*, *1*, 57–89.

Chave, A., and D. Thomson (2003), A bounded influence regression estimator based on the statistics of the hat matrix, *J. Roy. Stat. Soc.: Series C (Appl. Statist.)*, *52*(3), 307–322.

Chave, A., and D. Thomson (2004), Bounded influence magnetotelluric response function estimation, *Geophys. J. Int.*, *157*(3), 988–1006.

Chave, A. D., and A. G. Jones (2012), *The Magnetotelluric Method: Theory and Practice*, Cambridge University Press.

Chu, D., and R. Gordon (1999), Evidence for motion between Nubia and Somalia along the Southwest Indian Ridge, *Nature*, *398*(6722), 64–67.

Constable, S. (2007), Geomagnetism, in *Treatise on Geophysics*, pp. 237 – 276, Elsevier, Amsterdam.

Constable, S. C., R. L. Parker, and C. G. Constable (1987), Occam's inversion: A practical algorithm for generating smooth models from electromagnetic sounding data, *Geophysics*, *52*(3), 289–300.

Corti, G. (2008), Control of rift obliquity on the evolution and segmentation of the Main Ethiopian Rift, *Nat. Geosci.*, *1*(4), 258–262.

Corti, G. (2009), Continental rift evolution: from rift initiation to incipient break-up in the Main Ethiopian Rift, East Africa, *Earth-Sci. Rev.*, *96*(1), 1–53.

Cummer, S., and U. Inan (2000), Modeling ELF radio atmospheric propagation and extracting lightning currents from ELF observations, *Radio Sci.*, *35*(2), 385–394.

Cumming, W. (2009), Geothermal resource conceptual models using surface exploration data, in *Proceedings, Thirty-Fourth Workshop on Geothermal Reservoir Engineering*, Stanford University, Stanford, California,.

Davies, G. (1998), A channelled plume under Africa, *Nature*, *395*(6704), 743–744.

de Siqueira, A., C. Lobban, N. Skipper, G. Williams, A. Soper, R. Done, J. Dreyer, R. Humphreys, and J. Bones (1999), The structure of pore fluids in swelling clays at elevated pressures and temperatures, *J. Phys.: Condens. Matter*, *11*(47), 9179.

Desissa, M., N. Johnson, K. Whaler, S. Hautot, S. Fisseha, and G. Dawes (2013), A mantle magma reservoir beneath an incipient mid-ocean ridge in Afar, Ethiopia, *Nat. Geosci.*, *6*(10), 861–865.

Dickson, M., and M. Fanelli (2013), *Geothermal energy: utilization and technology*, Routledge.

Dosso, H., and J. Chen (2000), Analogue model study of EM induction in elongated conductors – 2D and 3D induction arrow responses, *Earth Planets Space*, *52*(5), 355–360.

Ebinger, C. (2005), Continental break-up: the East African perspective, *Astron. Geophys.*, *46*(2), 2–16.

Egbert, G. (1990), Comments on 'Concerning dispersion relations for the magnetotelluric impedance tensor' by E. Yee and K.V. Paulson, *Geophys. J. Int.*, *102*(1), 1–8.

Egbert, G. (1992), Noncausality of the discrete-time magnetotelluric impulse response, *Geophysics*, *57*(10), 1354–1358.

Egbert, G., and A. Kelbert (2012), Computational recipes for electromagnetic inverse problems, *Geophys. J. Int.*, *189*(1), 251–267.

Egbert, G. D. (1997), Robust multiple-station magnetotelluric data processing, *Geophys. J. Int.*, *130*(2), 475–496.

Egbert, G. D., and J. R. Booker (1986), Robust estimation of geomagnetic transfer functions, *Geophys. J. Int.*, *87*(1), 173–194.

Egbert, G. D., and M. Eisel (1998), *EMTF: Programs for Robust Single Station and Remote Reference Analysis of Magnetotelluric Data: UNIX (and PC) Version.*

Eisel, M., and G. Egbert (2001), On the stability of magnetotelluric transfer function estimates and the reliability of their variances, *Geophys. J. Int.*, *144*(1), 65–82.

Endeshaw, A. (1988), Current status (1987) of geothermal exploration in Ethiopia, *Geothermics*, *17*(2), 477–488.

Farquharson, C. G., and M. P. Miensopust (2011), Three-dimensional finite-element modelling of magnetotelluric data with a divergence correction, *J. Appl. Geophys.*, *75*, 699–710.

Farquharson, C. G., D. W. Oldenburg, E. Haber, R. Shekhtman, et al. (2002), An algorithm for the three-dimensional inversion of magnetotelluric data, *72th Ann. Internat. Mtg., Soc. Expl. Geophys*, pp. 649–652.

Finlay, C., S. Maus, C. Beggan, T. Bondar, A. Chambodut, T. Chernova, A. Chulliat, V. Golovkov, B. Hamilton, M. Hamoudi, et al. (2010), International geomagnetic reference field: the eleventh generation, *Geophys. J. Int.*, *183*(3), 1216–1230.

Fletcher, R., and C. Reeves (1964), Function minimization by conjugate gradients, *Comput. J.*, *7*(2), 149–154.

French, S., V. Lekic, and B. Romanowicz (2013), Waveform tomography reveals channeled flow at the base of the oceanic asthenosphere, *Science*, *342*(6155), 227–230.

Fukao, Y., T. Koyama, M. Obayashi, and H. Utada (2004), Trans-pacific temperature field in the mantle transition region derived from seismic and electromagnetic tomography, *Earth Planet. Sc. Lett.*, *217*(3), 425–434.

Füllekrug, M. (2005), Detection of thirteen resonances of radio waves from particularly intense lightning discharges, *Geophys. Res. Lett.*, *32*(13).

Gamble, T., W. Goubau, and J. Clarke (1979), Magnetotellurics with a remote magnetic reference, *Geophysics*, *44*(1), 53–68.

Gauß, C. (1839), Allgemeine Theorie des Erdmagnetismus, *Resultate aus den Beobachtungen des magnetischen Vereins im Jahre 1838*, pp. 1–57.

Gebregzabher, Z. (1986), Hydrothermal alteration minerals in Aluto Langano geothermal wells, Ethiopia, *Geothermics*, *15*(5), 735–740.

Gianelli, G., and M. Teklemariam (1993), Water-rock interaction processes in the Aluto-Langano geothermal field (Ethiopia), *J. Volcanol. Geotherm. Res.*, *56*(4), 429–445.

Gizaw, B. (1993), Aluto-Langano geothermal field, Ethiopian Rift Valley: physical characteristics and the effects of gas on well performance, *Geothermics*, *22*(2), 101–116.

Glaßmeier, K.-H., H. Soffel, and J. Negendank (Eds.) (2009), *Geomagnetic Field Variations*, vol. 1, Springer, Berlin.

Grayver, A., and M. Burg (2014), Robust and scalable 3-D geo-electromagnetic modelling approach using the finite element method, *Geophys. J. Int.*, *1*, 168.

Greenbaum, A. (1997), *Iterative methods for solving linear systems*, Society for Industrial and Applied Mathematics, Philadelphia, USA.

Gurubaran, S. (2002), The equatorial counter electrojet: Part of a worldwide current system?, *Geophys. Res. Lett.*, *29*(9), 51–1.

Haber, E., and U. M. Ascher (2001), Fast finite volume simulation of 3D electromagnetic problems with highly discontinuous coefficients, *SIAM Journal of Scientific Computing*, *22(6)*, 1943–1961.

Han, N., M. Nam, H. Kim, T. Lee, Y. Song, and J. Suh (2008), Efficient three-dimensional inversion of magnetotelluric data using approximate sensitivities, *Geophys. J. Int.*, *175*(2), 477–485.

Hautot, S., R. T. Single, J. Watson, N. Harrop, D. A. Jerram, P. Tarits, K. Whaler, and G. Dawes (2007), 3-D magnetotelluric inversion and model validation with gravity data for the investigation of flood basalts and associated volcanic rifted margins, *Geophys. J. Int.*, *170*, 1418–1430.

Heise, W., H. Bibby, T. Caldwell, S. Bannister, Y. Ogawa, S. Takakura, and T. Uchida (2007), Melt distribution beneath a young continental rift: the Taupo Volcanic Zone, New Zealand, *Geophys. Res. Lett.*, *34*(14).

Heise, W., T. Caldwell, H. Bibby, and S. Bannister (2008), Three-dimensional modelling of magnetotelluric data from the Rotokawa geothermal field, Taupo Volcanic Zone, New Zealand, *Geophys. J. Int.*, *173*(2), 740–750.

Houser, C., G. Masters, P. Shearer, and G. Laske (2008), Shear and compressional velocity models of the mantle from cluster analysis of long-period waveforms, *Geophys. J. Int.*, *174*(1), 195–212.

Hultqvist, B., M. Øieroset, G. Paschmann, and R. Treumann (1999), Plasma transfer processes at the magnetopause, in *Magnetospheric Plasma Sources and Losses*, *Space Sciences Series of ISSI*, vol. 6, edited by B. Hultqvist, M. Øieroset, G. Paschmann, and R. Treumann, pp. 207–283, Springer.

Hursan, G., and M. Zhdanov (2002), Contraction integral equation method in three-dimensional electromagnetic modeling, *Radio Science*, *37*(6), 1–13.

IRENA Headquarters (2013), Working together to build an east and southern African clean energy sector, Brochure, PO Box 236, Abu Dhabi, United Arab Emirates.

Jiracek, G. (1990), Near-surface and topographic distortions in electromagnetic induction, *Surv. Geophys.*, *11*(2-3), 163–203.

Johnston, J., L. Pellerin, and G. Hohmann (1992), Evaluation of electromagnetic methods for geothermal reservoir detection, *Transactions-Geothermal Resources Council*, *16*, 241–245.

Jones, F., and A. Price (1970), The perturbations of alternating geomagnetic fields by conductivity anomalies, *Geophys. J. R. Astr. Soc.*, *20*(3), 317–334.

Kamm, J., and L. Pedersen (2014), Inversion of airborne tensor VLF data using integral equations, *Geophys. J. Int.*, *198*, 775–794.

Keir, D., C. Ebinger, G. Stuart, E. Daly, and A. Ayele (2006), Strain accommodation by magmatism and faulting as rifting proceeds to breakup: seismicity of the northern Ethiopian rift, *J. Geophys. Res.*, *111*(B5).

Kelbert, A., A. Schultz, and G. Egbert (2009), Global electromagnetic induction constraints on transition-zone water content variations, *Nature*, *460*(7258), 1003–1006.

Kelbert, A., N. Meqbel, G. Egbert, and K. Tandon (2014), ModEM: A modular system for inversion of electromagnetic geophysical data, *Comput. Geosci.*, *66*, 40–53.

Kendall, J., G. Stuart, C. Ebinger, I. Bastow, and D. Keir (2005), Magma-assisted rifting in Ethiopia, *Nature*, *433*(7022), 146–148.

Kendall, J., S. Pilidou, D. Keir, I. Bastow, G. Stuart, and A. Ayele (2006), Mantle upwellings, melt migration and the rifting of Africa: Insights from seismic anisotropy, *Geological Society, London, Special Publications*, *259*(1), 55–72.

Kim, S., A. Nyblade, J. Rhie, C. Baag, and T. Kang (2012), Crustal S-wave velocity structure of the Main Ethiopian Rift from ambient noise tomography, *Geophys. J. Int.*, *191*(2), 865–878.

Kimbel, W., and L. Delezene (2009), 'Lucy' redux: A review of research on Australopithecus afarensis, *Am. J. Phys. Anthropol.*, *140*(S49), 2–48.

Koch, S., and A. Kuvshinov (2013), Global 3-D EM inversion of Sq variations based on simultaneous source and conductivity determination: concept validation and resolution studies, *Geophys. J. Int.*, *195*(1), 98–116.

Koch, S., and A. Kuvshinov (2015), 3-D EM inversion of ground based geomagnetic Sq data. Results from the analysis of Australian array (AWAGS) data, *Geophysical Journal International*, *200*(3), 1284–1296.

Koyama, T., H. Shimizu, H. Utada, M. Ichiki, E. Ohtani, and R. Hae (2006), Water content in the mantle transition zone beneath the North Pacific derived from the electrical conductivity anomaly, *AGU Geophys. Monogr. Ser.*, pp. 171–179.

Koyama, T., H. Utada, and D. Avdeev (2008), Fast and memory-saved 3-D forward modeling code for MT by using integral equation method, in *Abstract book*, 19th workshop on electromagnetic induction in the Earth, China.

Koyama, T., A. Khan, and A. Kuvshinov (2013), Three-dimensional electrical conductivity structure beneath Australia from inversion of geomagnetic observatory data: evidence for lateral variations in transition-zone temperature, water content and melt, *Geophys. J. Int.*, *196*, 1330–1350.

Kustowski, B., G. Ekström, and A. Dziewoński (2008), Anisotropic shear-wave velocity structure of the Earth's mantle: A global model, *J. Geophys. Res.*, *113*(B6).

Kuvshinov, A. (2012), Deep electromagnetic studies from land, sea, and space: progress status in the past 10 years, *Surv. Geophys.*, *33*(1), 169–209.

Kuvshinov, A., and N. Olsen (2006), A global model of mantle conductivity derived from 5 years of CHAMP, Ørsted, and SAC-C magnetic data, *Geophys. Res. Lett.*, *33*(18), L18,301.

Laird, D. (2006), Influence of layer charge on swelling of smectites, *Applied Clay Science*, *34*(1), 74–87.

Lee, K. (2001), Classification of geothermal resources by exergy, *Geothermics*, *30*(4), 431–442.

Lesher, J. (1978), Xenophanes' scepticism, *Phronesis*, *23*(1), 1–21.

Lüdmann, T., C. Kalvelage, C. Betzler, J. Fürstenau, and C. Hübscher (2013), The Maldives, a giant isolated carbonate platform dominated by bottom currents, *Mar. Pet. Geol.*, *43*, 326–340.

Mackie, R., and T. Madden (1993), Conjugate direction relaxation solutions for 3-D magnetotelluric modeling, *Geophysics*, *58*(7), 1052–1057.

Mackie, R., and T. Madden (1993), Three-Dimensional magnetotelluric inversion using conjugate gradients, *Geophys. J. Int.*, *115*(1), 215–229.

Mackie, R., J. Smith, and T. Madden (1994), 3-Dimensional electromagnetic modeling using finite-difference equation – The magnetotelluric example, *Radio Science*, *29*(4), 923–935.

Manoj, C., A. Kuvshinov, S. Maus, and H. Luhr (2006), Ocean circulation generated magnetic signals, *Earth Planets Space*, *58*(4), 429–437.

Marcuello, A., P. Queralt, and J. Ledo (2005), Applications of dispersion relations to the geomagnetic transfer function, *Phys. Earth Planet. Inter.*, *150*(1), 85–91.

Mareschal, M. (1986), Modelling of natural sources of magnetospheric origin in the interpretation of regional induction studies: a review, *Surv. Geophys.*, *8*(3), 261–300.

Matzka, J., N. Olsen, C. Maule, L. Pedersen, A. Berarducci, and S. Macmillan (2009), Geomagnetic observations on Tristan da Cunha, South Atlantic Ocean, *Ann. Geophys.*, *52*(1), 97–105.

McPherron, R. (2005), Magnetic pulsations: their sources and relation to solar wind and geomagnetic activity, *Surv. Geophys.*, *26*(5), 545–592.

Meqbel, N., G. Egbert, P. Wannamaker, A. Kelbert, and A. Schultz (2014), Deep electrical resistivity structure of the northwestern US derived from 3-D inversion of USArray magnetotelluric data, *Earth Planet. Sci. Lett.*

Milsch, H., L. Kristinsdóttir, E. Spangenberg, D. Bruhn, and Ó. Flóvenz (2010), Effect of the water–steam phase transition on the electrical conductivity of porous rocks, *Geothermics*, *39*(1), 106–114.

Mogi, K. (1958), Relations between the eruptions of various volcanoes and the deformations of the ground surfaces around them, *Bull. Earthq. Res. Inst. Tokyo Univ.*, *36*, 99–134.

Mohr, P. (1983), Ethiopian flood basalt province, *Nature*, *303*, 577–584.

Muñoz, G. (2014), Exploring for geothermal resources with electromagnetic methods, *Surv. Geophys.*, *35*(1), 101–122.

Newman, G., and D. Alumbaugh (2002), Three-dimensional induction logging problems, Part 2: A finite-difference solution, *Geophysics*, *61*, 484–491.

Newman, G., E. Gasperikova, G. Hoversten, and P. Wannamaker (2008), Three-dimensional magnetotelluric characterization of the Coso geothermal field, *Geothermics*, *37*(4), 369–399.

Newman, G. A., and D. L. Alumbaugh (2000), Three-dimensional magnetotelluric inversion using non-linear conjugate on induction effects of geomagnetic daily variations from equatorial gradients, *Geophys. J. Int.*, *140*, 410–424.

Nie, X., L.-W. Li, N. Yuan, and T. S. Yeo (2013), A fast integral equation solver for 3D induction well logging in formations with large conductivity contrasts, *J. Comp. Phys.*, *61*, 645–657.

Nurmukhamedov, A., I. Chernev, D. Alekseev, and A. Yakovlev (2010), 3-D geoelectric model of the Mutnov steam hydrothermal deposit, *Izv., Acad. Sci., USSR, Phys. Solid Earth (Engl. Transl.)*, *46*(9), 739–750.

Nyblade, A. (2011), The upper-mantle low-velocity anomaly beneath Ethiopia, Kenya, and Tanzania: Constraints on the origin of the African superswell in eastern Africa and plate versus plume models of mantle dynamics, *Geological Society of America Special Papers*, *478*, 37–50.

Olsen, N. (1992), Day-to-day C-response estimation for Sq from 1 cpd to 6 cpd using the Z:Y-method, *J. Geomagn. Geoelectr.*, *44*(6), 433–447.

Olsen, N., K. Glassmeier, and X. Jia (2010), Separation of the magnetic field into external and internal parts, *Space Sci. Rev.*, *152*(1-4), 135–157.

Padilha, A. L. (1999), Behaviour of magnetotelluric source fields within the equatorial zone, *Earth, Planets Space*, *51*(10), 1119–1126.

Pankratov, O., D. Avdeyev, and A. Kuvshinov (1995), Electromagnetic field scattering in a heterogeneous Earth: A solution to the forward problem, *Izv., Acad. Sci., USSR, Phys. Solid Earth (Engl. Transl.)*, *31*, 201–209.

Parker, R. (1980), The inverse problem of electromagnetic induction: existence and construction of solutions based on incomplete data, *J. Geophys. Res.*, *85*(B8), 4421–4428.

Parkinson, W. D. (1959), Directions of rapid geomagnetic fluctuations, *Geophys. J. R. Astr. Soc.*, *2*(1), 1–14.

Parkinson, W. D. (1962), The influence of continents and oceans on geomagnetic variations, *Geophys. J. Int.*, *6*, 441–449.

Patro, P., M. Uyeshima, and W. Siripunvaraporn (2013), Three-dimensional inversion of magnetotelluric phase tensor data, *Geophys. J. Int.*, *192*, 58–66.

Pizzi, A., M. Coltorti, B. Abebe, L. Disperati, G. Sacchi, and R. Salvini (2006), The Wonji fault belt (Main Ethiopian Rift): structural and geomorphological constraints and GPS monitoring, *Geological Society, London, Special Publications*, *259*(1), 191–207.

Pulkkinen, A., A. Klimas, D. Vassiliadis, V. Uritsky, and E. Tanskanen (2006), Spatiotemporal scaling properties of the ground geomagnetic field variations, *J. Geophys. Res.*, *111*(A3).

Pürschel, M., R. Gloaguen, and S. Stadler (2013), Geothermal activities in the Main Ethiopian Rift: Hydrogeochemical characterization of geothermal waters and geothermometry applications (Dofan-Fantale, Gergede-Sodere, Aluto-Langano), *Geothermics*, *47*, 1–12.

Püthe, C., and A. Kuvshinov (2014), Mapping 3-D mantle electrical conductivity from space: a new 3-D inversion scheme based on analysis of matrix Q-responses, *Geophys. J. Int.*, *197*(2), 768–784.

Puzyrev, V., J. Koldan, J. de la Puente, G. Houzeaux, M. Vazquez, and J. M. Cela (2013), Efficient pre-conditioned iterative solution strategies for the electromagnetic diffusion in the Earth: finite-element frequency-domain approach, *Geophys. J. Int.*, *193*, 678–693.

Rango, T., R. Petrini, B. Stenni, G. Bianchini, F. Slejko, L. Beccaluva, and T. Ayenew (2010), The dynamics of central Main Ethiopian Rift waters: Evidence from δD, δ^{18}O and ^{87}Sr/^{86}Sr ratios, *Appl. Geochem.*, *25*(12), 1860–1871.

Reykjavik Geothermal (2014), Corbetti geothermal power. Advancing dependable, clean geothermal energy in Ethiopia, Brochure.

Ritsema, J., H. van Heijst, and J. Woodhouse (1999), Complex shear wave velocity structure imaged beneath Africa and Iceland, *Science*, *286*(5446), 1925–1928.

Ritsema, J., A. Deuss, H. Van Heijst, and J. Woodhouse (2011), S40RTS: a degree-40 shear-velocity model for the mantle from new Rayleigh wave dispersion, teleseismic traveltime and normal-mode splitting function measurements, *Geophys. J. Int.*, *184*(3), 1223–1236.

Rodger, C. (1999), Red sprites, upward lightning, and VLF perturbations, *Rev. Geophys.*, *37*(3), 317–336.

Rodi, W., and R. Mackie (2001), Nonlinear conjugate gradients algorithm for 2-D magnetotelluric inversion, *Geophysics*, *66*(1), 174–187.

Saemundsson, K. (2008), East African Rift System – An Overview., in *Exploration for Geothermal Resources, organized by UNU-GTP, GDC and KenGen, at Lake Bogoria and Lake Naivasha, Kenya, Oct.*

Sahle, Y., L. Morgan, D. Braun, B. Atnafu, and W. Hutchings (2014), Chronological and behavioral contexts of the earliest middle stone age in the Gademotta formation, Main Ethiopian Rift, *Quaternary International*, *331*, 6–19.

Saibi, H., E. Aboud, and S. Ehara (2012), Analysis and interpretation of gravity data from the Aluto-Langano geothermal field of Ethiopia, *Acta Geophys.*, *60*(2), 318–336.

Samrock, F., and A. Kuvshinov (2013), Tippers at island observatories: Can we use them to probe electrical conductivity of the Earth's crust and upper mantle?, *Geophys. Res. Lett.*, *40*(5), 824–828.

Sasaki, Y., and M. Meju (2006), Three-dimensional joint inversion for magnetotelluric resistivity and static shift distributions in complex media, *Journal of Geophysical Research*, *111*.

Schmucker, U. (1970a), An introduction to induction anomalies, *J. Geomagn. Geoelectr.*, *22*, 9–33.

Schmucker, U. (1970b), Anomalies of Geomagnetic Variations in the South-Western United States, Bull, *Scripps Inst. Ocean*, *13*.

Schmucker, U. (1999a), A spherical harmonic analysis of solar daily variations in the years 1964–1965: response estimates and source fields for global induction – I. Methods, *Geophys. J. Int.*, *136*(2), 439–454.

Schmucker, U. (1999b), A spherical harmonic analysis of solar daily variations in the years 1964–1965: response estimates and source fields for global induction – II. Results, *Geophys. J. Int.*, *136*(2), 455–476.

Schumann, W. (1952), Über die strahlungslosen Eigenschwingungen einer leitenden Kugel die von einer Luftschicht und einer Ionosphärenhülle umgeben ist, *Z. Naturforsch., A: Astrophys., Phys. Phys. Chem.*, *7*, 149.

Schwarzbach, C., and E. Haber (2013), Finite element based inversion for time-harmonic electromagnetic problems, *Geophys. J. Int.*, *193*, 615–643.

Schwarzbach, C., R.-U. Börner, and K. Spitzer (2011), Three-dimensional adaptive higher order finite element simulation for geo-electromagnetics - a marine CSEM example, *Geophys. J. Int.*, *187*, 63–74.

Semenov, A., and A. Kuvshinov (2012), Global 3-D imaging of mantle conductivity based on inversion of observatory C-responses – II. Data analysis and results, *Geophys. J. Int.*, *191*(3), 965–992.

Shimizu, H., H. Utada, K. Baba, T. Koyama, M. Obayashi, and Y. Fukao (2010), Three-dimensional imaging of electrical conductivity in the mantle transition zone beneath the North Pacific Ocean by a semi-global induction study, *Phys. Earth Planet. In.*, *183*(1), 252–269.

Shimizu, H., A. Yoneda, K. Baba, H. Utada, and N. Palshin (2011), Sq effect on the electromagnetic response functions in the period range between 10,000 and 100,000 s, *Geophys. J. Int.*, *186*(1), 193–206.

Simmons, N., A. Forte, L. Boschi, and S. Grand (2010), GyPSuM: A joint tomographic model of mantle density and seismic wave speeds, *J. Geophys. Res.*, *115*(B12).

Simpson, F., and K. Bahr (2005), *Practical Magnetotellurics*, Cambridge University Press.

Singer, B. (1995), Method for solution of Maxwell's equations in non-uniform media, *Geophys. J. Int.*, *120*, 590–598.

Singer, B. (2008), Electromagnetic integral equation approach based on contraction operator and solution optimization in Krylov subspace, *Geophys. J. Int.*, *175*, 857–884.

Siripunvaraporn, W., G. Egbert, Y. Lenbury, and M. Uyeshima (2005), Three-dimensional magnetotelluric inversion: data-space method, *Physics of the Earth and Planetary Interiors*, *150*(1-3), 3–14.

Sokolova, E., and I. Varentsov (2007), Deep array electromagnetic sounding on the Baltic Shield: External excitation model and implications for upper mantle conductivity studies, *Tectonophysics*, *445*(1), 3–25.

Stening, R. (1995), What drives the equatorial electrojet?, *J. Atmos. Terr. Phys.*, *57*(10), 1117–1128.

Sugiura, M. (1964), Hourly values of equatorial Dst for the IGY, *Ann. Int. Geophys. Yr.*, *35*.

Svalova, V., and K. Povarov (2015), Geothermal energy use in Russia. Country update for 2010-2015, in *Proceedings World Geothermal Congress 2015*, pp. 19–24.

Swift, C. (1967), A magnetotelluric investigation of an electrical conductivity anomaly in the South Western United States, Ph.D. thesis, Massachusetts Institute of Technology, Cambridge, Mass.

Tambach, T., P. Bolhuis, E. Hensen, and B. Smit (2006), Hysteresis in clay swelling induced by hydrogen bonding: accurate prediction of swelling states, *Langmuir*, *22*(3), 1223–1234.

Tarits, P., and M. Mandea (2010), The heterogeneous electrical conductivity structure of the lower mantle, *Phys. Earth Planet. In.*, *183*(1), 115–125.

Teklemariam, M., S. Battaglia, G. Gianelli, and G. Ruggieri (1996), Hydrothermal alteration in the Aluto-Langano geothermal field, Ethiopia, *Geothermics*, *25*(6), 679–702.

Tietze, K., and O. Ritter (2013), Three-dimensional magnetotelluric inversion in practice – the electrical conductivity structure of the San Andreas Fault in Central California, *Geophys. J. Int.*, *195*(1), 130–147.

Tikhonov, A. (1950), On determining electrical characteristics of the deep layers of the Earth's crust, in *Sov. Math. Dokl*, vol. 2, pp. 295–297.

Troiano, A., M. Di Giuseppe, Z. Petrillo, C. Troise, and G. De Natale (2011), Ground deformation at calderas driven by fluid injection: modelling unrest episodes at Campi Flegrei (Italy), *Geophys. J. Int.*, *187*(2), 833–847.

Um, E. S., M. Commer, and G. A. Newman (2013), Efficient pre-conditioned iterative solution strategies for the electromagnetic diffusion in the Earth: finite-element frequency-domain approach, *Geophy. J. Int.*, *193*, 1460–1473.

Ussher, G., R. Harvey, C.and Johnstone, and E. Anderson (2000), Understanding the resistivities observed in geothermal systems, in *Proceedings World Geothermal Congress*, pp. 1915–1920.

Utada, H., T. Koyama, M. Obayashi, and Y. Fukao (2009), A joint interpretation of electromagnetic and seismic tomography models suggests the mantle transition zone below Europe is dry, *Earth Planet. Sc. Lett.*, *281*(3), 249–257.

Valori, A., M. Teklemariam, and G. Gianelli (1992), Evidence of temperature increase of CO_2-bearing fluids from Aluto-Langano geothermal field (Ethiopia): a fluid inclusions study of deep wells LA-3 and LA-6, *Eur. J. Mineral.*, *4*(5), 907–919.

Viljanen, A., R. Pirjola, and O. Amm (1999), Magnetotelluric source effect due to 3D ionospheric current systems using the compleximage method for 1D conductivity structures, *Earth, Planets Space*, *51*(9), 933–946.

Vineeth, C., T. Kumar Pant, and R. Sridharan (2009), Equatorial counter electrojets and polar stratospheric sudden warmings – a classical example of high latitude-low latitude coupling, in *Annales Geophysicae*, vol. 27, pp. 3147–3153, Copernicus Group.

Volland, H. (1984), Atmospheric electrodynamics, *Physics and Chemistry in Space*, *11*.

Vozoff, K. (1972), The magnetotelluric method in the exploration of sedimentary basins, *Geophysics*, *37*, 98–141.

Wait, J. (1954), On the relation between telluric currents and the Earth's magnetic field, *Geophysics*, *19*, 281–289.

Wamalwa, A., K. Mickus, L. Serpa, and D. Doser (2013), A joint geophysical analysis of the Coso geothermal field, south-eastern California, *Phys. Earth Planet. Inter.*, *214*, 25–34.

Weidelt, P. (1972), The inverse problem of geomagnetic induction, *Z. Geophys.*, *38*, 257–289.

Whaler, K., and S. Hautot (2006), The electrical resistivity structure of the crust beneath the northern Main Ethiopian Rift, *Geological Society, London, Special Publications*, *259*(1), 293–305.

Wiese, H. (1965), Geomagnetische Induktionspfeile in der ČSSR hervorgerufen durch grossräumige elektrische Leitfähigkeitsstrukturen, *Stud. Geophys. Geod.*, *9*(4), 415–419.

Wilson, J. (1968), Static or mobile Earth: the current scientific revolution, *Proc. Am. Philos. Soc.*, pp. 309–320.

Woldegabriel, G., J. Aronson, and R. Walter (1990), Geology, geochronology, and rift basin development in the central sector of the Main Ethiopia Rift, *Geol. Soc. Am. Bull.*, *102*(4), 439–458.

Xu, T., E. Sonnenthal, N. Spycher, and K. Pruess (2006), TOUGHREACT – a simulation program for non-isothermal multiphase reactive geochemical transport in variably saturated geologic media: Applications to geothermal injectivity and CO_2 geological sequestration, *Comput. Geosci.*, *32*(2), 145–165.

Yee, E., and K. Paulson (1988), Concerning dispersion relations for the magnetotelluric impedance tensor, *Geophys. J. Int.*, *95*(3), 549–559.

Yee, E., and K. Paulson (1990), Reply to the 'Comments on: Concerning dispersion relations for the magnetotelluric impedance tensor' by G.D. Egbert, *Geophys. J. Int.*, *102*(1), 9–13.

Yee, K. (1966), Numerical solution of initial boundary value problems involving Maxwell's equations in isotropic media, *IEEE Trans. Antennas Propag.*, *14*(3), 302–307.

Yirgu, G., C. Ebinger, and P. Maguire (2006), The Afar volcanic province within the East African Rift System: introduction, *Geological Society, London, Special Publications*, *259*(1), 1–6.

Younger, P. (2014), Missing a trick in geothermal exploration, *Nat. Geosci.*, *7*(7), 479–480.

Zhang, L., T. Koyama, H. Utada, P. Yu, and J. Wang (2012), A regularized three-dimensional magnetotelluric inversion with a minimum gradient support constraint, *Geophysical Journal International*, *189*, 296–316.

Zhdanov, M. S., A. Green, A. Gribenko, and M. Cuma (2010), Large-scale three-dimensional inversion of EarthScope MT data using the integral equation method, *Izvestiya, Physics of the Solid Earth*, *46*, 670–678.

Zhengyong, R., T. Kalscheuer, S. Greenhalgh, and H. Maurer (2013), A goal-oriented adaptive finite-element approach for plane wave 3-D electromagnetic modelling, *Geophys. J. Int.*, *194*, 700–718.

Acknowledgements

During my PhD I met a lot of people that were somehow involved in this work and that contributed in various ways to the successful completion of the studies in Ethiopia at Aluto volcano and on the Maldives at Gan geomagnetic observatory. To all those I want to express my sincere thank.

First of all I would like to thank my supervisor Alexey Kuvshinov. His motivating and sparkling enthusiasm about the subject of EM induction and his inexhaustible stream of ideas always were a source of energy to me which kept me going during my PhD studies. I also remember with happy memories our pre- and post-conference trips together through the Australian Bush and the Caribbean jungle of Mexico and the team building exercises at the Rhine.

I would like to express my gratitude to my second supervisor Andy Jackson for the efforts he put into the projects at Aluto and Gan and for his active support of social events within our group that result in the warm and familiar atmosphere and made my stay here as enjoyable as it was.

I am very grateful to Jenneke Bakker, who is the other PhD student involved in the Aluto project. Thank you for your patience and your purposefulness in solving the problems we faced during the fieldwork and the unforgettable journey we made together through the North of Ethiopia after the survey.

I sincerely thank Shimeles Fisseha, our project partner from the Institute of Space Science and Astronomy (IGSSA) of Addis Ababa University, for his help regarding the paperwork for the project, the accomplishment of the survey and the data interpretation.

Many thanks to Michael Becken, Heinrich Brasse, Eva Schill and Yassine Abdelfettah for providing MT stations for the survey at Aluto.

I would like to express my gratitude to Juliet Biggs and Mike Kendall – the initiators and our partners of project ARGOS. I would particularly like to thank the members of the Afar Rift consortium. The possibility they offered to me to attend their meetings gave me important insights into work in Ethiopia. Here I would like to thank especially Kathy Whaler and Nicholas Johnson for sharing their experience and inside knowledge about how to successfully accomplish a MT survey in Ethiopia.

Many thanks to Hjalmar Eysteinsson, Thorleifur Finnsson and Markos Melaku from Reykjavik Geothermal for their local support in Ethiopia and for providing the Polaris bikes.

I would also like to express my thankfulness to Bernhard Friedrichs, Ulrich Matzander and Martin Wilde from Metronix especially for their online support during the fieldwork.

I thank Ulrich Kalberkamp for sharing his information about MT studies at the Tendaho Geothermal field in Ethiopia.

For their contribution to the successful accomplishment of the survey, their immense help and their contribution to good spirits during the fieldwork I would like to thank Behailu Woldesmayet and Yohannes Lemma from the GSE, Elias Lewi from the IGSSA and the students Bereket Gebresilassie and Fantahun Gebre.

My deepest gratitude goes to Girma Andarge, Neway Abera and all the workers and mechanics from the EEPCO geothermal power plant. I would like to mention especially Hussen, Bashir and Bonso and say thanks for your immense help throughout the whole survey (chigger yehlem!) and for becoming good friends. I deeply hope that you are all doing well and that we meet again. Thanks also to all the nameless donkeys, who carried our heavy equipment up to the highest summits of Aluto by the time all motorized bikes needed maintenance.

At this point I would like to thank our drivers Mifta and Dagem for their efforts and for safely driving us around as long as there was air in the tyres.

I thank the crew of Bethlehem Hotel in Ziway for hosting us and for providing us this beautiful accommodation during the survey. Here I especially would like to thank Hana. I wish you all the best with the project you started in Ziway.

For their immense help in getting our equipment out of the customs in Addis Ababa I deeply thank Fassil and Yelebe Birhanu.

I also thank the business man from Nairobi for lending us money to pay the hotel costs in Addis Ababa at the end of the reconnaissance trip. Due to a power outage the credit card payment system was down and we wouldn't have reached the flight back to Zurich in time.

Furthermore I would like to thank Michael Becken for his help regarding the data processing and Naser Meqbel, for his great help in getting started with the ModEM code.

For the work at the geomagnetic observatory on Gan Island I like to express my thanks to Jakub Velimsky and Ahmed Muslim. The stays with you on the Maldives and the technical and constructional work under the equatorial sun definitely belong to the most outstanding happenings during my PhD.

My deepest gratitude goes to my friends, who accompanied me during the last years and during my time in Zurich - many thanks especially to Stephan, Christoph, Moritz and Lisa.

Finally and above all I would like to acknowledge my parents Albrecht and Brigitte and my family for their constant support and their sincere interest in what I'm doing.